IMPACT BEHAVIOUR
OF FIBRE-REINFORCED
COMPOSITE
MATERIALS
AND STRUCTURES

Edited by

S R Reid and G Zhou

CRC

Impact behaviour of fibre-reinforced composite
materials and structures

Impact behaviour of fibre-reinforced composite materials and structures

Edited by

S R Reid and G Zhou

CRC Press
Boca Raton Boston New York Washington, DC

WOODHEAD PUBLISHING LIMITED

Cambridge England

Contents

Preface

The last three decades have witnessed a steady increase in the use of light-weight polymeric composites for structural applications. In addition to their excellent quasi-static mechanical properties such as high specific stiffness and strength, it has become essential for these composite structures to perform well under various types of impact loading. For example, in the aerospace industry, the residual compressive strength of an impact-damaged composite structure has become the design-limiting factor. Major aspects of current damage-tolerant design philosophies in other industrial sectors are similar to that of the aerospace industry. Consequently, this book brings together nine chapters that deal with the various aspects of impact behaviour of fibre-reinforced composite materials and structures. Contributions are provided by some of the world's leading experts in the field. It is hoped that the detailed presentation of a wide range of topics within a single volume will form a sound basis for further studies of impact behaviour and also serve as a useful reference source.

The book has a broad scope and covers both experimental and analytical approaches to understanding the impact response of fibre-reinforced composites, and the effects of impact damage and failure under conditions ranging from low velocity to hypervelocity impact. It is intended to be useful not only to practising engineers, academics, researchers and designers in the field, but also to materials scientists, postgraduate research students, and manufacturers of composite materials and structures. Numerous references are given at the end of each chapter to enable the reader to explore the topics covered in greater detail. Impact problems concerning composite structures involve diverse disciplines, and require the combined skills of engineers, materials scientists and mathematicians. Thus, a degree of overlap between the sections of some chapters is unavoidable. Since the book focuses exclusively on the impact behaviour of continuous fibre-reinforced composite materials and structures, the general subject of composite materials is not covered in depth. Also, short fibre-reinforced composite materials and structures are not considered.

Chapter 1 presents an overview of impact performance of various notched composite beams, assessed by Charpy and Izod impact methods. Details of various experimental approaches are explained, and the ability of the composites to absorb impact energy is discussed together with the associated failure processes. The analytical predictions of the impact energy absorbed based on these methods is presented. Chapter 2 contains a summary of the various destructive and non-destructive techniques for detecting as well as quantitatively characterising impact damage. Particular emphasis is placed on the emerging variants of some well-established techniques such as X-radiography and ultrasonics where the three-dimensional distribution of damage is demonstrated. Some examples, illustrating the capacity as well as the effectiveness of certain selected techniques, are presented. Chapter 3 provides an in-depth examination of some of the experimental techniques that have been used to characterise several composites under various uniaxial states of stresses at high strain rates. It also deals with the low velocity impact responses of beam structures. Additionally, numerical modelling of impact damage is discussed, and some of the issues regarding both stress-based and fracture mechanics-based failure criteria are examined, along with the issue of scaling. Chapter 4 serves as an introduction to impact-damage tolerant composite structural design. The concepts as well as the key issues in damage tolerant design are examined. The sources and effects of damage are described. It also discusses damage tolerant design criteria. The development of analytical and FEM-based models for characterising both the impact event and damage tolerance, respectively, is presented.

Chapter 5 is a comprehensive treatise on both impact damage resistance and damage tolerance assessment of thick glass fibre-reinforced laminates subjected to low velocity and high energy impact. In this chapter, impact response and dominant damage mechanisms occurring during impact are discussed from an experimental perspective and their energy-absorbing characteristics are described. Details of compression after impact tests are also presented. Considerable discussion is devoted to the advantages and disadvantages of both conventional and newly proposed damage tolerance assessment methods, which are illustrated with numerical examples. In Chapter 6, the elastic impact stress analyses of flat plates and cylinders, both made of carbon/epoxy, are provided. Comparisons are made between an analytical model and experimental data for low velocity impact response and this is supplemented with numerical examples. The justification for the quasi-static approximation of low-velocity impact responses is presented with examples. Geometric scaling issues are discussed. Chapter 7 examines the impact responses of and associated damage in graphite/epoxy plates under impact velocities ranging from very low to above the ballistic limit. Two major aspects are covered. One is concerned with obtaining experi-

mentally the plate impact response histories generated by using a gas gun. The other is concerned with predicting analytically the plate impact responses under imperfect boundary conditions by using Mindlin plate theory. The correlation between the two is discussed with numerical examples. Chapter 8 presents a detailed study on the penetration and perforation of glass/polyester laminates and glass/polyester skinned sandwich panels with foam cores under impact velocities ranging from low to above the ballistic limit. The development of two semi-empirical models is discussed, and the nose-shape effects of both indentors and projectiles are examined. One model predicts penetration and perforation energies by using a dynamic enhancement factor. The other model is developed for high velocity impacts where inertia effects dominate. The correlation between the two is discussed with numerical examples. Extensive discussion of and comparisons with experimental data are provided. Chapter 9 deals with the damage analysis of both flat plates of varying thickness and cylinders, made of graphite/epoxy, graphite/PEEK and Kevlar/epoxy, under normal as well as oblique hypervelocity impacts. The damage caused by both the direct impact of projectiles and secondary debris clouds from perforated laminates is examined in detail. Considerable discussion is devoted to the correlation between impact energy and damage crater size.

We wish to express our gratitude to all the contributing authors for their efforts and outstanding cooperation, and to Mrs Patricia Morrison of Woodhead Publishing Limited for her enthusiasm and patience throughout this project. Finally, we would like to thank our wives, Susan and Juan for their support and patience.

SR Reid and G Zhou

List of contributors

GREAVES L G
Mechanical Sciences Sector, DERA, Famborough, Hants GU14 0LX, UK

HANCOX N L
AEA Technology, Harwell, Oxfordshire OX1 0RA, UK

HARDING J
Department of Engineering Sciences, University of Oxford, Oxford OX1 3PJ, UK

KIM J-K
Department of Mechanical Engineering, Hong Kong University of Science and Technology, Clear Water Bay, Kowloon, Hong Kong

LAMONTAGNE C G
Institute of Aerospace Studies, University of Toronto, Ontario M3H 5T6, Canada

REID S R
Department of Mechanical Engineering, UMIST, Manchester M60 1QD, UK

RUIZ C
Department of Engineering Sciences, University of Oxford, Oxford OX1 3PJ, UK

SIERAKOWSKI R L
Department of Civil Engineering, Ohio State University, Columbus, OH 43210, USA

SWANSON S R
Department of Mechanical and Industrial Engineering, University of Utah, Salt Lake City, UT 84112, USA

TENNYSON R C
Institute of Aerospace Studies, University of Toronto, Ontario M3H 5T6, Canada

TSAI C Z
Institute of Applied Mechanics, National Taiwan University, Taipei 106, Taiwan

WEN H M
Department of Mechanical Engineering, UMIST, Manchester M60 1QD, UK

WU E
Institute of Applied Mechanics, National Taiwan University, Taipei 106, Taiwan

ZHOU G
Department of Aeronautical and Automotive Engineering, Loughborough University, Leicestershire LE11 3TU, UK

An overview of the impact behaviour of fibre-reinforced composites

N L HANCOX

1.1 Introduction

Impact may be defined as the *relatively* sudden application of an impulsive force, to a *limited* volume of material or part of a structure. The proviso is that *relatively* and *limited* are capable of an extraordinarily wide range of interpretations. The effects of impact are widely known and yet analysing the phenomenon and relating effects to the forces acting and the materials' properties, in order to predict the outcome of a particular event, can be very difficult. The results of an impact can be largely elastic, with some energy dissipated as heat, sound, internally in the material, etc. Alternatively there may be deformation, permanent damage, complete penetration of the body struck or fragmentation of the impacting or impacted body, or both, as demonstrated in Chapters 5, 7, 8 and 9.

For fibre composite materials it is permanent damage, possibly subsurface and barely visible, penetration and fragmentation, that are of interest. There are various ways of analysing the impact process; in terms of the energy deposited and gross damage produced, micro energy dissipation or by considering the stresses acting on flaws in the material and the effects that are generated. The latter method, which is known as fracture mechanics, is extensively employed with metals but will only be alluded to here. In practice the impact behaviour of composites merges into the general area of damage mechanics.

Much of the early pioneering work on the properties of composites under impact is still relevant as the concepts employed in the analysis are the same though the results, depending specifically on the materials used (fibre, resin), interface and method of fabrication, may have been superseded. For this reason many of the earlier references concerning the impact behaviour of composite materials are employed here. This is not a detailed historical treatment and references are chosen for their appropriate nature rather than for being first (or last!) in the field.

In this chapter it is intended to view impact in a general way. Later

contributions will focus on specific situations in which the material and/or impact process is more closely defined. The general principles set out in Chapter 1 should, however, be applicable in all situations.

1.2   Composite materials

To discuss the impact behaviour of composites it is helpful initially to consider the nature of the materials. Modern polymer composites based on glass, carbon, aramid, ceramic or polymer fibres in a polymer matrix are heterogeneous and anisotropic materials. They have a low density, high strength and stiffness and hence excellent specific properties (the ratio of the property to the density or specific gravity) in the fibre direction. They can be relatively easily formed into components with complex shapes by vacuum pressure compaction or pressing at temperatures of no more than ~200°C for 1 h or more, though post curing may be needed. Because of the need to have long fibres for optimum properties and, in many cases, easier and effective processing, composite structures are often shells. They have excellent properties within the plane of the shell, in the fibre direction in tension, and to a lesser extent, in compression. The performance transversely, through the thickness and in shear and impact, is poorer. Generally, properties which are matrix dependent are much lower than those which are governed by the fibre. Nevertheless the role of the matrix is vital in composite behaviour; protecting the fibre, transferring stresses and, in some cases, alleviating brittle failure by providing alternative paths for crack growth.

1.2.1 Properties of fibres and resins

Reinforcing fibres usually have a diameter of 5–10 μm, though it may be up to ~100 μm, for certain types (e.g. boron), and a modulus and strength of the order of 70–800 GPa and 1000–7000 MPa, respectively. The failure strain is ~0.27–5.0%. Carbon and aramid fibres may exhibit an increasing modulus with increasing strain due to changes in their internal structure during stressing. The resins, whether thermosets or thermoplastics, have a modulus and strength of the order of 2–5 GPa and 50–100 MPa, respectively, and a strain to failure of ~1% upwards. It should be noted that resin failure strain is usually well in excess of the minimum figure. Properties of resins are usually strain rate dependent and markedly influenced by temperature (see a fuller treatment in Chapter 3). This occurs because the glass transition temperature, Tg, which is indicative of the upper working temperature, is ~80–200°C for most resins. This is much closer to room temperature than is the case for the melting or degradation point of most structural

Table 1.1. Some fibre and resin properties

Material	Density (Mgm^{-3})	Tensile modulus (GPa)	Tensile strength (MPa)	Strain to failure (%)
Glass fibre	2.49–2.55	73–86	3400–4500	3.5–5.4
Carbon fibre	1.7–2.0	160–827	1400–7070	0.27–1.9
Aramid fibre	1.39–1.45	73–160	2400–3400	1.4–4.6
Inorganic fibre	2.0–3.97	152–462	1720–3900	
Phenolic resin	1.0–1.35	3.0–4.0	60–80	~1.8
Polyester resin	1.1–1.23	3.1–4.6	50–75	1.0–6.5
Epoxy resin	1.2–1.2	2.6–3.8	60–85	1.5–8.0
Bismaleimide resin	1.2–1.32	3.2–5.0	48–110	1.5–3.3

materials. Hence creep can be a problem with polymers at relatively low temperatures.

Some fibre and resin properties are summarised in Table 1.1. It should be noted that these are indicative of the property range for the materials. Individual grades/types of material, the way the property is measured, etc., might cause variations outside the limits given.

1.2.2 Composite properties

Table 1.2 lists some composite properties. These are again indicative of the performance of 60 v/o (fibre volume fraction), unidirectional fibre com- posites. Values will vary with the type of fibre (e.g. grade of carbon fibre), method of test, matrix and way the specimens were fabricated. The im- portant points to appreciate are the very significant differences between longitudinal and transverse properties, the lesser difference between longi- tudinal tensile and compressive strengths and the disparity between the interlaminar shear strength (ILSS) and tensile/compressive strengths. Shear modulus is in the range 2.5–5.0 GPa for all of the materials. Longitudinal tensile and compressive strain to failure is essentially that of the fibre. Trans- versely the figure may be lower, ~0.3–0.5%, and is governed by the prop- erties of the interface and resin matrix. Laminates, containing layers of fibres with different orientations within a plane, may have higher impact, shear and transverse properties, but lower longitudinal performance. Charpy impact energy for unnotched materials, stressed in the longitudinal or fibre direction, varies widely depending on the interface, matrix and experimental details. There may also be errors due to the scaling up of results for different cross section specimens. Charpy impact strength in the transverse direction (i.e. at right angles to the fibre) can be very low.

It is common to use G_c, the critical strain energy release rate, as a measure

Table 1.2. Some properties of unidirectional composite materials

Material	ρ (Mg m⁻³)	E_{lt} (GPa)	E_{tt} (GPa)	σ_{lt} (GPa)	σ_{tt} (MPa)	σ_{lc} (GPa)	τ (MPa)	G_{1c} (J m⁻²)	G_{2c} (J m⁻²)	Imp st. l, (kJm⁻²)	Imp st. t, (kJm⁻²)
Glass	1.8–2.0	37–53	9.0–13.6	1.2–1.9			53–83	125–3300	600–1200	Up to 609	Up to 28
Carbon	1.54–1.66	125–330	5.9–10	1.76–2.9	30–80	0.78–1.6	70–127	60–3300	154–2033	8–150	0.2–4.0
Aramid	1.36–1.4	66–107	4.1	1.29–1.5	27	0.19–0.28	38–69	1100		20–40	

Where ρ is the density, E_{lt} and E_{tt} are the longitudinal tensile and transverse tensile moduli, respectively, σ_{lt}, σ_{tt} and σ_{lc} are the longitudinal tensile, transverse tensile and longitudinal compressive strengths, respectively, τ is the shear strength (also known as the interlaminar shear strength or ILSS), G_{1c} and G_{2c} are the critical works of fracture for the 1 and 2 deformation modes and Imp st. l, and Imp st. t, are the longitudinal and transverse Charpy impact strengths.
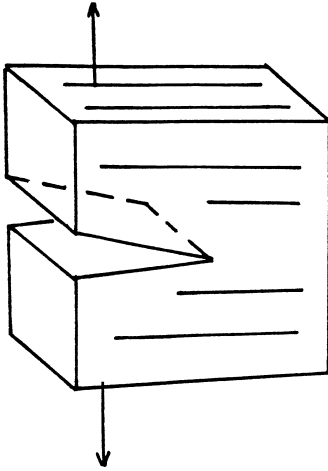
1.1 G_{1c}. Crack propagation parallel to the fibres. The horizontal lines show the fibre direction.

of toughness, though some workers distinguish between initiation and propagation energies for this quantity. Often G_c is equated to 2γ, where γ is the work of fracture or the energy required to produce a new surface in a material. It is important to remember that both γ and G_c refer to a specific mode of deformation (a tensile type opening for G_{1c}) and that the direction of the fibres in relation to the sense of deformation must be clearly defined, see Fig. 1.1. In Table 1.2, G_{1c} refers to the extension of a crack parallel to the fibre direction and is thus analogous to the transverse Charpy impact energy. G_{1c} defined in this way is also known as the mode 1 interlaminar shear work of fracture. More information on fibre, resin and composite properties is available, for instance, as is a simple description of the various deformation modes associated with G_{1c}, G_{2c} and G_{3c}.[1] A general account of composites fracture mechanics and toughening mechanisms is given in Hancox and Mayer.[2] More details and descriptions of the experimental difficulties of determining the critical strain energy release rates and the influence of materials' and testing parameters on the results have been recorded.[3] For metals, figures of 4–140 kJm^{-2} have been reported for the work of fracture, γ.[4]

An advantage of composites, compared with more conventional materials, is the ability of the designer/fabricator to tailor mechanical and thermal properties over a wide range by suitable choice of fibre type, orientation, loading (within limits), and possibly the resin. It is possible to reduce in-plane anisotropy to give a quasi-isotropic material and improve shear and transverse (though not through-thickness) performance by laminating. However, the specific property in a given direction is reduced as

more 'redundant' material has been added. Laminates, with successive layers orientated differently, are in some ways akin to plywood. Alternatively, a wide range of woven, knitted and needled fabrics, often based on glass or aramid fibres, is available for reinforcement. The first two types of fabric possess good reinforcement in more than one direction in a plane without the need for laminating. Disadvantages are that strength and stiffness properties are reduced because of out-of-plane deviations of the fibres due to the weaving process and lower fibre volume fraction, possibly fibre/fibre wear at cross over points and physical damage to the fibre occurring during needling.

It has so far been implicit that long/continuous fibre tows are used in composite construction. Many products, especially those reinforced with glass fibre, employ short (sub-micron or mm), intermediate (cm) or randomly laid, continuous fibres in a plane, or combinations of these, for reinforcement. These materials, with thermoset or thermoplastic matrices and sometimes special additives to aid processing, are known as bulk or dough moulding compounds, injection moulding feedstock and stampable mat thermoplastics. Sheet moulding compound contains, in addition to chopped fibres, continuous or woven glass fabric. These types of composite are very widely used because of the relative ease with which they can be pressed, moulded or extruded into useful components.

One difficulty arising in the discussion of the properties of composites relates, ironically, to one of the virtues of the materials – the ability of the user to tailor their properties to suit the design. There is a huge number of fibre lay-ups, fibre types, combinations and forms, resin matrices, additives and cure schedules to choose from and it can be very difficult to extrapolate from, or relate, the results for one unique combination to those of another. This has the effect of making quoted property measurements appear very diverse.

1.3   Failure processes

New situations and materials tend to be judged initially by comparison with existing ones. Since the principle class of construction materials used in high performance applications is metals, composites are usually compared with them. Generally, metals tend to be dense, stiff, strong, good conductors of heat and electricity, isotropic and inexpensive. In particular many show plastic behaviour before failure and it may be possible to remove the effects of deformation/damage by annealing and/or reworking the material. Unfortunately, at least on a significant scale, polymer matrix fibre composites do not exhibit this type of behaviour – elastic deformation is followed by irreversible damage and failure. Another important influence on composite

performance, especially in failure, is the heterogeneous nature of the material on a micro/meso scale.

Composites are generally strong, and have a reasonable impact resistance, if the applied stress is in the fibre direction. In other directions they tend to be weak and to have a low impact resistance. Small secondary stresses in the transverse direction or unexpected stresses due to an impact, in a weak direction, can easily cause damage. Because of the ease with which localised permanent damage can be produced and the low values of γ or G_{1c} for failure parallel to the fibres, or between plies in a laminate, G_{1c} is sometimes regarded as critical and the focus of most attention in impact work. Fracture mechanics methods of determining G_{1c} are favoured over traditional measurements of impact strength, from which γ and arguably G_{1c} can be determined, because of their greater accuracy and virtual elimination of extraneous energy absorption. However, the assumptions implicit in fracture energy determinations may not be true for fibre composites, where crack propagation may be dominated by crack blunting, fibre pull-out and fibre/matrix delamination. It has been suggested that in such circumstances conventional fracture toughness may not necessarily be the best measure of overall toughness.[5] Impact tests can be more useful, although not so readily analysed as fracture toughness measurements, and can be conducted at strain rates more representative of the deformation rates seen in service. The topic can be a contentious one of which the reader should be aware.

There are five basic mechanical failure modes that can occur in a composite after initial elastic deformation. These are:

- Fibre failure, fracture, and, for aramids, defibrillation.
- Resin crazing, microcracking and gross fracture.
- Debonding between the fibre and matrix.
- Delamination of adjacent plies in a laminate.
- Fibre pull out from the matrix and stress relaxation.

In practice, debonding and delamination are not always distinguished. A very detailed list of types of damage in composites and associated references is given in Chapter 2.

Behaviour is modified by external conditions. Polymeric fibres, which depend for their properties on molecular alignment, suffer a fall-off in performance above ~100°C, aramids degrade at elevated temperatures, carbon fibres, if unprotected from air, oxidise at 300–400°C and glass will soften at 500–800°C. The environment, particularly water, causes the plasticisation of thermosets, lowering the Tg and causing microcracking and debonding and possibly corrosive effects in stressed glass fibre composites. The interface, at which mechanical keying and chemical bonding are involved, is

very sensitive to moisture. Sometimes the effects are reversible on drying out – sometimes they are not. All these factors are of relevance to impact performance because of their influence on composite mechanical properties.

1.3.1 Why are composites prone to impact damage?

The lack of plastic deformation in composites means that once a certain stress level is exceeded permanent damage, resulting in local or structural weakening, occurs. Unlike a metal, which may undergo plastic deformation but can retain its integrity (e.g. water tightness), composites stressed above a certain level, though possibly retaining some structural properties, are permanently damaged. A blow with an energy of ~1 J or less at ~2 ms^{-1} can cause irreversible damage in a realistic composite laminate. To summarise, the reasons for a low impact strength are:

- Low transverse and interlaminar shear strength.
- Laminar construction, which is required if the reinforcing fibres are to be used efficiently and anisotropy reduced.
- No plastic deformation.

1.3.2 Estimation of the stresses acting in an impact

It is informative to try to estimate the stress generated by an impact. The situation is very complex and our simple approach merely indicates the order of magnitude of the stress. Consider a steel ball of radius ~25 mm and mass 0.5 kg, with an energy of 1 J impacting a surface at a velocity, V, of 2 ms^{-1}. The compression stress generated, σ_c, is, given by

$$\sigma_c = V(E_{ct}\rho)^{0.5} \qquad [1.1]$$

where E_{ct} is the transverse compressive modulus and ρ the density.[6] Typical values of these quantities are 10 GPa and 2×10^3 kgm^{-3}, respectively, giving $\sigma_c = 9$ MPa. In practice, compressive loading could cause localised bending and transverse failure in suitably oriented plies and generate interlaminar shear stresses. The compressive stress will continue to act until the impacting body rebounds. The stress wave will propagate into the impacted material, with a decreasing amplitude, and be reflected at the back surface as a tension wave.

It is possible to apply the theory of Hertzian contact stresses[6] to the estimation of the impact stress. This indicates that if the diameter of the contact area is $2a$ the maximum shear stress appears below the point of contact at a depth of ~a/2. The maximum contact stress, q_0, for indentation on a plane surface is

$$q_0 = 0.7aE/R \hspace{3cm} [1.2]$$

This assumes a common Poisson's ratio of 0.3 and that the controlling modulus is that of the composite through its thickness ~10 GPa. If a = 0.25 mm and R, the radius of the impactor, is 25 mm as before, the maximum compressive stress is found to be ~70 MPa and the maximum shear stress, ~0.31 q_0, is 22 MPa. Both approaches neglect, among other points, the differences in the properties of the impacting and impacted bodies, geometrical effects and the heterogeneous, anisotropic nature of the composite. In addition, whether a static theory of contact stresses can be applied to an impact situation is open to debate. In view of all these factors the results are approximate but they do indicate the potential for damage.

1.4   Measurement of impact strength

1.4.1   Izod and Charpy methods

The Izod and Charpy tests have been used for many years to assess the impact performance of metals particularly with respect to the brittle/ductile transition temperature and notch sensitivity.[7,8] The Izod test is still widely used for polymers. In the Izod test a rectangular or square cross section bar of specified dimensions is clamped at one end and struck towards the top of the test piece with a pendulum. For the Charpy test a beam is rested freely against two anvils and struck in the centre by a pendulum. In the former case, if the specimen is notched, the notch is at the top of the clamped section and usually faces the direction of strike. Charpy specimens may be machined with U or V notches in the centre of the beam opposite the direction of strike, see Fig. 1.2. For metal specimens, dimensions are controlled as stated in the various national standards. In either test, and with any material, the impact energy may be overestimated because energy is:

- Stored elastically in the specimen prior to failure.
- Energy is dissipated acoustically, thermally, in the kinetic energy of the failed parts, etc.

Despite the somewhat arbitrary nature of the tests, difficulties of cross-correlating information and of scaling impact energies to bodies with different cross sections, they were readily adapted by the plastics industry and national standards established. The Izod impact testing of rigid plastics[9] and the impact behaviour of plastics including the effects of flow direction in moulded specimens, notching, notch tip radius and notch depth and the relation of the impact energy to the stress concentration factor[10] are both covered. Also dealt with very thoroughly are the Izod and Charpy impact
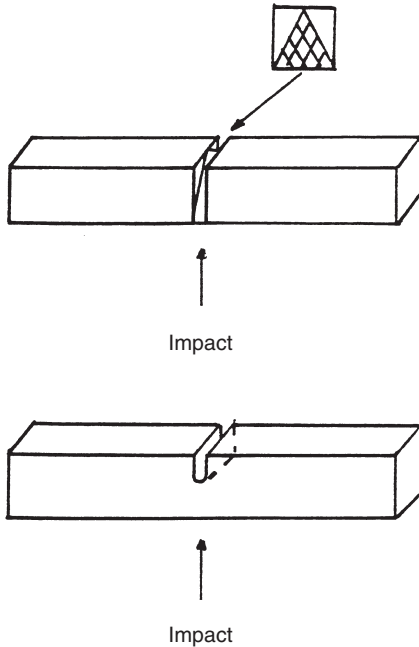
Impact

Impact

1.2 Charpy test specimens with triangular and U-shaped notches. The arrow shows the direction of impact.

procedures for plastics.[11] When carbon fibres were developed, and the potential of carbon fibre composites in aerospace was realised, these test methods, especially the Charpy, were adapted for composites, including glass and aramid fibre materials. If the striking arrangement in a Charpy test is such as to load the specimen in 4 rather than 3 point bending, see Fig. 1.3, the work of fracture is increased, presumably because of the different shear stress patterns in the two cases. Sometimes the Charpy test is viewed as an accelerated static test, but there is evidence that the energy stored to maximum load differs in the static and impact cases, with laminated specimens exhibiting a reduced modulus, and hence greater energy storage, in impact.[12] A similar conclusion has been reached for sandwich panel specimens with composite skins. In this case quasi-static testing gave results 50–65% less than impact measurements.[13] The physical cause is probably related to differences in the transverse shear behaviour at the different strain rates in the two cases. In parallel with the work on traditional impact tests the fracture mechanics approach was developed to describe composite fracture. This method is more complex theoretically and experimentally but arguably, for some materials, is more suitable for use in design.

Impact

Support

Impact

Support
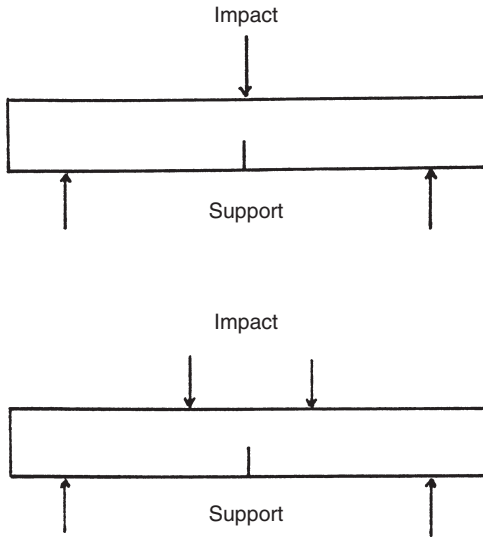
1.3 Schematic diagram of Charpy specimens impacted in 3 and 4 point loading, respectively.

To some extent the effect of the notch is to reduce the sources of error due to stored energy. In this respect a chevron notch is often used in the Charpy test. This is formed by making two opposing cuts from the base of the specimen to the top, meeting at a point on the top surface. This leaves a triangular shaped cross section of material joining the two halves of the specimen, see Fig. 1.2. The argument is that if the specimen is struck at the back failure starts at the apex before significant energy storage due to bending occurs elsewhere in the specimen. Thus the recorded impact energy is more nearly the true value. Notches are also used to determine if the material is notch sensitive. If a scratch or surface flaw, acting as a stress raiser, severely reduces the impact strength of a component, because the stress concentration at the notch tip cannot be relieved, it is important to establish this prior to use.

One method of expressing impact energy, for a plastic or a composite, is in terms of the formula

$$U = E/b(d - c) \qquad\qquad [1.3]$$

where U is the impact energy, and E the energy registered in the test, for a specimen of breadth b, and depth d, containing a notch of depth c. This is a simple scaling formula. By adopting a fracture mechanics approach it can be shown[2] that the fracture energy may be expressed thus:

$$U = E/\phi b(d - c) \qquad\qquad [1.4]$$
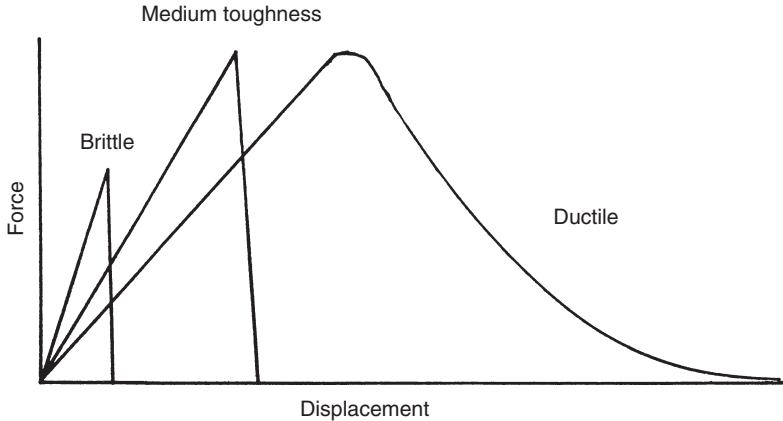
1.4 Idealised load displacement characteristics for brittle, medium toughness and ductile material. Note that the materials will differ in elastic properties – hence the different slopes. Real characteristics will be much less smooth.

where ϕ is a calibration factor which depends on specimen and crack dimensions and compliance. In using either the Charpy or Izod test it is most important to specify the fibre direction in relation to the main stresses applied by the impact force.

A trawl through the literature reveals that the Charpy test is much more widely used for composites than the Izod method. The variety of specimen shapes and notches is large – a typical specimen might be 6×6 mm in cross section and 60 mm in length with a U, V or chevron notch, the former up to half the thickness of the specimen and for a V notch an angular opening of 30 or 45°. In another case the specimen was a laminate 2 mm thick, 13 mm wide, with a V notch on either side in the thickness. Pendulum strike velocities are typically ~2–4 ms^{-1} with energies, governed by the mass of the pendulum, of 0.4–15 J, and exceptionally up to 100 J. Some idealised load displacement traces, which could be obtained from machines with an instrumented striker head or tup, are shown in Fig. 1.4. Instrumenting the striker enables the force as a function of time into the impact, or displacement, to be obtained. The characteristics are for brittle, intermediate and tough materials, respectively. The difference in the areas under the curves in the three cases is obvious. Real traces tend to be a lot less clean because of ring in the system, possibly bouncing of the striker and repeated impact and complex material behaviour. A variety of impact tests using the DYNA3D FEA code were recently analysed and it was concluded that ringing or noise is due to local bending of plies around the tip of the impactor.[14]

By integrating the area under the load or force displacement curve, and noting the value up to the maximum load or the load at first failure, it is possible to deduce the energy required to start or initiate damage and relate it to the energy to propagate damage and the total energy involved, as indicated in Fig. 5.4 of Chapter 5 and Fig. 8.3 of Chapter 8. The ratio of the propagation energy, E_p, to the initiation energy, E_i, is known as the ductility index, D.[15]

$$D = E_p / E_i \qquad\qquad [1.5]$$

Values range from zero upwards. The zero value indicates that, in this type of test, the material is behaving in a completely brittle manner. The larger D, the more energy is used in propagating failure compared with that to cause initiation. Note that a high index does not imply a material with high absolute toughness. What is required in practice is a large initiation energy and a large propagation energy. The reader should be aware that some authors define D as the ratio of propagation to total energy, E_t. An analogous situation arises with G_{1c} measurements where there is a relatively low initiation energy followed possibly by a higher propagation value. Some typical figures for G_{1c}, for unidirectional sized and untreated glass fibre epoxy composites, are given by Krawczak and Pabiot.[16] For crack initiation in the sized material the figure is $87 \, Jm^{-2}$ and $438 \, Jm^{-2}$ for propagation. For unsized fibre the figures are 224 and $185 \, Jm^{-2}$, respectively, indicating that in this case once a crack is initiated it propagates more easily.

1.4.2 Other methods of determining impact energy

An increasingly popular method of assessing impact energy is the falling dart test,[17] which was originally developed for rigid plastics. The standard covers both instrumented and uninstrumented testing procedures. The test piece, either 60 mm in diameter or 60×60 mm square, and 1–4 mm thick, is supported on a hollow steel cylinder with an inside diameter of 40 mm. It may be clamped in position. The steel striker has a polished hemispherical head, either 10 or 20 mm in diameter, and is allowed to fall from a height of up to 2 m onto the specimen (equivalent to a maximum velocity of $6.3 \, ms^{-1}$). For a puncture test on a composite, a strike velocity of $4.4 \, ms^{-1}$ and a total striker mass of 5–20 kg (equivalent to energies of 48–193 J) are preferred. Many variants of the dropped weight test are described in the literature, with specimens ranging in size from 127×127 mm square to 100 mm in diameter, and impactors with tip radii of 5–12.7 mm. Other variants are noted in Chapters 5 and 8. The impact velocity can be varied, within reason, to suit a particular requirement. Details of the impact testing of skinned sandwich panels, sometimes using specially shaped impactors, are
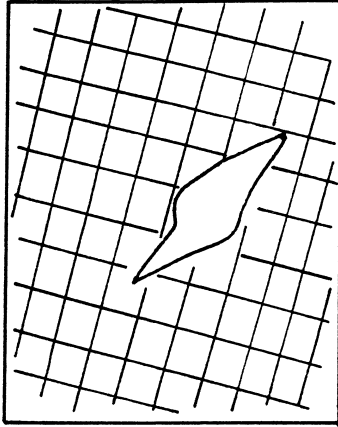
1.5 C-scan of a laminated carbon fibre composite panel impacted at 50 ms^{-1} with a 6 mm diameter indenter. Note damage development along a diagonal.

given in Hildebrand.[13] It was noted that pyramidal and hemispherical indenters gave different results and it was concluded that these different test methods are not even qualitatively comparable.

Another way of assessing the impact energy in a Charpy, or falling weight, test is to repeatedly impact the same specimen, until failure occurs, under conditions which do not cause immediate failure, or to increase the impact energy on each successive blow until failure occurs. While this may be acceptable for ranking materials or designs, the build up of damage, which is not quantified before failure, makes the absolute interpretation of the results uncertain.

To increase the impact velocity it is necessary to fire the projectile at the specimen. This may involve a conventional bullet, an anti-tank shell, a small ball ~1–40 g in weight fired by a gas gun, a soft projectile,[18] or a liquid drop.[19,20] See Chapters 7–9 for further details. The impact velocity can range from 20–100 ms^{-1} to 6000 ms^{-1} plus. Under certain conditions the projectile may penetrate the specimen cleanly or it may cause overall flexing, fibre break out at the back surface or considerable delamination. The latter can be assessed ultrasonically. In laminated specimens the damage pattern may show greater development in certain directions corresponding to less favourably oriented plies, see Fig. 1.5. One problem is having a specimen which is sufficiently large that the damage does not interact with the boundaries.

One study of soft body impact involved firing a 3 g gelatine pellet at 90–190 ms^{-1} at a carbon thermoplastic matrix target. The damage was assessed by measuring the extent of delamination ultrasonically. The

damage was similar in form to that due to an aluminium projectile, though less extensive. The erosion, or impact damage of composites by repeated liquid impact, has been studied at velocities of $90\,ms^{-1}$ upwards. A liquid or a soft body behaving compressibly exerts a pressure of ρcV on the surface it strikes, where ρ is the density, V the impact velocity and c the stress wave velocity in the liquid. Liquid flowing outwards from under a curved surface causes considerable localised shear damage, particularly if the initial pressure has ruptured the surface. At high velocities, $\sim 1000\,ms^{-1}$, the compression wave generated by the liquid drop, on being reflected as a tension wave from the back surface of the specimen, causes scabbing, or the removal of material, if the transverse tensile strength is low. This has been observed in carbon fibre composite specimens. Fibres end-on to the direction of impact have an increased resistance to liquid erosion, probably due to the much better compressive properties of the fibre in the longitudinal, as compared with the transverse, direction. Practically, elastomer coatings (e.g. polyurethanes) are used to protect surfaces from liquid and solid particle erosion.

In many of the cases involving high velocity impacts, with either hard or soft bodies, the experiment has been set up to test a special combination of projectile and material/design and the object is to determine the behaviour of the specimen rather than to derive a more fundamental impact energy; see Chapter 9.

Three other areas of impact study involve:

- Barely visible impact damage (BVID).
- The measurement of a property after impact.
- The impacting of stressed bodies.

All are somewhat specialised and are related to damage tolerance, and the latter to the effects of superimposed stresses on impact behaviour. A general discussion of damage tolerant structural design is given in Chapter 4. BVID occurs when an object, such as a tool, is dropped accidentally onto a composite structure. For example, a thin shell-like, highly stressed aerospace component is particularly vulnerable in this respect. The danger is that the damage is so slight that it is not readily noticed by the naked eye but nevertheless compromises the load bearing capacity of the component. Apart from the obvious step of avoidance, possible solutions to this problem are the incorporation of sensitive sensors in the component and the use of damage tolerant matrices. An FEA analysis[14] attributes back surface tensile damage in an impacted laminate, with little or no evidence of damage at the front, to localised bending in the vicinity of the impactor. If the back of the specimen is not visible this would be classified as a type of BVID.

Since many crucial aerospace composite components are stressed in compression it is usually the compression strength that is evaluated after

the impact. If the composite suffers debonding as a result of impact the compression strength will be affected because plies can act independently; limited microbuckling could occur on loading in compression and the strength would be reduced. Broken fibres would be an additional cause of a reduction in compression strength, possibly because of the complex stress field in the vicinity of the break. The compression strength after impact, CAI, is related to BVID, though the impact energies involved are probably greater than in the latter case. The approach to evaluating the damage is different, however. The crucial parameter is now how much a given energy or velocity impact reduces the strength of the material or component. Clearly the greater the strength retention, for given conditions, the better the material. As an illustration of the effect, a drop weight test with an impact energy of 30 J causes a reduction in the compressive stress of a laminate of ~30–40%.[21] The authors developed a model based on the assumption that the change in compressive strength is related to the degradation of flexural stiffness in the impacted laminate. Fitting parameters are required and have to be determined experimentally but the model then gives a good fit to the data for the complete range of impact energies involved. Another, typical, account of the evaluation and analysis of the process for carbon fibre laminates is given in Ishai and Shragai.[22] Generally the resulting degradation is influenced by clamping conditions and specimen geometry, since these can determine the nature of the damage produced under impact (e.g. shear delamination vs fibre failure). For similar studies see Chapter 5.

The study of the impact of pre-stressed materials was initiated[23] and more recently explored in a lengthy programme whose results have been summarised.[24,25] The aim is to establish the combined effects of impact and a superimposed tensile or compressive stress. The combination is usually more damaging than either factor on its own. In the earlier work unidirectionally reinforced carbon and glass fibre specimens were stressed in tension up to 1.5–2.0 GPa and impacted with a wedge-shaped pendulum with a maximum energy of 4 J. The form of the results is shown in Fig. 1.6. The stress to cause failure, after impact in the unstressed state, falls linearly with increasing impact energy. This is equivalent to an ordinary notch sensitivity tensile test. Specimens stressed at the time of impact, however, require a lower stress to cause complete failure when tested to destruction after impact. It was noted that generally a high fibre strength and low fibre modulus lead to a higher impact performance. Later work investigated the effect of the wedge radius and role of delamination on the onset of failure – a low transverse strength could decrease the impact response. Rigidly supporting the back of the specimen caused different behaviour. Now the specimen could not bend when struck and no compressive fracture was
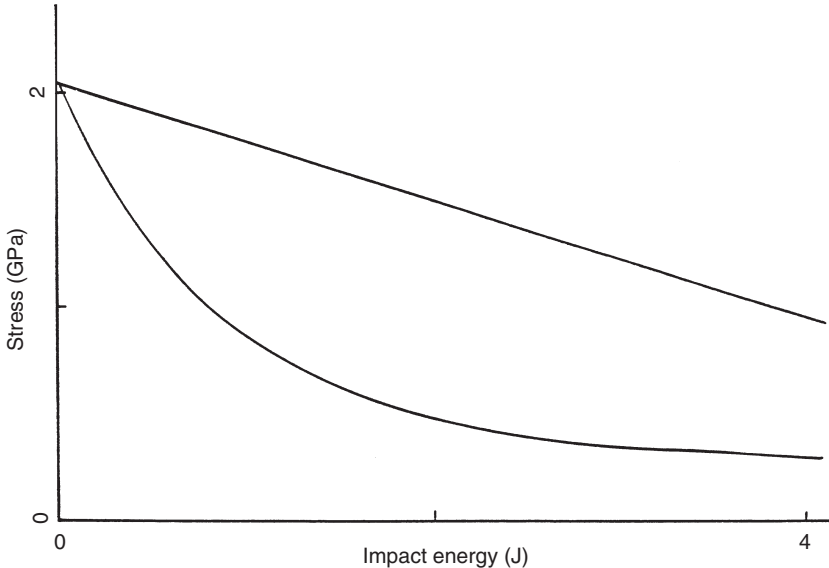
1.6 Effects of tensile prestress on impact energy. The upper line is for specimens impacted unstressed and then tested to failure in tension. The lower curve is for specimens impacted in the stressed state. In practice the prestress had to be adjusted to get impact on failure. The material was an intermediate modulus, unidirectional, carbon fibre/epoxy composite.

observed running in from the impacted face. There was also an optimum fibre volume loading ~67 v/o for maximum toughness.

In the later work,[24,25] carbon and glass fibre epoxy and thermoplastic laminates, prestrained in tension or compression up to 0.5%, were impacted at velocities ranging from a few meters per second up to 2.78 kms^{-1} using pendula, small projectiles and rifle bullets. The corresponding impact energies could be as high as 2.69 kJ. Damage was assessed visually and by using ultrasonic C scanning. Generally, impact with or without prestraining caused delamination, breakout of rear plies and sometimes complete penetration. The damage diameter, as determined by C scan, for different types of carbon fibre laminate as a function of prestrain, is shown in Fig. 1.7. Similar results were obtained with glass and aramid fibre panels. Compressive prestrain appeared more damaging than tensile prestrain, probably because the initial delamination allows the individual plies to buckle more easily under compression. Simultaneous strain and impact lowered the failure strain below that observed in the sequential case, see Fig. 1.8. Reasonable success was achieved in modelling the behaviour of cross ply laminates using the VEC-DYNA3D FEA code. It was possible to account for
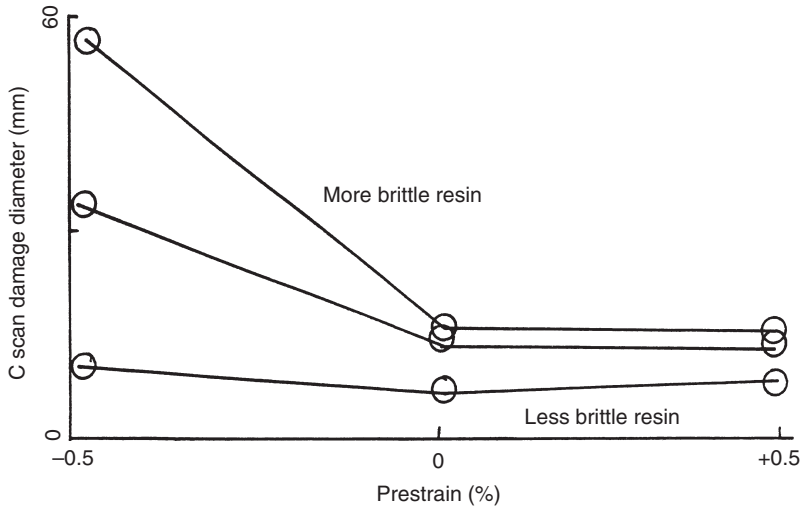
1.7 Delamination diameter, determined by C-scan, for carbon fibre composite laminated panels impacted at 50 ms⁻¹ with a 6 mm diameter impacter at an energy of 1.1 J. Tensile prestrain has a minimal effect but compressive prestrain, combined with a more brittle epoxy resin leads to considerable damage.
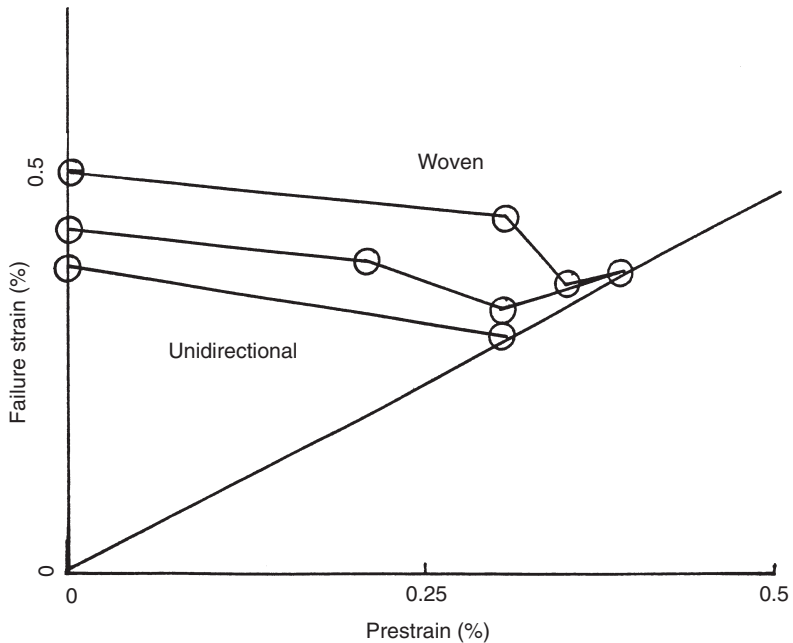
1.8 Effects of prestress on failure strain of a carbon fibre laminate. The figure shows the failure strain of the material impacted whilst prestrained and then, if required, strained to failure. The highest result is for a woven material. The impact velocity was 80 ms⁻¹ and the impact energy 2.8 J.

penetration and the type and extent of damage. Overall it is important to use the correct boundary conditions. Potential failure mechanisms are complicated and interrelated and if one is not correctly assigned this may effect the predictions.

Although much information on impact has been generated experimentally it is frequently very difficult to compare results because of differing specimen dimensions, boundary conditions, testing procedures, etc. The reader may be forgiven for thinking that the subject is poorly regulated and somewhat arbitrary. It has been suggested[26] that specimen details seem to be resolved by a process of random choice. Certainly anyone perusing much of the literature on the impact properties of composites is struck by the way in which most papers approach the experimental side, appearing to use whatever materials and equipment are to hand rather than making a choice which fits in with other work. Having said that, the present author must confess to having tested specimens, 1×1 m square $\times 100$ mm or more in thickness, by dropping steel cylinders, weighing up to 500 kg, onto the surface from a height of about a meter. The problem is that in many cases the modelling of the behaviour of a structure in an impact situation is so difficult that the best way to tackle the problem is to test the real structure in the most realistic way possible. No doubt as our knowledge and computational ability progress this will become less necessary but at present there is often nothing like a field trial.

1.5   Theoretical prediction of impact energy

Having discussed the methods for measuring impact energy and indicated the spread of results obtained it is necessary to develop a theoretical framework to describe the impact process. There are three approaches:

- Evaluate the bulk stored strain energy.
- Micromechanics – calculate the energy stored or dissipated in the fibre, resin and interface and in other failure processes.
- Linear elastic fracture mechanics (LEFM).

The first approach considers the elastically stored strain energy, while the second method covers dissipative processes. As was previously mentioned, because of energy storage in a specimen at the extremities, the first method will overestimate the energy required to create the two new surfaces resulting from the fracture of the specimen. LEFM is more mathematical and fibre composites do not always meet the assumptions made because of conditions at the crack tip leading to stress relief. While we shall mention fracture mechanics this approach will not be developed here.

1.5.1   Strain energy

If a body is stressed in tension, compression, flexure or shear, a simple strength of materials method[27] can be used to calculate the stored strain energy. The area under a stress strain curve, up to the strain ε, is equal to the energy, U, stored in the body, or

$$U = \int_0^\varepsilon \sigma d\varepsilon \qquad [1.6]$$

If the material obeys Hooke's law, $\sigma = E\varepsilon$, the energy, per unit volume, is

$$U = E\varepsilon^2/2 \text{ or } \sigma^2/2E \qquad [1.7]$$

A similar expression applies for the energy in shear, per unit volume, viz.:

$$U = \tau^2/2G \qquad [1.8]$$

The following expressions for the strain energy in a rectangular beam of breadth, b, depth, d, and length, l, are useful:

$$U_t, U_c = \sigma_{lt}^2 bdl/2E_{lt}, \sigma_{lc}^2 bdl/2E_{lc} \text{ (tension, compression)} \qquad [1.9]$$

$$U_{bc} = 1/9 \times \sigma_{lt}^2 bdl/2E_{lt} \text{ (cantilever, beam 3 point loading)} \qquad [1.10]$$

$$U_s = 4/15 \times \tau^2 bdl/G \text{ (shear, 3 point loading)} \qquad [1.11]$$

Note that in all of the formulae it is the maximum stress that is specified. A short span to depth ratio, <5:1, favours shear delamination rather than flexural failure. Similar expressions could be written for the transverse case provided the stress strain characteristic is linear.

Evaluating the flexural strain energy for a unidirectionally reinforced beam of the dimensions mentioned in Section 1.4.1, viz. $6 \times 6 \times 60$ mm, and assuming that the stress is in the fibre direction, gives strain energies in the range ~4.7–8.2 J for 60 v/o glass fibre composites in flexure and ~3 J for carbon composites stressed similarly. Values for shear, assuming a shear modulus of 5 GPa, are ~0.3–0.8 J for glass composites and ~0.6–1.8 J for carbon composites. Mechanical properties have been taken from Table 1.2 and lower pairs of properties have been taken together (e.g. 37 GPa and 1.2 GPa for the modulus and strength of glass composites, respectively). Note that these figures refer to the energy theoretically stored in a specimen with the volume specified above, viz. $6 \times 6 \times 60$ mm.

Another way of using the strain energy approach with specimens of a constant area but of different thickness, t, is to put

$$U \propto \sigma^2 t/2E \qquad [1.12]$$

If the fibre, with a volume fraction of V_f, is making the major contribution to strength and modulus and the same type of fibre is being used throughout, the expression becomes

$$U \alpha V_f t \qquad\qquad [1.13]$$

It has been noted[28] that at higher impact velocities different modes of flexural response may be excited and reflective stress wave effects observed. For projectiles small compared with the target dimensions, the target may be cleanly penetrated as the velocity increases. The hole left is approximately the same size as the projectile. For a laminate with a thickness of t and a hole of radius, r, the energy required to create two new surfaces is given by $4\pi r t \gamma$, where γ is the fracture energy. The critical velocity, V, for this to occur can be estimated as follows. Assume that the impact is such that all the strain energy is transferred to the piece of composite that is ejected in the impact, i.e. there is no time for the stress wave generated to disperse the impact energy throughout the bulk of the specimen.

Then the kinetic energy, $1/2 \times \pi r^2 t \times \rho V^2$, is equal to $\pi r^2 t \times \sigma^2/2E$ and we have

$$V = \left(\sigma^2 / \rho E\right)^{1/2} \qquad\qquad [1.14]$$

Note that this will overestimate V as energy is used in creating new surfaces.

1.5.2 Micromechanics

In this method the energy absorbed in the composite, U, by several failure mechanisms is calculated. Mechanisms include:

- Fibre failure, U_f.
- Resin crazing or cracking, U_m.
- Fibre/resin debonding, U_d.
- Fibre pull-out from the matrix across a failure surface, U_p.
- Fibre relaxation and stress redistribution to the matrix, U_r.
- Multiple fibre failure, U_{mf}.
- Multiple matrix failure, U_{mm}.

Not all the mechanisms necessarily occur in one failure situation (e.g. propagation of a crack parallel to the fibres in a unidirectional composite will not involve fibre failure or significant fibre pull-out). The last two depend on the relative strains to failure of the two components and the fibre volume fraction, V_f. With a sufficiently low V_f the matrix may be able to take the full load applied to the composite when the fibres fail and immediate failure of the complete composite will not occur.

The total fracture energy is given by the sum:

$$U_{tot} = U_f + U_m + U_d + U_p + U_r + U_{mf} + U_{mm} \qquad\qquad [1.15]$$

Details of the calculations to evaluate the U terms are discussed, with varying degrees of sophistication, by many authors.[29–35] Typical expressions for U_d, U_r and U_p are:

$$U_d = V_f \sigma_f^2 y / 2 \, E_f \qquad\qquad\qquad [1.16]$$

$$U_r = V_f \sigma_f^2 l_c / 3 \, E_f \qquad\qquad\qquad [1.17]$$

$$U_p = V_f \sigma_f l_c / 12 = V_f \sigma_f^2 d / 24 \, \tau \qquad\qquad [1.18]$$

where y is the debond length of the fibre, V_f and σ_f the fibre volume fraction and fibre tensile strength, respectively, τ the interfacial shear strength, d the fibre diameter and l_c the critical stress transfer length. A simple relation among these quantities is $l_c/d = \sigma_f/2\tau$. For details of the derivation see Kelly and Macmillan.[35]

A general difficulty in using these equations is obtaining realistic information for fibre/resin debond strength, estimating the shear stress at the fibre/resin interface when a fibre is pulled out of the matrix and how this varies with distance along the fibre and the value or spread in values of debond length. Further complications arise if the models are applied to laminates or randomly reinforced structures rather than unidirectional composites. The energy U_p usually makes the largest contribution to the fracture energy/work of fracture. Taking the lower values of σ_f and τ for carbon and glass fibre from Table 1.1, assuming a fibre diameter of 10 μm and a fibre volume loading of 60 v/o, equation [1.18] gives values of U_p of ~6.8 and 11.2 kJm^{-2} for glass and carbon, respectively. Values may vary widely, for a material based on one type of reinforcement, because of differences in y, l_c and τ. It is suggested that the theories work reasonably well when the mechanisms on which they are based are the main ones involved in the failure of the material in question.

What is clear is that the fracture energy is proportional to the volume fraction of fibre, fibre strength or its square and the length of fibre pulled out. If equation [1.18] is written with the pull out length expressed in terms of the fibre diameter and interfacial shear strength, work of fracture is inversely proportional to the latter. These conclusions, which are largely intuitive, are in accord with those deduced from bulk energy considerations. Bounds on composite properties have been considered by Ashby[36] who remarks that it is very difficult to model toughness. He suggests an upper bound proportional to the fibre volume fraction and characteristic strength and fibre displacement involved in fibre pull-out, plus weighted contributions from the fracture of the fibres and matrix. The former is associated with crack bridging by fibres.

1.5.3   Fracture mechanics

If samples of composite material containing increasingly deep cracks are loaded in tension, say, the strength or load measured might decrease linearly with crack depth, or it might decrease more steeply, see Fig. 1.9. In the
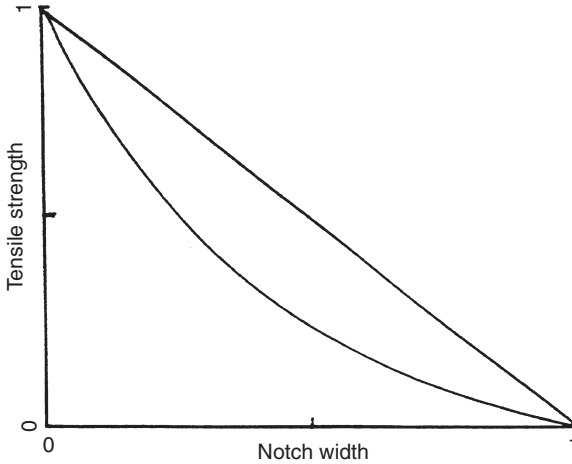
1.9 Possible effects of a crack on the tensile strength of a fibre composite. The straight line is for a material which is notch insensitive and the curved line for one which is notch sensitive. The scales are normalised.

latter case the material is said to be notch sensitive and in the former case notch insensitive. Examples of notch insensitive materials are surface untreated carbon fibre composites and low bond strength glass fibre composites. Ways of analysing the behaviour of the notch sensitive material by fracture mechanics have been presented.[3,37,38] The latter give an expression for G_{1c} in terms of the stress intensity factor, k_{1c}, and the independent elastic compliances of the composite, S_{11}, S_{22}, S_{12}, S_{66}. The calculation of k_{1c} from elastic and fracture data has been discussed.[39] The values tend to increase with fibre volume loading. The advantage of the fracture mechanics approach is that given a knowledge of k_{1c}, etc. it is possible to use the technique to predict the sensitivity of stressed structures to flaws. Detailed accounts of the application of fracture mechanics to composites and some of the difficulties arising have been recorded.[3,40,41] Stress relief at the crack tip due to fibre resin debonding is a complicating factor and methods have been suggested and developed to modify fracture mechanics to deal with this situation.

For the past two decades there has been a great deal of work devoted to measuring G_{1c} and G_{2c} very accurately and reproducibly. Two vital aspects of the work are to ensure that the body is deformed in the appropriate fracture mode (modes 1, 2, 3) and that no extraneous energy is supplied to the system or stored in it prior to failure. Generally, as can be seen from Table 1.2, values of G_{1c} and G_{2c}, for failure modes parallel to the fibres, are low.

In the author's experience in making measurements on very high
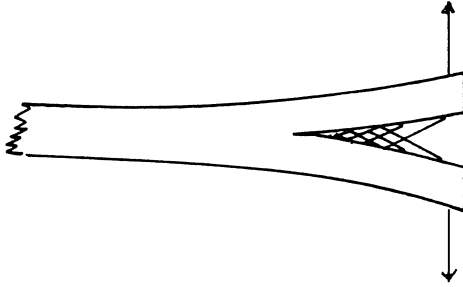
1.10 An exaggerated view of the bridging of a crack in a
     unidirectional fibre composite. The arrows show the direction of
     loading.

modulus unidirectional carbon fibre composites, G_{1c} may initially be much less than $100\,Jm^{-2}$, though there is considerable doubt as to how to extrapolate to the true initiation energy. The fracture energy then increases rapidly with increasing crack length to a plateau value of $\sim500–1000\,Jm^{-2}$. Part of this increase may be due to fibre bridging of the crack path,[42] see Fig. 1.10. The effect is sufficiently noticeable to make it very difficult or impossible to split a $60 \times 20 \times 2\,mm$ cracked unidirectional carbon fibre composite made from very high modulus carbon fibre and an epoxy resin, using only the hands (i.e. no wedges or tools). Bridging may be due to the non-alignment or mingling of plies or to the crack propagating in parallel planes on either side of the distinct interlaminar layer. This type of bridging should be distinguished from that leading to fibre pull-out referred to in Section 1.5.2. There the fibres were essentially perpendicular to the failure surface.

1.6   The effect of the matrix on fracture toughness

The very low values of γ and G_{1c} for failure parallel to the fibres in a unidirectional composite, and the very low transverse Charpy impact strength, have been, and are, a cause of concern to designers and users of composites. In principle it may be possible to design so that all the stress is in the fibre direction and secondary stresses are minimal. However, impacts and accidentally applied loads may cause cracking and failure in a direction parallel to the fibres or between plies with ease. G_{1c} for this direction is approximately the same as that for an unreinforced epoxy resin, $\sim100–200\,Jm^{-2}$. It seems obvious that if a tougher matrix is used the impact and fracture performance of the composite should benefit. By adding up to $\sim10–20\%$ of toughening agents, such as carboxy terminated butadiene or amine terminated butadiene, urethane, thermoplastics etc. the strain to failure and work
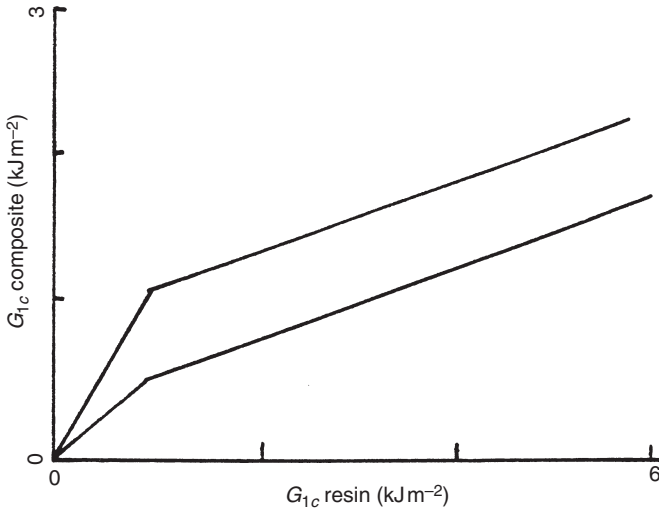
1.11 Schematic diagram showing relationship between G_{1c} for the composite and for the resin. Results usually fall within the bands shown.

of fracture of unreinforced epoxies can be improved dramatically by one or two orders of magnitude.[43]

Several attempts to use toughened matrices in composite materials indicated a rapid initial increase in G_{1c}, parallel to the fibres, of up to ~400–700 Jm^{-2} and then a slower rate of increase.[44-46] This is illustrated schematically in Fig. 1.11. One reason for the disappointing result may be the constraint on the development of the plastic deformation zone in the resin rich area between plies. An experimental observation has been made of this limited deformation, for unidirectional composites.[47] Another explanation[48] is that the rigid fibres constrain the resin phase, thus creating a stress state with a high hydrostatic tensile component. This will tend to promote voiding, crazing and brittle fracture. An earlier insight on this was provided[49,50] which calculated the effect of triaxial stress on the failure strain of brittle and ductile resins. The former resin had approximately twice the initial modulus and three times the strength of the latter. Using the distortion energy criterion it was shown that the failure strain in the ductile resin was reduced compared to that in the brittle material. The lower elongation modulus and strength of the ductile material are the governing factors rather than the elongation at failure.

It was noted[46] that rubber toughening increased mode 1 delamination energy more than that of mode 2. To gain full advantage of rubber or other toughening mechanisms it is necessary to improve the fibre resin bond strength. If not, the material will fail at the interface before the full benefit

of the toughened matrix is realised. In addition, the adding of a higher elongation phase reduces the stiffness of the composite, due to fibre microbuckling, and lowers Tg.

Interleaving composites using thin, discrete layers of a ductile resin has been reported.[51] It improves carbon fibre/bismaleimide impact resistance by up to 80% and leads to an improvement in the CAI. The ductile layer reduces impact induced delamination. It was found that the improvement in G_{1c} was considerably less than for G_{2c}, which could be increased by up to 200–300%. It was suggested that for composites G_{1c} is not as good an indicator of impact resistance as G_{2c}. Using thicker interleaving layers increased G_{1c} much more but could have adverse effects on other properties. Another variant[52] involves changing the morphology of a polyether imide film inserted between layers of fibre, by chemical means. This, it was claimed, gave good fracture toughness in the centre of the film thickness and good adhesion to the carbon fibres at either surface. G_{1c} and G_{2c} were 2.2 and $1.4\,kJm^{-2}$, respectively, values which were 3–5 times those for the unmodified carbon fibre dicyanate composite.

1.7   Crush strength

Normally our aim is to minimise the effects of impact so that a material or a structure can continue to operate effectively. Alternatively, composite structures, including fibre hybrids, can be used in crush protection devices in which essentially brittle fibres and resins exhibit toughness through intrinsic micro-failure processes involving fibre and resin cracking, delamination and fibre pull out. The structures that have been developed are usually filament wound or resin transfer moulded tubes containing a large number of weak sites, which stop simple catastrophic failure and ensure a controlled collapse during which the load is reasonably constant. This is illustrated schematically in Fig. 1.12. Systems based on brittle fibres crush by splaying or fragmentation whereas the use of a ductile reinforcement leads to crushing by a folding mechanism. Another design employs a series of linked, square cross section boxes. To assist in starting collapse, the ends of the structure are usually chamfered. The energy absorbed per unit mass of crushed material, U_{cr}, can be as high as $200\,kJkg^{-1}$ for carbon PEEK composites, $125\,kJkg^{-1}$ for carbon epoxy composites and $60\,kJkg^{-1}$ for glass composites.[53] These values are reduced by the presence of moisture. For comparison, the figures for mild steel and aluminium are 25–30 and 10–$16\,kJkg^{-1}$, respectively.[54-57] The last reference is a complete book on the topic. In the use of these components as automobile crash protection devices, for example, there are other factors in addition to the specific energy absorbtion that need to be considered. For instance, the ability to manufacture the structures economically and reproducibly is very important.
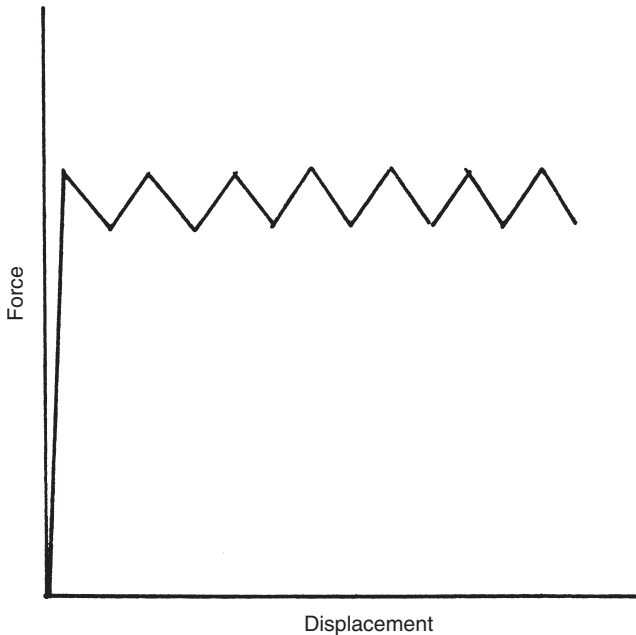
1.12 Idealised force displacement characteristic for a material which fails in a controlled manner in crushing. Units are arbitrary.

1.8   Summary

Fibre-reinforced polymer matrix composites are anisotropic, heterogeneous materials with significant properties in one or two directions, which do not deform plastically. If stresses are applied in the principal fibre direction(s) the modulus and strength are excellent. This is also usually the case for impact strength. In other directions, transverse to the fibres, or in shear, the properties are essentially those of the interface or resin matrix and are much lower. Many common metals are deformable and yet continue to possess adequate mechanical, if not aesthetic, properties afterwards and can be reformed by the application of heat and force. This is not so for composites. Once the elastic limit is exceeded permanent damage is produced which cannot be simply repaired and the mechanical performance is severely compromised. In this respect composites are more like wood than metals. It is these differences that must be remembered when working with composites.

The interlaminar (or between ply) direction is the one in which fibre composites are particularly weak and prone to splitting. This type of deformation, known as mode 1, is regarded as limiting and much of the work on impact, fracture and failure concentrates on measuring and analysing

this behaviour. Attempts to improve G_{1c} and the splitting or delamination performance have met with limited success. At the other extreme, potential uses of composites rely on the very high energy per unit mass which can be absorbed in the complete failure of the material in a controlled manner.

Models to account for impact behaviour are based on the bulk strain energy which can be stored prior to failure (proportional to the ratio of the square of the strength to the modulus, in the appropriate direction), micromechanical dissipation mechanisms in which resin cracking, debonding and delamination are particularly prominent and fracture mechanics. Each can be effective in a carefully monitored situation in which the assumptions of the model are fully met and adequate materials' properties known. However, the behaviour of a structure may be more than that of the idealised behaviour of its parts.[58]

Future progress in understanding and predicting impact behaviour and in using composites in spite of their perceived impact properties will depend on one or more of the following:

- Matching the design to the material and the proposed use.
- Careful control of the materials and manufacturing process, to preclude fibre movement during resin flow for instance, to give optimised properties.
- Numerical modelling of specific situations to extract any advantage from local fibre placement, modified resin properties, etc.
- Greater use of protective or sacrificial coatings for structures though at a loss of some mass efficiency.
- Incorporation of damage monitoring devices in critical structures.
- Third direction reinforcement even at the cost of reducing planar properties.
- Development of resins with an intrinsic strength and interfacial bond strength that match the transverse strength of the fibre, while remaining easily worked and not too expensive.

1.9   Final reflection

Scanning three decades of information on the impact performance of polymer matrix fibre composites is a sobering experience. Thirty years ago, as I well recall, some materials would shatter on impact and others completely defibrillate to leave something looking like a shaving brush. Impact energy in the fibre direction could easily be as high as 100–200 kJm^{-2}. Now there are many more types and varieties of reinforcing fibre, with excellent and well defined properties, optimised surface finishes and improved and toughened resins. Design tools, and the information on which to base the

design, are much better and knowledge of the fracture mechanics of anisotropic bodies has been extended. Numerical stress analysis is now routinely available and routinely used. The production of carbon fibres is ~10000t per annum and these, and other types of fibre, are extensively employed in leading edge technologies. Indeed they sometimes make the applications possible.

And yet what has changed? Despite very extensive research and development the upper work of fracture, in the fibre direction, is essentially the same, and the interlaminar or interply work of fracture is still very low. Composite structures, if struck, tend to delaminate too easily and mechanical performance is reduced.

The key to the past and continuing success of composites is in their intelligent use and an acceptance of their limitations. Glass sheet, which can be easily shattered, is widely used across the world in buildings and road transport. Concrete and brickwork are even more widely and extensively employed, household crockery and cooking pots have been used for tens of thousands of years and timber, complete with splits along the grain and warping, again has very extensive usage in most societies. In each case it is a matter of knowing the limitations of the material and working with and within them.

Let me end on a positive note. Composites are now used very successfully in crash survival cells in Formula 1 and other types of racing car doing a job that metals could not.

Acknowledgements

References

1 Matthews F L and Rawlings R D, *Composite Materials: Engineering and Science*, ch 11, 12, London, Chapman and Hall, 1994.
2 Hancox N L and Mayer R M, *Design Data for Reinforced Plastics*, London, Chapman and Hall, 1994.
3 Friedrich E (ed), *Applications of Fracture Mechanics to Composite Materials*, vol 6, Composite Materials Series, New York, Elsevier, 1989.
4 Bowen D H, 'Fibre-reinforced ceramics', *Fibre Sci Tech*, 1968 85–112.
5 Friend C M, 'Toughness in metal matrix composites', *Mat Sci Tech*, 1989 **5** 1–7.

6 Timoshenko S P and Goodier J N, *Theory of Elasticity*, 3rd edn., pp 409–14, 492–9, New York, McGraw Hill, 1970.

7 Fenner A J, *Mechanical Testing of Materials*, ch 7, London, George Newnes, 1965.

8 'Impact testing', *Engineer's Digest*, 1983 **44**(March) 32–5.

9 ISO Recommendation 180, Determination of the Izod Impact Resistance of Rigid Plastics, 1962.

10 Recommendations for the Presentation of Plastics Design Data, pt 1, Mechanical Properties, Sect. 1.2, Impact Behaviour, BS 4618, 1972.

11 Impact Resistance of Plastics and Electrical Insulating Materials, *ASTM D 256–87*, 1988.

12 Adams D F and Miller A K, 'The influence of transverse shear on the static flexure and Charpy impact response of hybrid composite materials', *J Mat Sci*, 1976 **11** 1697–710.

13 Hildebrand M, 'A comparison of FRP-sandwich penetrating impact test methods', *VTT Pub* 281, Technical Research Centre of Finland, Espoo, 1996.

14 Murphy D, 'Non-linear analysis provides new insights into impact damage of composite structures', *Composites*, 1994 **25** 65–9.

15 Mallick P K and Broutman L J, 'Static and impact properties of laminated hybrid composites', *J Test Eval*, 1977 **5** 190–200.

16 Krawczak P and Pabiot J, 'Fracture mechanics applied to glass fibre/epoxy matrix interface characterisation', *J Comp Mat*, 1995 **29** 2230–53.

17 EN ISO 6603-1 and 6603-2, Determination of instrumented impact behaviour of rigid plastics. pt 1, Falling dart method; pt 2, Instrumented puncture test, 1991.

18 Morita H and Wilson Tsang P H, 'Soft body impact damage on CF PEEK laminates using gelatin projectile', *J Rein Plas Comp*, 1997 **16** 1330–41.

19 Hancox N L, 'The erosion of carbon fibre-reinforced plastic by repeated liquid impact', *Wear*, 1973 **23** 71–81.

20 Schmitt G F, 'Liquid impact erosion – a unique form of wear for aerospace materials', *SAMPE J*, July/August 1977 16–22.

21 Papanicolaou G C and Stavropoulos C D, 'New approach for residual strength prediction of impacted CFRP laminates', *Composites*, 1995 **26** 517–23.

22 Ishai O and Shragai A, 'Effect of impact loading on damage and residual compressive strength of CFRP laminated beams', *Comp Struct*, 1990 **14** 319–37.

23 Butcher B R, The notch toughness of fibre composites, pt 1–4, *AERE R7801*, 1974; *R7802*, 1974; *R8843*, 1977; *R9576*, 1979.

24 Tweed J H, Lee R J, Dyson J R, Hancox N L and McCarthy J C, 'Impact performance of stressed composites', *ECCM* 7, 1996 **1** 111–16.

25 Hancox N L, 'Making an impact: composites in the automotive industry', *Materials World*, 1996 197–9.

26 Hogg P J and Turner S, *The Mechanical Testing of Long Fibre Composites: Harmonization and Standardization in the UK*, London, Department of Materials, Queen Mary College, 1988.

27 Timoshenko S P, *Strength of Materials*, pt 1, ch 11, Princeton, NJ, Van Nostrand, 1962.

28 Dorey G, 'Fracture of composites and damage tolerance', *AGARD LS 124*, 6.1–6.12, 1982.

29 Piggott M R, 'Theoretical estimation of fracture toughness of fibrous composites', *J Mat Sci*, 1970 **5** 669–75.

30 Williams T, Allen G and Kaufman M S, 'The impact strength of fibre composites', *J Mat Sci*, 1973 **8** 1765–87.
31 Marston T U, Atkins A G and Felbeck D K, 'Interfacial fracture energy and toughness of composites', *J Mat Sci*, 1974 **9** 447–55.
32 Wells J K and Beaumont P W R, 'Construction and use of toughness maps in a fracture analysis of the micromechanics of composite failure', *ASTM STP 787*, 1982 147–62.
33 Wells J K and Beaumont P W R, 'Debonding and pull-out processes in fibrous composites', *J Mat Sci*, 1985 **20** 1275–84.
34 Kim J K and Mai Y W, 'High strength, high fracture toughness fibre composites with interface control – a review', *Comp Sci Tech*, 1991 **41** 333–78.
35 Kelly A and Macmillan N H, *Strong Solids*, 3rd edn., ch 6, Oxford, Oxford University Press, 1986.
36 Ashby M F, 'Criteria for selecting the components of composites', *Acta Metall Mat*, 1993 **41** 1313–35.
37 Beaumont P W R and Phillips D C, 'Tensile strength of notched composites', *J Comp Mat*, 1972 **6** 32–46.
38 Beaumont P W R and Harris B, 'The energy of crack propagation in carbon fibre-reinforced resin systems', *J Mat Sci*, 1972 **7** 1265–79.
39 Beaumont P W R, 'A fracture mechanics approach to failure in fibrous composites', *J Adhes*, 1974 **6** 107–37.
40 Dharan C K H, 'Fracture mechanics of composite materials', *J Eng Mat Tech*, 1978 **100** 233–47.
41 Garg A C, 'Fracture behaviour of carbon fibre-reinforced composites: a review', *J Mech Beh Mat*, 1988 **1** 103–210.
42 Dorey G, 'Damage tolerance and damage assessment in advanced composites', in *Advanced Composites* (I K Partridge, ed), ch 11, London, Elsevier Applied Science, 1989.
43 Hancox N L, 'High temperature, high performance composites', *Adv Mat Man Proc*, 1988 **3** 359–89.
44 Huntson D L, Moulton R J, Johnston N J and Bascom W D, 'Matrix resin effects in composite delamination: mode 1 fracture aspects', *ASTM STP 937*, 1987 74–94.
45 Bradley W L, 'Understanding the transition of neat resin toughness into delamination toughness in composites', *Key Eng Mat*, 1989 **37** 161–98.
46 Jordan W M, Bradley W L and Moulton R J, 'Relating resin mechanical properties to composite delamination fracture toughness', *J Comp Mat*, 1989 **23** 923–43.
47 Hancox N L and Wells H, 'The effect of resin matrix properties on the impact and mechanical properties of unidirectional CFRP', *AERE R 7296*, 1973.
48 Yee A F, 'Modified matrix materials for tougher composites', *ASTM STP 937*, 1987 385–96.
49 Gaggar S K and Broutman L J, 'Effect of matrix ductility and interface treatment on mechanical properties of glass fibre mat composites', *Poly Eng Sci*, 1976 **16** 537–43.
50 Christensen R M and Rinde J A, 'Transverse tensile characteristics of fibre composites with flexible resins: theory and test results', *Poly Eng Sci*, 1979 **19** 506–11.
51 Masters J E, 'Improved impact and delamination resistance through interleafing', *Key Eng Mat*, 1989 **37** 317–48.

52 Kim Y S and Kim S C, 'Toughened carbon fibre composites with morphology gradient', *Macromol Sym*, 1997 **118** 371–6.
53 Ramakrishna S, 'Microstructural design of composite materials for crashworthy structural application', *Mat Des*, 1997 **18** 167–73.
54 Hull D, 'Research on composite materials at Liverpool University', *Phys Tech*, 1983 **14** 99–103, 112.
55 Karbhari V M and Haller J, 'Effects of preform structure on progressive crush characteristics of flange stiffened tubular elements', *Comp Struct*, 1997 **37** 81–96.
56 Farley G L, 'Effects of fibre and resin matrix maximum strain on the energy absorbtion of composite materials', *J Comp Mat*, 1986 **20** 322–34.
57 Mamalis A G, Manolakos D E, Demostheneous G A and Ioannidis M B, *Crashworthyness of Composites Thin Walled Structural Components*, Lancaster, PA, Technomic Publishing, 1998.
58 Greenhalgh E, Bishop S M, Bray D, Hughes D, Lahiff S and Millson B, 'Characterisation of impact damage in skin-stringer composite structures', *Comp Struct*, 1996 **36** 187–207.

2

Recent developments in impact damage assessment of fibre composites

J-K KIM

2.1 Introduction

Damage in fibre-reinforced composites can be caused by many different sources that include static and fatigue loading, low energy impact during the manufacture and in service, and environmental factors such as moisture absorption and corrosion. The low energy impact, in particular, can be potentially dangerous as it can produce extensive subsurface delaminations that are not visible on the laminate surface. It has been proven that the presence of internal damage causes substantial losses in strength and stiffness of the composite components.[1] The damage induced by low energy impact is often a complex mixture of three principal failure modes, namely, interlaminar damage (delaminations), intralaminar damage between fibres (transverse matrix cracking and fibre-matrix interface debonding) and intralaminar damage across fibres (fibre fracture). As recognised also in Chapters 1 and 3, the first two mechanisms are sensitive to the properties of the matrix material and the fibre-matrix interface, the third to the fibre performance, especially the failure strain. Useful reviews on this topic are available.[2,3]

It is also well known that the delamination patterns at each interface are different in size, shape, and orientation. The matrix cracks also propagate in different manners in each layer. To fully understand the damage state, not only must the surface damage be evaluated, but also the position and spatial geometry of all delaminations and transverse matrix cracks within the composite must be accurately identified. An accurate description of the impact damage state is a prerequisite to reliable assessment of residual mechanical properties. This is because the residual properties of a composite after impact are a complex function of the depth and lateral extent of damage present within the composite.[4] Further, quantitative, analytical tools need to be developed to correlate the information obtained from damage characterisation techniques to the residual mechanical properties. The relationships between the impact load applied, the extent and modes

of damage introduced and the residual properties are invaluable information for proper damage tolerant design of composite components and structures, see also Chapter 4.

The paramount importance of accurate damage assessment in fibre-reinforced composites has lead to the development of experimental techniques that can be classified into destructive and non-destructive means. Among the destructive techniques are the de-ply method and cross-sectional fractography, both of which are designed to visualise the characteristic internal damage state. The non-destructive methods involve detection, measurements of the size and location of damage state based on optical microscopy, X-rays, ultrasonic, acoustic emission, laser optics, interferometry/shearography, thermal instruments, etc. There have been several excellent comprehensive reviews[3,5–11] that describe a wider range of measurement techniques for destructive and nondestructive evaluation (NDE) of composite materials. In this chapter, a comprehensive overview is presented of destructive and nondestructive techniques that have been widely used to characterise impact damage in fibre-reinforced composites. Particular emphasis is placed on in-depth study of several different types of radiography and ultrasonic methods as the means of quantitative evaluation of internal damage in fibre composites. Brief accounts are also presented on other destructive and nondestructive techniques, such as de-ply and cross-sectional fractography, visual inspection, tap test, acoustic emission techniques, laser holography and shearography, infrared thermography and fibre optics.

2.2   Destructive techniques

A description is presented in this section of the range of techniques available for destructive characterisation of composite damage. The operating principles of the techniques are mentioned along with the main advantages and disadvantages in their application.

2.2.1   De-ply technique

In the de-ply technique, the damaged composite specimen is soaked in a solution of gold chloride to allow penetration of the solution into the internal cracks. After excessive solution is removed from the surface, the laminate is exposed to a temperature of about 150°C for 1–2h to completely vaporise the solvent. During the drying operation, the gold chloride crystallises and is deposited on the internal fracture surfaces. The laminate is subsequently baked at about 400°C for 1h, resulting in partial pyrolysis of the polymer matrix. The individual laminae are then separated, i.e. de-plied, with a sharp blade, and are examined under an optical microscope. Delaminations and matrix cracks are easily visible with the aid of oblique light
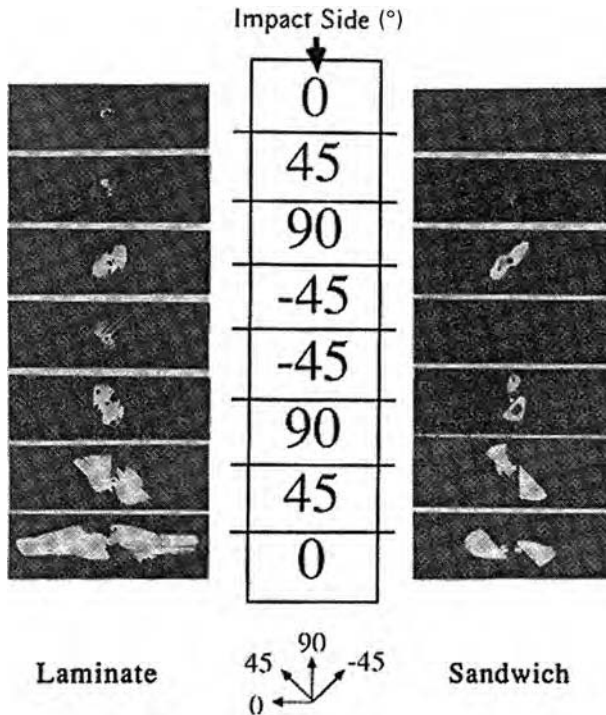
2.1 Shape and size of delaminations in a [0°/45°/90°/–45°] carbon fibre-epoxy matrix composite laminate after impact loading of 3.78 J. (After Kim and Jun[12].)

due to the deposited gold, whilst fibre fracture can be detected directly. To further facilitate de-plying after impact, non-sticking Kapton films were also inserted along the ply edges.[12]

Owing to its ease and simplicity of use, the de-ply technique has been widely employed to characterise impact damage in composites.[13–17] The de-ply technique is a reliable, quantitative means of measuring the size and shape of delaminations at individual laminar interfaces and thus to establish the three-dimensional (3D) map of internal damage. The typical example illustrated in Fig. 2.1 indicates that the delamination area induced by low-energy impact increased towards the back surface of the laminate and was largest in the farthest interface. The delamination had a 'peanut' shape with peculiar regularity over the whole interfaces. The shape and extent of delaminations were consistent with the predictions made previously based on an impact delamination model.[18] Due to the high accuracy and reliability, the results of the de-ply technique can be used to calibrate
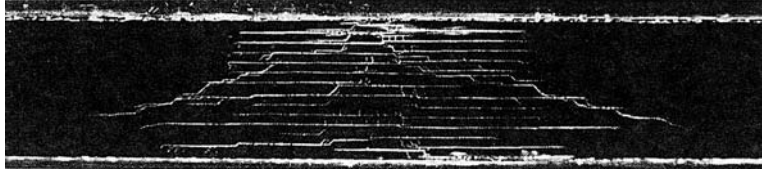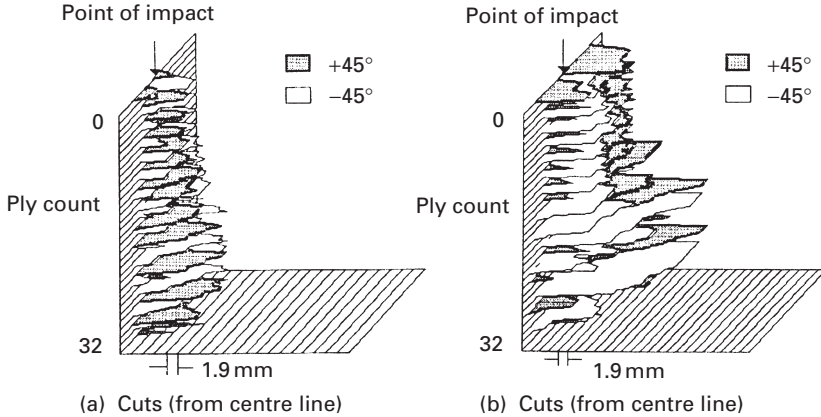
2.2 Cross-sectional view of an impact-damaged 56-ply quasi-isotropic carbon fibre-epoxy matrix composite laminate showing damage of a prominent 'top-hat' shape. (After Chester and Clark[20].)

the sensitivity of other nondestructive techniques that are discussed in the following. However, this technique is rather time-consuming and destructive; and it cannot be used with thermoplastic matrix composites due to the difficulties involved in partial pyrolysis of the matrix material.

2.2.2 Cross-sectional fractography

The cross-sectional fractography involves sectioning a sufficient number of thin strips of material at different locations and orientations over the whole damaged region.[19] A series of optical or electronic microscopic images of these cross-sections are used to construct a 3D map that can illustrate the spatial distributions of delamination and transverse matrix cracks. The cross-sectional fractography shown in Fig. 2.2 presents a damage distribution through the laminate thickness of a certain cross section. The most predominant type of damage throughout the indicated area was a network of interconnecting delaminations and transverse matrix cracks, and the whole damage had a characteristic 'top-hat' shape[18,20] with increasingly larger delamination area approaching the back surface of the laminate. Once the series of two dimensional (2D) fractographic images taken from different sections are combined, it is possible to construct an isometric 3D map of the whole damage. Such 3D damage maps are shown in Fig. 2.3 for a 32-layer quasi-isotropic carbon fibre-epoxy matrix composite laminate after impact loading of varying energy levels.[21]

It was argued that there were no other non-destructive methods of characterising impact damage in as much detail as can be obtained by the cross-sectioning fractographic method.[19] Other examples can also be found in Fig. 9.1–9.3 of Chapter 9. However, it is well accepted that this technique also has a few limitations: any cracks running parallel to the cutting direction cannot be detected; it is time-consuming and laborious to prepare specimens, as for the de-ply technique; and extreme precautions should be taken to avoid introducing new cracks during the specimen preparation.

Point of impact

+45°
−45°

0

Ply count

32 ⊣⊢ 1.9 mm

(a) Cuts (from centre line)

Point of impact

+45°
−45°

0

Ply count

32 ⊣⊢ 1.9 mm

(b) Cuts (from centre line)

2.3 3D damage maps of a [±45°]$_s$ carbon fibre-epoxy matrix composite laminate after impact loading at cumulative energies of (a) 80 J and (b) 310 J. (After Gweon and Bascom[21].)

2.3   Nondestructive techniques

2.3.1   Visual inspection and optical microscopy

One should not ignore the great deal of information that can be obtained by casting an eye over a composite structure. It is possible to obtain useful information about the internal quality of quite thick optically transparent composite components by examining them visually against a brightly lit background. The visual inspection is particularly useful for moving components made from composites and sandwich structures, such as helicopter rotor blades, turbine compressor buckets and water impellers. Periodic check of blade deflection can be used to monitor safe residual life, since the loss of strength is most often accompanied by reduction in stiffness. Careful visual inspection can also help identify the regions to be inspected by more sophisticated non-destructive methods. Reliability of visual inspection may be improved by using conventional dye penetrants.

It was shown that visual inspection of glass fibre-thermoset matrix composites could reveal internal defects and damage.[22] The reduction in transmission of light by delaminations can be accurately quantified using a solid state camera, whose image can be stored in a computer for the construction of digitised images. An optical microphotograph of a glass woven fabric vinyl ester matrix composite taken with the aid of transmitted light is shown in Fig. 2.4.[23,24] In addition to the extensive delamination observed in the central impact area, minute interface debonding occurred along the warp and weft directions of woven fabric in the surrounding regions near the back surface of impact, which contributed considerably to the total damage
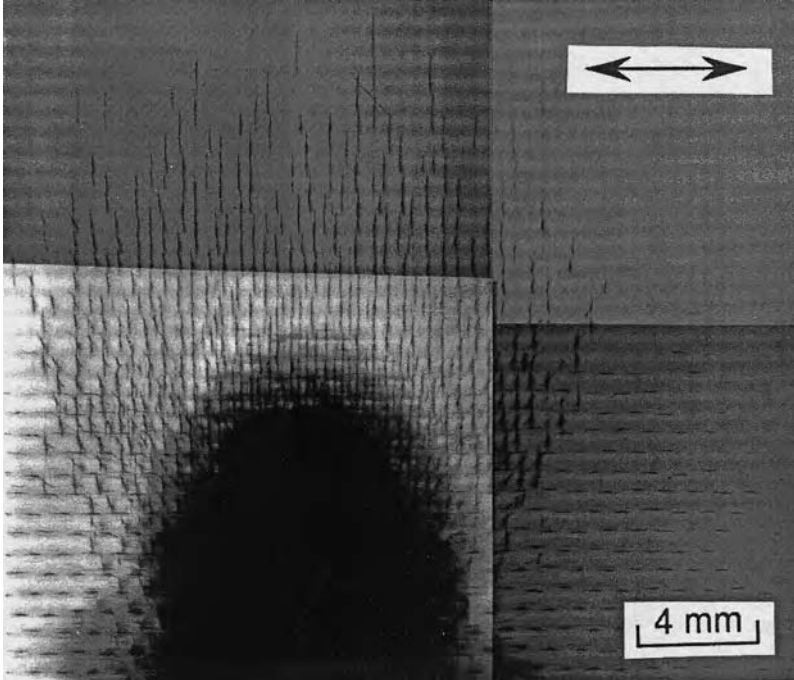
2.4 A magnified view of impact damage in a glass woven fabric-vinyl ester matrix composite. (After Hirai *et al.*[23])

area of the laminate. It was found that the total damage area varied significantly depending on the fibre-matrix interface bond strength which was affected by silane coupling agent applied onto the glass fibre surface.

2.3.2 Tap test

The tap test involves tapping of thin composite laminate parts using a coin or a special tap hammer. This technique has been commonly used for in-service inspection because it does not require sophisticated, expensive equipment. The tap test relies on the different acoustic resonance of the loose upper layer compared to surrounding material, and thus is only sensitive to laminar-type flaws, including delaminations and debonds of fairly large area. Therefore, this method suffers from subjective interpretation, reduced sensitivity with flaw depth and complex flaw geometry, and an inability to calibrate effectively for either flaw size or depth. This means that the applications of thicker laminates and more highly loaded designs make this approach inadequate in many cases. A few attempts have been made with mixed success to instrument the tap test by employing a
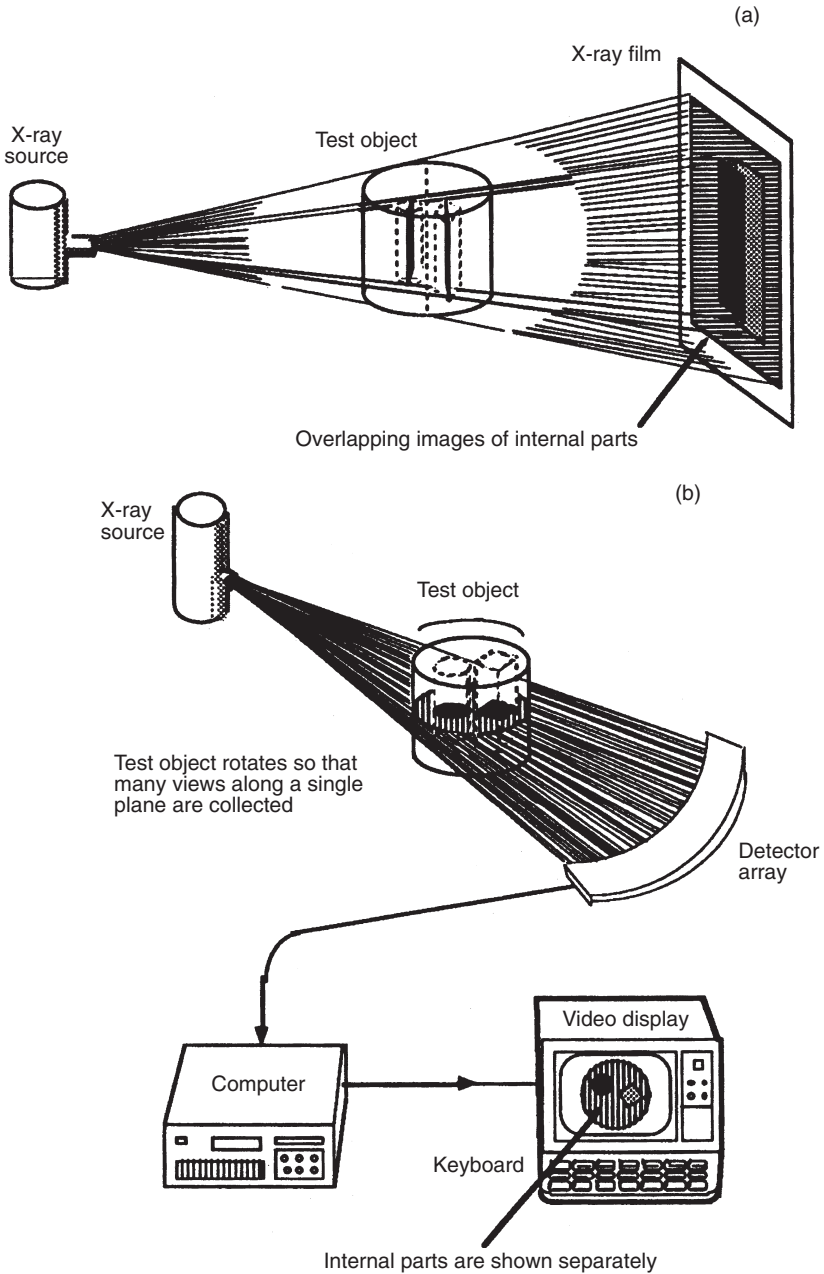
machine-type tapper and instrumentation for signal interpretation. A major advantage of using a mechanised tapper is improved repeatability in tap impact and location, while the instrumentation offers spectral analysis of the detected audio signals.

2.3.3 X-radiography

X-radiography is one of the most useful forms of NDE because it can be used effectively on very complicated structures. X-ray techniques have long proved complementary to other techniques in finding volumetric defects in composite materials. The X-radiography relies on the differential absorption coefficient being directly related to material density and a function of the atomic number or scattering of X-ray photons as they pass through a material. The principle of conventional radiography is schematically illustrated in Fig. 2.5 along with that of X-ray tomography (to be discussed in Section 2.3.3.2). In conventional radiography by transmission, no attempt is made to determine the distance along the path of the position of the defect. In general, flaws or structural features that can cause a significant change (say, at least 1–2% in material thickness or density) in the attenuation of X-ray photons can be detected.

   X-radiography is particularly useful for the detection of defects in bonded honeycomb core sandwich structures. The low density and thin composite skins usually provide minimal interference so that X-rays can image the core material. Particular examples of honeycomb core defects include blown core, crushed core, condensed core, fatigued, cut or corroded core, and foaming adhesive voids. It is also possible to detect water intrusion into the honeycomb core using this technique. However, internal damage, such as delaminations, in polymer matrix composite (PMC) laminates poses some difficulties in detection because delaminations tend to lie between plies and present a very small apparent thickness change. In addition, there is little difference between absorption by the polymer matrix, fibres and air gaps. This requires a liquid having a high X-ray absorption coefficient, e.g. zinc iodide, to penetrate into the damaged area to be examined, most often by means of destructive procedures such as drilling a hole at the damage centre. The penetrant does not always reach small damage areas and delaminations, particularly those emanating from embedded and isolated internal structures, suggesting that X-radiography is not sufficiently reliable and comprehensive for PMCs.[25] However, other types of composites based on metal and ceramic matrices (MMCs and CMCs) require little or no specimen preparation. In this regard, the X-radiographic techniques are inherently more suitable for MMCs and CMCs than PMCs.

   Significant progress has been made in recent years in developing X-ray imaging techniques without relying on films, achieving state-of-the-art

(a)

X-ray film

X-ray
source

Test object

Overlapping images of internal parts

(b)

X-ray
source

Test object

Test object rotates so that
many views along a single
plane are collected

Detector
array

Computer

Video display

Keyboard

Internal parts are shown separately

2.5 Schematic diagrams comparing (a) conventional X-ray
      radiography and (b) X-ray computed tomography (CT).

methods, such as computed tomography (CT) and its variations. Unlike conventional radiography which produces a shadowgraph representing the attenuation experienced by the X-rays, the CT process utilises X-ray intensity measurements and computes an image of the specimen cross-section. The computed image is a highly accurate representation with a very fine resolution of the attenuation scale. The real time viewing of X-ray images can reduce the demand for X-ray films. Various new types of X-radiography techniques that have been used for damage characterisation of composite materials are discussed in the following.

2.3.3.1 De-ply and stereo radiography

De-ply radiography[26] involves a combination of standard radiography and the aforementioned de-ply technique (see Section 2.2.1). The laminate is first penetrated with a solution of zinc iodide and the resin is subsequently pyrolysed in a furnace, resulting in the separation of the individual layers. The radiographs of these laminae provide a 3D map of damage pattern. The series of radiographs shown in Fig. 2.6 present the extent of notch tip damage in a $[0°/90°]_{2S}$ double-notched carbon fibre-epoxy matrix composite laminate after fatigue loading.[26] The dark images of the photograph indicate the dye penetrant-filled cracks. The notch-tip damage mechanisms were clearly identified, namely longitudinal splitting in the 0° layers, delamination at the 0°/90° interfaces and transverse ply cracking in the 90° layers.[27,28] It was highlighted that longitudinal splits and delaminations in the interior plies were much shorter than those in the exterior plies, as has been reported previously.[29] The comparison of the radiographs taken before and after pyrolysis indicated that the resolution of the image was severely impaired by pyrolysis although the overall distribution of damage was visible after pyrolysis.[26] This technique also has a major limitation in that each radiograph represents the sum of the image from both sides of an individual lamina. To resolve the damage at the individual laminar interfaces, a proper image analysis combined with a progressive subtraction procedure is required.

Stereo radiography[16,26,30] is a simple technique where two X-ray photographs are taken of the same material at two different orientations to create an image from both the right and left eye perspectives. The two X-ray photographs are then combined together to visualise the damaged region in three-dimensions with the aid of a stereo viewer or computer aided tomographic techniques. The depth of the delamination is determined relying on viewer's perception of natural depth, and the depth perception effect can be augmented by increasing the difference in the angles of inclination between the two radiographs. The stereo radiographs illustrated in Fig. 2.7 show a damage zone at a notch tip of a $[0°/{-}45°/90°/{+}45°]_{2s}$
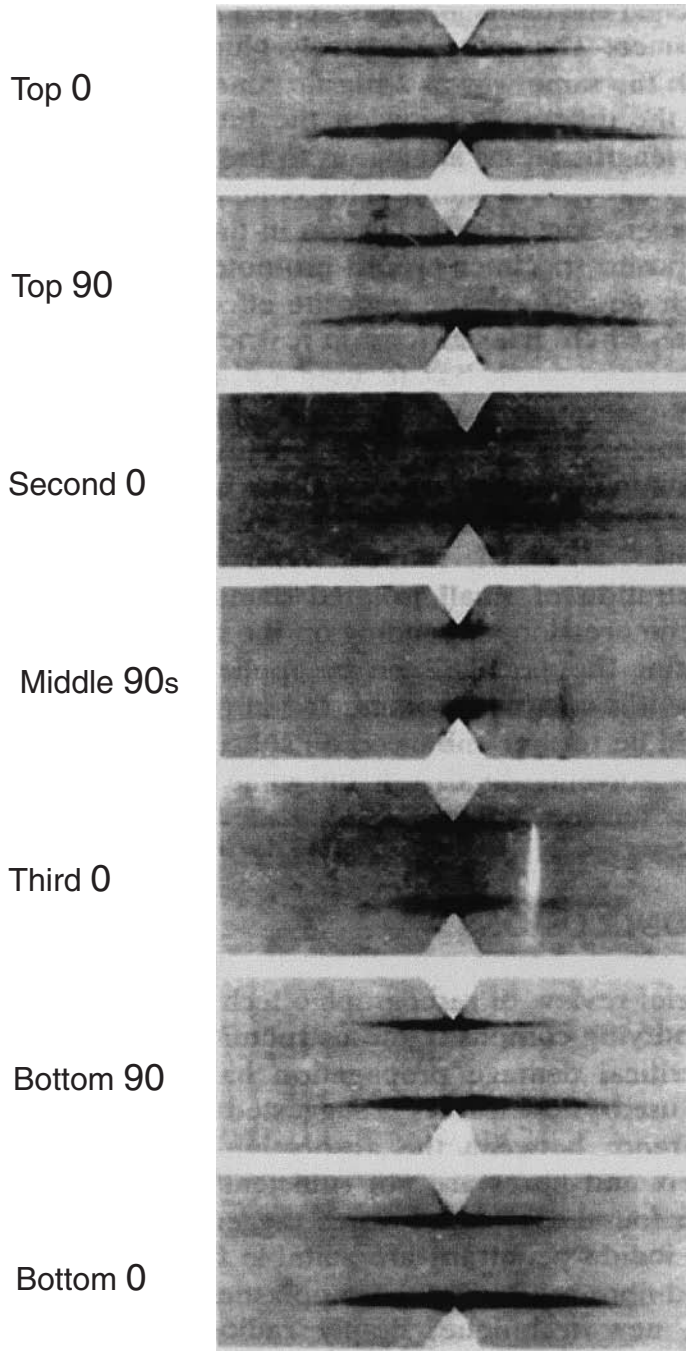
2.6 De-ply X-radiographs of a $[0°/90°]_{2S}$ double-notched carbon fibre-epoxy matrix composite laminate after fatigue loading. (After Kortschot and Zhang[26].)

5.0 mm
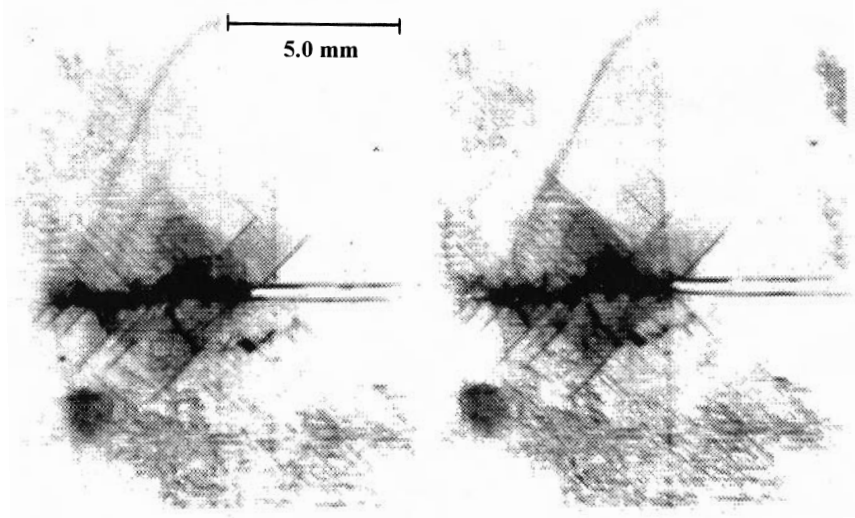
2.7 Stereo X-radiographs of the notch-tip in a quasi-isotropic carbon fibre-epoxy matrix composite graphite/epoxy panel. (After Kortschot and Zhang[26].)

carbon fibre-epoxy matrix composite laminate after fatigue loading.[26] Once viewed with an appropriate sterographic viewer, the depth of each delamination zone can be made more apparent than shown in two-dimensions.

Apart from the aforementioned radiographic techniques combined with de-ply and stereo analysis methods, X-radiography can also be performed in conjunction with the destructive cross-sectional method to further enhance the resolution of images. Figure 2.8 illustrates the planar view and a series of cross-sectional views of the same damage for a quasi-isotropic 48-ply carbon fibre-epoxy matrix composite laminate.[25,31] A small hole of 1 mm in diameter was drilled at the impact centre and a penetrant liquid, diiodobutane (DIB), was subsequently allowed to penetrate into the delaminations. To overcome the difficulties in penetrating the solution into small, tight delaminations and transverse cracks, micro-focus techniques were employed in the cross-sectional radiography. Examination of both of the radiographs enabled definition of the extent and boundaries of delamination. It is interesting to note that the delamination area through the thickness exhibited a barrel shape with the delamination area being larger at the central plies than in plies near the surface. This feature appears rather different from the previous observation of a 'top-hat'-shaped damage pattern[18] for similar lay-up sequence and constituent materials.
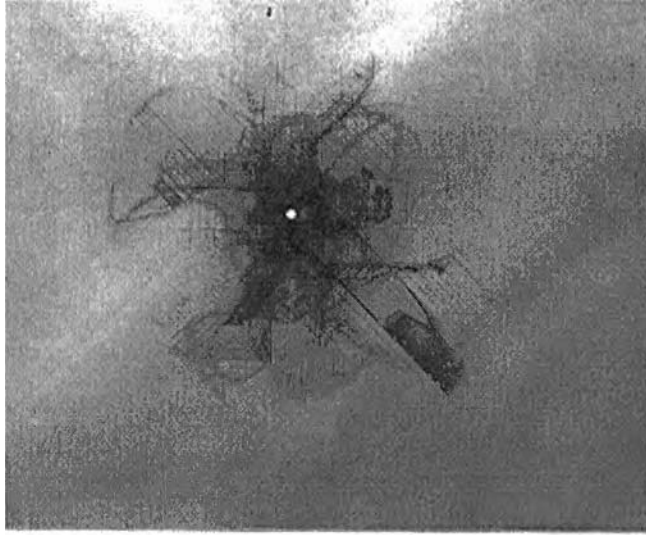
(a)
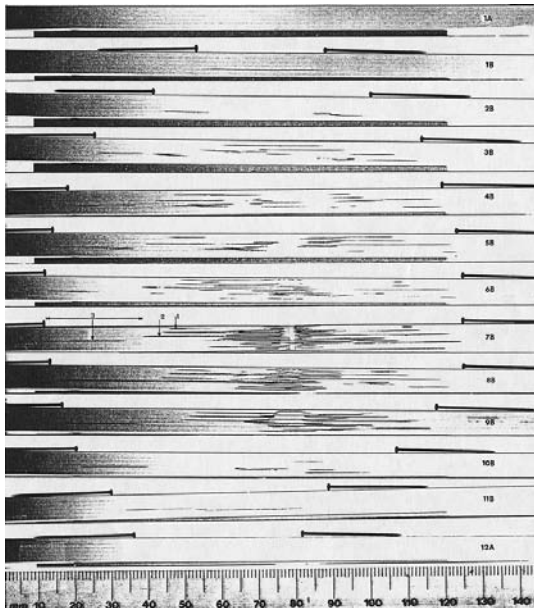
(b)

2.8 (a) Planar view of penetrant-enhanced X-ray photograph and (b) the corresponding microfocus-enhanced cross-sectional X-radiographs of a [±45/0/90]$_{6s}$ carbon fibre-epoxy matrix composite laminate. (After Girshovich *et al.*,[25] Gottesman and Girshovich[31].)

2.3.3.2 X-ray computed tomography (CT) and X-ray tomographic microscopy (XTM)

The use of 'tomography' (literally meaning 'the picture of a slice') was pioneered in medical diagnostics where the systems are commonly known as 'computerised axial tomography' (CAT) or 'computed tomography'.[32-35] The intensity of the X-rays is normally in the range of 60–100 KeV for medical applications, while 100–650 KeV is required for industrial applications. Combining the power of a computer with the traditional radiographic technique, the computed tomography (CT) is capable of reconstructing a 3D map from a finite number of radiographic images.[36,37] Figure 2.5(b) illustrates the operation of a CT scanner. The collimated X-ray beams go through the test object, which are received by a row of detectors placed opposite the X-ray source. After the sample is rotated by a small angle, another two-dimensional absorption image is obtained. This process continues until 180° of sample rotation has been recorded. During the rotation, the attenuation of the intensity of the X-ray beam is measured in a finite number of angular increments. Data acquisition is achieved by a computer that carries out reconstruction of the object with the aid of a suitable algorithm. Therefore, a tomographic image looks like a slice taken across the object in a two-dimensional projection.

Major advantages of using X-ray CT techniques are good contrast sensitivity and high resolution. It was claimed[38] that dimensional changes less than 0.01% and variations of density less than 0.1% could be detected, and the resolution of typical CT instruments for medical and industrial applications was as high as 25 μm. Although it is relatively difficult to provide enough resolution to detect tightly closed delaminations compared to ultrasonic C-scan techniques,[25] the CT technique has been successfully applied to resolve composite defects, such as matrix cracks, delaminations and fibre bundles.[39] Figure 2.9 illustrates conventional X-radiography and CT images of impact damage in a carbon fibre-epoxy matrix composite. It was noted that a CT image alone provided much better resolution of the outline of the damage area than the planar view of X-radiography. Internal damage in an SiC fibre-reinforced aluminium matrix composite under static tension was also successfully observed by the *in situ* X-ray CT technique based on a synchrotron radiation.[40] The CT images taken at the maximum stress allowed identification of interface debonding and matrix cracking that triggered failure of the composite. The X-ray CT technique has major disadvantages, such as the high capital cost for instrumentation, and the need for 360° access to construct 3D images, indicating difficulties for its application as a field inspection tool.[37]

Based upon the same principle as the X-ray CT system, X-ray tomographic microscopy (XTM)[34,38,41–43] is equipped with a much greater volume
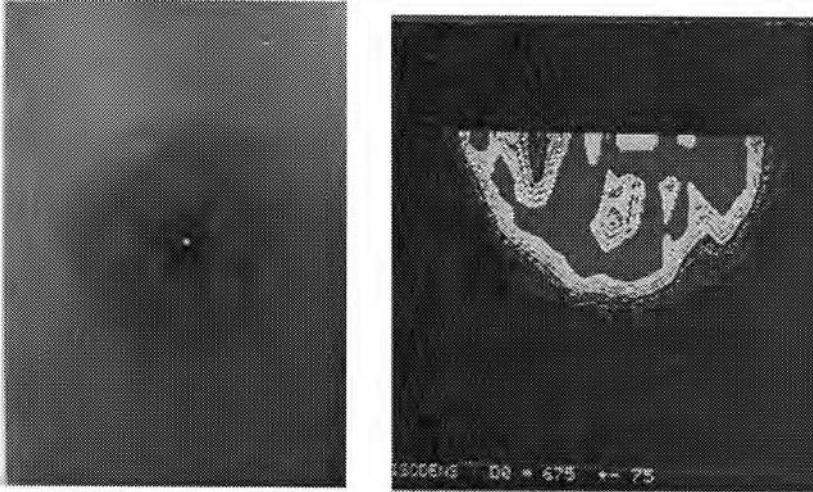
2.9 Comparison of conventional X-radiography and computed tomography (CT) images of 28 layer quasi-isotropic carbon fibre-epoxy matrix composite laminate after impact. (After Bathias and Cagnasso[39].)

resolution and faster data acquisition system. When focused high energy parallel X-rays (synchrotron radiation) are used from the radioactive sources, the spatial resolution can become better than $10\,\mu m$. Figure 2.10 illustrates a schematic diagram of key elements in the XTM based on an electro-optic X-ray detector, such as the charge couple device (CCD).[44] The radiation source produces highly collimated X-ray beams that pass through a sample positioned on a rotation stage. They pass through a magnifying optical lens and are eventually converted into a visible light by means of a single crystal fluorescent scintillator screen of $CdWO_4$. Lenses are used to alter the X-ray image formats in the electro-optic X-ray detector. The visible light image is recorded on a two-dimensional charge couple device (CCD) detector. Tomographic software converts the X-ray absorption profile data into a two-dimensional construction of linear attenuation coefficients of the sample interior. Then the data from multiple hundred slices are recorded simultaneously to build a 3D image by means of a high-speed, digital image-processing computer.

Figure 2.11(a) is an XTM micrograph taken 0.9 mm under the surface of a $[0°/90°]_s$ cross-ply SCS6 fibre-calcium aluminium silicate (CAS) matrix composite, while Fig. 2.11(b) is the corresponding SEM micrograph taken after sectioning the specimen to the same slice plane as the XTM image.[45] The XTM image indicates a crack running across the specimen right above a 90° fibre (arrow A). In addition, a broken fibre fragment (arrow B) and another microcrack at the corner (arrow C) were also detected. The same
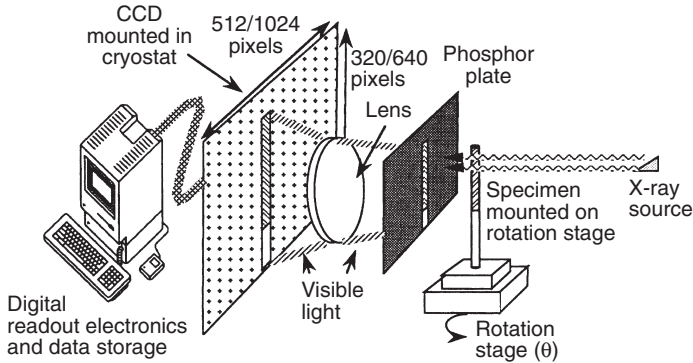
2.10 Schematic diagram of the key elements in an X-ray tomographic microscope (XTM). (After Deckman *et al.*[44])

cracks at the same locations were manifested in the SEM photograph. Of particular note is the thickness of crack A which was revealed to be less than 1.5 μm along the entire length. Although the pixel sampling size of the X-ray detector used was only 5.6 μm, the high contrast provided by the crack made it possible to image much smaller cracks. This has a practical implication in that the nominal spatial resolution and the ability to detect are not always the same.

In summary, both the X-ray CT and XTM techniques can provide a non-destructive means of evaluating impact damage and other internal features of composite materials in both qualitative and quantitative ways.

2.3.4　Ultrasonic techniques

Ultrasonic measurements are most commonly used to detect damage in composite structures. The basic principle of all these techniques is that ultrasonic pulses – usually in the frequency rage from 1 to 20 MHz – are generated which: (i) are transmitted through the material to a transducer (through-transmission mode); or (ii) are reflected back to the input transducer by defects or materials inhomogeneities (reflection or pulse-echo mode).[46] In both techniques, a piezoelectric transducer is placed on one surface of the specimen to introduce sound waves in the ultrasonic frequency range. In general, a frequency of 10 MHz or higher is used for thin laminates while the frequency can be as low as 2 MHz for thick laminates. As the sound waves propagate through the material, some of them are interrupted by the presence of defects or materials inhomogeneities, and the energy levels are attenuated. Some of these attenuated waves propagate though the specimen, while other waves are reflected back to the surface. The amplitude, frequency dependence and arrival times of detected

(a)

(b)
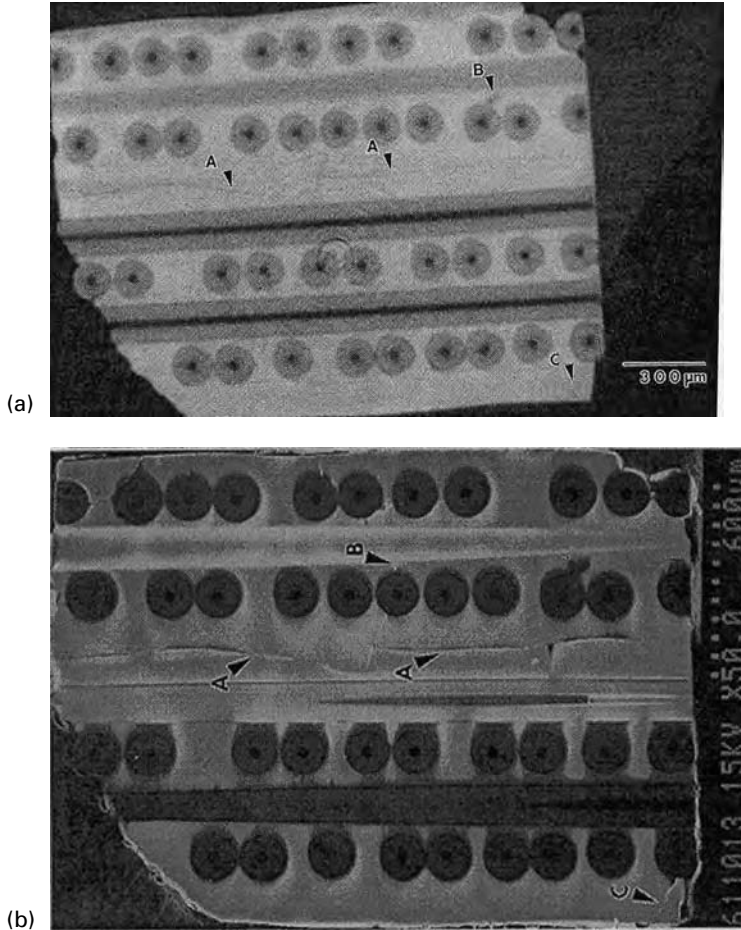
2.11 Microphotographs of a cross-ply SCS6 fibre-CAS matrix
composite: (a) XTM image; (b) SEM photograph obtained after
sectioning the specimen to the same slice place as in (a). (After
Kinney et al.[45])

pulses are used for defect analysis. Careful examination of the dependence of ultrasonic attenuation on frequency allows materials properties to be assessed or damage to be monitored.

In the through-transmission mode where two transducers are used, the axes of the sending and receiving transducers must be perfectly aligned across the thickness of specimen for maximum efficiency. Only one transducer can be used in this mode if a reflector, such as a glass plate, is placed on the back surface of the specimen to return the transmitted signals to the sending transducer. In this case, the signal received may become weak as it

has to travel twice through the specimen thickness. This test approach is most commonly used for production inspection of composite components. In contrast, the pulse-echo mode uses only one transducer and thus requires access to only one side of the specimen. Flaws are detected by monitoring the time of arrival and the signal strength of reflected echoes. Thus, this mode is commonly used for *in situ* inspection, as the single-transducer approach makes it simpler to apply in a manual test.

A coupling medium with high acoustic impedance, e.g. de-ionised water, grease or gel, is needed between the transducer and the specimen to maximise the energy transfer. In a manufacturing operation, coupling to composites is usually achieved by immersing the specimen completely in a water tank. Immersion in water has an advantage over other coupling media in that the coupling remains uniform and thus the ultrasonic sound waves can be more focused and collimated. Coupling can also be obtained by squirting a narrow stream of water on the part surface, through which the ultrasonic wave is transmitted. It is well accepted that ultrasonic techniques are better suited to MMCs than to PMCs because ultrasound is rapidly attenuated by polymeric materials. For example, the attenuation of 7 MHz ultrasound by glass fibre-epoxy resin is $3\,dB\,cm^{-1}$ which is much higher than $10^{-3}\,dB\,cm^{-1}$ for MMCs.

2.3.4.1   Three modes of image presentation

Once the composite part is scanned at regular intervals across its surface, the ultrasonic map of defects can be presented in three different modes, namely A-scan, B-scan and C-scan. They are described in the following with reference to Fig. 2.12.[46]

(i) A-scan. In the A-scan mode, the attenuated signals are displayed as a series of peaks against the time scale on an oscilloscope. The position of the signal's echo along the time axis allows the location of the defect in the thickness direction to be determined, while the amplitude of the echo can give some indication of the size and nature of the defect.

(ii) B-scan. In the B-scan analysis mode, cross-sectional measurement can be made along any vertical plane, eliminating the need for destructive cross-sectioning of specimen. B-scan is basically a series of very close-spaced A-scans through the thickness of specimen.

(iii) C-scan. The well-established ultrasonic technique for advanced composite materials is the C-scan mode where the extent of damage or internal inhomogeneity can be examined (see Fig. 5.9 in Chapter 5) and the depth profile of damage can be obtained by varying the time gate for C-scan data acquisition. In the conventional C-scan analysis, the transducer is moved in a plane parallel to the specimen surface in a rectilinear raster pattern to provide a planar view of the defect in a 'one shot' image. This

(a)

(b)

— Front surface
— Delamination
— Back surface

(c)

— Top of plate
— Bottom of plate

(d)
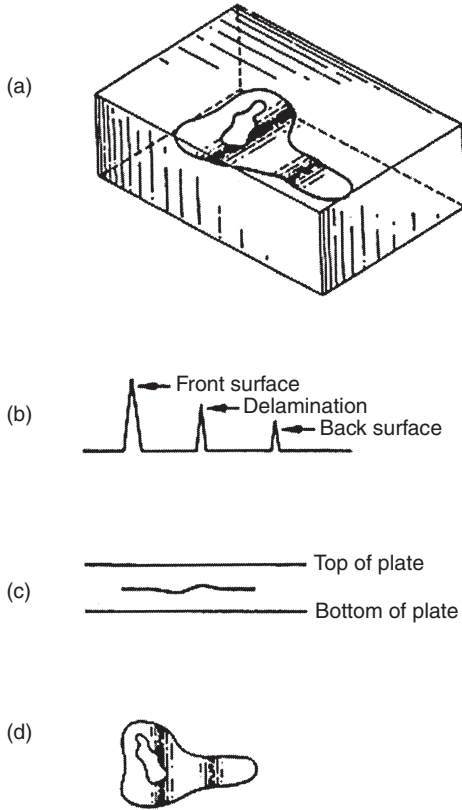
2.12 Comparison of ultrasonic scanning techniques: (a) A specimen containing a delamination; (b) A-scan wave; (c) B-scan view; (d) planar view of the C-scan. (After McIntire[46].)

image eliminates the need to produce multiple scans and is ideal for rapidly identifying gross anomalies in on-line inspection. High ultrasonic attenuation, i.e. weaker transmitted signals, are shown in either dark grey or black colour in the C-scan image. Once the presence of a defect is identified on a C-scan, its location in the thickness direction can be obtained using the A-scan or B-scan analysis. Nevertheless, if there are several defects present at the same distance in the plane direction, but at different locations in the thickness direction, the ultrasonic waves may be highly attenuated by the first defect encountered and the other defects below it may not be clearly detected, due to the so-called 'shadow or shielding effect'.[25] Recent advances in hardware and software have facilitated a remarkable improvement in both the image quality and quantity of information that an ultrasonic C-scan system can provide.[47]
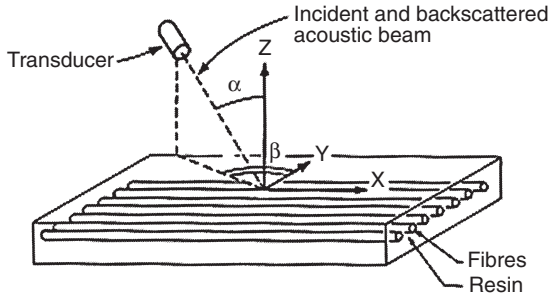
α = Angle of incidence
β = Angle between y-axis and the transmitter
    beam trajectory on the layer plane

2.13 Schematic presentation of set-up for ultrasonic backscattering
      technique. (After Bar-Cohen and Crane[48].)

2.3.4.2 *Acoustic backscattering technique*

In the acoustic backscattering technique, the transducer which serves as
both transmitter and receiver, is positioned at a small angle, $\alpha = 11°$, to the
normal to the test structure and at an angle of rotation, or azimuthal angle,
β. A schematic diagram of the testing arrangement is presented in Fig. 2.13.
Positioning the transducer at a small angle off normal incidence directs the
strong front and back surface reflections away from the backscattered
signal. When the selected azimuthal angle, β, is such that the transducer or
the ultrasonic beam is normal to the fibre direction or cracks in any layers
of the structure, the backscattered signal would have a maximum ampli-
tude. A plot of the signal intensity as a function of the azimuthal angle may
be used to check if the composite structure has been stacked correctly.[48]
The acoustic backscattering technique is particularly useful for detecting
matrix cracks and other types of defects, such as wavy or misaligned fibres,[6]
as well as linear voids. However, due to the difficulties involved in mani-
pulating the angular mechanisms and the long inspection time arising from
the requirement of multiple scans at a variety of orientations, this technique
has remained primarily a laboratory tool.

Nevertheless, the acoustic backscatter C-scan method has been success-
fully used to resolve delaminations in a carbon fibre-epoxy matrix com-
posite laminate after low-velocity impact.[19] Figure 2.14 presents a typical
acoustic backscatter result in two formats. The shaded dot patterns shown
in the upper right-hand corner indicate the damage within the 5.1 cm square
area of the specimen. The shade intensity was proportional to the amount
of total damage through the laminate thickness. The other format repre-
sents a 3D backscatter energy C-scan which was converted from the shaded
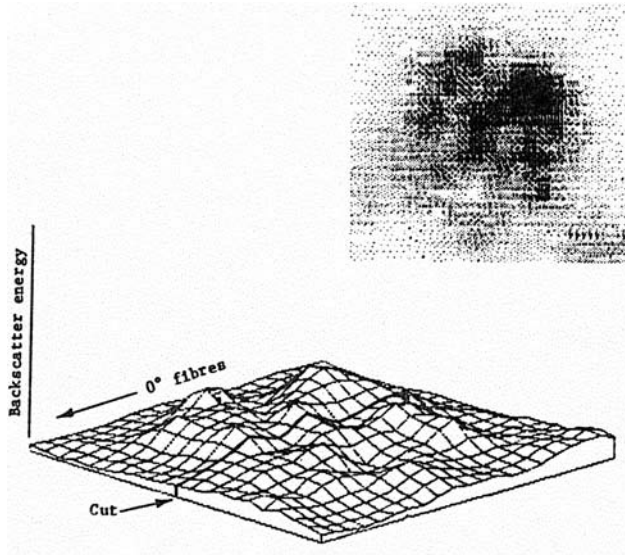
2.14 Acoustic backscattering C-scan image of an IM7G/3501-6 carbon
fibre-epoxy matrix composite. (After Boll *et al.*[19])

image. The irregular distribution of the energy intensity peaks suggests that all damage did not radiate from the impact centre and the isolated damage area was most likely due to delaminations that were redirected by transverse matrix cracks.

### 2.3.4.3   *Acoustic microscopy techniques*

A useful variant of conventional ultrasonic technique is acoustic microscopy.[49] An acoustic microscope provides much higher sensitivity to critical impact damage than a C-scan. Two different types of acoustic microscopes are currently used: the scanning laser acoustic microscope (SLAM) and the scanning acoustic microscope (SAM). The SLAM is based on a through-transmission mode and operates at frequencies in the range of 10–500 MHz. A scanning laser detector is employed to generate real time images of internal features at a rate of about 1/30 s per image. In the SAM, the specimen is scanned line by line using a very fine ultrasonic beam. Two different types of acoustic wave modes are being used: the burst-wave mode and the pulse-wave mode. The main differences between the two modes are such that the burst-wave mode uses a group of 30–40 waves of high frequency of 100 MHz–1.5 GHz for detection of defects on or near the surface, whereas the pulse-wave mode uses a single wave of low frequency of 10–100 MHz to detect mainly internal damage and discontinuities.
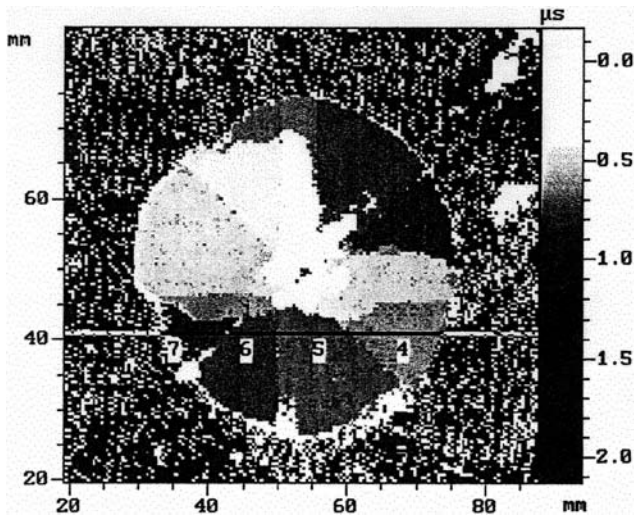
2.15 SAM photograph of the gross impact damage in a 16 layer [(−45°/0°/45°/90°)₂]s carbon fibre-bismaleimide (BMI) matrix composite. (After Gao and Kim[52].)

   In the pulse-wave mode, a specially designed lens is used to focus the ultrasonic waves onto a spot located at a depth of up to 2–3 mm beneath the specimen surface. The reflected waves are received back from the spot, typically in less than 100 ns, and are transmitted to a synchronous display to build up a image for the scanned area. SAM images can be generated for the cross sections (B-scan analysis), for the entire specimen thickness (multiple C-scans), or for specific depths (ply-by-ply C-scan analysis). The ply-by-ply C-scan analysis is a useful imaging technique where the damage accumulated through the thickness can be viewed by monitoring the amplitude of the ultrasonic signals at a specific depth of the specimen. Further, time-of-flight (TOF) analysis has been developed to allow the selection of narrow time gates and thereby to analyse the acquired 3D volume of data based on the travel time (i.e. time of flight) of reflected waves. Once the data are fixed with respect to the front and rear surface echoes, the information about travel time permits the internal damage to be identified. Therefore, in the TOF analysis, the internal features at any plane can be mapped topographically relative to the front surface or any sub-surface planes, resolving the distribution, size and shape of defects throughout whole specimen thickness, i.e. 'volume visualisation'.[50–52]
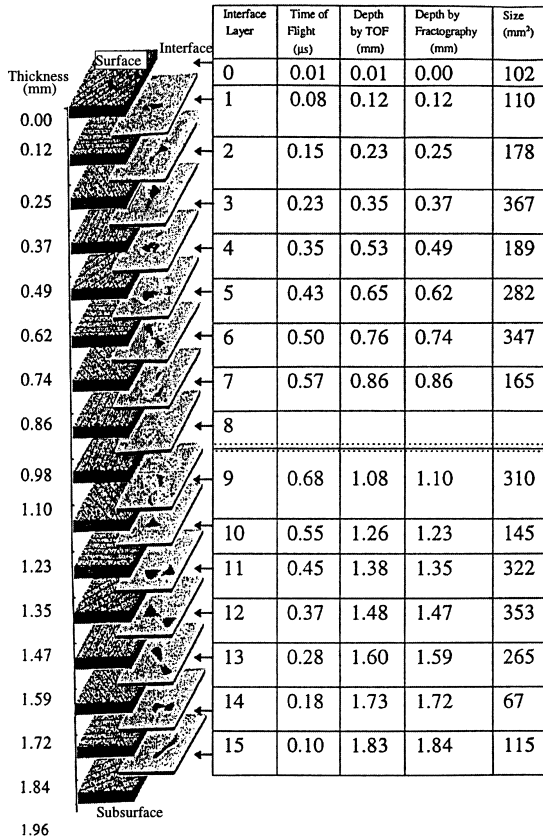   The 3D distributions of impact damage in carbon fibre composite laminates containing several different types of thermosets and thermoplastics were studied using SAM.[11,52–54] Figure 2.15 illustrates a SAM photograph of the gross damage in a carbon fibre-bismaleimide (BMI) matrix composite

(a)   (b)
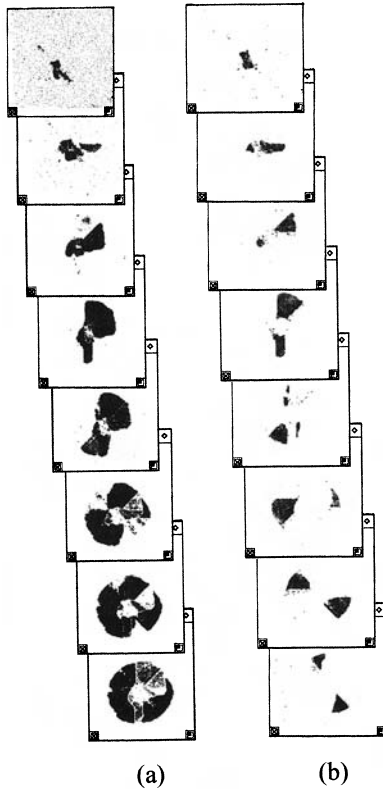
2.16 SAM photographs taken from (a) ply-by-ply C-scan; (b) TOF analysis for the composite as in Fig. 2.15.

obtained from the multiple C-scan. The total damage area had a circular shape, consistent with previous observations from conventional C-scan analysis for similar systems and lay-up sequence.[20,25,31,55,56] The level of grey colour from light to dark grey indicates the depth of the layers containing such delaminations from the front surface. The corresponding SAM images of ply-by-ply C-scan and TOF analyses for the top eight layers are presented in Fig. 2.16. The ply-by-ply C-scan images provided information about accumulated damage toward the back surface, while the TOF images allowed accurate measurements of damage area and shape at the individual layers. It is highlighted that the delaminations on individual layers had a peanut shape with the size being roughly identical and their major axis corresponding to the fibre direction in the immediate lower ply.[26] This indicates that the lay-up sequence had a significant influence on the impact damage behaviour of the composite.

The depth and size of delaminations at the individual layers were further evaluated using the TOF analysis, whose results were compared with the

Thickness (mm): 0.00, 0.12, 0.25, 0.37, 0.49, 0.62, 0.74, 0.86, 0.98, 1.10, 1.23, 1.35, 1.47, 1.59, 1.72, 1.84, 1.96

Surface — Interface — Subsurface

Interface Layer	Time of Flight (μs)	Depth by TOF (mm)	Depth by Fractography (mm)	Size (mm²)
0	0.01	0.01	0.00	102
1	0.08	0.12	0.12	110
2	0.15	0.23	0.25	178
3	0.23	0.35	0.37	367
4	0.35	0.53	0.49	189
5	0.43	0.65	0.62	282
6	0.50	0.76	0.74	347
7	0.57	0.86	0.86	165
8				
9	0.68	1.08	1.10	310
10	0.55	1.26	1.23	145
11	0.45	1.38	1.35	322
12	0.37	1.48	1.47	353
13	0.28	1.60	1.59	265
14	0.18	1.73	1.72	67
15	0.10	1.83	1.84	115

2.17 Location of delaminations determined from the TOF analysis and destructive cross-sectional fractography for the composite as in Fig. 2.15.

cross-sectional fractography, as shown in Fig. 2.17. To overcome the shadow effect of SAM, scanning and analysis were performed from both the front and rear surfaces. The TOF depth of delamination was determined from the known travel time of the reflected waves and the total thickness of laminate. The location of delaminations measured based on the two techniques agreed excellently, the difference being mostly 0.01–0.02 mm. This result is deemed remarkable in view of the fact that the nominal thickness of the individual layer was 0.125 mm. The delamination area was non-uniformly distributed throughout the laminate thickness while the delaminations near the surfaces were relatively small.

The impact damage resistance of carbon fibre composite laminates as determined by several damage parameters was shown to be controlled by the type of matrix material and the processing condition.[54] Figure 2.18 shows the SAM images generated from the TOF analysis of the impact
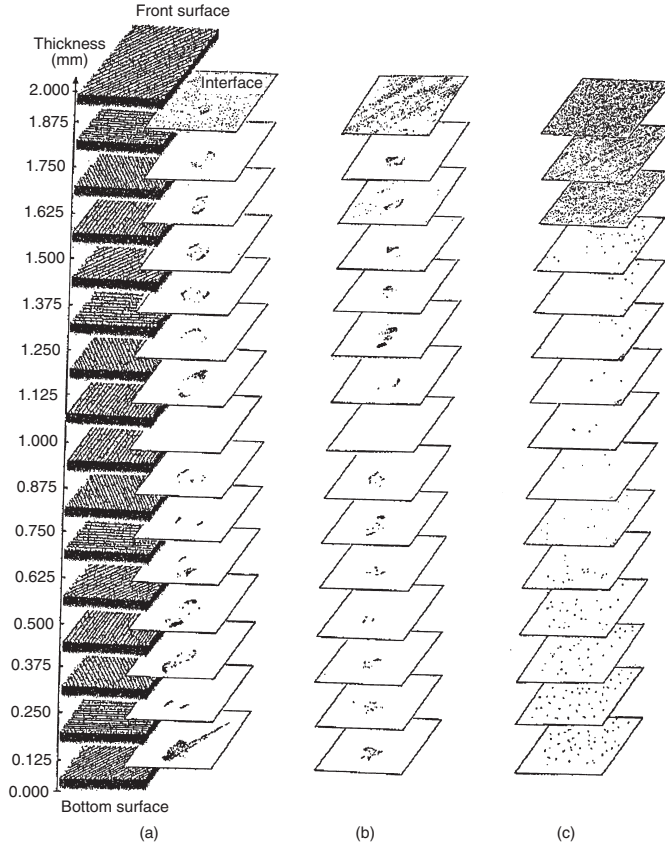
2.18 SAM images obtained from the TOF analysis of the impact
damage in quasi-isotropic (a) carbon-epoxy; (b) slow-cooled
carbon-PEEK; (c) fast-cooled carbon-PEEK composite laminates at
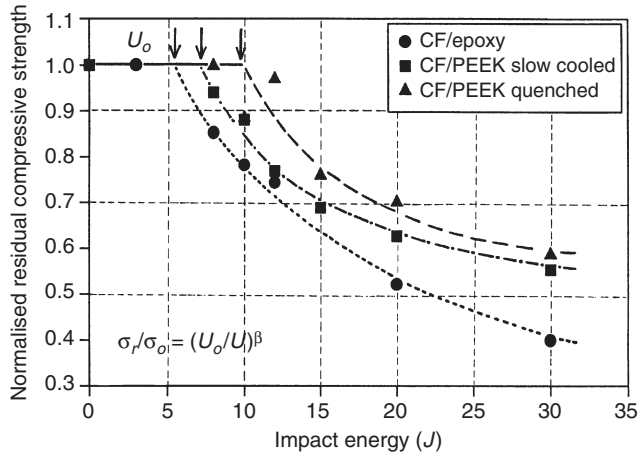an impact energy of 12 J. (After Gao and Kim[54].)

damage in carbon fibre composites containing epoxy and polyetherether-
ketone (PEEK) matrices. The reflected signals observed in the front and
back several layers of the fast-cooled carbon-PEEK system did not repre-
sent damage, but were due to the high damping characteristics of PEEK.
Figure 2.19 presents the corresponding total delamination area plotted as
a function of impact energy for the same materials. It is obvious that the
delamination area was smaller in the order of fast-cooled, slow-cooled
carbon-PEEK and carbon-epoxy systems for a given impact energy level.
Meanwhile, the incipient impact energy, U_i, below which no delamination
occurred was determined from the exponential relationship and was found
to be lower in the same order, indicating that the impact damage resistance
was superior in composites of the same order. The ability to predict the
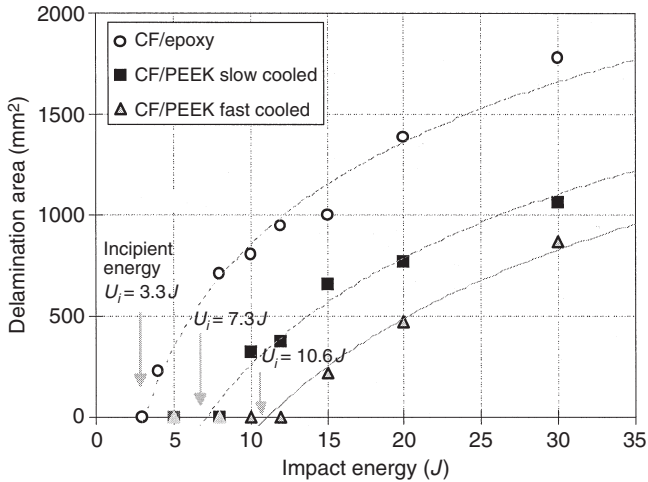
2.19 Total delamination area plotted as a function of applied impact energy for the composites as in Fig. 2.18. The incipient impact energies, U_i, for three composites are indicated. (After Gao and Kim[54].)

residual strength of a damaged structure is of particular importance for an effective damage tolerant design. Impact damaged composites experience significant strength reductions when subjected to compression due to local instabilities originating from the impact damage.[1,57]

Compression-after-impact (CAI) tests were conducted to assess the residual performance of a damaged composite, and the compressive strengths normalised with the undamaged strength are plotted as a function of impact energy in Fig. 2.20. The residual strengths were higher in the order of fast-cooled, slow-cooled carbon-PEEK and carbon-epoxy systems, although the absolute strength values were slightly higher for the slow-cooled composites than for their fast-cooled counterparts. The threshold impact energy, U_0, below which no strength degradation took place was also highest for the fast-cooled carbon-PEEK system. All these observations were attributed to the fact that slow-cooled composites contained PEEK matrix of a high degree of crystallinity which gave rise to high strength and stiffness, whereas the relatively high ductility of amorphous-rich PEEK matrix in the fast-cooled composites enhanced the interlaminar fracture resistance. The foregoing results strongly indicate that strength/stiffness and interlaminar fracture resistance/impact damage resistance are mutually exclusive and that processing conditions should be optimised if balanced mechanical performance is to be achieved. The SAM was also used to evaluate the failure mechanisms under compression-after-impact (CAI) loading.[52] The laminate failed by buckling due to delamination growth in

2.20 CAI residual strength as a function of applied impact energy for the composites as in Fig. 2.18. The threshold impact energies, U_0, for three composites are indicated. (After Gao and Kim[54].)

the transverse direction which was triggered by the impact damage present in several layers near the specimen surface. The delaminations induced by impact in the other layers were not affected by the CAI test, indicating that the location and size of delaminations played a dominant role in controlling the buckling instability under compression, and thus determined the residual compressive strength.

A B-scan image was taken of the cross-section along the line shown in Fig. 2.15, and is compared with the fractography obtained from the destructive cross-sectioning, as illustrated in Fig. 2.21. The location and distribution of major delaminations present at different planar locations of four neighbouring laminar interfaces were identified, and were roughly identical to those obtained from the fractography. However, the B-scan analysis was unable to delineate small cracks that were overshadowed by major delaminations running parallel to them at similar planar positions. For example, the small crack extending from the delamination at interface 5 was invisible in the B-scan image. This indicates that although being a convenient and non-destructive means of identifying location and size of impact damage in composites, the B-scan analysis has a limited resolution for small cracks that are overlapped by other major cracks.

Apart from the foregoing discussion on characterisation of impact damage in composites, the SAM technique has also been widely used for applications in other types of fracture of composites. The SAM study of carbon fibre composite laminates containing epoxy and polyetheretherketone (PEEK)[58] revealed that the interlaminar crack fronts in mode I and mode II delamination fracture tests had a zigzag shape on the microscopic
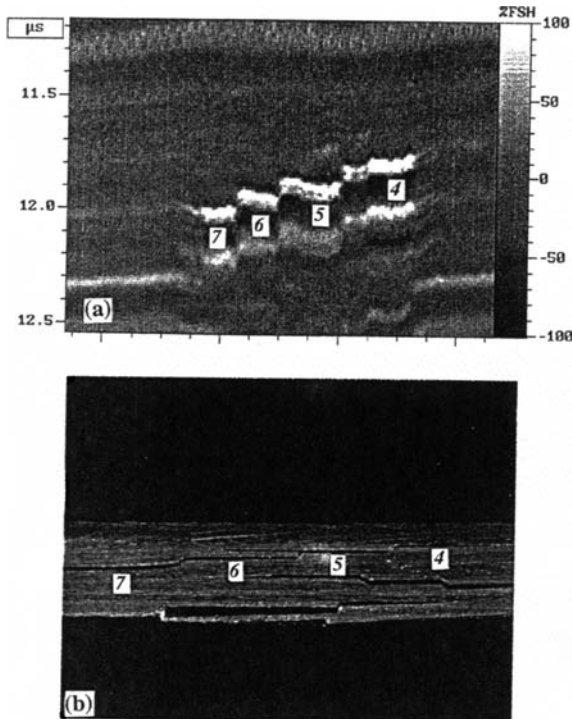
2.21 B-scan image of the impact damage along the line shown in Fig. 2.15, which is compared with the corresponding cross-sectional fractograph. (After Gao and Kim[52].)

scale, while the front shape in mode I had a thumb-nail shape on the macroscopic scale. The delamination initiation was found to correlate well with the non-linear point in the corresponding load-displacement record. Interface debonding and surface opening cracks at the nitride-braze joint[59] and gold-steel adhesive joint[60] were also successfully detected using the SAM. Apart from composite materials and adhesive joints as discussed above, the SAM technique has been widely used for failure analysis of integrated circuit microelectronic components.[61–63]

In summary, the ultrasonic SAM techniques are a proven, powerful tool for reliable and accurate characterisation of impact-induced internal damage in composites. In particular, the combination of the ply-by-ply C-scan and TOF analysis is an efficient technique in 3D mapping of multi-layer delaminations, which in turn allows accurate measurements of delamination size and shape. Excellent correlation has been established with the results obtained from cross-sectional fractography. Nevertheless, the capabilities are still limited to the detection of damage whose characteristic dimensions are relatively large compared to the wavelength of ultra-
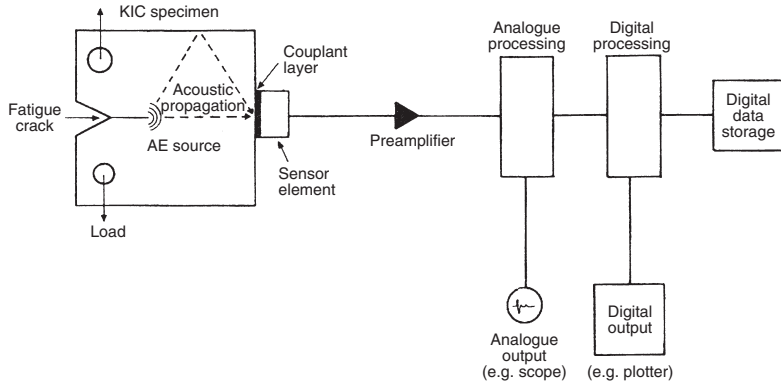
2.22 Schematic diagram of the layout of an acoustic emission system. (After Arrington[67].)

sound. Furthermore, the SAM techniques often fail to detect matrix cracks linking delaminations in the adjacent layers, and cannot provide accurate delamination patterns that are shielded partly or totally by the damage present in other layers, due to the 'shadow effect'.[64]

2.3.5   Acoustic emission (AE) techniques

When load is applied to a material or structure, small local failures occur which are accompanied by the release of stored elastic energy in the form of stress waves. By using appropriate instrumentation, these stress waves can be detected, recorded and processed to provide information about the failures and to locate their origins. The acoustic emission (AE) technique involves the detection of elastic acoustic (mostly ultrasonic) energy which is released by the materials undergoing deformation and fracture processes.[65,66] Figure 2.22 shows a schematic diagram of AE operation.[67] The stress waves travel from the source to the sensor which receives all direct as well as reflected signals. To detect and process the low level events, it is necessary to use high gain analogue electronics. The received signals may be recorded for remote or delayed analysis and for storage. There are many different types of sound sources that an AE monitoring system can detect, including crack initiation and propagation, chemical reaction such as corrosion, microdynamic events such as twinning, phase transformations and dislocation movement. The sensors cannot detect a crack that is not propagating, nor determine the size of cracks. However, with adequate stimuli, AE techniques can be used to monitor the behaviour of materials in real time and to locate these emission sources. In addition, AE techniques are capable of monitoring the entire system at the same time, identifying the
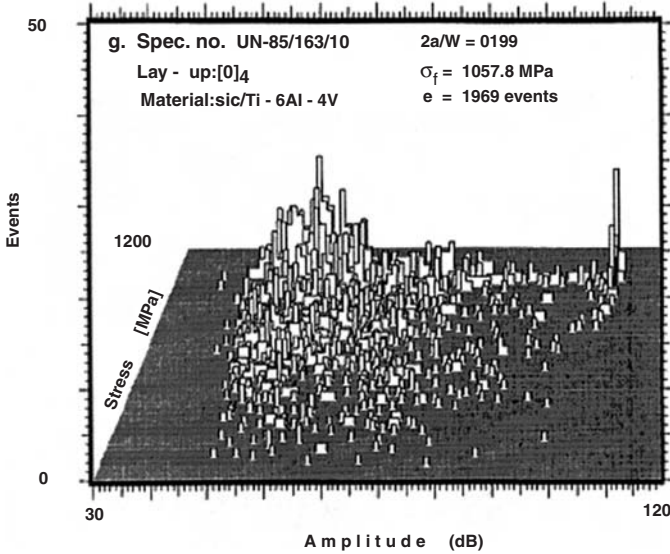
major failure mechanisms. Major disadvantages include the requirement for stress, chemical activity or other stimuli to generate the acoustic emission events. Because of this requirement, stabilised non-moving cracks cannot be detected.

This technique has been extensively used in the proof testing of pressure vessels and beams made with glass fibre composites; to detect moisture and corrosion in honeycomb sandwich structures; and to monitor and characterise the damage growth mechanisms in PMCs under cyclic loading. The AE technique has also been successfully applied to monitor fibre breakage during the fibre fragmentation tests of PMCs containing carbon and aramid fibres.[68–71] The AE signals corresponding to fibre fracture were separated from those due to matrix cracking based on the fast Fourier Transform (FFT) analysis,[71] and thereby the fibre-matrix bond strength were measured. Although many attempts have been made to distinguish different failure modes in PMCs, interpretation of the results has entailed difficulties arising from the complexity of the failure processes.[72] This was because many different modes of damage occurred on the micro- and macro-scales, and at the same time they interacted with each other.
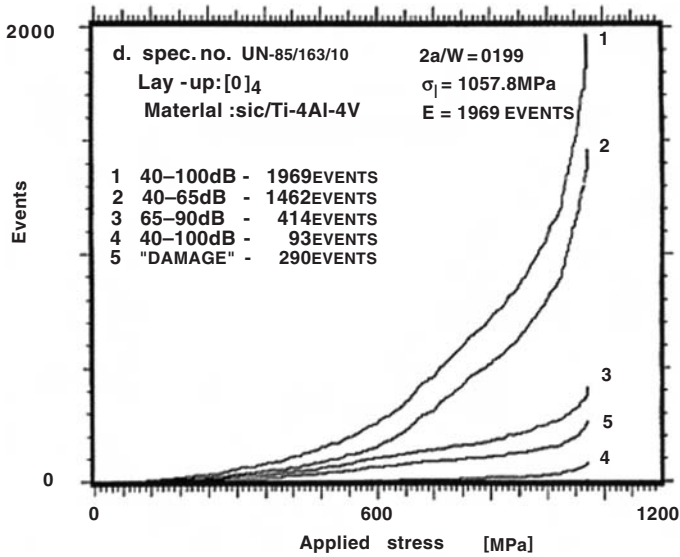
In MMCs, however, the mode of damage is less complicated than in PMCs, and the matrix dominated failures, such as delamination and matrix cracks, are less likely to occur. It was possible to distinguish the failure modes by grouping received AE signals according to the energy level.[73,74] It was proposed that fibre breakage generated high amplitude events (90–100 dB); matrix plastic deformation and cracking caused primarily mid-range amplitude events (65–90 dB); and low amplitude events (40–65 dB) were caused by interfacial debonding and the fretting among the existing fracture surfaces. The characteristics of the AE event accumulation corresponded very well with the observed failure process and the rate of damage growth. A typical three dimensional amplitude distribution histogram (ADH) in Fig. 2.23(a) presents the sequence of events accumulated for a unidirectional SiC fibre/Ti-6Al-4V matrix composite, while Fig. 2.23(b) shows the corresponding accumulative events of four different amplitude ranges and of the 'damage events' as a function of far-field applied stress. These figures clearly indicate that the low amplitude events dominated the whole failure modes because extensive matrix cracks, fibre-matrix interface debonding and fibre pull-out occurred in the specimen. The ADH also suggests that the majority of low amplitude events were generated after the occurrence of high amplitude events arising mainly from fibre breakage.

2.3.6 Laser holography and shearography

A hologram is an interference pattern that can be used to construct the optical wavefront emanating from an object. It is formed by the

g. **Spec. no.** **UN-85/163/10**   2a/W = 0199
Lay - up:[0]$_4$ σ_f = 1057.8 MPa
Material:sic/Ti - 6Al - 4V   e = 1969 events

(a)

d. **spec. no.** **UN-85/163/10**   2a/W = 0199
Lay -up:[0]$_4$ σ_I = 1057.8MPa
Materlal :sic/Ti-4Al-4V   E = 1969 EVENTS

1 40–100dB - 1969 EVENTS
2 40–65dB - 1462 EVENTS
3 65–90dB - 414 EVENTS
4 40–100dB - 93 EVENTS
5 "DAMAGE" - 290 EVENTS

(b)

2.23 (a) 3D amplitude distribution histogram (ADH) for a unidirectional SiC fibre/Ti-6Al-4V matrix composite; and (b) the corresponding accumulative events of four different amplitude ranges and of the 'damage events.' Curve 1 represents the total number of events generated; curve 2 for low-range amplitude events; curve 3 for mid-range amplitude events; curve 4 for high-range amplitude events; curve 5 for those events having intensities above the 'damage events'. (After Awerbuch and Bakuckas[74].)
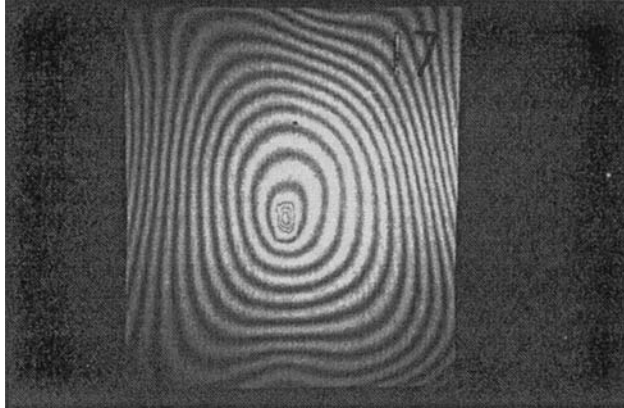
2.24 Real-time holographic image of a cross-ply carbon fibre-epoxy matrix laminate containing a foreign object. (After Rubayi *et al.*[76])

superposition of two wavefronts, namely object and reference beams, on a suitable recording material such as photographic film. If properly illuminated by the reference beam, one can see a fringe pattern due to the variation in the relative phase of the wavefront. Laser illumination provides the spatial and temporal coherence in the light beam to allow the observation of the fringe pattern.[75] The holographic inspection technique is sensitive to very small amounts of relative motion in the specimen surface. Typically, a specimen is tested by taking an image at rest and stressing the part surface by mechanical or thermal means. The stress causes the area of the surface over the flaw to deform more than the surrounding material. Displacements as small as one-quarter wavelength of the laser light being used cause a fringe to appear in the interference pattern. Conventional interferometric holography produces interference patterns from two holograms of a component. Each hologram is produced by recording the speckle interference between a coherent reference beam and the coherent object beam which illuminates the specimen surface. A typical holographic interferometric image is shown in Fig. 2.24 for a cross-ply carbon fibre-epoxy matrix composite laminate containing a foreign object.[76]

Due to the extreme sensitivity of the holography to relative displacement, vibration has been a major issue in a production environment. To avoid this problem, shearography[77] has been developed to provide greater immunity to vibration, allowing rapid scanning of large areas of composite components. The term 'shearography' was introduced to describe a particular form of 'speckle-shearing interferometry'. Unlike holography, the shearography uses no separate reference beam. Instead, the returning object beam is doubly imaged with one of the images shifted or 'sheared'

2.25 Shearographic fringe pattern of a filament wound composite cylinder containing a delamination. (After Hung[78].)

relative to the unshifted one. Therefore, the interference pattern reveals only the degree of differential motion of the surface along the direction of the shearing. In other words, the fringes observed in shearography are contours of the derivative of displacement rather than of displacement itself. This makes shearography especially suited to many production environments. An example of a shearographic image for a carbon fibre composite skin-foam core sandwich panel is shown in Fig. 2.25.[78] A major advantage of shearography is its insensitivity to whole-body motion and reaction to differential movement within the body because the speckle-forming rays for any locality in the image arrive from two different positions.

2.3.7 Infrared (IR) thermography

The physical basis of infrared (IR) thermography is well established as a standard non-destructive inspection technique.[79] This technique is based on the principle that an application (or removal) of heat on the surface of a test piece results in surface temperature change. The surface temperature profile varies as the heat diffuses when there are material inhomogeneities, including delaminations, cracks or internal foreign objects. The surface temperature change shows a maximum within a short time immediately after heating, and decreases as the heat diffuses into the surrounding material. The time required for peak response and the surface temperature equalisation varies depending on the heat excitation and the thermal properties of the test piece. An IR camera is used to monitor the surface temperature of the structure
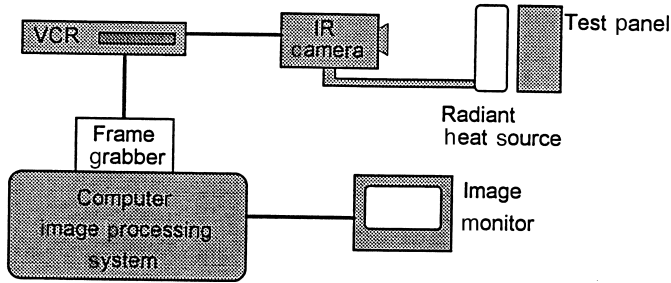
2.26 Schematic diagram of a typical infrared thermographic inspection system.

2.27 Single-sided IR thermograph of debonding between the carbon fibre composite skin and aluminium honeycomb core. (After Puttick[85].)

and anomalies in the temperature distribution reveal the presence of defects. IR imaging is performed in two different methods: one-sided and two-sided inspection. In one-sided (or pulse-echo) inspection, the surface of a test piece is subjected to a temperature change and the inspection is performed by observing the temperature variations on the same surface. If there are any internal defects, the surface area over such discontinuities will retain the heat longer than the surrounding uniform region.[7,80] Figure 2.26 shows a typical one-sided IR inspection system. The two-sided (or through-transmission) IR inspection involves heat excitation on one side and IR imaging on the opposite side. In contrast to the one-sided inspection system, internal defects will act as a thermal barrier and appear cooler than the surrounding uniform region on the inspection side.

The IR thermograph has been successfully applied to a wide range of composite structures.[81–84] Figure 2.27 illustrates a typical single-sided IR

thermograph of debonded carbon fibre laminate skin from an aluminium honeycomb core.[85] It was argued that the IR thermography had proven capability of revealing barely visible impact damage in a carbon fibre-epoxy matrix system to a degree comparable to that achieved by other non-destructive testing techniques, such as ultrasonic C-scan. With the additional advantages of non-contact, one-sided and rapid inspection of a large area, the IR thermography offers an attractive method for field inspection of composite structures.[80] However, detection of defects within a thick composite structure may be very difficult because of the inherent characteristics of the technique associated with lateral thermal diffusion. The through-transmission method can detect deeper defects than the pulse-echo technique, but for defects close to the surface, the resolution is superior for the pulse-echo method.

2.3.8 Fibre optics

Most of the techniques discussed above are designed mainly for post-damage inspection. In many applications, however, there are obvious demands for automatic, *in situ*, and remote-working systems as a strain gauge and/or damage indicator. The growth in optical fibre sensor technology has led to many interesting applications for fibre composite structures. These applications include a technique based on optical fibre sensors that are surface-mounted or embedded within the structural components.[86–90] The advantages of embedded optical fibre sensors include light weight, small size, low transmission losses, dielectric properties, and high strength. Besides these advantages over conventional sensors, optical fibre sensors also offer real-time damage monitoring, post-time evaluation, and strain assessment. The possibility of real-time monitoring of structural integrity, especially during impact loading, makes this technique very attractive.

Optical fibres have been extensively used in composite materials and structures to assess cracks and impact damage as fibre breakage sensors.[86,87,91–93] The detection of damage size and location was possible, because when damage occurred in the host structure the optical fibres fractured and thus light was emitted at the damage zone with significantly attenuated light reaching the output ends.[94] The structure was considered sound or undamaged along the optical fibre if the light transmitted on one end was fully transmitted to the other. Further applications of this technique in future will be to integrate all regions of the structure prone to damage and/or inaccessible by ordinary inspection techniques with the network of optical fibres, and to connect them to a computer that can automatically and continuously monitor the loading state and damage development.

Use of optical fibre sensors also has a major limitation. The presence of optical fibres embedded in composite components causes local distortion

and a resin-rich region when the optical fibre diameter is larger than the thickness of the lamina containing it and due to misalignment with reinforcing fibres. Degradation of the mechanical properties of composites due to these adverse effects, however, were found to be negligible, with the exception of compressive strength.[95,96] No significant damage mechanisms associated with the embedded optical fibres were observed in low-velocity impact loading.[97]

2.4   Concluding remarks

Great numbers of experimental techniques have been developed and successfully employed to evaluate the damage state in fibre-reinforced composites subjected to impact loading. The advancement in understanding the damage modes and failure mechanisms upon impact has been possible with the development of state-of-the-art techniques, such as scanning acoustic microscopy (SAM) and X-ray tomographic microscopy (XTM). It is clear that the volume-visualisation SAM combined with ply-by-ply and time-of-flight (TOF) analyses has been the method of first choice for impact damage characterisation of composite laminates from both the detectability and image resolution viewpoints. The SAM indeed provides an effective and quick alternative to destructive, time-consuming de-ply and cross-section fractography techniques, capable of identifying damage shape, size and locations in 3D perspectives. Radiography of various natures provides some capabilities complementary to SAM and other techniques based on ultrasound. The X-ray computed tomography (CT) and XTM have a great potential for 3D evaluation of damage in composites. As sensors, optical fibres embedded within the composite have the ability to detect the occurrence and location of delaminations. The other techniques, including acoustic emission, laser optical methods and infrared thermal methods, currently have limited capabilities in damage detection and image processing, compared to the SAM and XTM. Table 2.1 summarises the applicability and sensitivity of damage detection by various destructive and non-destructive inspection techniques discussed in this chapter.

It appears that the technology to evaluate the damage or defects in composite materials is becoming mature, although none of the aforementioned techniques is perfectly ideal for obtaining all necessary information in desired conditions and locations. With the increasing applications of composite materials in many different industries, including not only the aerospace, automobile, marine, electronics and infrastructure industries but also the sporting goods and biomedical industries, the demand for advanced instrumentation for damage detection and imaging techniques will be ever increasing. In addition to the aforementioned inspection techniques, there are a number of other means of probing flaws, irregularities and defects

Table 2.1. Rating of major inspection techniques with respect to impact damage sensitivity.

Factor or consideration	De-ply technique	Fractography	Visual inspection	Scanning acoustic microscopy	X-ray tomographic microscopy	Thermal imaging	Acoustic emission	Laser holography
Damage type sensitivity								
Delaminations	Good	Very good	Good	Good	Fair	Fair	Poor	Fair
Fibre breakage	Fair	Good	Fair	Very poor	Good	Poor	Poor	Poor
Matrix cracks	Fair	Fair	Fair	Very poor	Good	Poor	Poor	Poor
Surface defects	Good	Good	Very good	Poor	None	Poor	Very poor	Poor
Damage size sensitivity	Good	Good	Fair	Good	Good	Fair	Very poor	Poor
Damage location sensitivity								
Distance from surface	Good	Very good	Fair	Good	Good	Poor	Very poor	Very poor

Source: Gao and Kim.[52]

within the engineering materials and structures. They are vibration techniques, use of eddy currents, microwaves and magnetic resonance, neutron activation analysis, magnetic particle testing, chemical methods, etc. These methods are not specifically discussed in this chapter because the applicability to composite materials is rather limited.

Acknowledgements

References

1 Kim J K, Mackay D B and Mai Y W, 'Drop-weight impact damage tolerance of CFRP with rubber-modified epoxy matrix', *Composites*, 1993 **24** 485–91.
2 Cantwell W J and Morton J, 'The impact resistance of composite materials – a review', *Composites*, 1991 **22** 347–72.
3 Abrate S, 'Impact on laminated composite materials', *Appl Mech Rev*, 1991 **44** 55–187.
4 McRae K I, McCray A G, Russell A J and Bowers C P, 'Ultrasonic imaging of delamination damage around fastener holes in a graphite/epoxy composite', in *Damage Detection in Composite Materials, ASTM STP 1128* (J E Masters, ed), pp 163–79, Philadelphia, American Society for Testing and Materials, 1992.
5 Summerscales J, *Non-destructive Testing of Fibre-reinforced Plastics Composites*, New York, Elsevier Applied Science, 1987.
6 Cawley P and Adams R D, 'Overview: defect types and nondestructive testing techniques for composites and bonded joints', *Mater Sci Technol*, 1989 **5** 413–25.
7 Jones T S and Berger H, 'Thermographic detection of impact damage in graphite-epoxy composites', *Mater Eval*, 1992 **50** 1446–53.
8 Bray, D E and McGride D, *Nondestructive Testing Techniques*, New York, Wiley, 1992.
9 Deaton J B and Rogowski R S, in *Review of Progress in Quantitative Nondestructive Evaluation* (D O Thompson and D E Chimenti, ed), vol 12A, p 395, New York, Plenum Press, 1993.
10 Burke S K, Cousland S M and Scala C M, 'Nondestructive characterization of advanced composite materials', *Mater Forum*, 1994 **18** 85–109.
11 Gao S L and Kim J K, 'Three dimensional characterisation of impact damage in CFRPs', *Key Eng Mater*, 1998 **141–143** 35–54.

12 Kim C G and Jun E J, 'Impact resistance of composite laminated sandwich plates', *J Composite Mater*, 1992 **26** 2247–61.
13 Freeman S M, 'Characterization of lamina and interlaminar damage in graphite/epoxy composites by the de-ply technique', *ASTM STP*, 1982 **787** 50–64.
14 Freeman S M, 'Correlation of X-ray radiograph images with actual damage in graphite-epoxy composites by the de-ply technique', *Proc Composites in Manufacturing 3*, pp EM84/101/1-EM84/101/13, Dearborn, MI, Society of Manufacturing Engineers, 1984.
15 Henneke II, E G, 'Destructive and nondestructive tests', *Engineered Materials Handbook*, vol. I: Composites, pp 774–8, Ohio, American Society for Metals, 1987.
16 Palazotto A, Maddux G E and Horban B, 'The use of stereo X-ray and de-ply techniques for evaluation instability of composite cylindrical panels with delaminations', *Exper Mech*, 1989 **29** 144–51.
17 Harris C E, 'Damage evaluation by laminate de-ply', *Manual on Experimental Methods for Mechanical Testing of Composites*, pp 147–9, Connecticut, Society of Experimental Mechanics, 1989.
18 Clark G, 'Modelling of impact induced damage in composite laminates', *Composites*, 1989 **20** 209–14.
19 Boll D J, Bascom W D, Weidner J C and Murri W J, 'A microscopy study of impact damage of epoxy-matrix carbon-fibre composites', *J Mater Sci*, 1986 **21** 2667–77.
20 Chester R J and Clark G, 'Modelling of impact damage features in graphite/epoxy laminates', in *Damage Detection in Composite Materials, ASTM STP 1128* (J E Masters, ed), pp 200–12, Philadelphia, ASTM, 1992.
21 Gweon S Y and Bascom W D, 'Damage in carbon fibre composites due to repetitive low-velocity impact loads', *J Mater Sci*, 1992 **27** 2035–47.
22 Ross C A and Sierakowski R L, 'Studies on the impact resistance of composite plates', *Composites*, 1973 **4** 157–61.
23 Hirai Y, Hamada H and Kim J K, 'Impact response of glass woven fabric laminates. Pt 1: effect of silane coupling agents', *Composites Sci Technol*, 1998 **58** 91–104.
24 Hirai Y, Hamada H and Kim J K, 'Impact response of glass woven fabric laminates. Pt 2: effect of temperature', *Composites Sci Technol*, 1998, **58** 119–28.
25 Girshovich S, Gottesman T, Rosenthal H, Drukker E and Steinberg Y, 'Impact damage assessment of composites', in *Damage Detection in Composite Materials, ASTM STP 1128* (J E Masters, ed), pp 183–99, Philadelphia, ASTM, 1992.
26 Kortschot M T and Zhang C J, 'Characterization of composite mesostructures and damage by de-ply radiography', *Composite Sci Technol*, 1995 **53** 175–81.
27 Spearing S M and Beaumont P W R, 'Fatigue damage mechanics of composite materials: part I', *Composites Sci Technol*, 1992 **44** 159–68.
28 Spearing S M and Beaumont P W R, 'Fatigue damage mechanics of composite materials: part II', *Composites Sci Technol*, 1992 **44** 169–77.
29 Harris C E and Morris D H, 'Role of delamination and damage development on the strength of thick notched laminates', *ASTM STP 876*, 1985 424–7.
30 Jamison R D, 'Microscopic techniques for damage assessment in laminated composites', in *Microstructural Science*, vol 14, pp 539–59 (M R Louthan Jr, I LeMay and G F Vander Voort, eds), Ohio, American Society for Metals, 1987.

31 Gottesman T and Girshovich S, 'Impact damage assessment and mechanical degradation of composites', *Key Eng Mater*, 1998 **141–143** 3–18.

32 Hopkins P P, Morgan I L, Ellinger H and Klinksiek R, 'Tomographic image analysis', *Mater Eval*, 1982 **40** 1226–8.

33 Chiang B, Hopkins S R and Morgan I L, 'Spatial resolution in industrial tomography', *IEEE Trans Nuclear Sci*, 1983 **NS-30** 1671–6.

34 Flannery B P, Deckman H, Roberge W and D'Amico K, 'Three-dimensional X-ray microtomography', *Science*, 1987 **237** 1439.

35 Widrig J E, McCabe D D and Conner R L, 'Nondestructive evaluation of fibre FP reinforced metal matrix composites', in *Testing Technology of Metal Matrix Composites, ASTM STP 964* (P R DiGiovanni and N R Adsit, eds), pp 227–47, Philadelphia, ASTM, 1988.

36 Kinney J H, Haupt D L, Nichols M C, Breunig T M, Marshall Jr, G W and Marshall S J, 'The X-ray tomographic microscope: three-dimensional perspectives of evolving microstructures', *Nucl Instr Meth Phys Res*, 1994 **347A** 480–6.

37 Buynak C F and Bossi R H, 'Applied X-ray computed tomography', *Nucl Instr Meth Phys Res*, 1995 **B99** 772–4.

38 Stock S R, Breunig T M, Guvenilir A, Kinney J H and Nichols M C, 'Nondestructive X-ray tomographic microscopy of damage in various continuous-fiber metal matrix composites', in *Damage Detection in Composite Materials, ASTM STP 1128* (J E Masters, ed), pp 25–34, Philadelphia, ASTM, 1992.

39 Bathias C and Cagnasso A, 'Application of X-ray tomography to the nondestructive testing of high-performance polymer composites', in *Damage Detection in Composite Materials, ASTM STP 1128* (J E Masters, ed), pp 35–54, Philadelphia, ASTM, 1992.

40 Hirano T, Usami K, Tanaka Y and Masuda C, '*In situ* X-ray CT under tensile loading using synchrotron radiation', *J Mater Res*, 1995 **10** 381–6.

41 Kinney J H, Stock S R, Nichols M C, Bonse U, Breunig T M, Saroyan R A, Nusshardt R, Johnson Q C, Busch F and Antolovich S D, 'Nondestructive investigation of damage in composites using X-ray tomographic microscopy (XTM)', *J Mater Res*, 1990 **5** 1123–9.

42 Ashley S, 'Watching how composites grow', *Mech Eng*, 1993 **115** 70–1.

43 Mummery P M, Derby B, Anderson P, Davis G R and Elliott J C, 'X-ray microtomographic studies of metal matrix composites using laboratory x-ray sources', *J Microscopy*, 1995 **177** 399–406.

44 Deckman H W, Dunsmuir J H, D'Amico K L, Ferguson, S R and Flannery B P, 'Development of quantitative X-ray microtomography', *Mater Res Soc Symp Proc*, 1991 **217** 97–110.

45 Kinney J H, Nichols M C, Bonse U, Stock S R, Breunig T M, Guvenilir A and Saroyan R A, 'Nondestructive imaging of materials microstructures using X-ray tomographic microscopy', *Mater Res Soc Symp Proc*, 1991 **217** 81–95.

46 McIntire P (ed) *Nondestructive Testing Handbook*, 2nd edn, vol 7, *Ultrasonic Testing*, American Society for Nondestructive Testing, 1991.

47 Kim J K, Leung L M, Hirai Y and Lee S W R, 'Impact performance of a woven fabric CFRP', *Polym Polym Composites*, 1996 **4** 549–61.

48 Bar-Cohen Y and Crane R L, 'Nondestructive evaluation of fibre-reinforced composites with acoustic backscattering measurements', *ASTM STP 787*, pp 343–54, Philadelphia, ASTM, 1981.

49 Kessler L W, 'Acoustic microscopy', *Metal Handbook,* vol 17, *Nondestructive Evaluation and Quality Control*, pp 465–82, Materials Park, OH, ASM International, 1989.

50 Smith B T, Heyman J S, Buoncristiani A M, Boldgett E D, Miller J G and Freeman S M, 'Correlation of the de-ply technique with ultrasonic image of impact damage in graphite-epoxy composites', *Mater Eval*, 1989 **47** 1408–16.

51 Smith B T, Farley G L, Maiden J, Coogan D and Moore J G, 'Damage assessment and residual compression strength of thick composite plates with through-the-thickness reinforcements', *Rev Prog Quant Nondestruct Eval*, 1991 **10** 1623–30.

52 Gao S L and Kim J K, 'Scanning acoustic microscopy as a tool for quantitative characterisation of damage in CFRPs', *Composite Sci Technol*, 1999 **59** 345–54.

53 Gao S L, Kim J K and Xian X J, 'Characterisation of impact damage in CFRPs using a scanning acoustic microscope', *Proc 11th Int Conf Composite Materals (ICCM-11)*, vol 6, pp 185–92, Australia, Gold Coast, 1997.

54 Gao S L and Kim J K, 'Effect of cooling rate on impact performance of carbon fibre/PEEK laminates', *Proc 8th European Conf Composite Materials (ECCM-8),* vol 1, pp 95–102, Cambridge, Woodhead Publishing, 1998.

55 Ishikawa T, Sugimoto S, Matsushima M, Hayashi Y, 'Some experimental findings in compression-after-impact (CAT) tests of CF/PEEK (APC-2) and conventional CF/epoxy flat plates', *Composites Sci Techol*, 1995 **55** 349–63.

56 Gosse J H and Hause L R, 'A quantitative non-destructive evaluation technique for assessing the compression-after-impact strength of composite plates', in *Proc 3rd Tech Conf Composite Materials*, pp 344–53, American Society for Composites, 1988.

57 Kim J K and Mai Y W, *Engineered Interfaces in Fibre Reinforced Composites*, ch 8, pp 329–65, New York, Elsevier 1998.

58 Todoroki A, Kobayashi H and Lee J G, 'Impact analysis of delamination cracks in carbon-fibre composites by scanning acoustic microscopy', *Composites Sci Technol*, 1992 **52** 551–9.

59 Kauppinen P and Kivilahti J, 'Evaluation of structural defects in brazed ceramic-to-metal joints with C-mode scanning acoustic microscopy', *NDT & E Intern*, 1991 **24** 187–90.

60 Cognard J, Sathish S, Kulik A and Gremond G, 'Scanning acoustic microscopy of the cellular structure of the interphase in a metal-adhesive bond', *J Adhesion*, 1990 **32** 45–9.

61 Moore T, McKenna R and Kelsall S, 'Correction of surface mount plastic reliability testing to nondestructive inspection by scanning acoustic microscopy', *Proc 29th Reliab Phys Symp*, 160–6, 1991.

62 Semmens J E, Martell S R and Kessler L W, 'New quantitative acoustic micro imaging methods for plastic moulding compound characterisation', EEP vol 10–11, pp 493–9, *Advances in Electronic Packaging*, American Society of Mechanical Engineers, 1995.

63 Yang J C, 'Non-destructive identification of defects in integrated circuit packages by scanning acoustic microscopy', *Microelectron Reliab*, 1996 **36** 1291–5.

64 Buynak C F, Moran T J and Martin R W, 'Delamination and crack imaging in graphite/epoxy composites', *Mater Eval*, 1987 **6B** 1203–11.

65 Hamstad M A, 'A review: acoustic emission, a tool for composite materials studies', *Exp Mech*, 1986 **26** 7–13.

66 Miller R K and McIntire P (eds), 'Acoustic emission testing', *Nondestructive Testing Handbook*, vol 5, Columbus, OH, American Society for Nondestructive testing, 1987.

67 Arrington M, 'Acoustic emission', in *Nondestructive Testing of Fibre Reinforced Plastic Composites*, vol 1, pp 25–63 (J Summerscales, ed), New York, Elsevier Applied Science, 1987.

68 Narisawa I and Ishikawa M, 'An evaluation of acoustic emission from polymer composite', in *Ultrasonic Spectroscopy* (Y Wada, ed), pp 38–43, Japan, Ministry of Education, Science & Culture, 1987.

69 Netravali A N, Henstenburg R B, Phoenix S L and Schwartz P, 'Interfacial shear strength studies using the single filament composite test', *Polym Composites*, 1989 **10** 226–41.

70 Vautey P and Favre J P, 'Fibre/matrix load transfer in thermoset and thermoplastic composite-single fibre models and hole sensitivity of laminates', *Composites Sci Technol*, 1990 **38** 271–88.

71 Park J M, Chong W M, Yoon D J and Lee J H, 'Interfacial properties of two SiC fibre-reinforced polycarbonate composites using the fragmentation test and acoustic emission', *Polym Composites*, 1993 **19** 747–58.

72 Eckles E F and Awerbuch J, 'Monitoring acoustic emission in cross-ply graphite/epoxy laminates during fatigue loading', *J Reinf Plast Composites*, 1988 **7** 265–83.

73 Awerbuch J, Gorman M R and Madhudar M, 'Monitoring acoustic emission during quasi-static loading-unloading cycles of filament wound graphite epoxy laminate coupons', *Mater Eval*, 1985 **43** 754–64.

74 Awerbuch J and Bakuckas J G, 'On the applicability of acoustic emission for monitoring damage progression in metal matrix composites', in *Metal Matrix Composites: Testing, Analysis and Failure Modes, ASTM STP 1032*, pp. 68–99 (W S Johnson, ed), Philadelphia, ASTM, 1989.

75 Vest C M, *Holographic Interferometry*, New York, Wiley, 1979.

76 Rubayi N, Liew S H and Wright M A, 'Application of holographic interferometry as a NDT method in composite plates', in *Nondestructive Testing and Evaluation for Manufacturing and Construction* (H L M dos Reis, ed), pp 435–49, New York, Hemisphere Publishing, 1990.

77 Hung Y Y, 'Shearography: a new optical method for strain measurement and nondestructive testing', *Opt Eng*, 1981 **21** 391.

78 Hung Y Y, 'Shearographic nondestructive testing', in *Nondestructive Testing Handbook*, 2nd edn, vol 9, pp 128–40, Special Nondestructive Testing Methods, American Society for Nondestructive Testing (P O Moore and P McIntire, eds), 1995.

79 ASTM Standard E1311–89, 'Standard test method for minimum detectable temperature difference for thermal imaging system', Philadelphia, ASTM.

80 Jones T S and Berger H, 'Nondestructive evaluation methods for composites', in *International Encyclopedia of Composites* (S M Lee, ed), vol 4, pp 37–49, New York, VCH, 1991.

81 Maldague X, Krapez J C and Ciel P, 'Temperature recovery and contrast computations in NDE thermographic imaging systems', *J Nondestructive Eval*, 1991 **10** 19–30.

82 Reynolds W N and Wells G M, 'Video-compatible thermography', *Brit J Nondestructive Testing*, 1984 **26** 40–4.

83 Hinton Y L, Shuford R J and Pergantis C G, 'Application of real-time thermography for CDT of composites', *Thermosense VIII*, Cambridge, MA, SPIE, 1984.

84 Wilson D W and Charles J A, 'Thermographic detection of adhesive bond and interlaminar flaws in composites', *Exp Mech*, 1981 **21** 276–80.

85 Puttick K E, 'Thermal NDT methods', in *Nondestructive Testing of Fibre Reinforced Plastic Composites*, vol 1 (J Summerscales, ed), pp 65–103, New York, Elsevier Applied Science, 1987.

86 Crane R M and Gagorik J, 'Fibre optics for a damage assessment system for fibre-reinforced plastic composite structures', *Rev Prog Quant Nondestruct Eval*, 1984 **28** 288–94.

87 Hofer B, 'Fibre optic damage detection in composite structures', *Composites*, 1987 **18** 309–16.

88 Spillman W B and Fuhr P L, 'Impact detection and location system for smart skins application', *Proc SPIE, Fibre Optic Smart Structures and Skins III*, 1990 **1370** 308–15.

89 Udd E, *Fibre Optics Sensors: An Introduction for Engineers and Scientists*, New York, Wiley, 1991.

90 Asanuma H, Ichikawa K and Kishi T, 'Health monitoring of a continuous fibre-reinforced aluminium composite with embedded optical fibre', *J Intell Mater Sys Struct*, 1996 **7** 307–11.

91 Kuhlman R, Duncan B and Clans R O, *Proc IEEE Southeast Conference*, vol 2, 1987.

92 Measures R M, Glossop N D W, Lymer J, LeBlanc M, West J, Dubois S, Tsaw W and Tennyson R C, 'Structurally integrated fibre optic damage assessment system for composite materials', *Appl Opt*, 1989 **28** 2626–33.

93 Hale K F, 'An optical fibre fatigue crack detection and monitor system', *Smart Mater Struct*, 1992 **1** 156–61.

94 Lu Z J and Blaha F A, 'A fibre optical strain and impact sensor system for composite materials', *SPIE Fibre Optic Smart Structures and Skin II*, 1989 **1170** 239–48.

95 Carman G P and Sendeckyj G P, 'Review of the mechanics of embedded optical sensors', *J Composite Technol Res*, 1995 **17** 183–93.

96 Choi C, Seo D C, Lee J J and Kim J K, 'Effect of embedded optical fibres on the interlaminar fracture toughness of composite laminates', *Composite Interfaces*, 1998 **5** 225–40.

97 Sirkis J S, Chang C C and Smith B T, 'Low velocity impact of optical fibre embedded laminated graphite/epoxy panels. part I: macro-scale', *J Composite Mater*, 1994 **28** 1347–70.

3

Modelling impact of composite structures using small specimens

C RUIZ AND J HARDING

3.1   Introduction

An essential pre-requisite for successful modelling of the impact response of any engineering structure is a knowledge of the mechanical properties of the materials used in manufacturing the structure at the appropriate rates of strain. For polymeric matrix fibre-reinforced composites the properties of principal interest are the elastic moduli and the failure strengths. These properties are likely to be strongly dependent on orientation. The extent to which they are also sensitive to rate of loading will depend, amongst other factors, on the nature and geometry of the reinforcement, the type of matrix, the direction of loading and the strength of the bonding between fibres and matrix and between neighbouring plies. The range of strain rates encountered in the impact of composite structures may be very wide, from as low as 1/s or less in low velocity soft-body impact of large structures to well in excess of $1000\,\mathrm{s}^{-1}$ in regions of localised deformation associated with high velocity hard-body impact.

When all these factors are considered this amounts to a very extensive database, well beyond what is currently available for any given composite material or class of composite material. Nevertheless a great deal of work has been done to determine the effect of strain rate on the mechanical responses of composite materials and some general trends have been identified. The usual approach is to develop designs of small specimens in which, for simple loading systems, the stress distribution is well understood and in which particular failure processes are expected to predominate. The results of such tests may then be used to investigate the impact response of simple structural elements where more complex stress systems are present and failure may result from an interaction between, and a combination of, several different processes. The design of these small specimens is complicated by the requirement that they should be suitable for testing over a wide range of strain rates. In particular, problems may arise at the higher strain rates. For example, in tests at strain rates greater than about $100\,\mathrm{s}^{-1}$

it is common to use techniques based on the split Hopkinson pressure bar principle in which the specimen is loaded by means of stress waves.[1] In developing the design of specimen it is necessary to achieve quasi-static equilibrium in the specimen at an early stage in the test and to avoid spurious wave reflections arising from an interaction between the specimen and the test equipment. Section 2 of this chapter deals with small specimen testing, giving a brief review of some of the techniques that have been used and some of the general trends in behaviour which have emerged.

Some of the problems which arise when looking at the impact response of simple structures are discussed in Section 3. Two beam structures are considered. In the first, dynamic photo-elasticity is used to study wave propagation in layered cantilever beams under transverse end impact with different strengths of bonding across the interface between the layers. In the second case, high-speed photography is used to observe the failure processes in the transverse impact of cross-ply carbon reinforced epoxy beams under three-point bending. For both geometries of loading and types of beam, analytical solutions are developed and rate-dependence of material properties does not feature.

The specific question of modelling impact damage is then raised in Section 4. Simplified approaches are considered first, involving scaling laws and empirical rules for damage development. This is followed by a discussion of the application of general finite element codes in terms of stress-based failure criteria, for predicting the initiation of damage, and fracture mechanics based criteria, for predicting damage propagation.

The emphasis of this chapter is in the measurement of tensile and shear properties since these are regarded as the most important intrinsic material properties needed by designers. Compression strength is affected by end conditions and results from a combination of structural and material behaviour.

3.2   Small specimen testing

In recent years several reviews have been written[1-3] describing the various techniques which may be used to obtain data on the mechanical properties of composite materials at high rates of strain. In the present article, therefore, only a brief summary will be given of a few of these methods. All are based on the split Hopkinson pressure bar in various forms so as to allow in-plane tension, compression and tension/shear properties and through-thickness tension, compression and interlaminar shear properties to be determined at impact rates of strain. This will be followed by a discussion of the general trends in the mechanical response observed under impact loading and their dependence on the nature and geometry of the rein-

forcement and the types of matrix. The section will conclude with some results illustrating the effects obtained in hybrid reinforced laminates when different fibre types are combined.

3.2.1 Specimens and techniques

3.2.1.1 The split Hopkinson bar apparatus

In principle the standard split Hopkinson bar (or Kolsky bar) apparatus consists of two long, thin cylindrical loading bars, the input bar and the output bar, between which is placed the specimen. In the original Kolsky bar[4] a short cylindrical specimen was tested in compression by means of a compressive stress wave in the input bar resulting from a projectile impacting at its free end. Stress waves propagating in the input and output bars are monitored by means of strain gauges and one-dimensional elastic wave theory is used to determine the stress and particle velocity at the ends of the bars in contact with the specimen. The velocity difference across the ends of the specimen and its integral with respect to time allow the specimen strain rate and strain to be determined. Once equilibrium has been established the stress measured at the ends of the loading bars gives a measure of the stress under which the specimen is deforming. A comparison between the stresses determined at the input and output ends of the specimen, σ_u and σ_l, respectively, in such a test on a woven reinforced glass/epoxy composite is shown in Fig. 3.1. The good agreement between the two indicates that equilibrium has been achieved early in the test.

3.2.1.2 In-plane compression tests

Although the original Kolsky bar method with a short cylindrical specimen has been used,[5] this specimen geometry is not ideal for measuring in-plane compressive strengths for composite materials which are normally obtained as thin laminates. In an alternative arrangement, therefore, thin parallel-sided compression specimens waisted in the thickness direction, similar to those developed for use in the tensile impact, have been employed. A schematic diagram of the test arrangement is shown in Fig. 3.2 and a typical specimen geometry is shown in Fig. 3.3. Dimensions S and d will be determined by the ply thickness and lay-up for the given laminate. The specimen is fixed into parallel-sided slots in the loading bars. Compressive stress waves are monitored at two stations, GI and GII, on the input bar, allowing a separation of the incident and reflected waves, and at one station, GIII, on the output bar, monitoring the transmitted wave. The use of two gauge
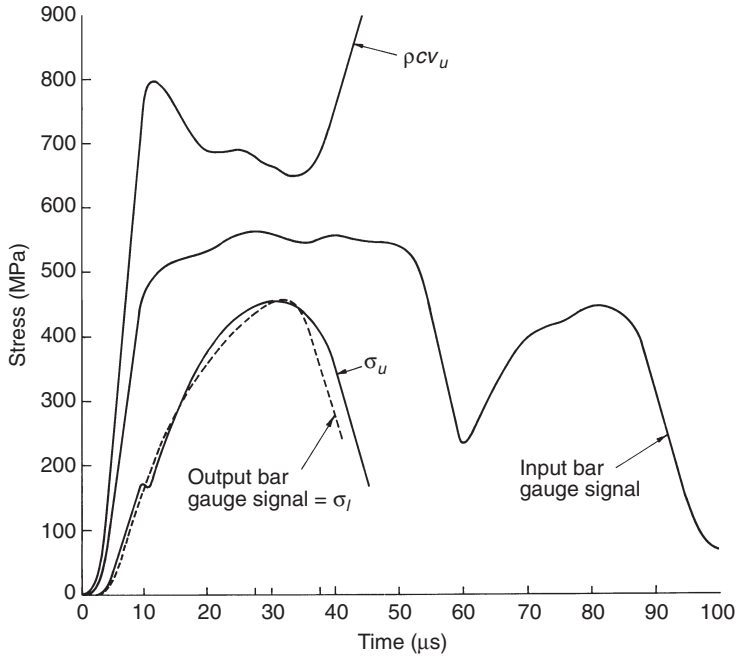
3.1 Comparison between input bar stress, σ_u, and output bar stress, σ_l, for impact compression test on cylindrical composite specimen.
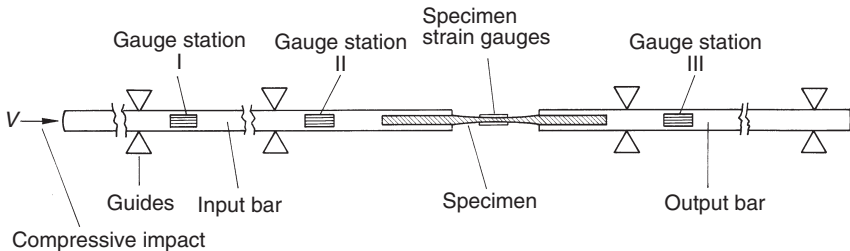
3.2 Schematic diagram of split Hopkinson bar arrangement for compression impact tests on thin strip composite specimens.

stations on the input bar adds complications to the wave analysis, full details of which have been given elsewhere,[6] but improves the accuracy with which the velocity difference across the specimen, and hence the strain, may be determined. Under transient loading, buckling of the long, thin loading bars is not a problem. Although local microbuckling of the specimen in the parallel test section may be the controlling mechanism of failure, this specimen geometry mirrors more closely than the cylindrical specimen the constraints
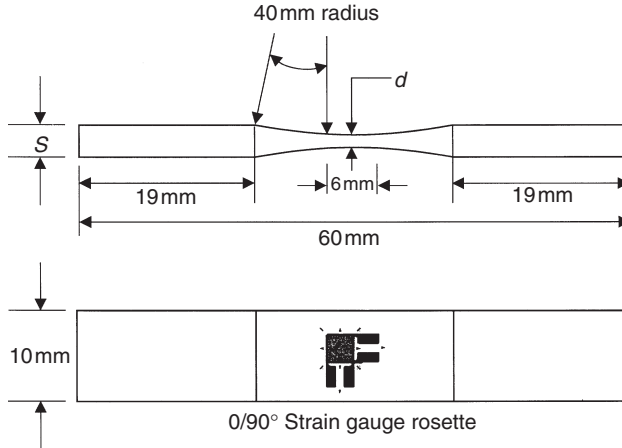
3.3 Dimensions of standard in-plane tension, compression and tension/shear specimen.

experienced in real engineering structures. Strain gauges attached to the parallel test section monitor the elastic deformation of the specimen and allow a measure to be made of both the compressive modulus and Poisson's ratio.

3.2.1.3 In-plane tension tests

The same thin strip design of specimen and arrangement of input and output bars may be used as for the compression tests. The first version of tensile Hopkinson bar designed for use with composite materials[7] employed a drop-weight loading system. In a more recent version, however, the tensile loading pulse is generated by means of a cylindrical projectile accelerated by a gas-gun.[8] The general arrangement is shown in Fig. 3.4. The test is initiated by increasing the gas pressure in chamber A until the projectile moves to the right and sustains the full gas pressure in chamber B. It then accelerates towards and impacts on the stopper block at the end of the loading bar causing a tensile stress wave to propagate back along the loading bar and into the input and output bars of the split Hopkinson bar assembly.

Standard methods of fixing tensile strip specimens to the loading bars are not suitable when using the split Hopkinson bar technique since they would introduce spurious reflections in the elastic wave analysis. It is necessary, therefore, to fix the parallel ends of the strip specimens directly into parallel sided slots in the loading bars using epoxy adhesive, as shown in Fig. 3.4. Since the adhesive has to be cured over a period of several days before
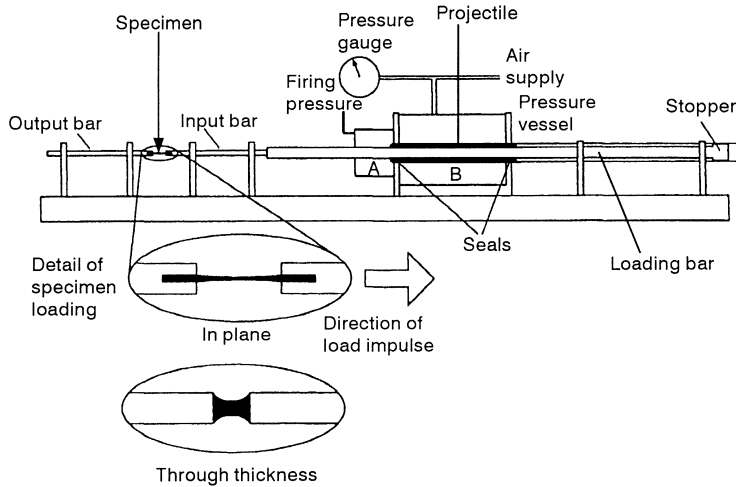
3.4 Schematic diagram of the loading system for the tensile split Hopkinson bar apparatus and methods of fixing in-plane and through-thickness tension specimens.
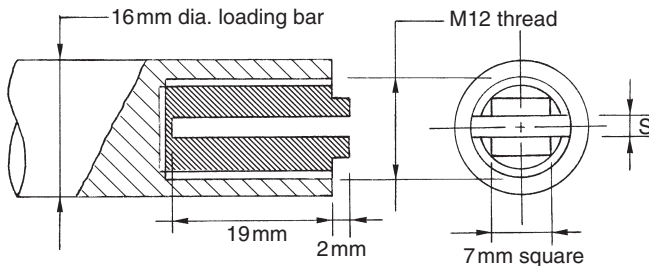

3.5 Modified method of fixing strip specimens to tensile loading bars using screw fixed end caps.

testing can proceed, when a large number of tests is to be performed it may be desirable to use disposable slotted end caps, see Fig. 3.5, allowing several specimens to be prepared for testing at the same time. In general, however, better results are obtained when specimens are fixed directly into parallel sided slots in the input and output bars.

3.2.1.4 In-plane shear tests (Rosen tests)

For cross-ply or woven reinforced laminates in-plane shear tests may also be performed on thin strip specimens if the tensile axis is cut at a ±45° orientation to the principal direction of reinforcement. Tests are performed in
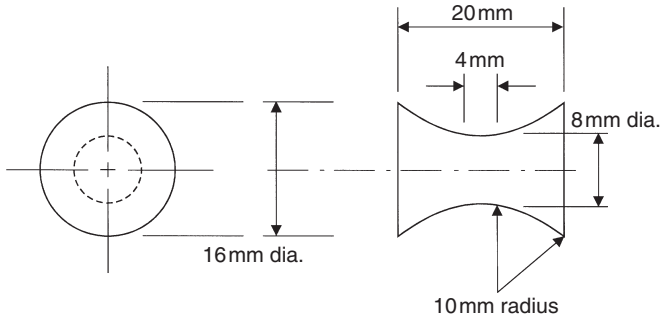
3.6 Dimensions of through-thickness tension and compression specimens.

exactly the same way as for the in-plane tension or compression tests. Strain gauge rosettes attached to the specimen parallel section allow the shear modulus to be determined at each rate of loading. A balanced lay-up in the test section of the general form $[(+45°/-45°)_n]_s$ is required.

3.2.1.5   Through-thickness tension and compression tests

For both test configurations waisted cylindrical specimens may be used, the compression specimens being tested in a standard compression split Hopkinson bar apparatus and the tension specimens on the tensile version of split Hopkinson bar, but with the specimens fixed directly with epoxy adhesive to the flat ends of the input and output bars, see Fig. 3.4.[9] Threaded caps, as in Fig. 3.5, may be used but are best avoided. Typical specimen dimensions are shown in Fig. 3.6 requiring the use of relatively thick laminates with lay-ups of up to 100 plies.

3.2.1.6   Through-thickness (interlaminar) shear tests

An impact test for composite materials in which a pure shear stress is applied on the interlaminar plane is very difficult to achieve. However, a special design of single-lap shear specimen has been developed,[10] see Fig. 3.7, which has the advantage of an approximately uniform shear stress on the central interlaminar plane in the region where failure occurs. It may be tested in a modified version of the compression split Hopkinson bar, as illustrated in Fig. 3.8. Strain gauge rosettes attached to the sides of the specimen measure the average shear strain in the region close to the failure plane. While this does not give a true measure of the local strain at failure, it does allow an estimate of the shear modulus to be made.
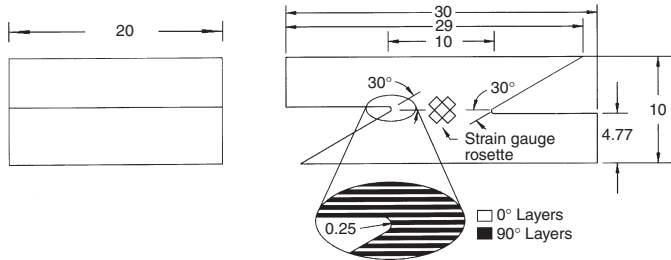
3.7 Dimensions of single-lap shear specimen showing lay-up details for cross-ply material (dimensions in mm).
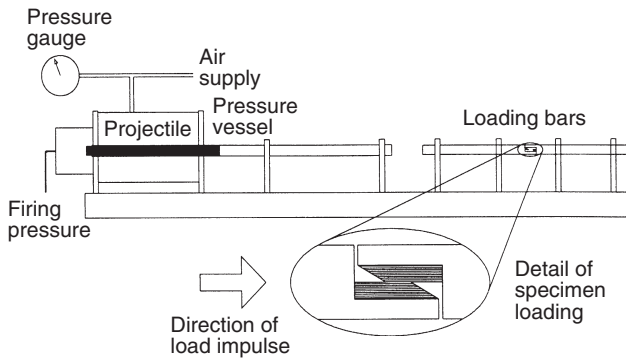

3.8 Loading system for single-lap shear specimens in compression split Hopkinson bar apparatus (dimensions in mm).

3.2.2 Strain rate effects in polymer matrix composites

Using tests of the type described above data have been obtained which illustrate some general trends in the mechanical response of composite materials at impact rates of strain.

3.2.2.1 Geometry of reinforcement

When unidirectionally-reinforced carbon/epoxy specimens are strained in a direction parallel to the fibres at rates from 10^{-3} to $10^{+3}\,\text{s}^{-1}$ no effect of strain rate on the tensile modulus, tensile strength or failure strain was observed,[7] Fig. 3.9. However, in similar tests on woven-reinforced carbon/epoxy specimens, a small increase in tensile modulus and strength and a small decrease in the failure strain over this range of strain rate was observed,[11] Fig. 3.10. The increase in modulus and strength is much more marked when woven-reinforced glass/epoxy specimens are tested in this
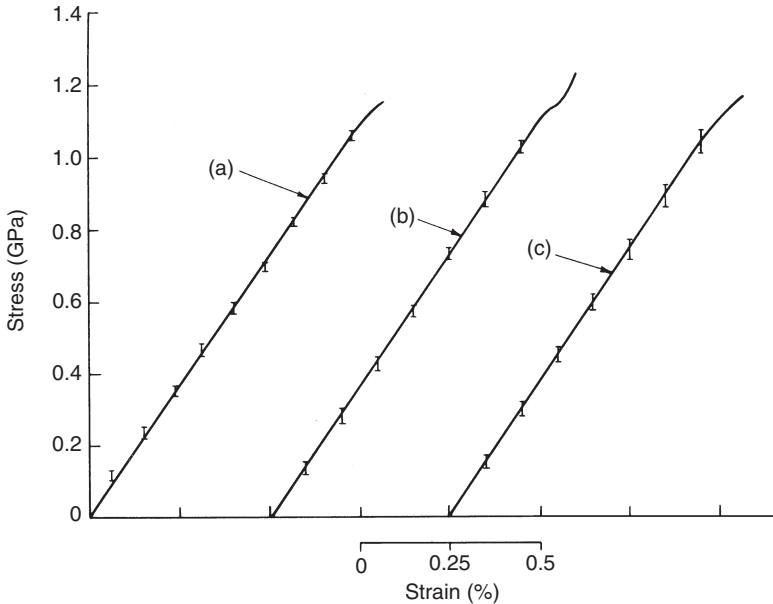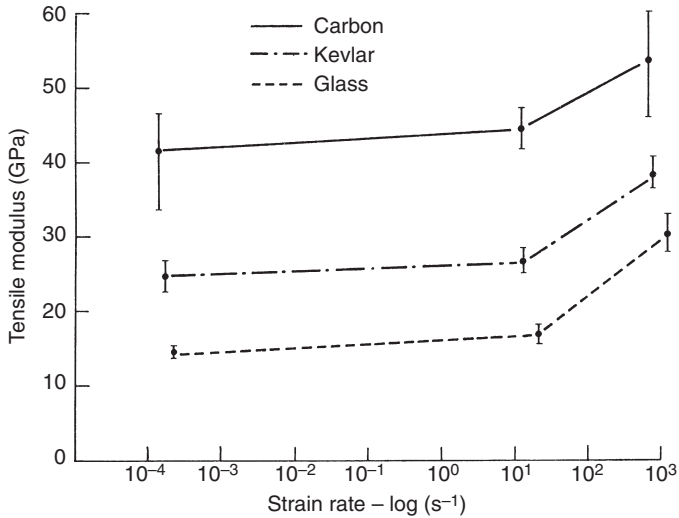
3.9 Effect of strain rate on the tensile stress-strain curve for UD carbon/epoxy (mean strain rate, s^{-1}: (a) 10^{-4}; (b) 10; (c) 450). (After Harding and Welsh[7].)

way while for this material the failure strain increases with increasing strain rate, see Fig. 3.11. Taken together, these results suggest that the strength of the carbon fibres is completely rate-independent and that the small rate dependence observed in the woven CFRP specimens arises from the resistance of the polymer matrix to the straightening of the woven fibres under the tensile load. It also seems likely that the strength of the glass fibres does increase with strain rate and that this allows the increase in the damage region seen in the impacted specimens preceding final failure, the reason for the increase in failure strain.

3.2.2.2 Fibre type

To study the effect of using different types of fibre on the strain rate dependence of fibre-reinforced polymers, a direct comparison has been made[12] of the rate dependence of three woven reinforced composites. The same polyester matrix was used in each case and each composite was reinforced with a satin-weave mat of identical geometry using carbon, kevlar or glass fibres. Tests were performed in tension at strain rates from 10^{-3} to 10^{+3}s^{-1}. While the absolute value of the tensile modulus depended
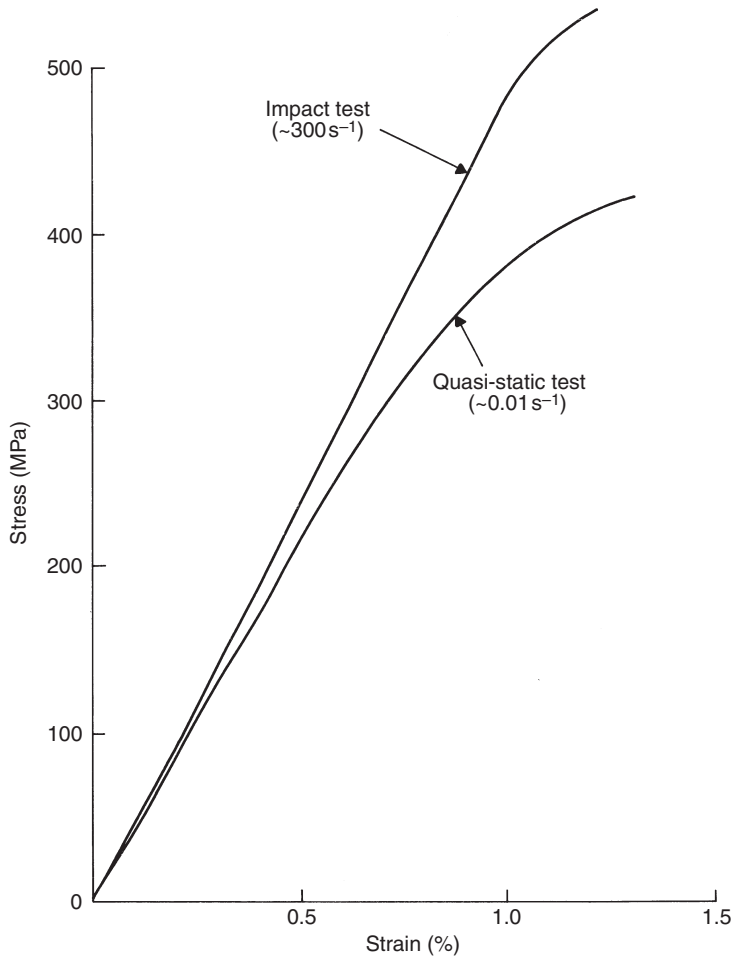
3.10 Effect of strain rate on the tensile stress-strain curve for woven carbon/epoxy. (After Harding and Li[11].)

on the fibre type, carbon fibres giving the highest tensile modulus and glass fibres the lowest, the rate-dependence of the modulus was the same for all three composites, see Fig. 3.12. This supports the earlier suggestion that the rate dependence of the tensile modulus in woven reinforced composites is due to the resistance of the matrix to the straightening of the woven fibre tows, i.e. it depends on the properties of the matrix and the geometry of the reinforcement. For all three fibre types some increase in tensile strength and failure strain with strain rate was apparent, the increase being much more significant for the glass-reinforced composite.
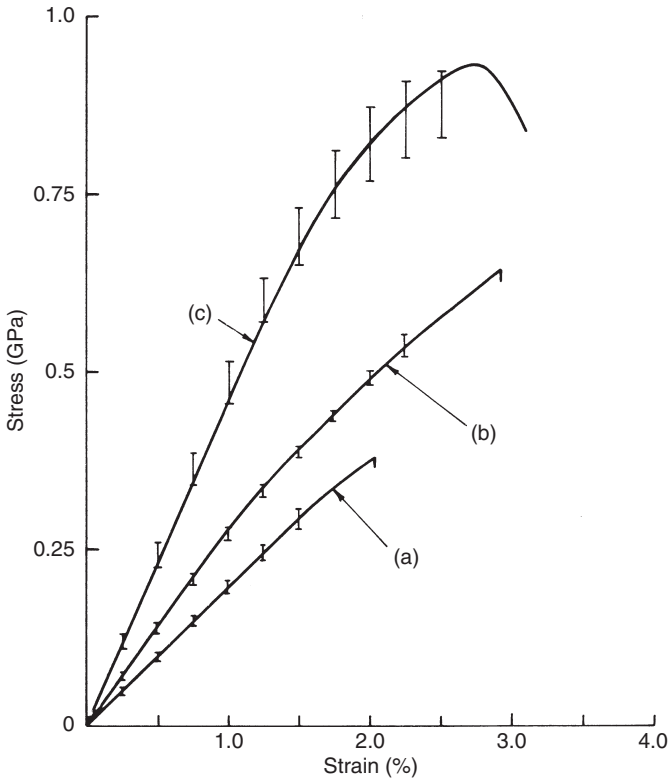
3.11 Effect of strain rate on the tensile stress-strain curve for woven glass/epoxy (mean strain rate, s^{-1}: (a) 10^{-4}; (b) 10; (c) 900). (After Harding and Welsh[7].)

3.2.2.3 Direction of loading

The mechanical properties of composites are strongly orientation depen-dent, with the highest strengths in directions parallel to the reinforcing fibres. However, since the matrix properties play a significant role in deter-mining the strain rate sensitivity of the composite, larger rate effects may be apparent in directions other than those parallel to the reinforcing fibres. This is expected to be the case for the in-plane shear modulus which is strongly dependent on the matrix properties. This is demonstrated in Table 3.1, which lists shear modulus values for balanced plain-weave glass/epoxy and carbon/epoxy laminates at a quasi-static and an impact rate.[13] Both laminates show a very significant increase in shear modulus with strain rate.

Composites are normally designed for strength in the plane of reinforcement and are usually relatively weak in the through-thickness

3.12 Effect of strain rate and fibre type on the tensile modulus for satin-weave/polyester laminates. (After Welsh and Harding[12].)

Table 3.1. Effect of strain rate on the in-plane shear modulus (GPa)

Material	In-plane shear modulus (GPa)		% age increase
	Quasi-static	Impact	
Glass/epoxy	1.69	3.55	110
Carbon/epoxy	2.73	4.02	47

Table 3.2. Effect of strain rate on the through-thickness tensile modulus of three woven reinforced laminates (GPa)

Material	Woven carbon (24 plies)	Woven glass (60 plies)	Hybrid carbon/glass (37 plies)
Quasi-static	6.50 ± 0.06	6.03 ± 0.56	6.47 ± 0.07
Impact	8.95 ± 0.30	8.47 ± 0.26	8.40 ± 0.14

direction where only small rate effects might be expected. However, a significant effect of strain rate on the tensile modulus measured in the through-thickness direction has been observed[14] for woven reinforced laminates. Results are listed in Table 3.2, which shows an increase of about 30% for all three laminates studied. Tests performed on cylindrical specimens in
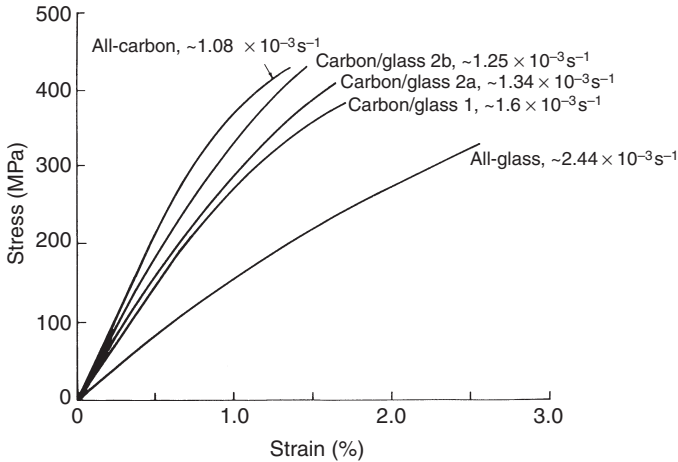
3.13 Effect of hybrid fraction on quasi-static stress–strain response of carbon/glass/epoxy laminates. (After Saka and Harding[16].)

through-thickness compression show very high failure strengths and a rate-sensitivity which depends on both the fibre type and the reinforcement geometry.

3.2.3 Strain rate effects in hybrid laminates

The marked effects of strain rate shown in the increase in the modulus, tensile strength and strain to failure for woven glass laminates suggest that an improved impact damage resistance in carbon reinforced laminates might be achieved by the use of hybrid carbon/glass lay-ups.

3.2.3.1 Stress-strain response

Tensile stress-strain curves for an all-glass, an all-carbon and three hybrid carbon–glass lay-ups, are shown in Fig. 3.13, at a quasi-static rate of about $10^{-3}s^{-1}$, and Fig. 3.14, at an impact rate approaching $10^{+3}/s$.

It is apparent that at both rates of strain the carbon fibres control the hybrid properties, raising the failure strength to close to that for the all-carbon laminate and reducing the failure strain to below 2%. The tensile modulus under impact loading, see Fig. 3.15, follows closely the 'rule of mixtures' prediction. The numbers in brackets in the figure correspond to the number of tests.

3.2.3.2 Effect of hybrid fraction on failure strength

All five laminates show a significant increase in tensile strength with strain rate, see Fig. 3.16, and for two of the three hybrid lay-ups the tensile strength
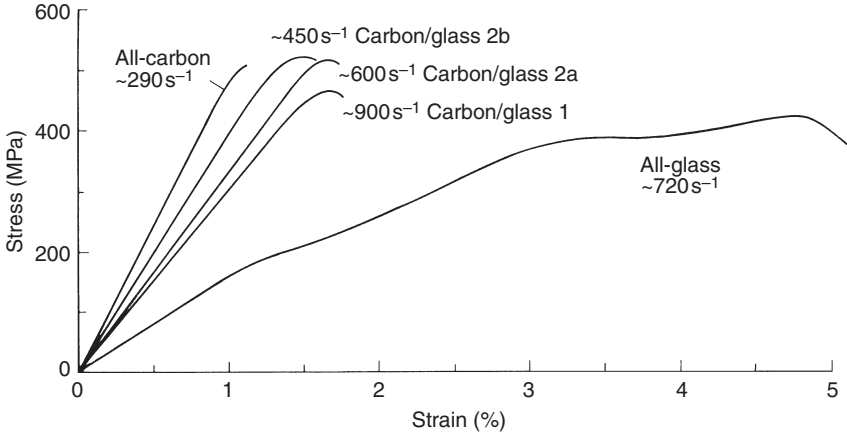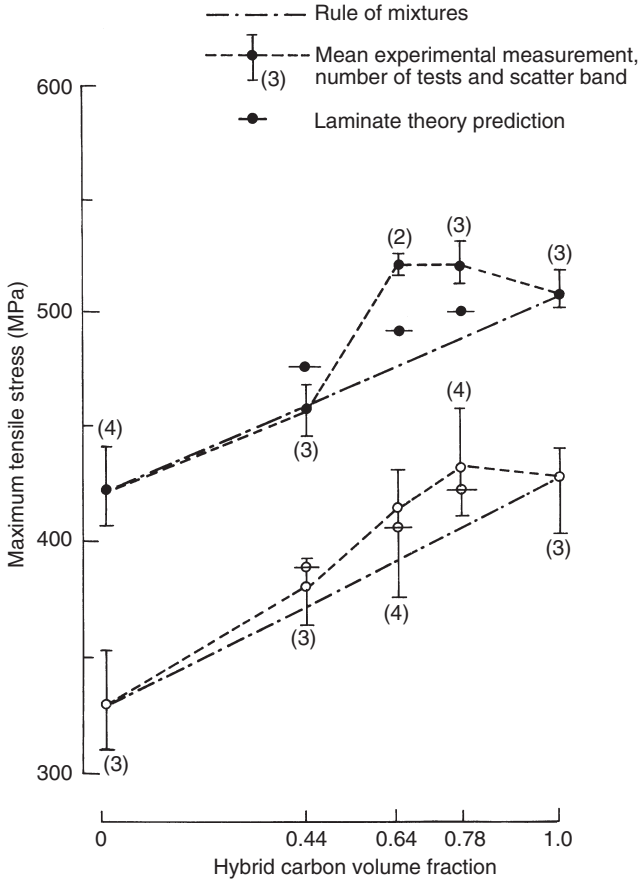
3.14 Effect of hybrid fraction on the impact stress–strain response of carbon/glass epoxy laminates. (After Saka and Harding[16]).
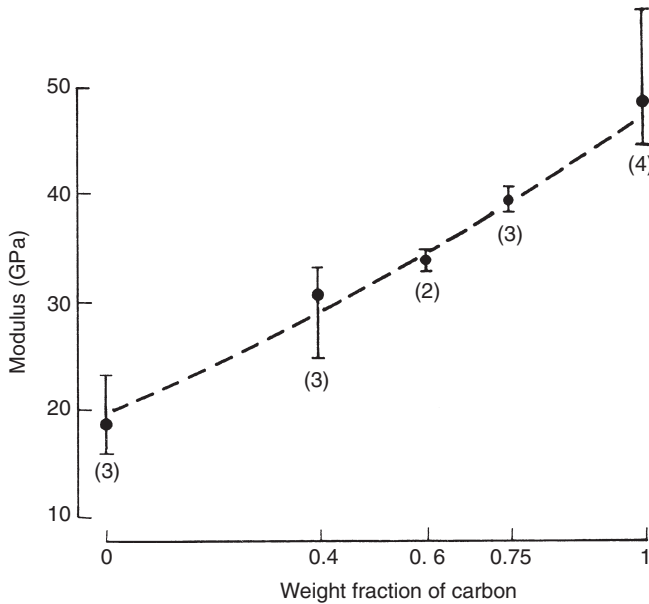
3.15 Effect of hybrid fraction on the impact tensile modulus. (After Saka and Harding[16].)

is significantly greater than is predicted by the rule of mixtures, i.e. a linear combination of the properties of the all-carbon and all-glass laminates. Classical laminate theory in conjunction with the Tsai–Wu failure criterion,[15] using strength properties obtained from tests on the all-glass and all-carbon

3.16 Effect of hybrid fraction on the failure strength: –◦– quasi-static tests, loading in warp direction; –•– impact tests, loading in weft direction. (After Saka and Harding[16].)

laminates, does predict an increased strength for the hybrid lay-ups above that for the rule of mixtures.[16] For two of the three hybrid lay-ups, however, the predicted increase is less than that observed experimentally. It seems clear, therefore, that, in addition to the hybrid fraction, the stacking sequence is also important since it will affect the out-of-plane stresses which are not taken into account in the laminate theory approach. However, some allowance for these effects may be made if finite element methods are used.[17]

3.2.3.3   Effect of hybrid fraction on the failure strain

Failure strains for the all-glass and all-carbon laminates and for the three hybrid lay-ups are shown in Fig. 3.17. For the all-carbon laminates, the mean
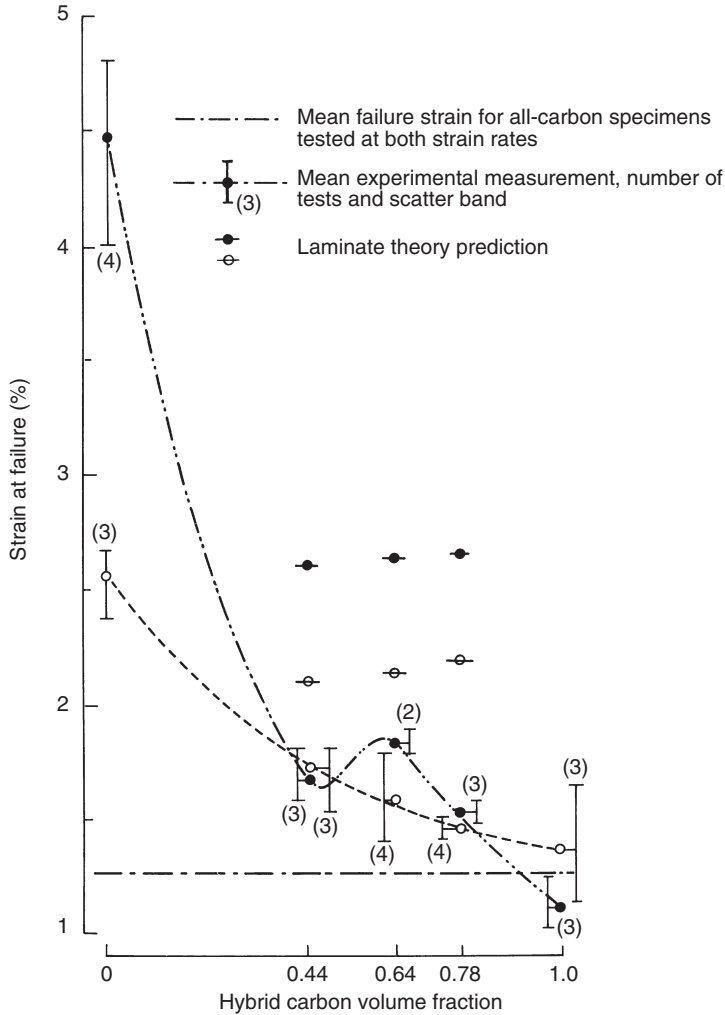
3.17 Effect of hybrid fraction on the failure strain: –⊖– quasi-static tests, loading in warp direction; –●– impact tests, loading in weft direction. (After Saka and Harding[16].)

quasi-static failure strain was slightly greater than that determined in the impact tests. For two of the hybrid lay-ups the failure strain was independent of strain rate while for the third the failure strain was greater under impact loading, further evidence for the importance of the stacking sequence. In all three cases, however, hybridisation had increased the failure strain significantly above the mean value for all-carbon laminates. Experimental scatter bands, given in Fig. 3.17, are seen to be quite large in several

cases so these results should only be taken as indicating general trends. It is apparent that the laminate theory approach, which modelled the hybrid failure strengths fairly closely, seriously overestimates the failure strains at both the quasi-static and the impact rates.

3.3   Structural analysis of impact

In the study of impact of composite structures three regimes are distinguished:

1   Impact at velocities of the order of $300\,\mathrm{m\,s}^{-1}$. Where the projectile penetrates or perforates the target, all the damage is confined to a small area around the point of impact and the structure itself plays no part in the process.
2   Impact at velocities within the range $50–300\,\mathrm{m\,s}^{-1}$. The stress waves originating from the point of impact transmit the load to the rest of the structure. A dynamic analysis which includes inertial loading and stress wave action is necessary.
3   At even lower impact velocities multiple wave reflections take place at the boundaries and quasi-static equilibrium is reached.

The ultra high-velocity impact (1) is of little practical interest except in military applications. Whether the target survives or is defeated depends primarily on the material properties in particular through-thickness compression and shear. The other two regimes (2) and (3) are of considerably greater interest.

Before finite element analysis became common practice, researchers studied the structural response of laminates by reference to simplified systems with a discrete number of degrees of freedom or by the solution of the elastodynamic equations. A comprehensive review of these methods may be seen in Abrate.[18] While FE analysis is the only practical way to study real situations, older and less fashionable techniques do offer certain advantages for the interpretation of simple experiments which highlight the important features of the phenomenon. As an illustration, an investigation into the impact loading of layered beams will be described next.

### 3.3.1   Response of laminated beams to impact: effect of interface

Stress waves initiated from the point of impact travel with a velocity dependent on the nature of the wave, i.e. whether it results in distortion or dilation, and on the value of the Young's modulus, the Poisson's ratio and the density of the material. Typically, a dilatational uniaxial wave travelling
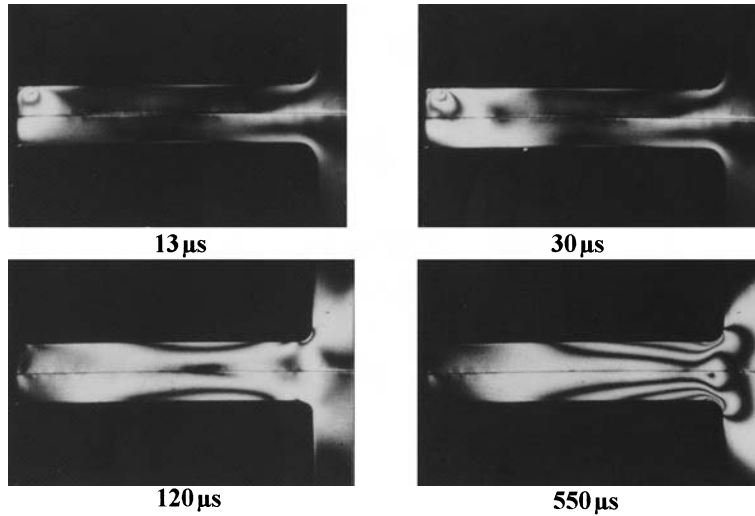
3.18 Two layer specimen with 'superglue' adhesive bonding. (After Ruiz and Xia[19].)

along a rod will do so at a velocity equal to $\sqrt{(E/\rho)}$. For a unidirectionally reinforced rod of carbon/epoxy this velocity is of the order of $10\,000\,\mathrm{m\,s^{-1}}$. When a rod consisting of several parallel UD layers is suddenly loaded at one end, the stress wave will travel faster in the layers than in the resin-rich interfaces. Since, for continuity, the displacement of both must be the same, the interface follows the deformation of the adjacent layers through the development of shear forces which change the state of stress from one of simple tension or compression prevalent under conditions of static loading. This effect is much more pronounced in the case of beams in which impact results in a complex state of shear (distortional) and dilatational waves. Dynamic photoelasticity has been used[19,20] to illustrate this phenomenon.

Figure 3.18 shows a sequence of photographs taken through a photoelastic polariscope of a cantilever beam consisting of two layers of epoxy joined together with a cyanoacrylate adhesive (superglue). On impact, a Hertzian-type stress system grows from the point of impact and the shear stress waves represented by the photoelastic fringes grow rapidly, crossing the adhesive line without being affected by it. The beam behaves in exactly the same way as a single continuous structure. If a compliant adhesive such as silicone rubber is used, as a stress wave reaches the interface it is partly reflected and partly transmitted causing the effect shown in Fig. 3.19. Similar situations arise when the beam consists of more than two layers, as illustrated in Fig. 3.20. In all cases, the interface gives rise to a shear-lag
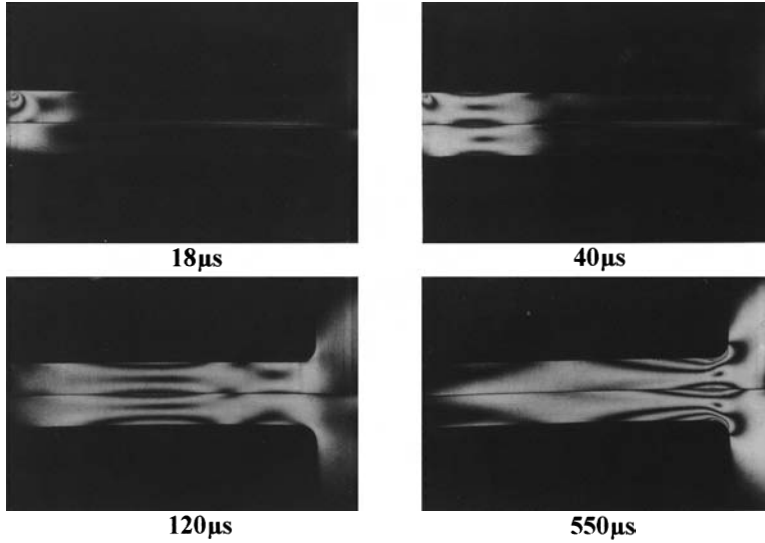
3.19 Two layer specimen with 'silicone rubber' adhesive bonding. (After Ruiz and Xia[19].)
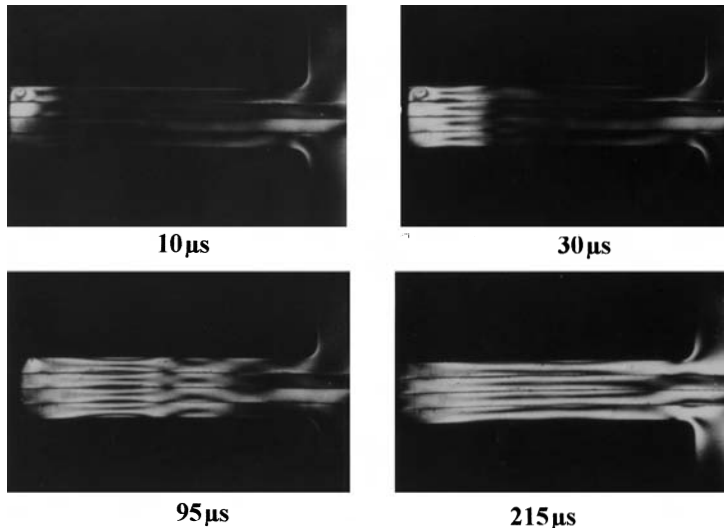
3.20 Four layer specimen with 'silicone rubber' adhesive bonding. (After Ruiz and Xia[19].)

effect. The role of the adhesive is to couple the bonded layers so as to ensure that the wavefronts travel together while increasing the relative freedom of movement between layers and thus altering the stress wave pattern. In the absence of adhesive, the layers are totally free to

expand, each one acts as an independent beam or waveguide with a substantial delay between top and bottom as seen from Figs. 3.19 and 3.20. Eventually, when the stress waves have been reflected at the support and at the free end of the beam a couple of times, stationary vibration is reached.

The shear stresses generated at the interface by the impact may be sufficient to cause shear failure. In contrast, under static loading, the relative magnitude of the shear stresses is lower and failure, when it occurs, is due to tension or compression. Consider a laminate beam composed of two identical layers of a quasi-isotropic composite material with E_{11}, E_{22}, G_{12} and v_{12} equal to 53.3 GPa, 14.3 GPa, 7.1 GPa and 0.28 respectively and a density of 1300 kg/m^3, bonded with an adhesive with $E = 3.0$ GPa, $v = 0.4$ and $\rho = 1000$ kg/m^3. The thickness of the adhesive is taken to be equal to 0.1 mm. Clamping the beam at one end, the response to an impact load at the other has been studied using the method of characteristics[21] and compared to the response under a statically applied end load. Under dynamic loading the values of the maximum tensile stress and of the maximum shear stress change with time, as do the positions in which they are found. In the static case, the maximum direct stress σ_T is at the uppermost surface in the proximity of the clamped end, the maximum shear stress τ is found at the neutral axis and the ratio (τ/σ_T) is approximately equal to 0.05. Even accounting for the weakness of the adhesive layer relative to the tensile strength of the composite, the most likely form of failure is tensile fracture rather than delamination. Consider now the case of an impact load applied in the form of a sudden step. Figure 3.21 shows that the ratio (σ_T/τ) is at first equal to 0.2 and, although the actual magnitudes of the stress may be low, the possibility of shear failure cannot be discounted. As time goes by, the ratio tends to oscillate around the static value of 0.05. It follows that failure through delamination, which was unlikely under static loading, may be the governing mode of failure under impact. The impact loading profile also has an effect on the stresses as shown in Fig. 3.21. A step followed by a linear decay over 200 μs gives a response very similar to the rectangular step pulse while a triangular pulse of the same duration tends to maintain the high (τ/σ_T) ratio over a longer time although the absolute values of the maximum stresses, now shown in the figure, are lower.

3.3.2   Response to low-velocity impact

As the impact velocity decreases and the time during which the load acts increases, a quasi-static state of equilibrium is reached through multiple stress wave reflections at the ends of the structure. To understand the
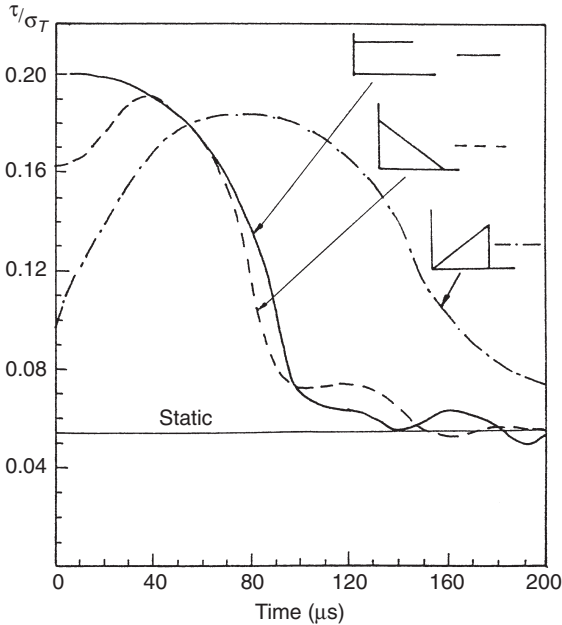
3.21 Response of a 2-layer cantilever beam to impact. Beam span
100 mm, height 20 mm. (After Ruiz and Xia[19].)

process, unidirectionally reinforced carbon/epoxy beams consisting of
alternate 0/90° plies have been tested in Oxford under 3-point bending with
a central impactor in the form of a wedge-ended cylindrical bar flying at
velocities between 5 and 7 m/s. The applied force was measured by
a strain gauge on the impactor and the central deflection was obtained
from a photographic record. Figure 3.22 shows the variation of force
with time for one of the beams at the lower end of the velocity range. The
beam did not fail and the trace follows a sinusoidal curve that would
be expected from a simple single degree of freedom mass-spring system.
At higher velocities, failure occurs as indicated in Fig. 3.23. While it takes a
relatively long time for the peak force and deflection to be reached, 2.5 ms
in the case illustrated, the actual process of failure once it starts is extremely
rapid, taking less than 0.1 ms. This process is illustrated in the sequence of
photographs shown in Fig. 3.24. Failure initiation, 6 μs after the peak force
has been reached, is by a tensile through-thickness crack appearing at the
rear face of the specimen. As the crack grows through the thickness, it
changes to an interlaminar crack. The delaminated layers spring out and
contract as the delamination extends and the process is repeated until the
kinetic energy imparted by the impactor is either totally spent or complete
fracture occurs. Test results are summarised in Tables 3.3–3.5.

Table 3.3. Summary of experimental results

	500 mm impactor long beam	400 mm impactor long beam	500 mm impactor short beam	400 mm impactor short beam
Mean failure deflection (mm)	8.74	8.78	1.54	1.52
Mean failure force (N)	638	630	4045	4550
Maximum velocity for non-failure (m/s)	5.620	5.691	6.012	6.687
Minimum velocity for failure (m/s)	5.622	5.566	5.916	6.716
Mean failure velocity (m/s)	5.621	5.629	5.964	6.702

Source: Hallett and Ruiz.[22]
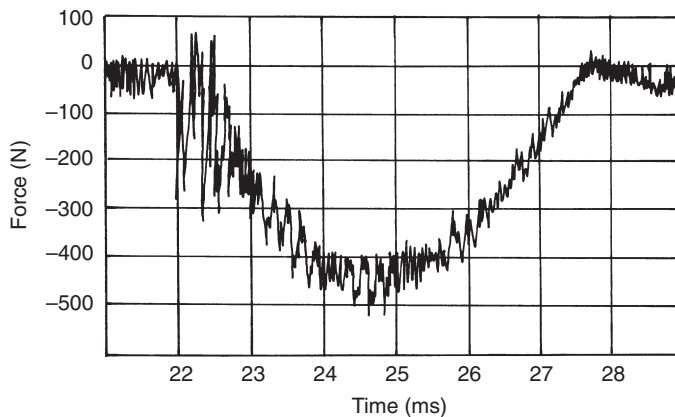
3.22 Variation of force with time for a beam tested at 2 m s^{-1} under 3-point impact. (After Hallett and Ruiz[22].)
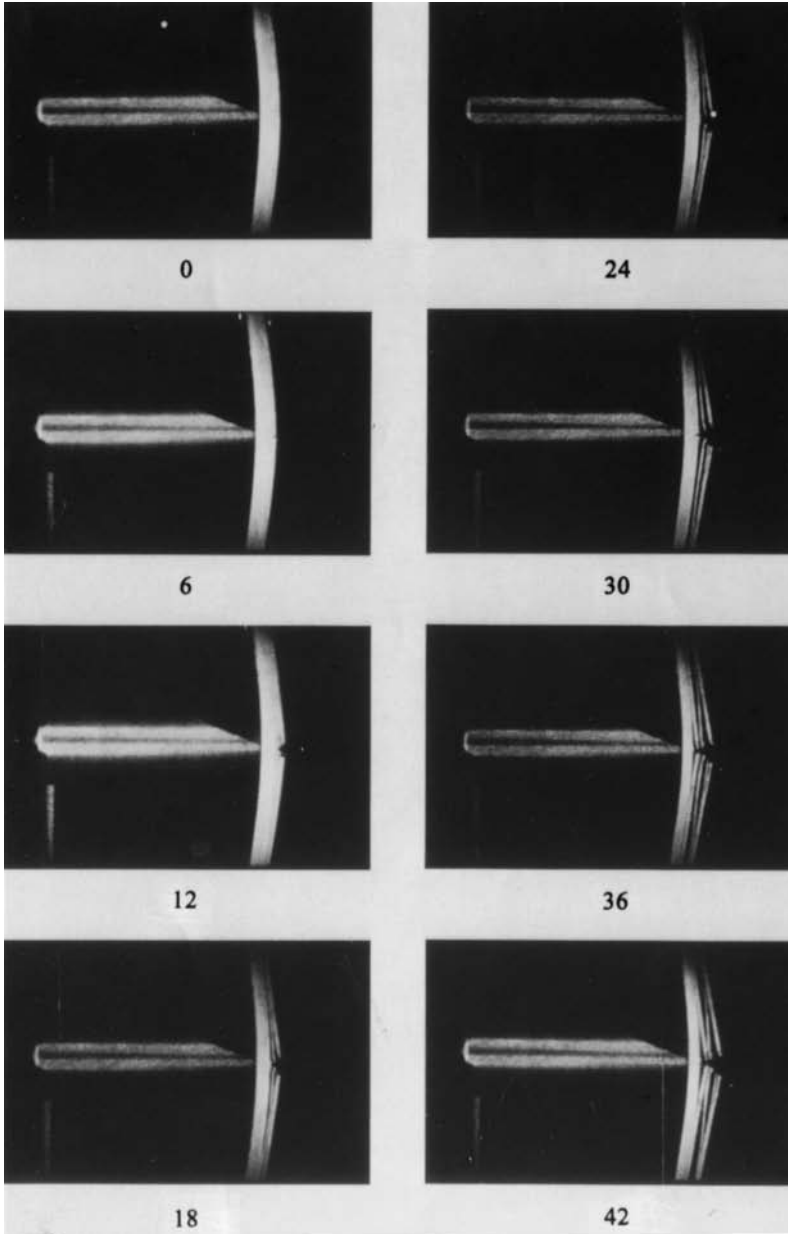
Table 3.4. Calculated results for SDOF system

	500 mm impactor long beam	400 mm impactor long beam	500 mm impactor short beam	400 mm impactor short beam
t (ms)	2.45	2.19	0.30	0.27
Maximum deflection (mm)	8.76	7.85	1.14	1.14
Maximum force (N)	595	533	5130	5130

Source: Hallett and Ruiz.[22]
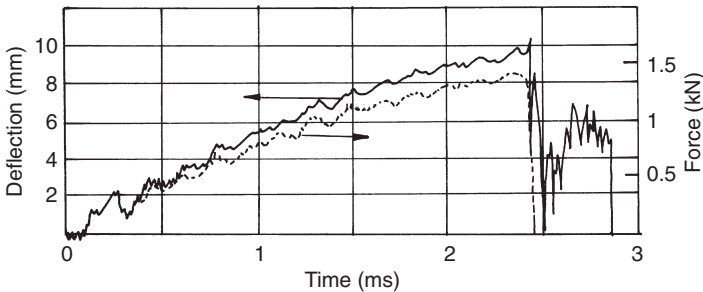
3.23 Variation of force and of deflection with time for the same beam tested at 5.9 m s⁻¹. (After Hallett and Ruiz[22].)

It has been argued that the difference between the kinetic energy of the impactor and the maximum potential energy that can be stored in the structure is responsible for the damage, the extent of which would be proportional to the excess in energy.[23] The tests do not seem to support this conclusion since the damage, once it occurs, is independent of the excess energy which is, moreover, either very small or virtually negligible. Once the velocity is just above a given critical value, failure occurs and the resulting damage is always considerable. A possible reason is that as the crack advances through the thickness, and the stress in the as yet uncracked 0° ply reaches a critical value, the potential energy drops and the strain energy released is sufficient to overcome the resistance to crack growth between the plies. A simple calculation, treating the beam as a single degree of freedom, confirms this observation.[22,24]

3.24 Sequence of high speed photographs for the beam of Fig. 3.23.
Zero corresponds to the instant when the peak force has been
reached, 2.5 ms after the impactor contacts the beam. Failure
completed after 42 μs. (After Hallett and Ruiz[22].)

Table 3.5. Test velocity range, mode of failure and energy

	500 mm impactor long beam	400 mm impactor long beam	500 mm impactor short beam	400 mm impactor short beam
Maximum test velocity (ms^{-1})	5.99	5.74	6.01	6.81
Minimum test velocity (ms^{-1})	5.58	5.83	5.83	6.59
Failed layers (ms^{-1})	9–12	8–10	25–32	31–32
Maximum potential energy (J)	2.61	2.09	2.93	2.96
Maximum kinetic energy (J)	2.96	2.17	2.98	3.06

Source: Hallett and Ruiz.[22]

3.4   Modelling of impact damage

3.4.1 Simplified approaches

The cost of testing precludes the establishment of a purely experimental base for the prediction of impact damage of composite structures. Modern finite element codes rely on a knowledge of mechanical properties of the material at the appropriate rates of strain and on the simplification of the problem to reduce the computational time and effort. It is possible to reduce the number and complexity of the tests with the support of numerical analysis. There is also a need for simple procedures to interpret experimental results quickly and efficiently with a minimum amount of effort and apply the experimental data to real situations without going through a full finite element analysis.

Scaling rules have been proposed by Ruiz[25] to relate laboratory scale impact tests on plates and beams to larger structures. Similar issues are discussed in Chapter 6. The rules have been applied to predict the energy required to perforate metallic shields consisting of one or two layers. The impact force depends on the velocity and mass of the projectile and on the

stiffness of the shield. As the projectile penetrates the target, the reaction force is dependent on the shear strength of the shield material, the projectile diameter and the shield thickness. All these variables can be combined in the form of a dimensionless number, $(M\upsilon^2 k)^{1/2}/\tau dt$ where M, υ and d are respectively the mass, velocity and diameter of the projectile and k, τ and t are the shield stiffness, shear strength and thickness. Alternatively, the minimum energy for perforation may be expressed as,

$$\frac{U_M}{U_{FS}} = \left(\frac{k_{FS}}{k_M}\right)^m \left(\frac{d_M}{d_{FS}}\right)^n \left(\frac{t_M}{t_{FS}}\right)^p \qquad [3.1]$$

where m, n, p are determined experimentally and the sub-indices M and FS refer to the model and to full scale, respectively.

This approach, originally developed for metallic targets, is also applicable to composites.[18] There is, however, an additional uncertainty in scaling due to the fact that the size of the individual components – fibre diameter, layer thickness, weave, etc. – cannot be changed. The type of failure will be influenced by the composite architecture as well as by the constituent materials themselves. The result is that it is not always possible to characterise the impact strength of a composite by means of a single parameter which could be obtained from a scaled-down experiment. It is generally agreed that for a given composite and impactor there is a threshold velocity below which no damage is sustained.[18] Above this velocity, the damage size may be defined as the projected delamination area observed on C-scans. Scaling is still possible since Malvern et al.[26] showed that the damage size increases linearly with kinetic energy. Robinson and Davies[27] claim that it depends on the 'damage energy', defined as the difference between the kinetic energy of the impactor and the elastic strain energy of the target when the peak force has been reached. Subsequent work by Davies et al.[28,29] indicates that the extent of the damage is also related to the difference between the peak force and a threshold force characteristic of the composite.

3.4.2 Application of general finite element codes

3.4.2.1 General considerations

The preceding simplified procedures for the study of impact damage rely on a knowledge of the states of stress and strain of the target which can be achieved through the application of finite element analysis. This would permit in the case of the beam previously considered, for example, calculation of the maximum strain at the back face and the strain energy release rate as the crack progresses through the thickness. Coupled with the maximum strain and critical strain energy release rate criteria, the finite

element analysis would then provide a complete method of solution which includes the determination of the states of stress and strain and modelling of damage initiation and growth. Although most finite element codes follow roughly similar procedures for the determination of stresses, they differ in the criteria applied to define the onset of failure and the growth of damage. Failure criteria can be based on stress considerations or on fracture mechanics. These give rise to two distinct approaches. A third approach consists in combining the two.

3.4.2.2   Stress based failure criteria

Any of the failure criteria proposed for design and prediction of strength of composites may be used within the finite element code.[30] The Chang–Chang criterion, implemented in DYNA-3D[31] combines elementary failure stresses in a system of quadratic equations covering the possibilities of failure resulting from fibre fracture, matrix cracking or delamination.

Once failure has occurred in an element, certain of the elastic moduli are reduced to zero according to which type of failure has taken place. This reduction takes place over 100 time steps in order to reduce the effect of dynamic instabilities associated with sudden load redistribution. The choice of 100 times steps is arbitrary and this creates some variability in the model because time step is dependent on mesh size as it is an explicit code. The explicit analysis requires the time step to be short enough such that an elastic stress wave cannot travel across the shortest dimension of the smallest element in one time step. The time step is thus automatically calculated by DYNA to meet this criterion. It is important to note that the failed properties (reduced moduli) are given to the whole element which has exceeded the failure criteria and not just along an interface between elements.

As reported in Hallett,[32] experimental results have been used to compare the validity of various failure criteria, including Chang–Chang. The conclusion is that, while it is always possible to explain experimental results *a posteriori*, it is not always possible to provide accurate predictions of the extent of damage. The force and deflection history predicted by the code for beams and plates is in good agreement with experimental observations and it is also possible to predict the onset of damage accurately. The extent of damage on the other hand is more difficult to predict. The type of element and the mesh density are known to affect the results. Brick elements representing each layer with contact elements to account for the interfaces would seem to be the best choice when striving for accuracy but practical limitations associated with computing power and human resources make it imperative to simplify the numerical model from the outset. Good results can be obtained combining several layers – up to four – in a single brick element and dispensing with interface elements,[33] although the predicted

amount of damage remains open to question. Shell elements have also been used with LS-DYNA[34] taking one integration point for each lamina and one element through the plate thickness. It was found that the model predicted the force-time and displacement-time plots but overpredicted the extent and matrix cracking and failed to explain the delamination observed in practice. Three dimensional bricks and 2D shell elements have also been used with the same code by Edlund.[35] The work of other authors who have also used plate elements with ABAQUS, DYNA and FE77[28,36,37] has been reviewed by Hallett.[32]

3.4.2.3   *Fracture mechanics based criteria*

While stress based criteria may be adequate to predict damage initiation, a fracture mechanics approach would seem preferable for the study of damage propagation since this involves the growth of cracks in the structure. A static finite element analysis has been conducted by Lammerand and Verpoest[38] on a (90/0/90) lay-up beam in three-point bending. This attempts to predict the initiation of cracks and the growth of a pre-existing delamination crack in the composite using forces and displacements at the nodes at the crack tip to calculate the strain energy release rates G_I and G_{II}. A fracture mechanics approach has also been followed by Lu and Liu[39] to perform a three dimensional analysis of plate specimens while Wu and Stringer[40,41] and Finn *et al.*[42,43] have combined fracture mechanics with experimental observations to propose a semi-empirical method for the prediction of damage. Their approach still relies on ad-hoc experiments to provide basic data rather than on the establishment of a theoretical basis of general validity. A problem faced by all authors is that classical fracture mechanics is strictly applicable only to continua, not to layered structures with features whose ruling dimensions are of the same order as those of the cracks, as is the case in most composites. It is generally agreed that delamination can be treated by fracture mechanics, although even then the critical strain energy release rates G_{IC}, G_{IIC} show such a large scatter that a correspondingly large margin of error may be expected when dealing with crack growth in composites. The lack of experimental data on strain rate sensitivity and high speed crack growth also restricts the application of fracture mechanics to static or quasi-static problems.

3.5   Conclusion

The behaviour of composite structures under impact is determined both by the mechanical properties of the material and by the structural response to stress wave transmission and reflection at the boundaries. The tests described in this chapter provide fundamental information on the material

properties. Strain rate sensitivity of fibre-reinforced composites results from the intrinsic properties of the constituent fibres and matrix and from the architecture of the system. It has been found that most fibre materials are fairly rate insensitive, in contrast with the polymeric matrix. Unidirectional composites are also less strain rate sensitive than woven composites.

At present, it is not possible to predict material properties in the absence of testing. Simple rules derived from the rule of mixtures or of anisotropic plasticity only provide rough estimates insufficiently accurate for the structural design and dimensioning.

In addition to simple tension, shear and compression, other tests help to bridge the gap between simple specimens and structures. These involve beams and panels in bending. The interpretation of the test data then requires a knowledge of the basic material properties and structural analysis, usually with finite elements. Such tests serve both to provide data and to validate numerical modelling.

References

1 Harding J, 'The effect of high strain rate on material properties', in *Materials at High Strain Rates* (T Z Blazynski, ed), ch 4, London, Elsevier Applied Science, 1987.
2 Sierakowski R L and Chaturvedi S K, *Dynamic Loading and Characterization of Fibre-Reinforced Composites*, ch 2, New York, Wiley 1997.
3 Harding J and Ruiz C, 'The mechanical behaviour of composite materials under impact loading', in *Impact Response and Dynamic Failure of Composites and Laminate Materials* (J K Kim and T X Yu, eds), Key Engineering Materials, vols 141–3, p 2, 403–25, Zurich, Trans Tech Publications, 1998.
4 Kolsky H, 'An investigation of the mechanical properties of materials at very high rates of loading', *Proc Phys Soc*, 1949 **B62** 676–700.
5 Harding J, 'Effect of strain rate and specimen geometry on the compressive strength of woven glass-reinforced epoxy laminates', *Composites*, 1993 **24**(4) 323–32.
6 Harding J, 'An extended Hopkinson-bar analysis', Solid Mechanics Group, UTC Rep 124, Department of Engineering Science, University of Oxford, 1998.
7 Harding J and Welsh L M, 'A tensile testing technique for fibre-reinforced composites at impact rates of strain', *J Mater Sci*, 1983 **18** 1810–26.
8 Saka K and Harding J, 'Behaviour of fibre-reinforced composites under dynamic tension', Oxford University Engineering Laboratory Rep 1602/85, 1985.
9 Hallett S R, 'Small specimen impact testing and modelling of carbon fibre T300/914′,' DPhil thesis, Department of Engineering Science, University of Oxford, 1997.
10 Dong L M and Harding J, 'A single-lap shear specimen for determining the effect of strain rate on the interlaminar shear strength of carbon-fibre-reinforced laminates', *Composites*, 1994 **25**(2) 129–38.

11 Harding J and Li Y L, 'Analysis of failure in woven carbon/epoxy laminates under quasi-static and impact loading', *Proc DYMAT 91, J de Physique IV Colloque No. C3, Suppl au J de Phys III*, 1991 **1** C3/51–C3/59 Octobre.

12 Welsh L M and Harding J, 'Effect of strain rate on the tensile failure of woven-reinforced polyester resin composites', *Proc DYMAT 85, Int Conf on Mechanical and Physical Behaviour of Materials under Dynamic Loading*, 405–14, J de Phys, Colloque C5, 1985.

13 Saka K, Li R K Y and Harding J, 'Behaviour of fibre-reinforced composites under dynamic tension', Oxford University Engineering Laboratory Rep 1714/87, 1987.

14 Li Y L, Harding J and Taylor M E C, 'Effect of strain rate on the through-thickness elastic properties of woven laminates', Oxford University Engineering Laboratory Rep 1847/90, 1990.

15 Tsai S W and Wu E M, 'A general theory of strength for anisotropic materials', *J Composite Mater*, 1971 **5** 58–80.

16 Saka K and Harding J, 'A simple laminate theory approach to the prediction of the tensile impact strength of woven hybrid composites', *Composites*, 1990 **21**(5) 439–47.

17 Li Y L, Ruiz C and Harding J, 'Failure analysis of woven hybrid composites using a finite element method', *Composites Sci Technol*, 1991 **41** 129–46.

18 Abrate S, 'Impact on laminated composite materials', *Appl Mech Rev*, 1991 **44** 155–90.

19 Ruiz C and Xia Y R, 'The significance of interfaces in impact response of laminated composites', *ASME, Composite Material Technology*, Houston, PD, 1991 **37** 161–6.

20 Xia Y R and Ruiz C, 'Shear effects between the layers of laminated beams under impact loading', *Proc Int Conf Design in Composite Materials*, pp 87–92, London, Institute of Mechanical Engineers, 1989.

21 Xia Y R and Ruiz C, 'Transient shear deformation at interfaces of laminated beams', *Int J Fracture*, 1991 **48** 205–18.

22 Hallett S R and Ruiz C, 'Fracture of composite beams under impact', *Proc 11th Int Conf Experimental Mechanics*, Oxford, 1998, to be published.

23 Davies G A O and Zhang X, 'Impact damage prediction in C-composite structures', *Int J Impact Eng*, 1995 **16** 149–70.

24 Ruiz C, Hallett S R and Gungor S, 'Application of fracture mechanics to laminated CFRP beams under impact', *Proc ECCM-8*, pp 118–24, Naples, 1998.

25 Ruiz C, 'Scaling in penetration and perforation mechanics', *Proc Size Effects in Fracture*, pp 11–17 Farnborough, Institute of Mechanical Engineers, 1986.

26 Malvern L E, Sun C T and Liu D, 'Delamination damage in central impacts at subperforation speeds on laminated Kevlar-epoxy plates', *ASTM STP 1012*, 1989 387–405.

27 Robinson P and Davies G A O, 'Impactor mass and specimen geometry effects in low velocity impact of laminated composites', *Int J Impact Eng*, 1992 **12** 189–207.

28 Davies G A O, Zhang X, Zhou G and Watson S, 'Numerical modelling of impact damage', *Composites*, 1994 **25** 342–50.

29 Davies G A O, Zhang X and Hitchings D, 'Modelling impact damage in laminated composites', *Proc NAFEMS World Congress*, pp 1216–31, Stuttgart, 1997.

30 ESDU, Data items 83014, 'Failure criteria for an individual layer of a FRC laminate under in-plane loading', 82025, 'Failure modes of laminates', ESDU, London.

31 Chang F K and Chang K Y, 'A progressive damage model for laminated composites containing stress concentrations', *J Composite Mater*, 1987 **21** 834–50.

32 Hallett S R, 'Impact strength of laminated composites', DPhil thesis, Oxford University, 1997.

33 Hou J, 'Modelling of low velocity impact of beams and plates', Oxford UTC for Solid Mechanics, Rep 119, April 1998.

34 Majeed O, Worswick M J, Straznicky P V and Poon C, 'Numerical modelling of transverse impact on composite coupons', *Canad Aero Space J*, 1994 **40** 99–106.

35 Edlund A, 'Finite element modelling of low velocity impact damage in composite laminates', *Proc ICCM-9*, **5**, 334–41, Madrid, 1993.

36 Eason T, Texas A&M Univ, private communication, July 1996.

37 Reddy J N, 'A refined shear deformation theory for the analysis of laminated plates', *NASA Contractor Rep 3995*, Springfield, VA, 1986.

38 Lammerand L and Verpoest I, 'The interaction between matrix cracks and delaminations during quasi-static impact of composites', *Composite Sci Technol*, 1994 **51** 505–16.

39 Lu X and Liu D, 'Finite element analysis of strain energy release rate at delamination front', *J Reinf Plast Composites*, 1991 **10** 279–92.

40 Wu H T and Springer G S, 'Measurements of matrix cracking and delamination caused by impact on composite plates', *J Composite Mater*, 1988 **22** 518–32.

41 Wu H T and Springer G S, 'Impact induced stresses, strains and delaminations in composite plates', *J Composite Mater*, 1988 **22** 533–60.

42 Finn S R, He Y F and Springer G S, 'Delaminations in composite plates under transverse impact loads – experimental results', *Composite Struct*, 1993 **23** 191–204.

43 Finn S R, He Y F and Springer G S, 'Delaminations in composite plates under transverse static and impact loads – a model', *Composite Struct*, 1993 **23** 177–90.

Impact damage-tolerant composite structural design

R L SIERAKOWSKI

4.1 Introduction

The introduction of continuous filament composite materials for use as primary structural components, particularly in aircraft application, has focused attention on issues related to the overall structural integrity of such structural components. The issues associated with structural integrity as developed for metals are shown in Fig. 4.1.

In particular, concerns have been raised by structural designers on key issues related to the damage tolerance capability and long term durability of structural components composed of composite materials. Both damage tolerance and durability are damage related issues which must be addressed by the designer in order that the strength and/or stiffness of the structure does not fall to an unacceptable level. Thus, the introduction of a definition of damage tolerance and durability is paramount to the issues of structural design.

In this chapter the topic of damage tolerance as a design issue is examined for structural components consisting of advanced structural composites. Such materials are combinations of two or more constituent materials consisting of fiber embedded in a matrix material, the strength and stiffness of the fibers being several orders of magnitude greater than the matrix material. While in general a variety of composite types are available – such as particulate, flake, and short fiber types – the focus of the discussion herein is directed at continuous fiber laminate composite constructions. In general, advanced composites are classified into five categories: (1) polymer matrix composites (PMC); (2) metal matrix composites (MMC); (3) ceramic matrix composites (CMC); (4) carbon/carbon (CC); and (5) hybrid composites (HC). It should be noted that the development of the damage tolerant design concept has evolved from the deployment of metals as structural components while the introduction of advanced composites of the types cited has refocused attention in this issue.

The concept of damage tolerance is examined herein for the case of continuous filament advanced composites of the polymer matrix type. Other

```
                    ┌─────────────┐
                    │ Structural  │
                    │ integrity   │
                    └─────────────┘
        ┌──────────────┬──────────┴──────┬──────────────────┐
┌───────────────┐ ┌───────────────┐ ┌───────────────┐ ┌──────────────────┐
│   Stiffness   │ │   Strength    │ │  Durability   │ │ Damage tolerance │
└───────────────┘ └───────────────┘ └───────────────┘ └──────────────────┘
```
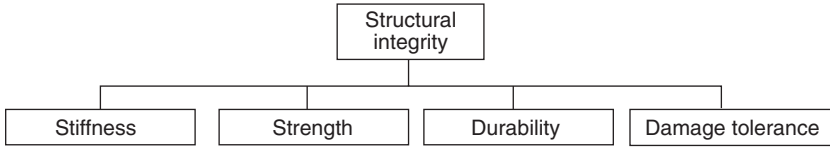
4.1 Structural integrity issues.

composite types such as MMCs, CMCs, CCs, and HCs are also important classes of composites, however, the wide use of PMCs, coupled with the knowledge base and experience established over recent years for this class of materials, represents the basis for focusing attention on these materials.

4.2   Damage tolerance

The issue of damage tolerance as known today is a concept whose roots can be traced back to the 15th century and Leonardo Da Vinci's notebook on the design of flying machines. In that treatise, Da Vinci addressed the safety aspects of structural design for wings by including a built-in redundancy in the design. This was to ensure that if one cord of a wing structure failed, a second would be in position to serve the same function as the failed component. This fail safe concept of design prevailed through the 1960s and resulted in the development of a fail safe design approach for metallic structures.[1] The design philosophy of this approach was based upon the fact that damage introduced by structural loading induced over the flight history of the aircraft could be detected at scheduled service intervals and by use of non-destructive techniques ensure that the retained design strength of the structure was not compromised below a safe threshold level. This fail safe approach was transcended in the 1970s to include damage resulting from manufacturing as well as in service use of structural components. The fail safe premise is that the damage (cracks) which can occur during the service life of a structural component must be detected in order to ensure design strength and stiffness requirements. The recognition of such damage has evolved to a damage tolerance approach which accepts the existence of damage (such as manufacturing flaws) and the requirement that the structure retain sufficient residual strength until the damage can be detected and corrective action taken. These concepts have evolved and can be incorporated into definition for damage tolerance which can be stated for materials used as structural components[2] as the ability of a structure to sustain anticipated loads in the presence of fatigue, corrosion, or accidental damage until such damage is detected through inspection or malfunctions and repaired. A relevent example on thick glass fiber-reinforced laminates can be seen in Chapter 5. The key issues which must be addressed in the damage tolerance concept for design are:

- The acceptance that damage will occur.
- That an adequate inspection system is available to detect the damage.
- That adequate strength can be maintained in the damaged structure.

Within the framework of the global structural integrity of a component, damage tolerance is a concept which insures the fail safe integrity of a structural component/system in the presence of damage for a specified period of time.

The other damage issue cited previously, durability, represents the ability of the structural component/system to resist cracking, degradation, and other damage effects over a specified time period. This subject will not be addressed in this article. Thus, damage tolerance is related to the acceptance of damage and its resultant effect on the retained strength/stiffness of the structural component, while durability refers to the resistance of the material comprising the structural component to resist the growth of damage. The key elements of the damage tolerance concept as described above are graphically depicted in Fig. 4.2.

Figure 4.2 illustrates the key features of damage tolerance design requirements, that is, the assumption that damage exists and that the structure is required to contain the assumed damage and maintain a minimum acceptable residual static strength. For aircraft structures, damage tolerance requirements for metallic structures have been discussed in MIL-A-83444 and MIL-STD-1530A.[3,4] The damage tolerance requirements developed for metals and cited in these documents have been applied to advanced composites. The assumed damage, which includes delaminations in ply splits between fibers, dents, holes and cuts, has a flaw size acceptance level which precludes failure in a test with simulated stresses considered to be encountered at twice the design life of the structural component. Also to be noted in this design requirement is the acceptance that the damage size should be large enough to be reliably found using non-destructive inspection techniques as depicted by a minimum detectable size as shown in Fig. 4.2(a). The time period associated with damage growth from the initial to critical size represents the detection period and represents a major difference in the damage tolerant design of metals versus composites. Indeed, generally metal structures are not inspected to detect damage but rather the structure is repaired or replaced when an initial flaw is calculated to reach its half life of anticipated failure. Figure 4.2(b) depicts the retained residual static strength available for a structural component in the presence of damage during in-service deployment. Design is based upon the requirement that damage growth is contained such that the available residual static strength is not reduced to an unacceptable level under the maximum in-service loading. Consequently, the acceptance of damage – identifying the location of damage and the size of damage – is a key factor which must be addressed in damage tolerant design.
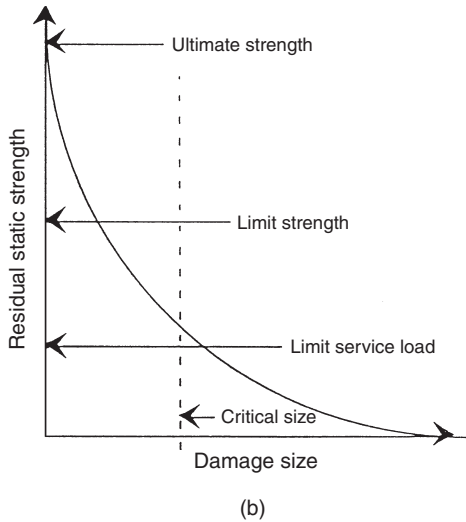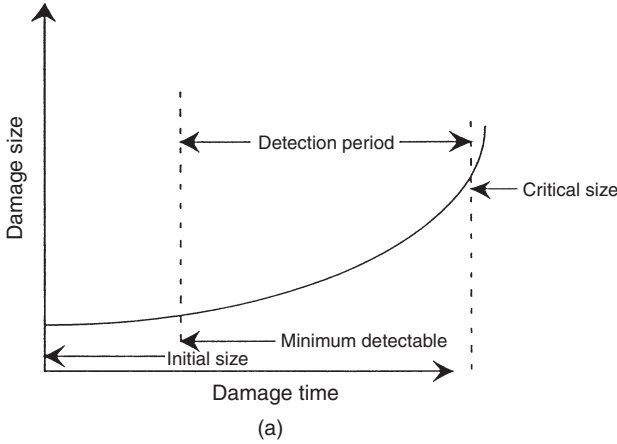
4.2 Damage tolerance.

4.3   Sources of damage

In considering sources of damage it is necessary to cite the differences between metals and composites in the development of damage and the controlling mechanisms of damage formation, as also discussed in Chapter 1. To illustrate some of these issues, for example, damage in metals can be introduced as manufacturing flaws and voids, and during in-service use damage can occur due to dents and surface scratches. For laminated composites, defects within the laminates, machining defects, and the effect of surface scratches are a few of the important damage sources. The damage

sources for both metals and composites represent controlling factors in damage formation. For the case of defects in composite laminates, such defects can be attributed to a large number of factors including:

- delamination;
- fiber breaks;
- ply gaps;
- resin rich/resin starved areas;
- fiber waviness, wrinkles, miscollimation;
- inclusions, contamination, foreign particles;
- improper stacking sequence;
- dents, scratches.

The variety in the type of defects in the case of both metals and composites illustrates the complexity of damage formation which, in turn, controls damage size leading to failure and which is the important factor in the damage design of a structural component. As noted in the case of composites, the wide variety of damage formation mechanisms further complicates identification of damage and thus damage tolerant design. To further illustrate the wide variety in the sources of damage, the following menu of sources of damage is presented.[5]

Fabrication/processing manufacturing damage

Abrasions, scratches, dents, punctures	Inclusions, bugs, foreign contamination
Cut fibers	
Knots, kinks	Tool installation/removal during processing
Improper slicing	
Voids	Mandrel removal problems
Resin rich, resin lean areas	Machining problems
Subquality materials	Shipping to propellant processing
Cure problems	Impact damage
	Proof testing

	Typical composite defects/
In-service damage	*assembly damage*
Vibration	Debonds
Shock	Delaminations
Lightning damage	Inclusions
Environment cycling	Voids, blisters
Flight loads	Fiber misalignment
Improper repair	Cut or broken fibers
In-storage creep or handling loads	Abrasions, scratches
Impact	Wrinkles
Scratches, dents, punctures	Resin cracks, crazing
Corrosion	Density variations
Erosion, dust, sand	Improper cure
Bacterial degradation	Machining problems

4.4   Damage tolerant design

As discussed, the sources of damage represent critical elements in the assessment of damage and subsequent failure modes of the structural material component. Consequently, in damage tolerant design, the critical elements which must be identified are loading events which are most severe and lead to unacceptable damage thresholds and the consequent failure mode associated with the introduced damage. As illustrated in the sources of damage menu, one event appears consistently important for damage tolerent design of composites and in particular, polymeric composites, that being impact damage. Transverse impact on laminated polymeric composites results in a delamination failure mode which adversely affects the retained strength/stiffness of the structural component. For design, the performance of a polymeric composite can be assessed by determining the residual properties of a structural component that are considered important to a specific design application. For example, in aircraft design using polymeric composites, the compression strength of the impact damage is considered as a critical design measure. In the case of laminated polymer composite construction, reduction in compression strength after impact, is influenced by the ply delaminations introduced as damage by the impact event. This strength reduction for advanced polymeric composites has evolved as a 'compression after impact' or CAI criteria. While this criteria appears adequate for PMCs, the researcher is cautioned that the concept of CAI applied to other composite material types and structural systems including the MMCs, CMCs, CCs, and HCs may not be applicable. Therefore the focus, as previously cited, is on PMCs, based upon knowledge and experience acquired and tested over recent years. Specifically, the failure modes of PMCs used in specific applications have, for the most part, been identified. For the case of laminated composites subject to transverse impact loading, delamination appears to be the principal failure mode. Referring again to the case of delamination as a type of damage, an assumption of damage size can be made, which for aircraft applications can be identified by the presence of an interply delamination, that has an area equivalent to a 1.0 inch (2.54 cm) diameter circle, this damage considered at an identified critical location. For the case of damage induced by impact, the presence of damage caused by a 1.0 inch (2.54 cm) diameter hemispherical impactor delivered at 100 ft/lb (133 J) of kinetic energy, or a kinetic energy event causing a 0.10 inch (0.54 cm) dent, have been used as damage thresholds. In the case of either event, the delamination damage introduced by impact should be such that the size of damage observed should in turn be such as to ensure the safety of flight at twice the design service life of the structural component.

While the previous remarks are relevant to the damage tolerance issue, it should be emphasized as discussed in Sierakowski and Newaz,[5] that

(a) Rigid support: contact stresses most important   (b) Compliant in bending: bending/membrane stresses most important
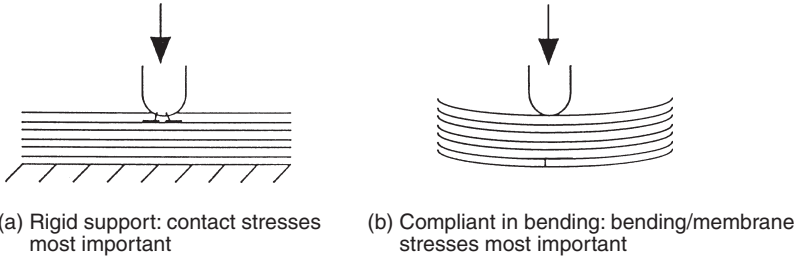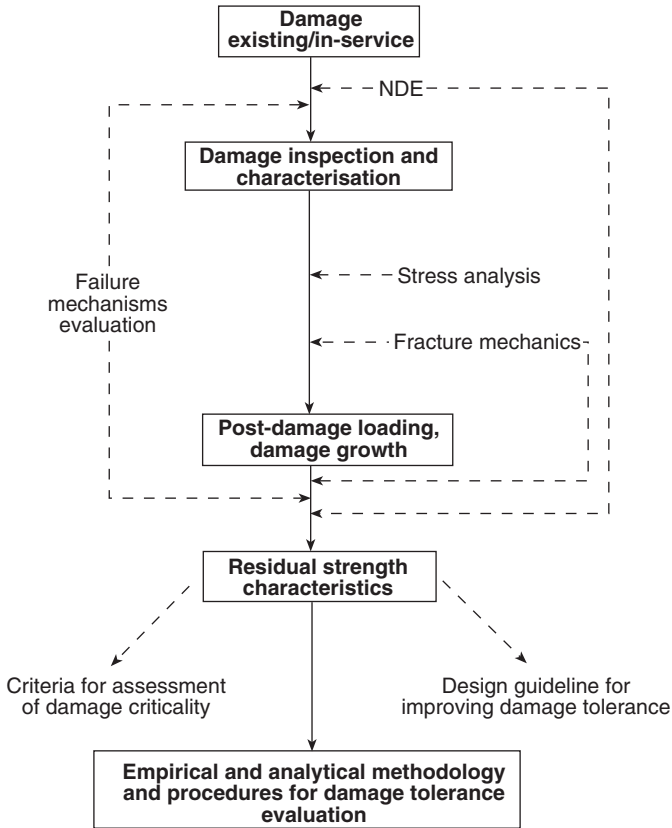
4.3 Boundary condition 'extremes' and relative importance of stresses.

impactor shape, laminate thickness, and structural supports are important in damage formation and size. As an example, the schematic shown in Fig. 4.3 illustrates the effects of a hemispherical impactor striking a laminated composite target of equal thickness with a rigid foundation support and with a non-rigid support. Other examples also exist in Figs. 5.13, 17, and 18 of Chapter 5. The formation of damage and subsequent damage formation in one case is front-to-back, while in the second case back-to-front. For the same striker velocity, the free support condition can result in greater overall internal damage (delamination), which appears innocuous on surface inspection. Thus, a number of aspects in damage tolerance design must be considered leading to various levels of design complexity associated not only with material issues but also with structural issues.

For polymer matrix composites at the material level, considering both thermoset and thermoplastic matrices, tough resins and high strain to failure fibers are desirable damage tolerant design (DTD) features. Still, further improvement can be obtained by containing damage to a controlled region using the existing microstructure architecture of the material as a means of arresting the damage. At the structural level, damage tolerance concepts can be introduced through load redistribution. Therefore, a number of advances in damage tolerance design can be considered at both the material and structural levels using improved matrix materials, damage containment, and load redistribution.

4.4.1   Damage tolerant design: overview

Engineering design considerations must take into account that structures consisting of advanced laminate composites can include fabrication flaws and in-service damage, which will affect the design allowables. Under in-plane compressive loading such damage can propagate and adversely influence the residual compressive strength of the damaged component. Likewise, existing delaminations can be expected to propagate under cyclic loading, reducing the service life of the component relative to the undamaged

```
                    ┌─────────────────────┐
                    │       Damage         │
                    │  existing/in-service │
                    └─────────────────────┘
                              │
                    ← - - NDE- - - - - - - - ┐
                              │
                    ┌─────────────────────┐
                    │ Damage inspection and│
                    │   characterisation   │
                    └─────────────────────┘
                              │
   Failure         ← - - - Stress analysis
   mechanisms
   evaluation      ← - - · Fracture mechanics-
                              │
                    ┌─────────────────────┐
                    │  Post-damage loading,│
                    │    damage growth     │
                    └─────────────────────┘
                              │
                    ┌─────────────────────┐
                    │  Residual strength   │
                    │   characteristics    │
                    └─────────────────────┘
                              │
   Criteria for assessment          Design guideline for
   of damage criticality            improving damage tolerance
                              │
                    ┌───────────────────────────────┐
                    │ Empirical and analytical      │
                    │ methodology and procedures for│
                    │ damage tolerance evaluation   │
                    └───────────────────────────────┘
```

4.4 Damage tolerance concepts.

component. In reviewing damage tolerance studies, such investigations focus on the determination of residual compressive properties of structural elements in the presence of damage with existing flaws or in-service damage. Such studies, while providing data on strength reduction in the presence of damage, fail to provide information on failure mechanisms and the potential for damage growth as a function of loading variables.

The current approaches to damage tolerant designs are based on a dominant failure mechanism associated with a critical crack size, such as that associated with delamination. However, the interaction of failure modes and progression of failure modes encountered in service remains a research issue. Current approaches to damage tolerance are generally semi-empirical in nature with bias toward reliance on experimental data. One approach is to assess the residual properties of damage structured components and relate the degraded properties to damage size and propagation. This in turn can be related to the state and distribution of stresses within the composite, a flow diagram of which is shown in Fig. 4.4.
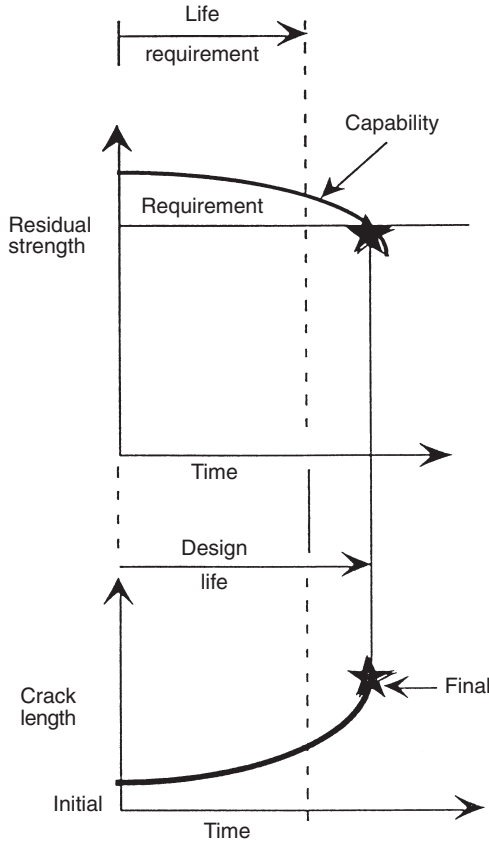
4.5 Residual strength, damage, service life.

While Fig. 4.4 provides one approach to the characterisation of damage tolerance, an alternative conceptional approach is illustrated in Fig. 4.5, which depicts the interrelationship between damage size, residual strength, and service life.

4.5   Impact damage

The previous sections have provided information on the concepts of damage tolerance, sources of damage, and damage tolerance design. Among the major topical sources of damage discussed, that is, manufacturing, assembly and normal service, impact induced damage is considered as a primary damage concern. In order to develop analytical methodologies for this type of event, it is important to understand the physical phenomena
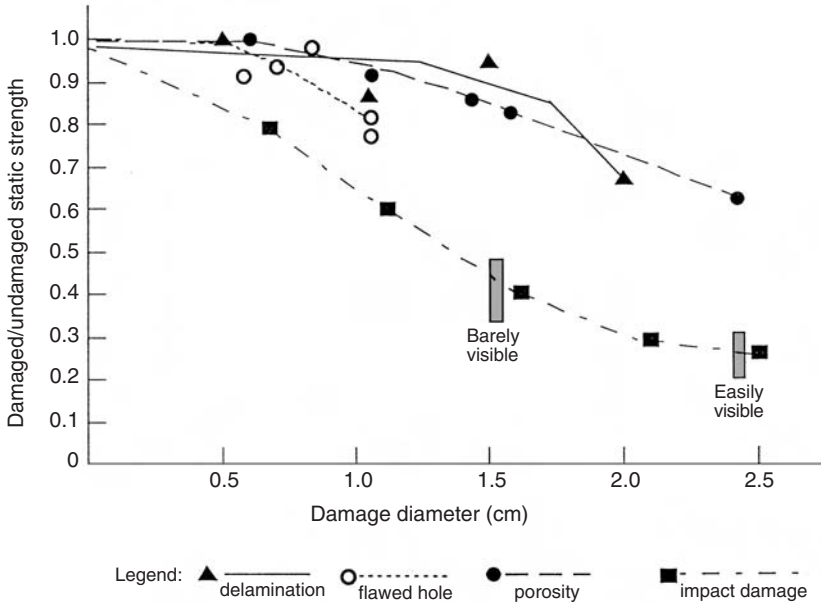
4.6 Defect damage severity.

associated with such events. Included in developing such an understanding are such topics as: characteristics of the striker and target; striker, target interaction; striker, target boundary conditions.

The effect of impact damage on the residual compressive strength of a composite is shown in Fig. 4.6. In this figure the effect of a small diameter impactor impacting a composite plate specimen at low-velocity shows the most severe damage which occurs for damage associated with delamination, a flawed hole, and porosity. Delamination damage caused by impact results in over a 50% reduction in the retained compressive strength at the barely visible damage (surface) level, relative to the undamaged static strength while a 75% reduction in strength is seen to occur at the point where visible damage is observed. At the point where damage is non-visible, the structural composite no longer meets its original design objectives. Thus, the need arises for the development of analytical models to predict damage tolerant information and for developing NDE tools for detecting damage. The latter point is extremely important for composites where surface damage may not be totally representative of the damage sustained by the structural component during the impact event. A fuller discussion of the topic is available in Chapter 2.

A more extensive discussion of these topics has been included.[5–9] The factors cited focus attention on the need to quantify the impact event and

to develop appropriate analysis for characterising the event. A number of models have been discussed in the literature,[10–87] each of which address selected analytical issues, as discussed in the following sections. Two other examples can be found in Chapters 6 and 7, respectively. These models can be broadly classified as being of the following types: empirical; numerical; semi-empirical; analytical.

The model developments include a discussion of local and global damage, which in turn includes such damage mechanisms as matrix cracking, interfacial debonding, crack coupling, delamination, fiber fracture, indentation and composite failure. The analytical models developed thus far can be further divided into three broad classifications: deformation mechanics; damage mechanics; residual strength degradation.

Damage mechanics models focus on developing predictors for evaluating the extent of damage, damage mechanisms, and damage thresholds. *Deformation mechanics* models are predictive models developed for evaluating damage effects including the effects of load history, fiber types, matrices, ply sequencing and orientation, and target thickness and curvature. *Residual strength degradation* models have been used to evaluate the acceptable retained strength of a damaged composite.

Each of these models, used as a predictive tool, addresses at least one of the key damage tolerant design issues, that is, the acceptance of damage, a means of predicting the extent of damage as related to NDE inspection, and the requirement that adequate strength be maintained within the damaged structure. A representative model from the literature selected for each of the three model classifications cited is presented in the following sections. For each model a basic tabulation of important parameters is presented. This information should be useful to designers when comparing models included in the references/bibliography as well as for the development of future models.

Model	
Model classification: deformation mechanics	
Striker/target parameters	
Striker	*Target*
Mass-small	Mass-small
Material-steel	Material-Gr/epoxy
Geometry-spherical	Geometry-203.2 mm × 203.2 mm
Velocity-3 m/s	Thickness-5.1 mm
Striker incidence-normal	Ply sequence-cross ply
	Support conditions-simply supported

Source: Lakshimarayana, et al.[73]

4.5.1 Analytical model

Numerical data for this investigation have been generated using ABAQUS, a general purpose FEM code capable of modeling multi-layered anisotropic materials, including bending-membrane coupling and shear deformation effects. The FEM element used in the study is an S8R isoparametric quadrilateral plate/shell element which has eight nodes and six engineering degrees of freedom at each node. Within each element an arbitrary number of layers, each with its own thickness, ply orientation, and properties, can be specified with the shear corrective factor specified. The element output includes the membrane stress resultants, bending stress resultants, and transverse shear stress resultants specified at the nodes or at the four integration points.

A specific test problem was addressed using ABAQUS and the element cited, this being a cross-plied laminated graphite/epoxy composite square plate, all edges simply supported, subjected to a central impact. The effects of geometry, ply orientation and stacking sequence, contact force history and impact velocities have been studied. Displacement-time histories associated with the configurations studied have been evaluated using three calculation procedures. These procedures were: (1) modal analysis; (2) a linear and transient response analysis; and (3) a nonlinear and transient response analysis. The calculated displacement time histories for the central deflection of a cross-plied composite plate for a 0.05 ms marching time step, a fixed maximum load and impact time history, and using calculation procedure (3) is shown in Fig. 4.7. The spatial variation in displacement for the case of procedure (3) at a specific impact velocity is shown in Fig. 4.8. Also, the through-the-thickness stress distributions have been calculated.

Commercial FEM nodes have been used to examine the impact response of laminated composite plates over a wide range of variables and have been shown to be useful in developing spatial time history response data. While geometric and material nonlinear FEM analytical capabilities are available, applicable constitutive models for composite laminates with multiple matrix cracks, fiber breaks, and delaminations are not available. In addition, the ability to predict the onset and subsequent growth of the life limiting failure mode, that is delamination, is needed. Also needed are the requirement to be able to experimentally determine the contact force history, characterisation of the damage using NDE test methods, and post-impact tests to determine residual stiffness and strength.
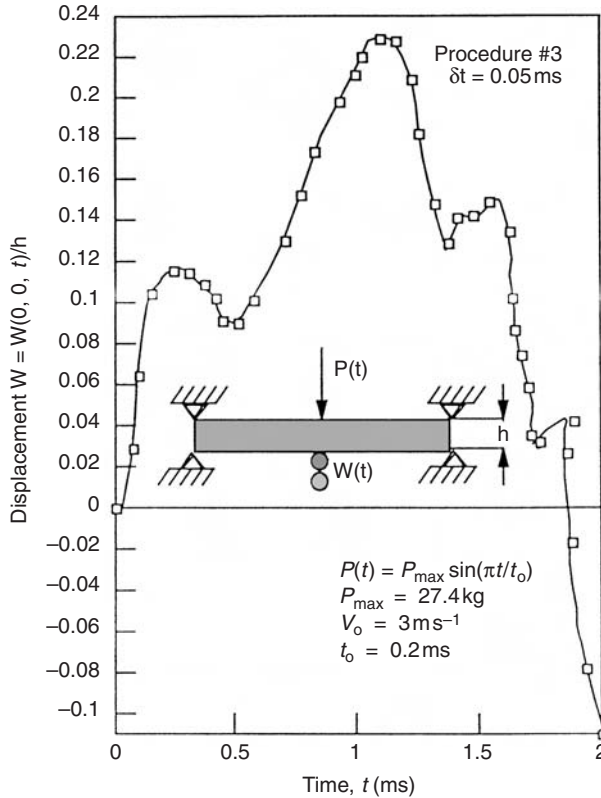
4.7 Displacement history with time as calculated by procedure 3. (After Lakshimarayana et al.[73])

The chart contains labels: Procedure #3, $\delta t = 0.05\,ms$; axes: Displacement $W = W(0, 0, t)/h$; Time, t (ms); with annotations P(t), W(t), h, and equations:

$$P(t) = P_{max} \sin(\pi t/t_o)$$
$$P_{max} = 27.4\,kg$$
$$V_o = 3\,ms^{-1}$$
$$t_o = 0.2\,ms$$

Model
Model classification: damage mechanics
Striker/target parameters

Striker	Target
Mass-small, large	Mass-small
Material-rigid	Material-Gr/epoxy
Geometry-spherical	Geometry-203.2 mm × 203.2 mm
Velocity-up to 70 m/s	Thickness-3, 5 ply
Striker incidence-normal	Support conditions-cylindrical bending
	Ply sequence-cross ply (0/90)

Source: Bogdanovich and Yarve.[57]

4.5.2 Analysis

The displacement strains and stresses are evaluated for a multi-layered orthotropic plate subjected to dynamic contact load as shown in Fig. 4.9.
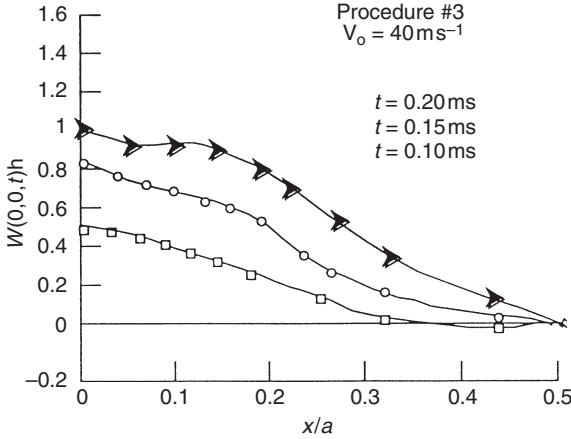
4.8 Spatial variation of transverse displacement as calculated by procedure 3. (After Lakshimarayana et al.[73])
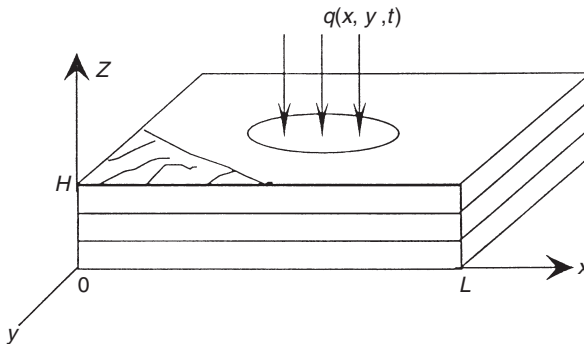
4.9 Dynamic load acting on a multi-layered composite plate. (After Bogdanovich and Yarve[57].)

The three-dimensional problem is formulated by introducing the strain components described through the displacement components $u_x(x, y, z, t)$, $u_y(x, y, z, t)$ and $u_z(x, y, z, t)$.

The strain-displacement relations are expressed by

$$\varepsilon_{xx} = \frac{\partial u_x}{\partial x}, \quad \varepsilon_{yy} = \frac{\partial u_y}{\partial y}, \quad \varepsilon_{zz} = \frac{\partial u_z}{\partial z},$$

$$\gamma_{yz} = \frac{\partial u_y}{\partial z} + \frac{\partial u_z}{\partial y}, \quad \gamma_{xz} = \frac{\partial u_x}{\partial z} + \frac{\partial u_z}{\partial x}, \quad \gamma_{yx} = \frac{\partial u_y}{\partial x} + \frac{\partial u_x}{\partial y}$$

[4.1]

while the stress–strain relations in a layer of the laminate are expressed as

$$Q_{xx}^{(k)} = Q_{11}^{(k)}\varepsilon_{xx} + Q_{12}^{(k)}\varepsilon_{yy} + Q_{13}^{(k)}\varepsilon_{zz} + Q_{16}^{(k)}\gamma_{xy}$$

$$Q_{yy}^{(k)} = Q_{21}^{(k)}\varepsilon_{xx} + Q_{22}^{(k)}\varepsilon_{yy} + Q_{23}^{(k)}\varepsilon_{zz} + Q_{26}^{(k)}\gamma_{xy}$$

$$Q_{zz}^{(k)} = Q_{31}^{(k)}\varepsilon_{xx} + Q_{32}^{(k)}\varepsilon_{yy} + Q_{33}^{(k)}\varepsilon_{zz} + Q_{36}^{(k)}\gamma_{xy}$$

$$Q_{yz}^{(k)} = \overline{Q}_{44}^{(k)}\gamma_{yz} + \overline{Q}_{45}^{(k)}\gamma_{xz} \qquad [4.2]$$

$$Q_{xz}^{(k)} = \overline{Q}_{54}^{(k)}\gamma_{yz} + \overline{Q}_{55}^{(k)}\gamma_{xz}$$

$$Q_{xy}^{(k)} = \overline{Q}_{61}^{(k)}\varepsilon_{xx} + \overline{Q}_{62}^{(k)}\varepsilon_{yy} + \overline{Q}_{63}^{(k)}\varepsilon_{zz} + \overline{Q}_{66}^{(k)}\gamma_{xy}$$

The $\overline{Q}_{ij}^{(k)}$ are the kth layer transformed stiffnesses.

The kinetic and potential energies for the problem can be expressed as

$$K = \int_0^L \int_0^A \int_0^H \rho^{(k)} \left[\left(\frac{\partial u_x}{\partial t}\right)^2 + \left(\frac{\partial u_y}{\partial t}\right)^2 + \left(\frac{\partial u_z}{\partial t}\right)^2 \right] dxdydz$$

$$P = \int_0^H \int_0^L \int_0^A \overline{Q}_{111}^{(k)}\varepsilon_{zz}^2 + 2\overline{Q}_{12}^{(k)}\varepsilon_{xx}\varepsilon_{yy} + 2\overline{Q}_{16}^{(k)}\varepsilon_{xx}\gamma_{xy}$$

$$+ 2\overline{Q}_{31}^{(k)}\varepsilon_{zz}\varepsilon_{xx} + 2\overline{Q}_{32}^{(k)}\varepsilon_{zz}\varepsilon_{yy} + 2\overline{Q}_{36}^{(k)}\varepsilon_{zz}\gamma_{yx} + \overline{Q}_{33}^{(k)}\varepsilon_{zz}^2 \qquad [4.3]$$

$$+ \overline{Q}_{22}^{(k)}\varepsilon_{yy}^2 + 2\overline{Q}_{26}^{(k)}\gamma_{xy}\varepsilon_{yy} + \overline{Q}_{66}^{(k)}\gamma_{xy}^2 + \overline{Q}_{44}^{(k)}\gamma_{zy}^2$$

$$+ 2\overline{Q}_{45}^{(k)}\gamma_{xz}\gamma_{yz} + \overline{Q}_{55}^{(k)}\gamma_{xz}^2\gamma_{yz} \, dxdydz$$

while the boundary conditions for the top and bottom surfaces are taken as

$$\sigma_{zx}(x, y, 0, t) = \sigma_{zy}(x, y, 0, t) = \sigma_{zz}(x, y, 0, t) = 0$$

$$\sigma_{zx}(x, y, H, t) = \sigma_{zy}(x, y, H, t) = 0 \qquad [4.4]$$

$$\sigma_{zz}(x, y, H, t) = -q(x, y, t)$$

The external work proposed by the loads is given by

$$A = \int_0^L \int_0^A q(x, y, t) u_z(w, y, H, t) dxdy \qquad [4.5]$$

The problem can now be formulated by developing the Lagrangian and taking the variation of the expression as follows.

$$\delta = \left\{ \int_0^t [K - P + A] dt \right\} = 0 \qquad [4.6]$$

In forming a solution to the problem posed, an approximation to the displacements is developed which includes coordinates associated with both the transverse z and in-plane x,y directions. The displacement fields are approximated as
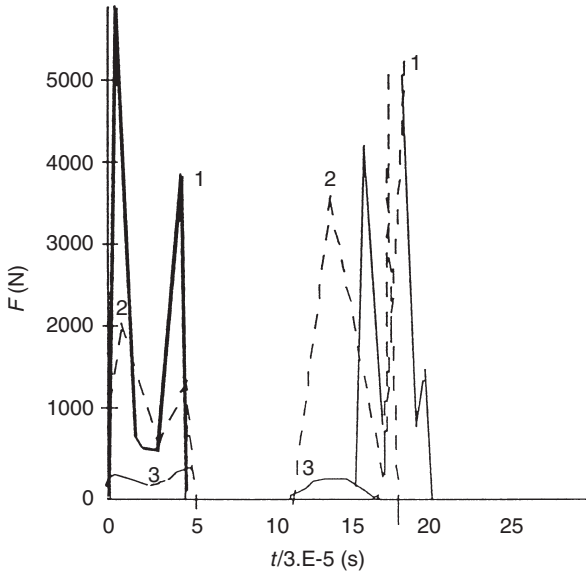
4.10 Impact force vs time: (1) $M = 25\,g$, $V_0 = 13.5\,m\,sec^{-1}$; (2) $M = 0.2\,g$, $V_0 = 4.5\,m\,sec^{-1}$; (3) $M = 17\,kg$, $V_0 = 0.48\,m\,sec^{-1}$. (After Bogdanovich and Yarve[57].)

$$u_x(x, y, z) = \sum_i \sum_j \sum_k u_{ijk}(t)Z_i(z)X_j^u(x)Y_k^u(y)$$

$$u_y(x, y, z) = \sum_i \sum_j \sum_k v_{ijk}(t)Z_i(z)X_j^v(x)Y_k^v(y) \qquad [4.7a,b,c]$$

$$u_z(x, y, z) = \sum_i \sum_j \sum_k w_{ijk}(t)Z_i(z)X_j^w(x)Y_k^w(y)$$

In the above expressions, polynomial spline functions are introduced into the displacement approximations, details of which are found in[71] and are used in the solution of illustrative problems. A similar solution procedure also exists in Chapters 6 and 7.

The transverse impact of a rigid striker interacting with a multi-layered two-dimensional target has been studied. For analysis, the impactor shape has been described by a smooth function in a local coordinate system. The initial conditions for the problem have been taken as zero displacement at time zero and an initial velocity V_0 at time zero. It is assumed that no penetration of the striker into the target plate takes place. The specific problem of a low-velocity rigid body impact on a rectangular G_r/E_p plate has been evaluated for different striker velocities and masses of the striker. The dependency of the contact force with time, for the conditions stated, has been evaluated with typical results shown in Fig. 4.10.
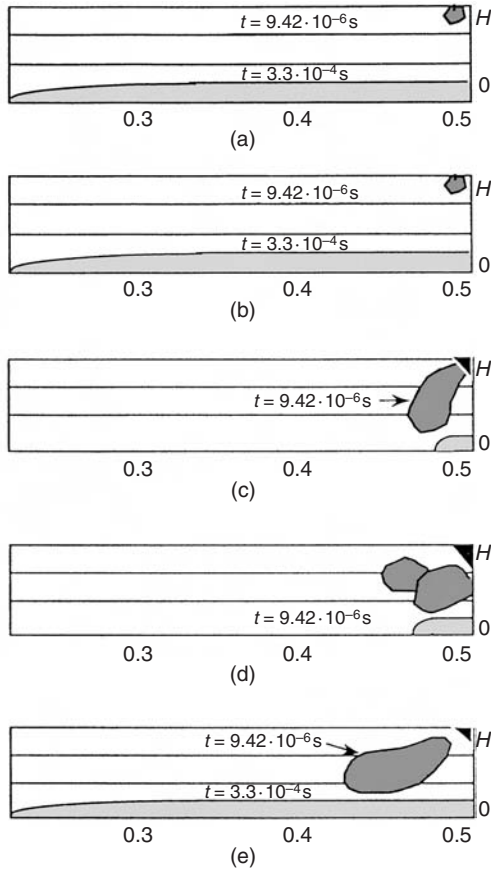
4.11 Impact damage zones for three-ply laminates at: $M = 17\,kg$, $V = 0.48\,m\,s^{-1}$ (a); $M = 25\,g$, $V = 13\,m\,s^{-1}$ (b); $M = 3\,g$, $V = 40.5\,m\,s^{-1}$ (c); $M = 1\,g$, $V = 70\,m\,s^{-1}$ (d); $M = 25\,g$, $V = 25\,m\,s^{-1}$ (e). (After Bogdanovich and Yarve[57].)

Also evaluated have been the components of the displacement vector, strain, and stresses at an arbitrary point in the target laminated plate taken during the impact event. Using the ultimate strength of the material as a damage metric, the strength of the material in the direction of the fibers, the transverse strength, and shear strength have been evaluated. Maps of the impact damage zones for the three-ply laminate subjected to variable striker mass and for various impact velocities are shown in Fig. 4.11. The results obtained from the three-ply maps shown in Fig. 4.11, as well as those obtained for five plies, suggest that the striker/target characteristics and the resultant interior stresses in the target are very sensitive to the velocity and mass of the striker for a given impact energy value. In addition, it is

observed that different failure modes within the target can be obtained, for example, at high velocities and for a small striker mass a small type of failure occurs.

MODEL
Model classification: residual strength
Striker/target parameters

Striker	*Target*
Mass-small	Mass-small
Material-steel	Material-Gl/epoxy, Gr/PEEK, Gr/epoxy
Geometry-hemispherical	Geometry-89 × 55 mm
Velocity/impact energy-15 J	Thickness-5.1 mm
Striker incidence-normal	Ply sequence-[−45/0/+45/90]2S
	Support conditions-clamped

Source: Guild *et al.*[76]

4.6   Impact damage tests

An instrumented drop weight impact machine has been used to introduce damage into three laminated composite materials, these being

Material	Fiber	Matrix
APC-2	AS-4	PEEK
Fibredux 924C	T800H	Toughened epoxy
Fibredux 913G	E-glass	Epoxy

Impact energies imparted to the clamped laminated composite plate specimens were insured in stages up to a maximum energy level of 15 J. Damage imparted to the specimens was assessed using a C-scan, NDE apparatus, with damage consisting of primarily delamination and accompanying transverse and shear cracks. The global shape of the damage observed was approximately circular while individual ply damage exhibited a lobal type of damaged area. The transverse cracks were found to densify with increase in impact energy and a schematic of the transverse cracking is shown in Fig. 4.12 for 1.5 J and 10 J impacted energies.

4.6.1 Compression after impact tests

Compression tests were performed on the damaged specimens at loading rates of 0.03 mm/minute, with the specimens supported using an anti-buckling
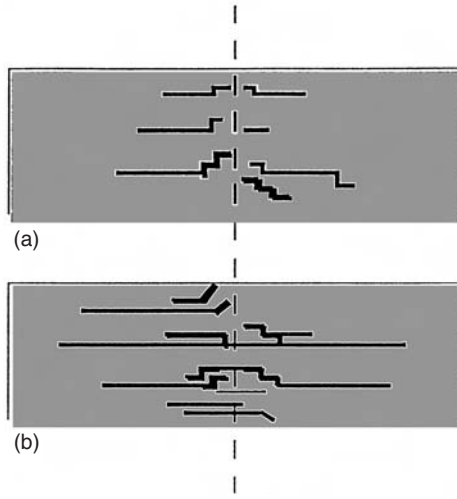
4.12 Transverse cracking at (a) 1.5 J and (b) 10 J impacts. (After Guild et al.[76])
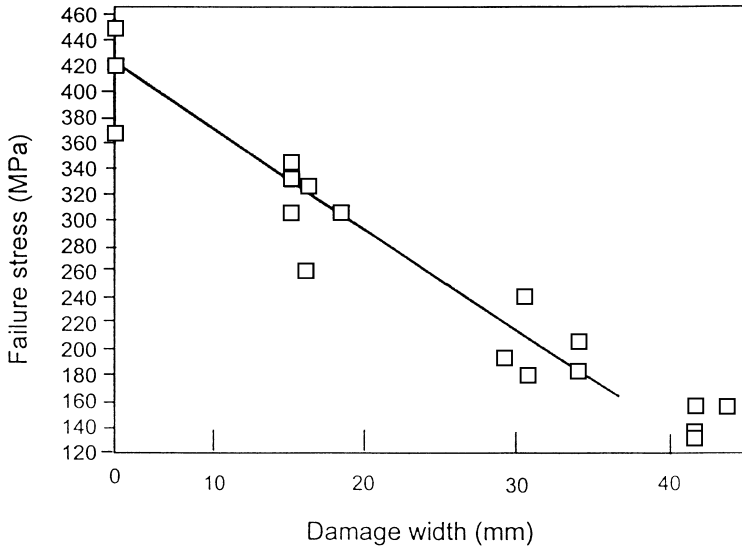
4.13 Compression strength as a function of damage width for graphite/epoxy specimens. (After Guild et al.[76])

guide. Compressive loading involved growth of the delaminations with subsequent failure. A plot of the compressive failure stress as a function of damage width was made for each specimen tested with a typical result for the graphite/epoxy specimens shown in Fig. 4.13.

(a) FEM model

(b) quarter section with grid

D   C

B

A

Pote

A   Equator   B
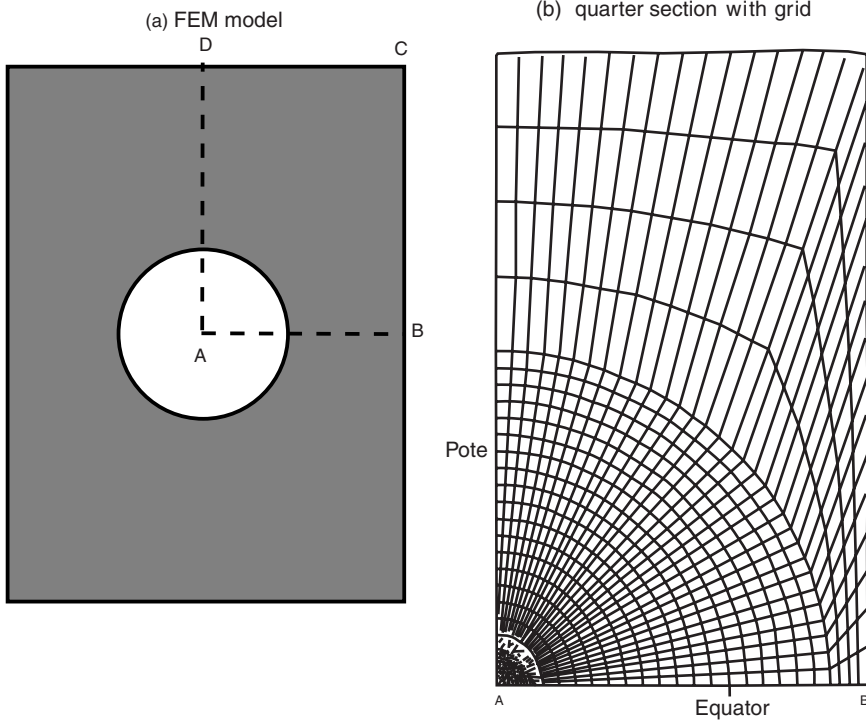
4.14 The (a) FEM model and the (b) quarter section of the grid. (After
      Guild *et al.*[76])

4.6.2 Model development

The model developed on the basis of the experiments performed is
premised on the tenet that the critical laminate properties which control
the performance of a laminate are the interlaminar mode II toughness,
that is, G_{IIC} during impact and mode I, the interlaminar toughness G_{IC} in
compression after impact, as also discussed in Chapter 1. The two model
parameters G_{IC} and G_{IIC} have been examined to evaluate the relative roles
of these two fracture mechanics parameters. Results from impact tests in-
dicate that toughened matrices with high G_{IIC} parameters contain the
impacted damage. However, for the evaluation of compressive strength
after impact, normalised plots of compression strength versus damage
width show a common master curve. Thus, the use of a thermoset or ther-
moplastic matrix does not appear to affect the subsequent growth of dela-
minations during compression. This data has led to the development of a
finite element model (FEM) which is based on describing the damage as
contained in a soft zone surrounded by a stiff region. The FEM model devel-
oped considers the damage area to be circular with a quarter section grid
of the specimen model used for analysis, as shown in Fig. 4.14. Eight noded
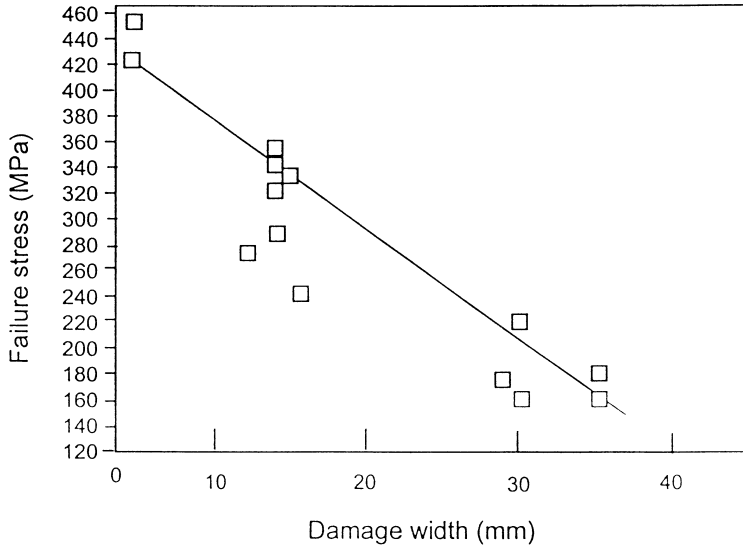
4.15 Compressive failure strength vs damage width. (After Guild
et al.[76])

membrane elements in plane stress have been used in conjunction with an
FEM packaged program. FEM analysis has been carried out for varying
values of reduced modulus in the damaged area. An example of the results
for the predicted compressive failure stress versus damage width has been
shown in Fig. 4.15 for graphite/epoxy specimens.

Using data obtained from FEM predictions of failure stress with damage
and the variation of modulus with damage area, the modulus of the damage
area can be implied for a given width of damage, with a summary of the
normalised modulus reduction with width shown in Fig. 4.16.

The change in modulus with damage width appears similar for the three
composite laminate materials studied, with all three laminates of identical
construction. Results suggest that failure in compression after impact is
related to a stress magnification as a result of the damaged area. CAI is not
related to the mode I fracture toughness G_{IC}, however increased damage
tolerance may be related to G_{IIC}. The occurring damage appears related to
laminate construction rather than the types of matrix such as thermosets,
toughened thermosets, and thermoplastics.

4.7   Summary

The references discussed have been used as representative illustrations of
a number of investigators who have contributed to the impact damage
problem of composite material targets in the areas of deformation mechan-
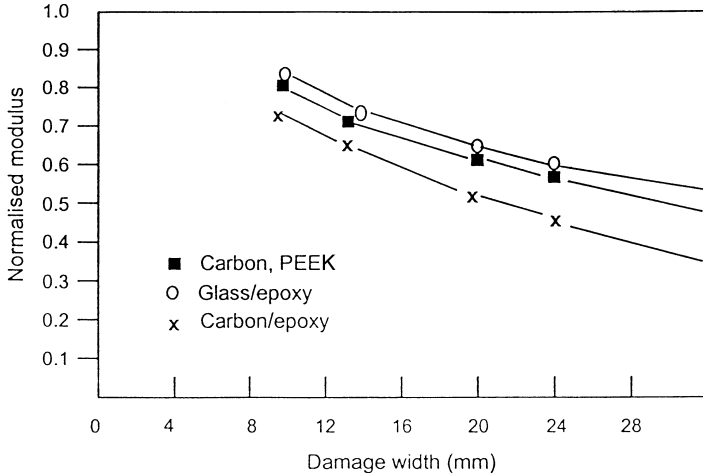
4.16 Predictions of normalised modulus with damage width.

ics, damage mechanics, and residual strength prediction. Other contributions by investigators have been included in the attached bibliography. As can be noted from the problems discussed, the prediction of impact response of laminated composite plates covers a wide spectrum of issues including contact force history, interlaminar stress distribution, and extent of damage which contributes to the overall loss in strength and stiffness of the structural component. Important parameters identified with these events include impactor material and nose shape, impact velocity, target material, laminate stacking sequence, target geometry, target support conditions, target curvature, and pre-stressing of the target. A systematic study of the three problem types: *deformation mechanics, damage mechanics, and residual strength prediction* can provide a basis for both the assessment and design of damage tolerant materials for the case of impact damage as the primary source of damage.

Some of the issues which require further study for damage tolerant design include:

1 Understanding the micromechanics of damage.
2 Understanding of the mesomechanics of relating the properties of the fiber, matrix, and fiber-matrix interface to the composite bulk properties.
3 Understanding how the material parameters G_{IC}, G_{IIC}, and G_{IIIC} affect damage tolerance.
4 Understanding the effects of stress and strain rate on damage formation of composites subject to impact loading.
5 Developing predictive techniques for establishing static failure loads in the presence of impact damage.

6 Developing the capability to predict critical damage metrics for impact damaged components.
7 Development of standardised laboratory test methods to assess damage independent of specimen geometry.
8 Developing uniform test methods and standardised methods for assessing damage characterisation.

Finally, the development of a design philosophy for impact tolerant composite materials/structures should include:

- Design of structural components to localise the damage upon impact.
- Design of structural components using redundant load paths.
- Design of structural components using high fracture toughness, notch insensitive matrix materials.
- Design of structural components to allow penetration by a high-velocity striker with minimum energy transfer to the structural component.

References

1 Reddick H K, Jr, 'Failure analysis and mechanics of failure of fibrous composite structures', *NASA Conf Pub* 2278, 129–51, 1978.
2 Curtis D, 'Regulations for continued airworthiness-damage tolerance in its widest sense,' DOT/FAA/AR-95/86, pp 173–86, 1995.
3 MIL-A-83444.
4 MIL-STD-1530A.
5 Sierakowski R L and Newaz G M, *Damage Tolerance in Advanced Composites*, Lancaster, PA, Technomics Publication, 1995.
6 Greszszuk L B, *Damage in Composite Materials Due to Low Velocity Impact*, *Impact Dynamics*, pp 55–94, New York, Wiley, 1982.
7 Sierakowski R L and Chaturvedi S K, 'Impact loading in filimentary structural composites', *Shock Vib Digest*, 1983 **15**(10) 13–31.
8 Abrate S, 'Impact on laminated compositee materials', *Appl Mech Rev*, 1991 **44**(4) 155–90.
9 Cantwell W J and Morton J, 'The impact resistance of composite materials – a review', *Composites*, 1991 **22**(5) 347–62.
10 Morris A W H and Smith R S, 'Some aspects of the evaluation of the impact behaviour of low temperature fibre composites', *Fibre Sci Technol*, 1971 **3** 219–42.
11 Rogers K F, Sidey G R and Kinston-Lee D M, 'Ballistic impact resistance of carbon-fibre laminates', *Composites*, 1971 **2** 237–41.
12 Ross C A and Sierakowski R L, 'Studies on the impact resistance of composite plates', *Composites*, 1973 **4** 157–61.
13 Broutman L J and Rotem A, 'Impact strength and toughness of fiber composite materials', *Foreign Object Impact Damage to Composites, ASTM STP 568*, pp 114–33, Philadelphia, ASTM, 1975.

14 Husman G E, Whitney J M and Halpin J C, 'Residual strength characterization of laminated composites subjected to impact loading', *Foreign Object Impact Damage to Composites*, pp 92–113, Philadelphia, ASTM, 1975.

15 Starnes J H, Jr, Rhodes M D and Williams J G, 'The effect of impact damage and circular holes on the compressive strength of a graphite/epoxy laminate', NASA TM 78796, 1978.

16 Aleszka J C, 'Low energy impact behaviour of composite panels', *J Test Eval*, 1978 **6**(3) 202–10.

17 Roylance D, 'Stress wave damage in graphite/epoxy laminates', *J Composite Mater*, 1978 **14** 111–19.

18 Takeda N, Sierakowski R L, Ross C A and Malvern L E, 'Delamination-crack propagation in ballistically impacted glass/epoxy composite laminates', *Exp Mech*, 1980 **4** 19–25.

19 Sykes G F and Stoakley D M, 'Impact penetration studies of graphite/epoxy laminates', *Proc 12th Nat SAMPE Tech Conf*, pp 482–93, 1980.

20 Amijima S and Fujii T, 'Compressive strength and fracture characteristics of fiber composites under impact loading', *Process in Science and Engineering of Composites, Proc 4th Int Conf Composite Materials* (T Hayashi, K Kawata and S Umekawa, eds), pp 399–413, Tokyo, Okasan, 1982.

21 Williams J G and Rhodes M D, 'Effect of resin on impact damage tolerance of graphite/epoxy laminates', *Composite Mats: Testing and Design (6th Conf), ASTM STP 787* (I M Daniel, ed), pp 450–80, Philadelphia, ASTM, 1982.

22 Elber W, 'Failure mechanics in low velocity impact on thin composite plates', NASA Tech Paper 2152, 1983.

23 Bostaph G M and Elber W, 'A fracture mechanics analysis for delamination growth during impact on composite plates', *Advances in Aerospace Structures, Materials, and Dynamics, Symp on Composites, ASME Winter Annual Meeting*, pp 133–7, Boston, ASME, 1983.

24 Sarma Avva V and Padmanabha H L, 'Compressive residual strength prediction in fiber-reinforced laminated composites subjected to impact loads', *Advances in Fracture Research, Proc 6th Int Conf on Fracture* (S R Valluri, D M R Taplin, P RamaRao, J F Knott and R Dubey, eds), pp 2890–907, 1984.

25 Williams J G, 'Effect of impact damage and open holes on the compression strength of tough resin/high strain fibre laminates', NASA Tech Memo 85756, 1984.

26 Sun C T and Chen J K, 'On the impact of initially stressed composite laminates', *J Composite Mater*, 1985 **19** 490–504.

27 Chamis C C and Sinclair J H, 'Impact resistance of fiber composites: energy absorbing mechanisms and environmental effects', in *Recent Advances in Composites in the US and Japan, ASTM STP 864*, (J R Vinson and M Taya eds), pp 326–45, Philadelphia, ASTM, 1985.

28 Tan T M and Sun C T, 'Use of statistical indentation laws in the impact analysis of laminated composite plates', *J Appl Mech*, 1985 **52** 6–12.

29 Teti R, Langella F, Crivelli V and Caprino G, 'Impact response of carbon cloth reinforced composites', *Proc 5th Int Conf on Composite Materials*, San Diego, pp 373–81, 1985.

30 Shivakumar K N, Elber W and Illg W, 'Prediction of impact force and duration during low velocity impact on circular composite laminates', *J Appl Mech*, 1985 **52** 675–80.

31 Manders P W and Harris W C, 'A parametric study of composite performance in compression-after-impact testing', *SAMPE J*, 1986 **22** 47–51.

32 Cantwell W J, Curtin P T and Morton J, 'An assessment of the impact performance of CFRP reinforced with high strain carbon fibre', *Composite Sci Technol*, 1986 **25**(2) 133–48.

33 Cairns D S and Lagace P A, 'Thick composite plates subjected to lateral loading', *J Appl Mech*, 1987 **54** 611–16.

34 Stevanovic M, Kostic M, Stecenko T and Briski D, 'Impact behaviour of CFRP composites of different stacking geometry', *Composite Eval*, 1987 78–83.

35 Dorey G, Sigerty P, Stellbrink K and Hart W G J, 'Impact damage tolerance of carbon fibre and hybrid laminates', Garteur TP-037, Royal Aircraft Est Tech Rept 87057, 1987.

36 Gause L W and Buckley L J, 'Impact characterization of new composite materials', *Instrumented Impact Testing of Plastics and Composite Materials, ASTM STP 936*, 248–61, 1987.

37 Bachrach W E, 'Impact damage in composite laminates', *Proc 4th Japan-US Conf on Composite Materials*, 53–62, 1988.

38 Bowles K J, 'The correlation of low-velocity impact resistance of graphite-fiber-reinforced composites with matrix properties', *Composite Materials: Testing and Design (8th Conf), ASTM STP 972*, 124–42, 1988.

39 Cantwell W J, 'The influence of target geometry on the high velocity impact response of CFRP', *Composite Struct*, 1988 **10** 247–65.

40 Williams J, Marshall I H and Carswell W S, 'Theoretical modelling of damage in composite laminates subject to low-velocity impact', *Composite Mat Response: Constitutive Relations and Damage Mechanisms* (G C Sih *et al.*, eds), pp 133–45, London, Elsevier, 1988.

41 Morton J, 'Scaling of impact-loaded carbon-fiber composites', *AIAA J*, 1988 **26** 989–94.

42 Davies G A O and Godwin E W, 'Impact behaviour of thermoplastic composites', *CADCOMP 88*, pp 371–82, New York, Springer Verlag, 1988.

43 Rotem A, 'Residual flexural strength of FRP composite specimens subjected to transverse impact loading', *SAMPE J*, 1988 **2** 19–25.

44 Wu H T and Springer G S, 'Measurements of matrix cracking and delamination caused by impact on composite plates', *J Composite Mater*, 1988 518–32.

45 Wu H T and Springer G S, 'Impact induced stresses, strains and delaminations in composite plates', *J Composite Mater*, 1988 533–60.

46 Hong S and Liu D, 'On the relationship between impact energy and delamination area', *Exp Mech*, 1989 **13** 115–20.

47 Vedula M and Koczak M J, 'Impact resistance of cross-plied polyphenylene sulfide composites', *J Thermoplastic Composite Mater*, 1989 **2** 154–63.

48 Cairns D S and Lagace P A, 'Transient response of graphite/epoxy and kevlar/epoxy laminates subjected to impact', *AIAA J*, 1989 **27** 1590–6.

49 Cantwell W J, 'The influence of target geometry on the high velocity impact response of CFRP', *Composite Struct*, 1989 **10** 247–65.

50 Cantwell W J and Morton J, 'The influence of varying projectile mass on the impact response of CFRP', *Composite Struct*, 1989 **13** 101–4.

51 Cantwell W J and Morton J, 'Comparison of the low and high velocity impact response of CFRP', *Composite Struct*, 1989 **20** 545–51.

52 Cantwell W J and Morton J, 'Geometrical effects in the low velocity impact response of CFRP', *Composite Struct*, 1989 **12** 39–59.

53 Morton J and Godwin E W, 'Impact response of tough carbon fibre composites', *Composite Struct*, 1989 **13** 1–19.

54 Quian Y and Swanson S R, 'Experimental measurement of impact response in carbon/epoxy plates', *Proc 30th AIAA/ASME/ASCE/AHS Structures, Structural Dynamics and Materials Conf*, paper #89-1276-CP, 1989.

55 Hsi-Yung Wu T and Chang F-K, 'Transient dynamic analysis of laminated composite plates subjected to transverse impact', *Comput Struct*, 1989 **31**(3) 453–66.

56 Clark G, 'Modeling of impact damage in composite laminates', *Composites*, 1989 **20** 209–14.

57 Bogdanovich A E and Yarve E V, 'Numerical analysis of laminated composite plates subjected to impact loading', *Proc Am Soc for Composites, 4th Tech Conf*, pp 399–409, 1989.

58 Lasser D and Leach D, 'Compressive properties of thermoplastic matrix composites', *Proc 34th Int SAMPE Symp*, pp 1464–73, 1989.

59 Poon C, Benak T and Gould R, 'Assessment of impact damage in toughened resin composites', *Theoret Appl Fract Mech*, 1990 **13** 81–97.

60 Curson A D, Leach D C and Moore D R, 'Impact failure mechanisms in carbon fiber/PEEK composites', *J Thermoplastic Composite Mater*, 1990 **3** 24–31.

61 Cantwell W J and Morton J, 'An assessment of the residual strength of an impact-damaged carbon fibre-reinforced epoxy', *Composite Struct*, 1990 **14** 303–17.

62 Cantwell W J and Morton J, 'Impact perforation of carbon fibre-reinforced plastic', *Composite Sci Technol*, 1990 **38** 119–41.

63 Qian Y, Swanson S R, Nuismer R J and Bucinell R B, 'An experimental study of scaling rules for impact damage in fiber composites', *J Composite Mat*, 1990 **24** 559–70.

64 Prichard J C and Hogg P J, 'The role of impact damage in post-impact compression testing', *Composites*, 1990 **21** 503–11.

65 Choi H Y, Downs R J and Chang F, 'A new approach toward understanding damage mechanisms and mechanics of laminated composites due to low-velocity impact: pt I-experiments, pt II-analysis', *J Composite Mater*, 1991 **25** 992–1038.

66 Prichard J C and Hogg P J, 'Effect of fibre and matrix type on the post impact compression strength of laminated polymer composite materials', *Proc ICCM-8 (SAMPE)*, pp 28R1–28R11, Covina, CA, 1991.

67 Li Y, Ruiz C and Harding J, *Modelling of the Impact Response of Fibre-Reinforced Composites*, Lancaster, PA, Technical Publishing, 1991.

68 Christoforou A P and Swanson S R, 'Analysis of impact response in composite plates', *Int J Solids Struct*, 1991 **27** 161–70.

69 Cairns D S and Lagace P A, 'A consistent engineering methodology for the treatment of impact in composite materials', *J Reinforced Plastics Composites*, 1992 **11**(4) 395–412.

70 Bogdanovich A E and Yarve E V, 'Numerical analysis of impact deformation and failure in composites plates', *J Composite Mater*, 1992 **26** 520–45.

71 Jegley D C, 'Effect of low-speed impact damage and damage location on behaviour of composite panels', NASA Tech paper 3196, 1992.

72 Guy T A and Lagace P A, 'Compressive residual strength of graphite/epoxy laminates after impact', *Proc 9th DOD/FAA/NASA Conf on Fibrous Composites in Structural Design, DOT/FAA/CT-92–25*, pp 253–74, 1992.

73 Lakshimarayana H V, Boukhili R and Gauvin R, 'Impact response of laminated composite plates: prediction and verification', *Composite Struct*, 1992 **28** 61–72.

74 Jackson W C and Poe C C, Jr, 'The use of impact force as a scale parameter for the impact response of composite laminates', NASA TM 104189, 1992.

75 Jegley D C, 'Effect of low-speed impact damage and damage location on behavior of composite laminates', NASA TN 3196, 1992.

76 Guild F J, Hogg P J and Prichard J C, 'A model for the reduction in compression strength of continuous fibre composites after impact damage', *Composites*, 1993 **24** 333–9.

77 Vietinghoff H, Poon C, Stanznicky P V and Gould R, 'An experimental investigation into the damage resistance and compression-after-impact strength of T800H/3900-2, IAR LTR-St-1909, IAR/NRCC, Ottawa, Canada, 1993.

78 Lagace P A, Williamson J E, Wilson Tsang P H, Wolf E and Thomas S, 'A preliminary proposition for a test method to measure (impact) damage resistance', *J Reinforced Plastic Composites*, 1993 **12** 584–601.

79 Iannone M and Marcone A, *Impact Damage in Composite Materials, Controlling Factors*, Madrid, ICCM, 1993.

80 Pevorsek D C, Chin H C and Bhatnagar A, 'Damage tolerance: design for structural integrity and penetration', *Composite Struct*, 1993 **23** 137–48.

81 Yigit A S and Christoforou A P, 'On the impact of a spherical indenter and an elastic-plastic transversely isotropic half-space', *Composite Eng*, 1994 **4** 1143–52.

82 Jones R, 'Residual strength of composites with multiple impact damage', *Composite Struct*, 1994 **24** 347–56.

83 Christoforou A P and Yigit A S, 'Transient impact response of a composite beam subject to elastic-plastic impact', *Composite Eng*, 1995 **5** 459–70.

84 Zhou G, 'Prediction of impact damage thresholds of glass fibre-reinforced laminates', *Composite Struct*, 1995 **25** 185–94.

85 Khan B, Rao R M V G and Venkatorsmen N, 'Low velocity impact fatigue studies on glass epoxy composite laminates with varied material and test parameters-effect of incident energy and fibre volume fraction', *J Reinforced Plastics Composites*, 1995 **14** 1150–9.

86 Scarponi C, Britti G, Barboni R, Marcone A and Iannone M, 'Impact testing on composite laminates and sandwich panels', *J Composite Mater*, 1996 **30** 1873–911.

87 Christoforou A P and Yigit A S, 'Impact of composite structures – the momentum balance method', *J Composite Mater*, 1996 **30** 1068–87.

5

Damage resistance and tolerance of thick laminated woven roving GFRP plates subjected to low-velocity impact

G ZHOU* AND L J GREAVES

5.1 Introduction

Fibre-reinforced laminated composites have been used extensively in load-bearing structures due generally to their light weight, high strength-to-weight and stiffness-to-weight ratios, superb fatigue strength limit, good corrosion resistance and reduced parts count. Applications of such structures are abundant in aircraft, high-performance vehicles, high-speed boats and marine vessels to name but a few. These composite structures may encounter a transverse impact load in scenarios such as: tool-dropping, hailstones, runway or road debris. Such events may induce damage in the form of matrix cracking, fibre fracture and delamination. This damage can alter the structural response during impact and reduce subsequent structural performance. Both strength and stiffness can be affected and in-plane compression strength is especially sensitive to this sort of damage. Therefore, a current and important design requirement in load-bearing composite structures is the ability to tolerate impact damage. This is true especially in the aerospace industry where most of the current damage-tolerant design philosophy is being developed and refined. In this chapter, we investigate the impact behaviour of particular non-aerospace composite materials, but still using an aerospace-type approach.

Impact damage can be a design limiting factor, but its consequences are not well understood and the subject as a whole is complex. It is therefore accounted for in current composite structural design simply by limiting the allowable compressive strain. For aerospace, the limit is 0.4%,[1] a conservative value when it is considered that most carbon fibre-reinforced composites have strains at failure of over 1.2%. Allowable strain for glass fibre-reinforced composites is similarly restricted[2] to a conservative level.

Various solutions for improving damage tolerance have been developed, for example, by modifying the composite system with toughened matrix,[3]

---

* Formerly research associate in the Department of Aeronautics, Imperial College.

interleaving,[4] stitching,[5] or z-pin reinforcement,[6] and show varying degrees of success. Nevertheless, the benefits of a cost-effective solution could materialise only if the allowable strain is further increased. This undoubtedly demands a thorough understanding of impact response, damage mechanisms, residual load-bearing capability and damage tolerance assessment of the composite structure under study.

In investigating the effects of impact on a composite structure it is usual to introduce damage through controlled impact testing, then to quantify or characterise the damage and finally to measure the residual strength of the structure. The conditions of an impact test are normally derived from some typical scenario and are defined by specifying the mass, nose shape, diameter and velocity of the impactor, lay-up, fibre volume fraction and geometry of the composite specimen, and the boundary conditions.

The effect of damage is examined by one of two related approaches, namely, impact damage resistance (IDR) and damage tolerance. IDR focuses very much on the identification of the onset of dominant damage mechanisms (for example, delamination), from impact response curves in terms of impact energy or absorbed energy. It is tempting to use these energy values as an indication of damage tolerance in the same way that toughness is related to damage tolerance in metallic materials. At a simplistic level, it might be expected that a composite system with a greater IDR would exhibit a greater damage tolerance. In practice, fibre-reinforced laminated composites are highly anisotropic, with usually multiple damage mechanisms, and IDR is not obviously related to damage tolerance. In fact, the two can conflict with each other. Moreover, the information that can be obtained from absorbed energy alone is too limited to be useful in composite structural design. Hence, the damage tolerance approach has been developed by conducting quasi-static tests on both impact damaged and intact specimens and then by relating their strength ratio to a range of the corresponding impact energies, damage sizes, or impact forces.

The conventional methodology for damage tolerance assessment in industry consists of four major sequential steps, namely: impact testing, damage characterisation, determination of static residual strength and damage tolerance assessment. The most critical loading mode to impact-damaged panels is in-plane compression. This is because of local instability associated with the presence of delamination.[7] Therefore, the assessment of impact damage tolerance focuses primarily on an examination of the ratio of the residual strength of an impacted panel to the strength of an intact panel (or strength retention factor) over a range of impact energies or projected delamination areas. This whole process for the given composite system is not only very costly and time-consuming but also extremely complex due to the large number of parameters that can be used to characterise the impact and the damage.

This chapter describes an investigation of the effects of impact on glass fibre composite laminate plates. The first part of the chapter is a brief description of the composite systems used in the study and their effective mechanical properties. This is followed by an overview of the various experimental procedures used to conduct quasi-static and impact tests, and the subsequent damage interrogation and panel compression tests. The third part describes the damage resistance of the laminated composite plates subjected to low-velocity and high-energy impact. In this section, impact response and the characteristics of the dominant damage mechanisms occurring during impact are examined and their energy-absorbing characteristics are described. The parameters affecting the onset and propagation of these damage mechanisms are discussed. The fourth part starts with the determination of compressive strength and stiffness needed for the assessment of impact damage tolerance. It is followed by an investigation of damage mechanisms responsible for a reduction of compressive strength and factors that affect these mechanisms during compressive loading. It continues with a discussion of the conventional assessment of impact damage tolerance and associated measures of damage with particular reference to their limitations. It concludes with discussions of a proposed method of damage tolerance assessment based on impact force data.

5.2   Characterisation of composite materials

5.2.1 Composite materials

The damage tolerance of any given composite system is dependent on the fibre type, fibre architecture, fibre surface treatment, matrix, layup and fibre volume fraction. It is also affected by environmental effects as discussed in.[7–10] Woven roving fabric laminates have proved to have superior impact energy absorbing properties to those of laminates made of unidirectional prepregs.[11–12] The work described in this chapter investigated two woven roving fabric laminated composite systems. Of primary interest was the assessment of their damage tolerance *per se*, though a direct comparison between the two composite systems is discussed wherever applicable.

Both materials consisted of plain-weave fabric, laminated with the warp fibres oriented in the 0° laminate direction and cured in a press at elevated temperature. The first material contained E-glass fabric impregnated with a polyester resin and was available in two nominal thicknesses: 10 mm and 25 mm. They both had a nominal fibre volume fraction of about 60% and also had about 30% more fibre tows in the warp direction than the fill direction. The translucent polyester resin made it easy to detect any near surface matrix cracking. The second material consisted of an S-glass fabric impregnated with a phenolic resin and was available in three nominal thicknesses:

5 mm (used only in mechanical property tests), 14 mm and 19 mm. The phenolic resin was opaque, which made visual damage detection more difficult. No further materials information can be disclosed due to commercial sensitivity.

5.2.2   Basic mechanical properties

The mechanical properties of these composite systems were initially unknown. They were characterised in tension, compression, in-plane shear, interlaminar shear and flexure.[13–15] Most properties were measured on 10 mm or 5 mm thick laminates of the E-glass and S-glass materials respectively. The specimens generally conformed to the ASTM or CRAG standards, but were tested at full laminate thickness (i.e. 5 mm or 10 mm). Those properties thought to be most important to impact damage (i.e. interlaminar shear (ILS) and flexure) were measured on full-thickness samples from the impact test panels. We observed the thickness effect in some of these two properties. This was explained by using the adapted Weibull's statistical strength theory.[15] This information about mechanical behaviour of these composite systems has proved, with hindsight, to be instrumental to a correct interpretation of impact behaviour.

The overall mechanical properties measured are summarised in Table 5.1. Two salient features are noteworthy, as they have important implications for the interpretation of subsequent data associated with impact behaviour and damage tolerance. Firstly, the compressive strengths in both directions were much lower than the tensile strengths. Secondly, the ILS strengths in the two directions were even lower. Thus, it was anticipated that ILS and compression failures would dominate the mechanical behaviour during impact. Furthermore, ILS strengths did not seem to be affected by thickness. Interestingly, the differing number of fibre tows in the two directions in the E-glass/polyester was correlated with ILS strength,[13] which is usually regarded as a resin-dominated property. It is also worth mentioning that these woven roving fabric laminates under tensile loading exhibited the bilinear stress-strain behaviour, or so-called 'knee effect', due to matrix microcracks caused by a straightening-out of crimped fibres.[14] This may contribute to the nonlinearity of plate deformation as well as the process of impact energy absorption during plate deflection.

5.3   Experimental procedures

The overall experimentation involved three parts: quasi-static indentation tests, impact tests and quasi-static residual strength tests. To carry out impact tests, two sets of circular plate specimens were cut from the laminate sheets, each with two testing diameters of 100 mm (small) and 500 mm

Table 5.1. Effective mechanical properties of composite materials

Property	Fibre direction	E-glass/polyester		S-glass/phenolic	
		10 mm	—	5 mm	—
Tensile modulus	0°	30.1 ± 1.9	—	29.6 ± 1.3	—
	90°	25.1 ± 1.5	—	30.5 ± 3.5	—
Tensile strength	0°	496 ± 22	—	723 ± 28	—
	90°	353 ± 21	—	530 ± 55	—
Compressive modulus	0°	32.3 ± 2.0	—	35.3 ± 5.1	—
	90°	25.9 ± 0.9	—	35.1 ± 2.6	—
Compressive strength	0°	289 ± 18	—	143 ± 7	—
	90°	227 ± 18	—	130 ± 16	—
In-plane shear modulus	±45°	4.0 ± 0.4	—	3.52 ± .28	—
In-plane shear strength	±45°	46 ± 1	—	37.6 ± 4.7	—
Interlaminar shear modulus	0°	2.6[a]	—	—	—
	90°	1.9[a]	—	—	—

Property	Fibre direction	E-glass/polyester		S-glass/phenolic	
		10 mm	25 mm	14 mm	19 mm
Interlaminar shear strength (3-point at a L/t of 8)	0°	19.3 ± 2.2	19.8 ± 1	16.2 ± 0.7	16.2 ± 1.3
	90°	16.5 ± 1	16.5 ± 1	12.6 ± 1.1	13.2 ± 1.1
Flexural strength (3-point at a L/t of 16)	0°	374 ± 40	273 ± 14	277 ± 24	245 ± 22
	90°	379 ± 23	266 ± 22	208 ± 20	—

Modulus is in GPa and strength is in MPa. [a] Data are from Hodgkinson[16].

(large) with sufficient margins left for clamping. Quasi-static indentation tests were conducted only on the small circular specimens due to limited amount of material available. Residual strength tests were carried out quasi-statically on rectangular panels extracted from the large impact-damaged circular plates.

5.3.1   Quasi-static tests

There were four reasons of conducting quasi-static indentation tests. Firstly, it was easier to develop some preliminary understanding of damage characteristics by executing a quasi-static test in a much better controlled manner. This knowledge of what to expect allowed the impact tests to be

carried out more effectively. Secondly, the quasi-static results could be treated as very low velocity impacts when examining the effect of impact velocity on damage at a later stage. Thirdly, it made it possible to examine the interaction of local indentation and global plate deflection and its effect on the onset of damage, which was significant in these thick laminates. Finally, it was a method to measure contact stiffness,[17] which was required for theoretical analysis and finite element modelling.[18]

Most of the specimens had electrical resistance strain gauges attached to measure radial strains at two locations, one (C1) at 15 mm away from the centre of the loading surface and the other (T1) at the centre of the distal surface (i.e. the surface on the opposite side to the indentor). In the first two tests, it was found that the location of C1 was too close to the contact area. It was therefore moved 5 mm further away on the remaining quasi-static specimens. Occasionally, for a further diagnosis, three additional strain gauges (C2, T2 and T3) were bonded at locations 35 mm away from the central axis, as indicated in Fig. 5.1. A linear variable differential transformer (LVDT) was used for measuring the maximum plate deflection which enabled local indentation to be calculated. A flat-ended indenter of 20 mm diameter was used in all the tests, both quasi-static and impact. The quasi-static tests were carried out using an Instron universal testing machine, on which the specimen was fixed by a purpose-built clamping device. The overall experimental set-up is illustrated in Fig. 5.1. A quasi-static load was applied to the centre of each clamped specimen at a cross-head speed of 5 mm/min.

5.3.2   Impact tests

Impact tests were restricted to low impact velocities but high incident kinetic energies (IKEs) were achieved through the use of high masses. They
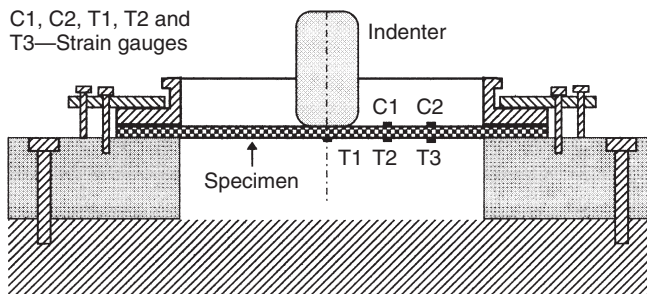
5.1 An experimental setup for quasi-static tests of circular laminate plates.

were conducted by using an instrumented, tailor-made, drop-weight test rig. Impact velocities regulated by selected drop heights were varied between 2 m/s and 8 m/s and their actual values were calculated through an elapsed time measured by a pair of photodiodes over a fixed distance. The photodiodes were positioned on the drop guide and were triggered by the passage of a steel-foil flag bolted onto the impactor. The triggering of the second photodiode took place only when the impactor struck the specimen. Measured impact velocities were within 3% of the free-fall predictions and the greater impact velocities were, the closer to the prediction they came. The impactor had a flat-ended nose, 20 mm in diameter, and could be adjusted with additional weights to give a range of impactor masses from 6 kg up to 105 kg. The combination of mass with a variety of impact velocities yielded a range of IKEs from 15 J up to 3000 J. The impactor was captured after rebound to prevent the repeated impact in each test. A simple illustration of experimental set-up is shown in Fig. 5.2.

All the small impact specimens were strain-gauged at the same two locations as the quasi-static ones. For selected large impact specimens, three or
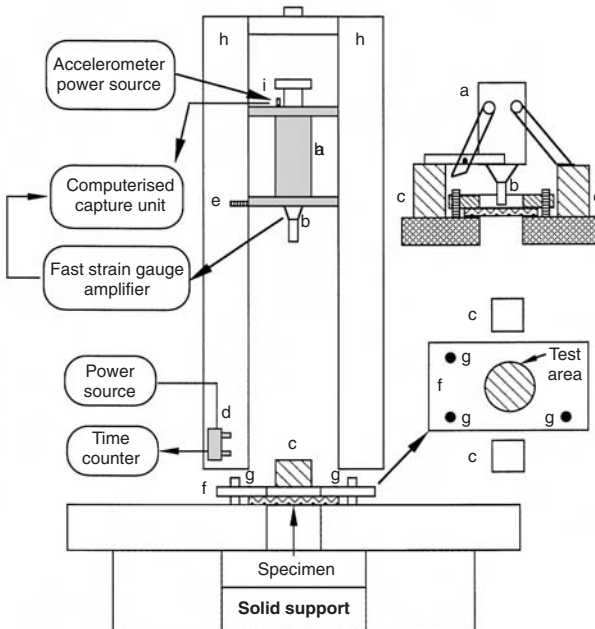
5.2 An experimental setup for drop-weight impact tests (a) impactor (b) strain-gauged load cell (c) rebound catch block (d) photodiodes (e) flag (f) clamping device (g) locking pin (h) drop guide (detached from drop tower) (i) accelerometer.

five additional strain gauges were bonded at locations 50 mm and/or 100 mm away from the central axis in a back-to-back arrangement. The purpose of these was to examine the local and global impact responses in an attempt to understand their interaction and its effect on the extent of damage.

In each test, the specimen was clamped on a rigid circular support of either 100 mm or 500 mm inner diameter. An instrumented impactor of known mass was dropped on to the centre of the specimen within a pair of U-shaped drop guides and its strain-gauged load cell provided an impact force-time history. With known impactor mass and impact velocity two successive integrations of impact force-time history gave impactor velocity and displacement histories from which absorbed energy (AE) history could be established.

As the strain-gauged load cell was calibrated quasi-statically, two checks under impact conditions were conducted to ensure reliability of data. One check was to mount an accelerometer on the impactor, that recorded an independent impact response for direct comparison with the load-cell response. Although the accelerometer was mounted at some distance from the load cell (see Fig. 5.2), the correlation between the two was still very good. The other check was to repeat some of the impact tests in order to verify that the results were repeatable.

5.3.3 Damage examination techniques

These laminates were thick and had some fibre waviness due to the nature of the woven roving fabric. It was therefore quite a challenge to examine the nature of the induced damage. Non-destructive testing (NDT) techniques such as ultrasonic C-scan and X-ray were employed in addition to destructive techniques such as sectioning. The effectiveness of these techniques in the present investigation was very much dependent on the type of damage to be detected. Discussion of a wider range of NDT techniques can be found in Chapter 2.

Matrix cracking and fibre breakage usually occurred on the laminate surfaces either where bending stresses were at a maximum or where there were high local contact stresses. They were easily detected by a visual inspection as the near surface matrix cracking manifested itself in a stress-whitened or discoloured patch.[17,20,41] A cross-sectioning in conjunction with the visual inspection was thus adequate for providing a qualitative and useful description of these damage mechanisms. For an invisible internal delamination, the ultrasonic C-scan became the major interrogation technique and was the only tool for determining quantitatively a 2-dimensional contour or projected area of damage. These areas were in turn used to establish the damage maps (i.e. Figs 5.10(a–b)). Due to a high attenuation of acoustic

energy, the ultrasonic scanning had to be carried out with a low frequency probe (0.5 or 1 MHz) in the through-transmission mode. X-ray radiography was used with dye penetrant injected into a pilot hole but proved to be completely inadequate because the laminates were too thick. A trial with an Andscan (hand-held ultrasonic scanner) proved to be equally unproductive. This is because the laminate surface was very uneven so that a proper coupling between a transducer and the laminate surface was very difficult. This unevenness of the laminate came from the original fibre waviness as well as local impact damage in the vicinity of the contact area.

5.3.4 Quasi-static compression tests of intact and damaged panels

Rectangular compression panels containing damage were extracted from the impacted large circular plates. Intact, i.e. unimpacted, panels of the same size were cut directly from the as-received sheets. The actual choice of the panel dimensions was a compromise between a number of interrelated and sometimes conflicting factors. The most obvious of these was the diameter limitation of the impact specimen, itself controlled by the clamping devices available on the impact apparatus. The compression panel, ideally, should be wide enough to fully contain the largest delamination area obtained in the impact tests. This size was not known at the time the compression specimens were designed. However, the specimens also had to be narrow enough for the thinnest intact panel not to buckle and also for the thickest one to fail at a load level that was within the available capacity of the testing machine. Having taken all these factors into account, the size of rectangular compression panels was chosen to be 350 mm long by 250 mm wide.

In order to avoid end-brooming and to enhance stability, both ends of each compression panel were potted with epoxy and then carefully machined parallel to each other. An anti-buckling support fixture was used to avoid a global buckling of the panel at the initial stage of loading. The central mechanism of the anti-buckling support fixture consists of two pairs of simple movable steel plates with a cylindrical edge on the contact side, as shown schematically in Fig. 5.3(a). These two pairs of plates were oriented so as to be normal to the panel surfaces and were parallel to the loading direction. The pairs were 180 mm apart and the plates finished 5 mm short of the end pots at each end to allow for panel compression, as shown in Fig. 5.3(b). Bolts on the support fixture drove the support plates against the panel surfaces and were finger-tightened only in each test. Loading was directly introduced to both ends of the panel through the 250-ton panel tester at a constant speed of 1 mm/min.
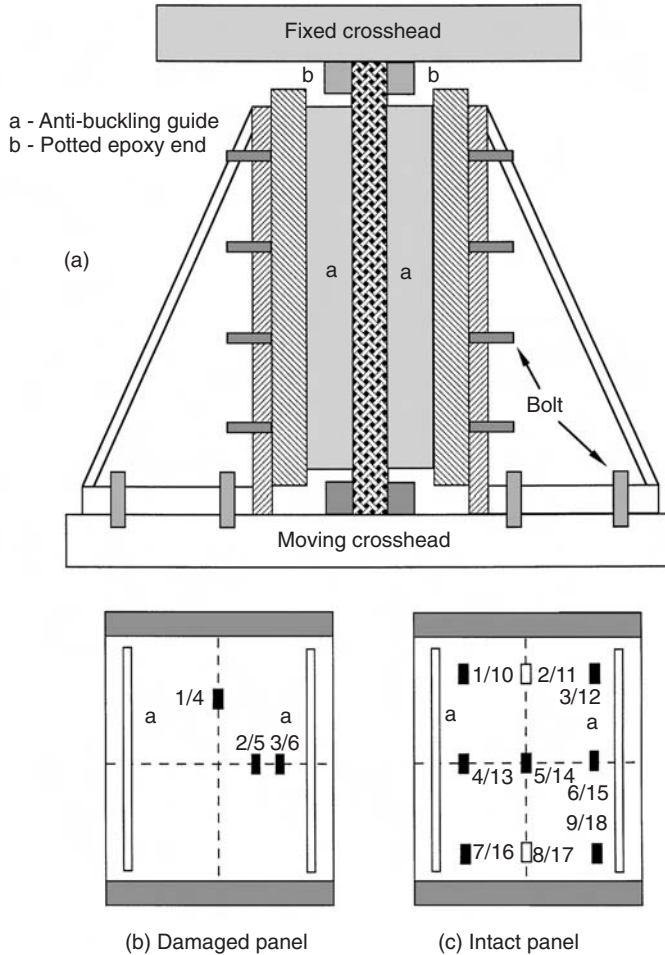
5.3 (a) An experimental setup for in-plane compression tests of composite panels. (b) Strain gauge locations on a damaged panel. (c) Strain gauge locations on an intact panel.

In order to examine the compressive behaviour of the panel, back-to-back strain gauges were bonded to a number of locations. For intact panels, at least seven pairs of strain gauges were bonded across the panel width as shown in Fig. 5.3(c) (the two open rectangles were used in one test), whereas for damaged panels, three pairs were used as shown in Fig. 5.3(b). The 1/4 pair on the longitudinal symmetry axis was used to monitor the global response of the panel (far-field strains). The 2/5 and 3/6 pairs on the horizontal symmetry axis were used to monitor local instability or the side-

ways propagation of delamination. In addition, two LVDTs were used to measure both end shortening and lateral deflection on the distal surface of some damaged panels, where there was no fibre breakage.

5.4   Impact damage resistance

Since the state of damage is very critical to the strength retention factor as discussed in Section 5.1, it is very important to understand how impact parameters, like loading rate and geometry, affect the initiation and propagation of damage as well as the characteristics of the energy-absorbing process. In addition, the effectiveness of measures of damage used in the conventional damage tolerance assessment could depend on the nature of the damage mechanisms. Furthermore, the impact force data-based approach[50–51] for damage tolerance assessment is very much dependent on a thorough understanding of the effect of damage on impact response during loading. Therefore, it is crucial for these issues to be addressed now, before proceeding to damage tolerance assessment.

It is helpful at this point to recap the essence of IDR. For low-velocity impact with a non-deformable impactor, IDR under the given impact conditions is generally defined by a threshold value of IKE, absorbed energy, or impact force at which an appreciable damage sets in. What this entails would be straightforward if the onset of damage in the laminate coincided with the ultimate failure which is usually indicated by fibre breakage. However, since delamination in the present case took place at a much lower load than fibre breakage, its subsequent propagation, potentially occurring before fibre breakage, could absorb an additional amount of the IKE. This has not been addressed in the study of IDR.

5.4.1   Impact response and dominant damage mechanisms

5.4.1.1   Impact response

Although the impact responses of the laminate specimens with different geometry were very different in fine details in terms of the magnitude of maximum impact force, impact duration and energy absorption, some features were common throughout. These features can be observed from a sequence of impact response curves with increasing IKE, shown in Figs 5.4(a–c), which were obtained from the 14 mm thick small S-glass/phenolic plates. (Similar sequences can be found in for the 19 mm thick S-glass/phenolic plates,[20,21] and[37] for the 10 mm and 25 mm thick E-glass/polyester plates, respectively.[21,37]) Obviously, when impacted at a relatively low IKE of 23 J in the present case, the laminate plate was not damaged and thus its
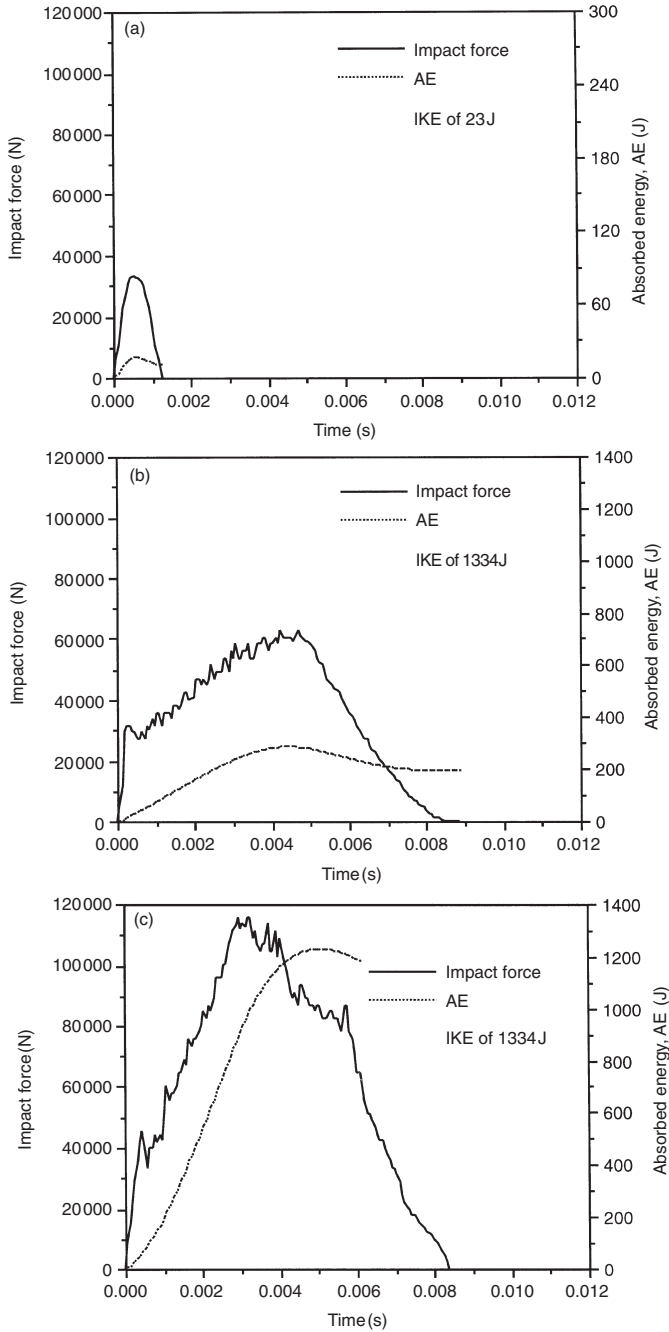
5.4(a–c) Impact force and AE histories for 14 mm thick S-glass/phenolic plates.

impact response was like half a sine wave, as seen in Fig. 5.4(a). When the given IKE was more than a certain value, delamination was initiated, and was accompanied by a rapid load drop (see Fig. 5.4(b)). Its further propagation dissipated most of the remaining absorbed energy (AE) and appears as reduced stiffness and ripples in the force-time curve. If the prescribed IKE was sufficiently high so that the local shear stress under impactor exceeded the shear strength of the laminate plate, shear-out of the top ply would occur. This shearing action through the plate thickness placed an upper limit on the laminate load-bearing capability and was manifested in a final load drop at the peak of the impact force-time curve, as seen in Fig. 5.4(c). This is the measure of the ultimate IDR under the present impact conditions. With practice, the occurrence of delamination and ply shear-out in these curves is fairly easy to identify.

The foregoing impact force-time curves were derived from the small plates with plate radius-to-thickness ratio of 3.6. As mentioned earlier, the characteristics of an impact response were expected to be affected by the plate radius-to-thickness ratio. In practice, the principal characteristics of the impact response from composite plates with similar small radius-to-thickness ratios (say 2–5) were very similar qualitatively. For the large plates with the radius-to-thickness ratio of 10–25, plate deflections generally exceeded respective plate thicknesses and then the contribution of membrane effect to the impact response increased significantly. Consequently, the interaction of local indentation and global deflection in these large plates became important to the development of damage. Unfortunately, the amount of oscillation (ringing) that accompanied the response also increased so that it usually masked the signal structure arising from the occurrence of damage. Therefore, an examination of impact strain response curves became necessary and was expected to shed some light on this aspect.

Typical impact strain-time and impact force-time curves are presented in Fig. 5.5. The maximum tensile strain gauge (T1) in the diagram shows a similar initial response to the force but with a flatter peak. Its slower recovery after the peak was expected because of permanent damage at the end of the event. Moreover, the response of two off-axis strain gauges (C1 and T2) along with the T1 highlights an important additional feature as schematically presented in Fig. 5.6. In this figure, the insert indicates three characteristic times during impact loading, designated t_1, t_2 and t_3. Up to the time t_1, the C1 strain gauge reached its peak in compression and the T2 strain gauge remained zero while the T1 strain gauge reached about 0.3% of strain. This indicates that the initial plate bending response was very localised. Beyond the time t_1, C1 started decreasing while T2 started increasing. T1 continued to increase but with reduced stiffness, which was reminiscent of the 'knee-effect' as mentioned in Section 5.2.2. At the time t_2 and
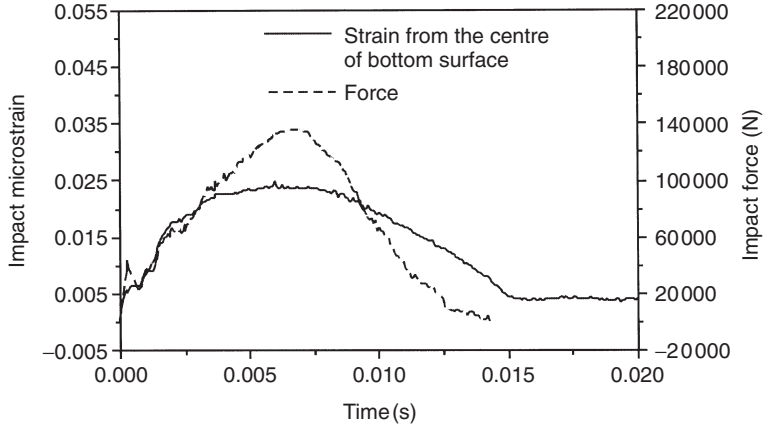
5.5 Impact strain and force histories for a 19 mm thick S-glass/phenolic plate with IKE of 2001 J.
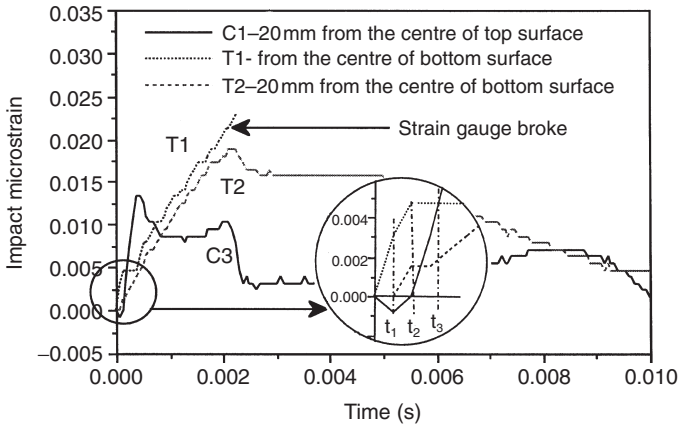
5.6 Impact strain histories for a 19 mm thick small S-glass/phenolic plate.

beyond, C1 switched its response from compression to tension after the onset of delamination and thus all the strain gauges showed tensile response. This compression-to-tension switching strongly suggests an increased contribution of membrane effect to a global response. This phenomenon has been fully explored in thin carbon/epoxy plates under quasi-static loading.[36] Moreover, as loading proceeded beyond t_3 and the following 0.5 ms, the tensile strain on the loading surface became greater than that of the distal surface, which indicates clearly an increase in local indentation.

Stage I: $F_{max} < F_i$

Stage II-1: $F_{max} = F_i$

Stage II-2: $F_{ult} > F_{max} > F_i$

Stage III-1: $F_{ult} = F_{max} > F_i$

Stage III-2: $F_{ult} < F_{max}$

(a)   (b)   (c)
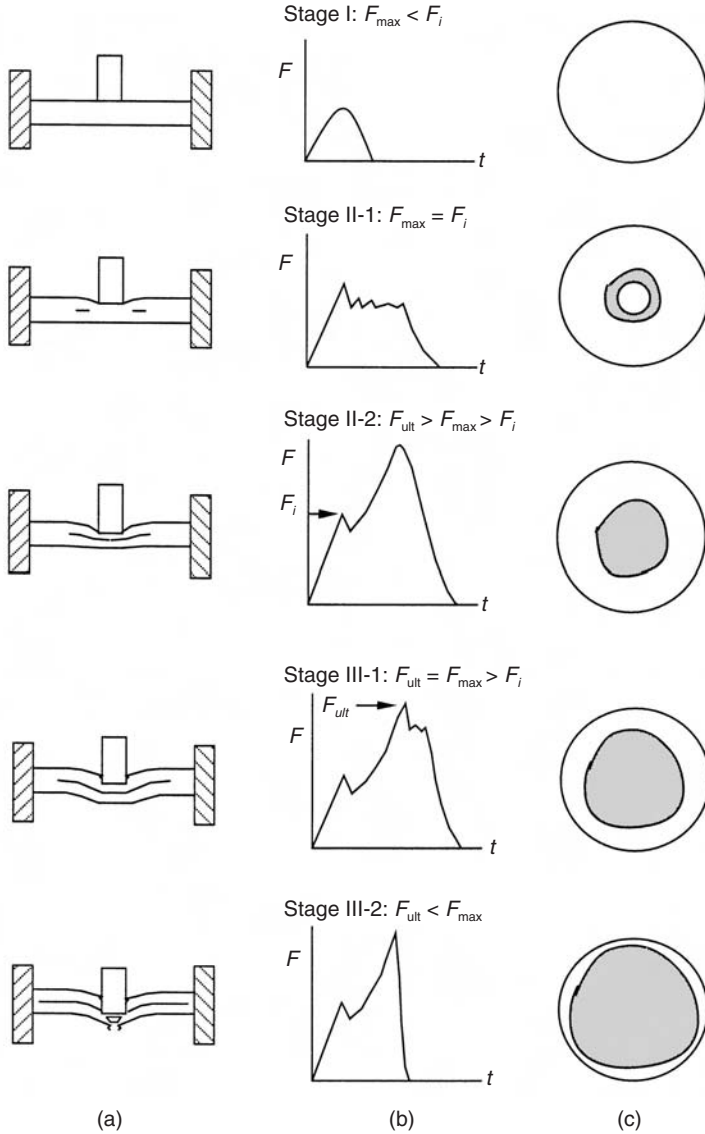
5.7 Three-stage damage sequence in thick laminate plates under low-velocity impact described by (a) deformation sketches, (b) impact response curves and (c) C-scan graphs.

If a greater IKE was supplied, the top ply right underneath the impactor would be sheared through when the plate reached the maximum bending, as discussed earlier on the small plates and illustrated in Fig. 5.7. Because of this membrane stretching, the impacted large plates have shown much

Table 5.2. Geometric effects on impact load-bearing capabilities of laminated composites

Material	Laminate thickness (mm)	Impact force small plate (kN)	Impact force large plate (kN)	Percentage increase (%)
E-glass/polyester	10	61 ± 1	92	51
	25	124 ± 6	144	16
Increased by	150%	103%	57%	
S-glass/phenolic	14	117 ± 1	157	34
	19	146 ± 2	164	12
Increased by	36%	25%	5%	

greater load-bearing capability than the small plates as will be seen from Table 5.2.

5.4.1.2   Dominant damage mechanisms

The use of the experimental techniques and processes described in Section 5.3.3 revealed that there were four types of damage mechanisms, on a macroscopic scale, operating during impact loading: matrix cracking, delamination, ply shear-out and fibre fracture. These failure modes would occur when stresses had exceeded the relevant strength values of the material. As these failure modes corresponded to strengths of very different magnitudes, they would be likely to occur sequentially and fibre breakage occurred only when a high IKE was provided. For example, matrix cracking usually took place first because its tensile strength in the region of 40–90 MPa was the lowest and this was followed by delamination because of its low ILS strength, as shown in Fig. 5.4(b–c). Obviously, the damage mechanism such as matrix cracking dominated only at the lower end of the IKE spectrum. The other damage mechanisms were dominant at the central region and the upper end of the spectrum. Of course, the perforation of the laminate plates occurred at the upper end. In most of the impact and quasi-static tests, delamination and ply shear-out were the two dominant damage mechanisms.

   In order to ascertain these observations, extensive cross examination was carried out involving ultrasonic C-scanning, cross-sectioning and the use of impact force-time and/or quasi-static load-strain curves. Additional diagnostic impact as well as quasi-static tests on the small specimens were also conducted at several selected IKE levels aiming at generating the maximum forces slightly below and above the thresholds as identified previously. All
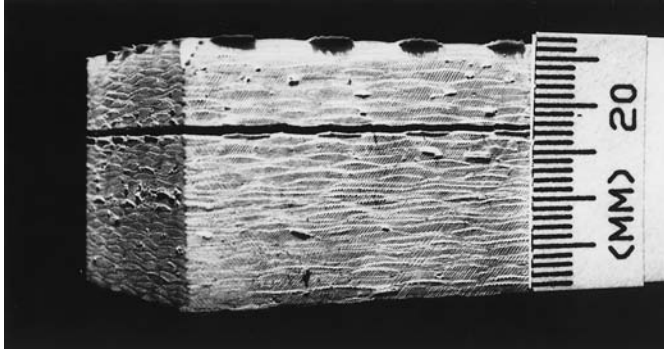
5.8 A through-the-thickness view of a single delamination in a 25 mm thick impacted E-glass/polyester panel (cut for CAI test).

these painstaking efforts[19–21] have confirmed the following failure sequence for both composite systems, which is illustrated schematically in Fig. 5.7(a–d). Localised matrix cracking occurred in the contact area before the onset of delamination but it was insufficient to have a noticeable effect on the impact response curves. The initial load drop as indicated in Fig. 5.4(b–c) was caused by the onset of delamination and the final load drop in Fig. 5.4(c) corresponded to ply shear-out. After this load drop, shearing of plies continued through the thickness resulting in the growth of a truncated cone of sheared-out material. Ultimately this cone forced the remaining plies, close to the distal face, to fracture with an explosive bang as illustrated at the bottom of Fig. 5.7(a). The sequence of damage development is similar to observations on various CFRPs, reported in[22–27] though some authors presented only quasi-static load-displacement curves.

Because of the nature of woven roving reinforcement in a single ply, the current thick laminates were more likely to have a single delamination than those made of unidirectional prepregs, especially when impacted at low up to medium level of IKE. Such a single delamination usually occurred between one-quarter and three-quarters of the way through the laminate thickness as shown in a photograph taken from a sectioned impacted specimen in Fig. 5.8. Moreover, the projected contour of the delamination was usually close to a circle as a C-scan graph in Fig. 5.9 shows, though the difference of ILS strengths between the warp and the fill direction was around 20%. Obviously, at high IKE more than one delamination could be generated (see Fig. 5.26(a–b)), especially when the IKE was sufficient to induce ply shear-out. The through-thickness distribution of delamination was not investigated in all cases, but it is thought that a single, nearly circular delamination was the normal form of damage, at least in the early
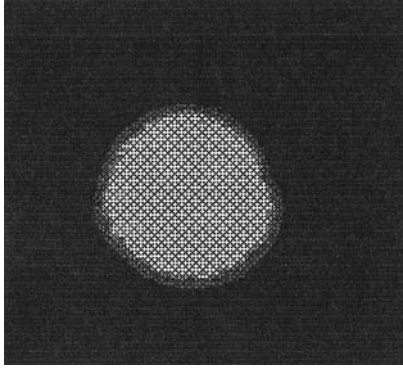
5.9 A C-scan graph showing a delamination in a 14 mm thick impacted S-glass/phenolic panel.

stages of the impact. In some thin UD-based quasi-isotropic carbon/epoxy laminates, it was often reported[28–30] that a projected delamination of a nearly circular shape was due to an overlapping of multiple 'peanut-shaped' delaminations of similar sizes. This morphology results from the tendency of UD composites to delaminate along fibre directions, which seems not to apply to the woven rovings in the present investigation.

Therefore, for the dominant damage mechanisms identified above, IDR comprises two separate elements: the resistance to the onset of delamination and its subsequent propagation and the resistance to ply shear-out or ultimate failure. In particular, resistance to delamination propagation in terms of IKE, as presented in Figs 5.10(a–b), is very much desired in the conventional impact damage tolerance assessment, as will be discussed in Section 5.5.4.

5.4.2 Effects of other parameters on impact damage resistance

Since both composite systems could be strain-rate sensitive even at low impact velocities, the loading rate in addition to laminate geometry may affect the nature of the damage and thus the damage tolerance. Therefore the effect of varying these parameters on damage must be understood in terms of IKE, impact force and absorbed energy. Because of the different thicknesses used for the different composite systems, a direct comparison between them remains qualitative. Discussion on the strain-rate effect under high impact velocities is available in Chapter 3.
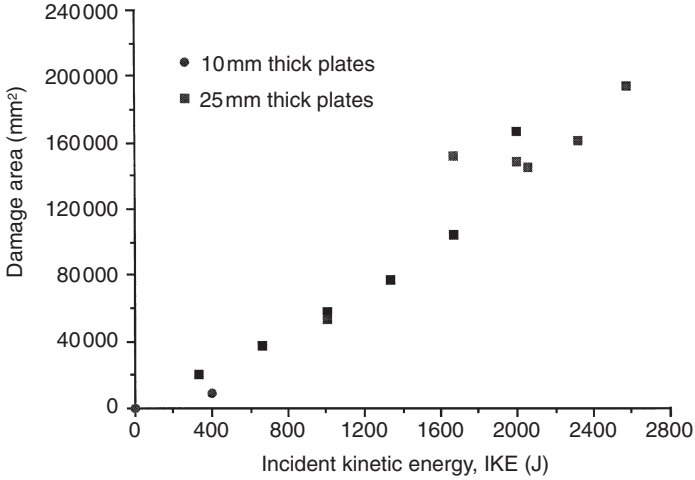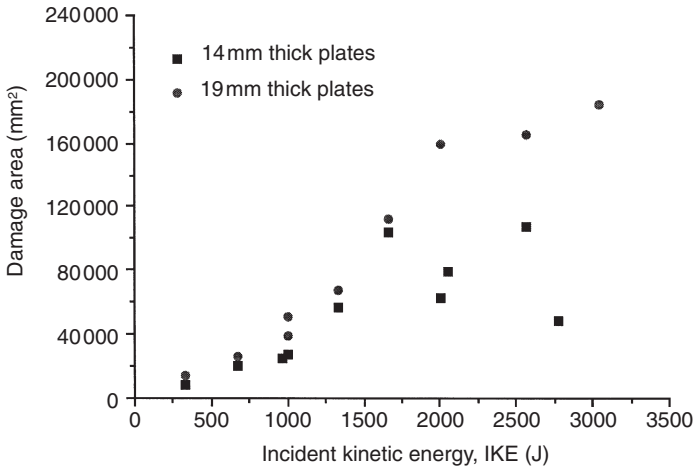
5.10 (a) Damage area as a function of IKE for E-glass/polyester plates.
(b) Damage area as a function of IKE for S-glass/phenolic plates.

5.4.2.1   Loading rate effect

The effect of loading rate on damage was examined phenomenologically in two ways. One was to examine the variation of impactor mass (inertia) with impact velocity being kept constant; the other was to examine the variation of impact velocity by using the same impactor. The former has been neglected in most low-velocity impact investigations either due possibly to assumption that inertia effect plays no part in low-velocity impact or possibly because it is just easier to ignore it. The inertia effect examined
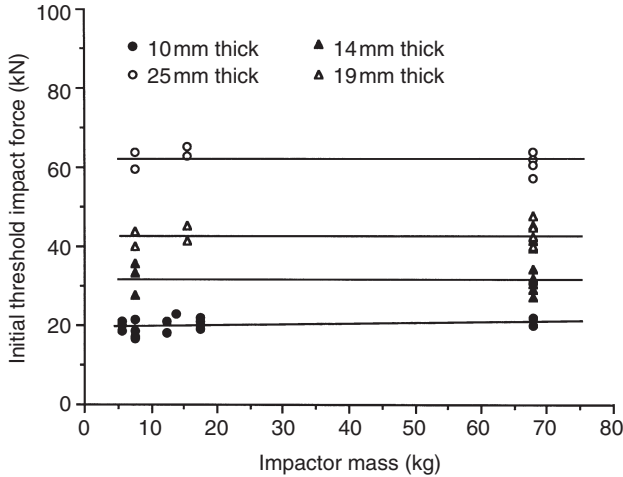
5.11 Initial threshold impact forces as a function of impactor mass for small E-glass/polyester and S-glass/phenolic plates.

here addressed half the problem as it arose only from the variation of impactor mass. The mass of the laminate plate during impact was not directly studied.

Figure 5.11 presents the variation with impactor mass of the threshold forces corresponding to the onset of delamination for both composite systems. In this diagram, a higher impact force at specific impact mass corresponds to a higher impact velocity (thus IKE). It seems to show that the force at the onset of delamination was independent of impactor mass for both composite systems irrespective of laminate thickness, even when impactor mass was increased by nearly nine times. This finding seems also in accordance with one of the analytical predictions given.[30] The inertia effect on delamination propagation was examined by increasing impactor mass while keeping impact velocity constant. As seen in Fig. 5.12, the growth of delamination area was sensitively related to an increase of impactor mass (and hence IKE) for both composite systems. Since IKE also increased with impactor mass in Fig. 5.12, this inertia effect on delamination area is further examined later by varying impactor mass and impact velocity simultaneously with IKE being kept constant.

The effect of impact velocity on resistance to specific damage mechanisms has been examined using two methods.[31] The effect was examined, in addition to the usual method in which impact velocity is varied, by directly comparing impact data with quasi-static. For delamination propagation, the examination procedure was quite involved as will be explained later. For the onset of delamination and ply shear-out, direct comparisons of the
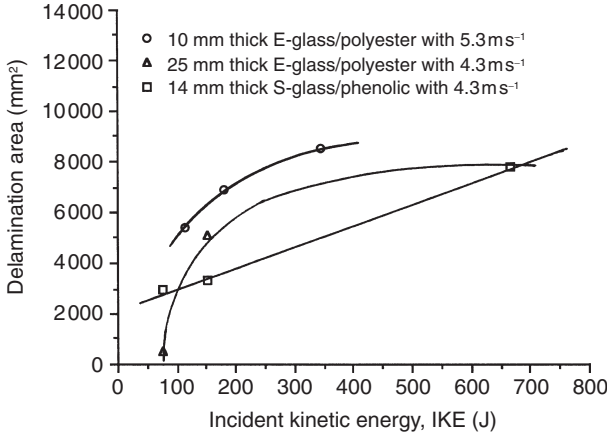
5.12 Delamination areas as a function of IKE with constant impact velocity for large laminate plates.
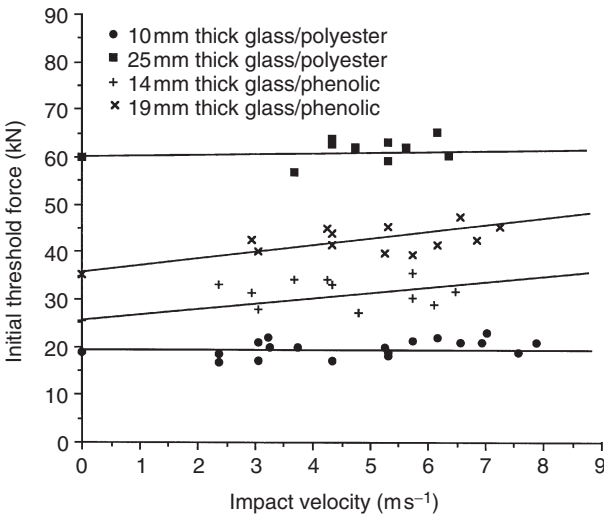
5.13 Initial threshold force for the onset of delamination as a function of impact velocity.

threshold forces were made between quasi-static and impact cases. In Fig. 5.13, both the quasi-static and impact threshold forces corresponding to the onset of delamination are plotted against velocity, which was varied from $8.3 \times 10^{-5}\,\mathrm{ms^{-1}}$ (i.e. 5 mm/min) to $8\,\mathrm{ms^{-1}}$. It can be observed that the E-glass/polyester system seemed to be independent of impact velocity irre-
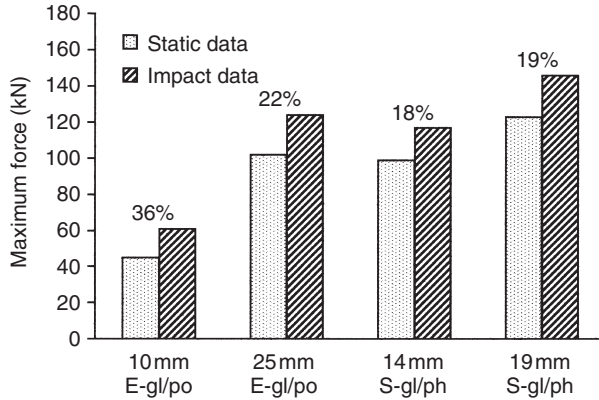
5.14 Comparison of load-bearing capabilities of small plates subjected to static and impact loadings.
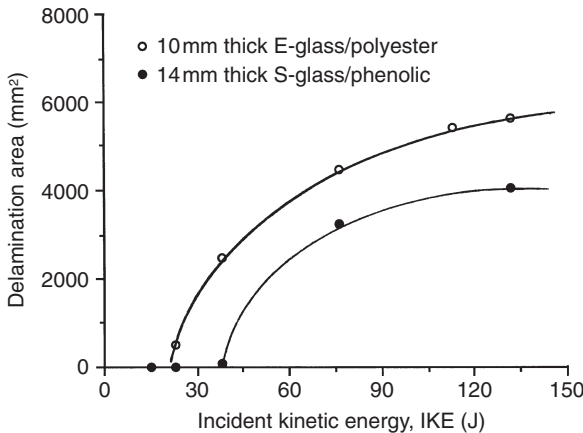
5.15 Delamination areas as a function of IKE with constant impactor mass of 8 kg.

spective of laminate thickness. However, the S-glass/phenolic system did show a modest increase in the threshold forces (over 20%) for both thicknesses with reference to the quasi-static values. For ply shear-out or laminate load-bearing capability, the results as summarised in Fig. 5.14 show that the effect of impact velocity was significant for the E-glass/polyester and was modest for the S-glass/phenolic.

The effect of impact velocity on delamination propagation was examined with a constant impactor mass and the results are shown in Fig. 5.15. There, delamination area is seen to increase with impact velocity and thus IKE, as

(a)

(b)
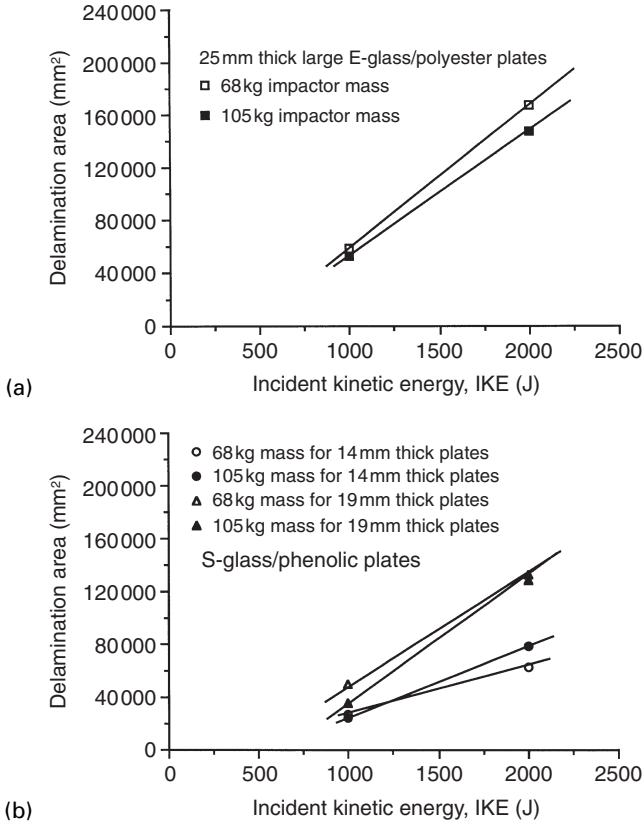
5.16 (a) and (b) Delamination areas as a function of two combinations of impactor mass and impact velocity for identical IKE.

expected. In order to separate out the effects of velocity, inertia and energy, it was also necessary to vary both impact velocity and impactor mass simultaneously while IKE was kept constant. In some cases appreciable variation of delamination area can occur.[31] However, in the present investigation, as shown in Fig. 5.16(a–b), differences in delamination area produced in this way were small. In conjunction with the results in Fig. 5.12–15, this could be attributed to one of the following two reasons. One is that the 20% variation of impact velocity associated with a change of impactor mass from 68 kg to 105 kg was insufficient due to the physical constraints of the present drop-weight impact rig. The other is that, for an identical IKE, the effect of impact velocity on delamination propagation was likely to cancel out the inertia effect. That is, increasing impact velocity while holding impactor
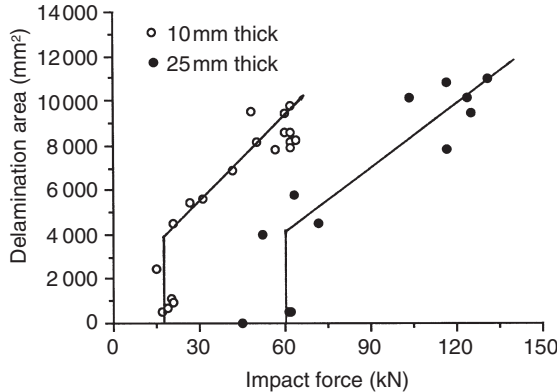
5.17 Delamination area as a function of impact force for small
E-glass/polyester plates.

mass constant may have produced a trend of delamination areas similar to that caused by increasing impactor mass while holding impact velocity constant. Consequently, the net effect caused by these combinations on delamination area for identical IKE would be small.

5.4.2.2 Laminate thickness effect

In the present impact tests, the geometry of the laminate plates was varied to allow an examination of its effect on impact response and IDR over a large range of IKE for each composite system. The test results are summarised in Table 5.2 which shows clearly that, for specimens of a constant diameter, the impact resistance to ply shear-out increased with an increase of thickness as expected for both composite systems.

In Fig. 5.13, the impact resistance to the onset of delamination increased by 216% with a thickness increase of 150% for small E-glass/polyester plates. For small S-glass/phenolic plates, a smaller increase of 36% in impact resistance was observed which was identical to the increase in thickness (36%). This appears to be independent of impact velocity. In Fig. 5.17, the thicker E-glass/polyester plates are seen to provide the greater impact resistance to delamination propagation for the same delamination area. In other words, for identical impact force, the delamination areas of the thicker plates were much smaller than those of the thin ones. Obviously, the penalty paid for this superior impact resistance was 150% weight increase. For S-glass/phenolic plates, however, there was little difference in the impact resistance to delamination propagation irrespective of plate diameter, as seen in Fig. 5.18(a–b). Interestingly, the resistance of this material to delamina-

(a)

(b)
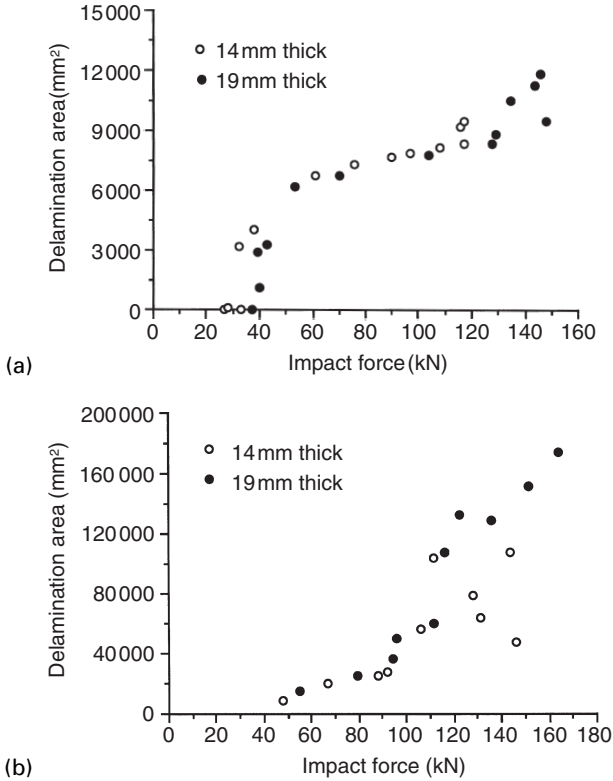
5.18 (a) Delamination areas as a function of impact force for small S-glass/phenolic plates. (b) Delamination areas as a function of impact force for large S-glass/phenolic plates.

tion propagation, if measured by IKE, seemed to become lower for the thicker plates, as shown in Fig. 5.10(b).

5.4.2.3   Plate diameter effect

Exploring the effect of plate diameter[32] is possibly of greater practical importance than that of thickness. A realistic thickness is easily obtained in laboratory conditions for most full-scale composite structures. On the other hand, the in-plane dimensions of real structures normally need to be scaled down for test specimens. Scaling in impact testing is discussed elsewhere.[32] A more general discussion is available, and[33] relevant quasi-static data can also be found.[34–36]

When the diameter of a laminate plate was increased from 100 mm to 500 mm, the increased membrane stretching was expected to contribute to IDR, especially in the relatively thin plates. In Table 5.2, the laminate load-bearing capabilities are clearly seen to increase rather than decrease as predicted by the static plate theory, while other experimental data based on carbon/epoxy plates[34–36] have shown insensitivity to a change in plate diameter. The present dynamic enhancement of load-bearing capability was believed to be due to a change in the state of three-dimensional stresses in the contact area. This resulted from a significant contribution of membrane stretching to the in-plane stress components, manifested in part by the compression-to-tension switching of an impact strain gauge response in Fig. 5.6. The effect of this appears to be either a reduction in the local shear stress component which was responsible for ply shear-out, or possibly an increase in effective strength resulting from the triaxial stresses. Obviously, the thicker a laminate plate became, the less significant this enhancement would be, as shown in the table.

Although an increase in plate diameter increased the degree of membrane stretching in the plate behaviour, it did not seem to affect the threshold forces corresponding to the onset of delamination[17,27] and thus not the initial impact resistance. Moreover, the size of delamination areas from the small plates did not overlap in any way with that of the large plates, so unfortunately direct comparison of their impact resistance to delamination propagation was not feasible.

5.4.3 Energy-absorbing characteristics of damage mechanisms

It was very likely that the damage mechanisms absorbing more IKE (such as delamination) had a greater effect on IDR and thus on damage tolerance. The onset of delamination was an unstable process associated with the sudden load drop and the jump in delamination area as described in Figs 5.17 and 5.18(a). Its subsequent propagation has been identified as the primary energy-absorbing damage mechanism. It appears to be a more desirable failure mode than ply shear-out, which could potentially lead to the plate perforation as illustrated in Fig. 5.19. In other words, the most effective process for completely absorbing a specified IKE in an impact event was through delamination propagation (OABCD) before the load-bearing capability was reached (at C or B′). This was preferable to absorbing the energy by fibre fracture (OAB′C′), because more energy is absorbed and the delaminated plate still possessed a considerable amount of residual load-bearing capability as will be discussed later. It is not difficult to see that the region CDC′E ought to be much greater than the region AB′EB, although the position of C′ is speculative. In Fig. 5.20(a–b) which sum-
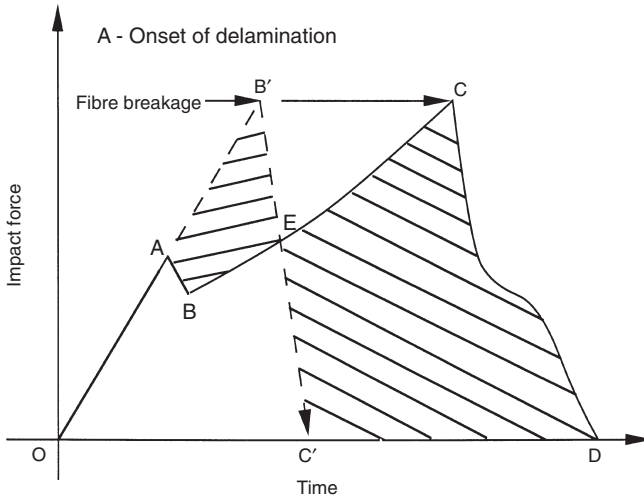
5.19 Illustration of energy absorption with and without delamination.

marises the results of groups of impact tests, the IDR corresponding to delamination propagation increased nearly linearly with an increase of energy absorption (AE). When ply shear-out occurred, the IDR started to level off so that some of the IKE was absorbed by continued ply shear-out.

It was shown that,[37] when ply shear-out did not occur, an amount of AE (E_{AE}) could be expressed by

$$E_{IKE} - E_R = E_{AE} = E_{mc} + E_{od} + E_{pd} = E_{mc} + G_{IIc}A \qquad [5.1]$$

in which E_R is rebound energy, E_{mc}, E_{od}, and E_{pd} denote an amount of AE from localised matrix cracking, onset of delamination, propagation of delamination, G_{IIc} is mode-II strain energy release rate and A is delamination area with the assumption of a single delamination. If rebound velocity in an impact test was measured so that E_R as well as E_{IKE} (IKE) were known, the corresponding delamination area would be approximately estimated providing that G_{IIc} was available and E_{mc} was negligible. In the present case with $G_{IIc} = 4.2\,kJ/m^2$ and $3.8\,kJ/m^2$ for the E-glass/polyester and S-glass/phenolic systems, respectively, the predictions of equation [5.1] are demonstrated in Fig. 5.20(a–b) with arbitrary E_{mc} as the latter was believed to be small and was impossible to quantify under the present impact conditions. When delamination areas were less than three-quarters of the small plate area, the predicted overall trends agreed reasonably well with the experimental data for both composite systems. An additional interesting feature was the effect of varying thickness on the relationship between delamination propagation and absorbed energy. For a given plate
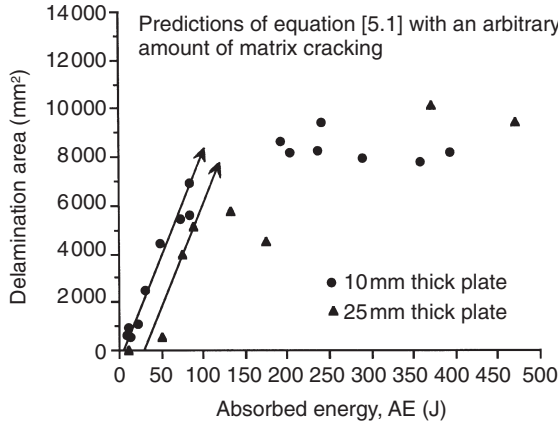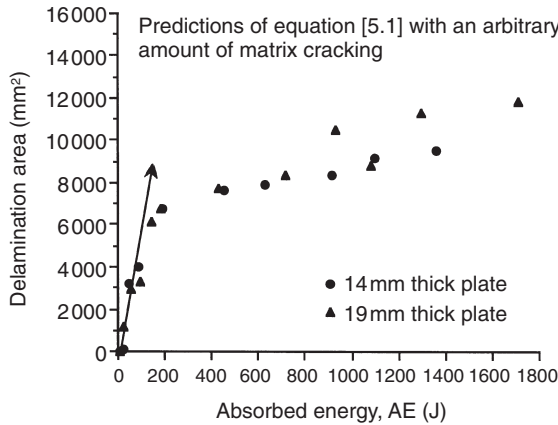
5.20 (a) Delamination area as a function of AE for small E-glass/polyester plates. (b) Delamination area as a function of AE for small S-glass/phenolic plates.

diameter, delamination area seemed to decrease with increasing laminate thickness for identical AE. This suggested that some of the IKE in the thicker laminate was dissipated in other deformation mechanisms so that not all the IKE was absorbed in initiating and propagating delamination.

A detailed discussion for the effect of G_{IIc} on energy absorption is available in Chapter 1.

5.5   Impact damage tolerance and assessment
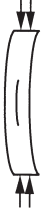
Naturally, for in-service load-bearing composite structures which also have a high risk of impact load, their damage tolerance holds the key to success.

The essence of damage tolerance is that the damaged composite structures are still capable of providing the desired performance, as defined by a set of mechanical requirements. As discussed in Section 5.1, the main measure of impact damage tolerance is the retention rate of compressive strength relative to the strength of the intact composite structure. The energy-based IDR alone provides only limited information. For a general damage tolerant structural design philosophy, see Chapter 4.

5.5.1 Compressive behaviour of intact and damaged panels

In-plane compressive strength and stiffness were determined by testing rectangular panels quasi-statically. Generally, either damaged or intact panels needed to be supported laterally by using the anti-buckling device as described in Section 5.3.4 to avoid a premature buckling. The back-to-back strain gauges were bonded at a number of selected locations and an examination of their responses provided an important physical insight into the development of panel deformation mechanisms leading to ultimate failure. For intact panels, at least seven pairs of strain gauges were bonded across the panel width with one row (either two or three pairs per row) close to each end and one on the middle section. For damaged panels, three pairs were used, as shown in Fig. 5.3(b–c). The gauge response in terms of bending strain (i.e. difference between gauges on opposite sides of the panel at the same point) and mean strains was used to characterise panel behaviour. A positive panel bending strain here means that a panel buckles towards the distal surface while a negative panel bending strain corresponds to buckling toward the impact surface. The mean strain is relatively small if buckling occurs and is relatively large if delamination opening occurs. Equipped with this understanding, four major deformation mechanisms were identified in the compression of the present panels as illustrated in Fig. 5.21.[38]

Typical load-panel bending strain and load-mean strain curves are shown in Fig. 5.22(a–b) from a damaged 10 mm thick E-glass/polyester panel. Assuming a circular shape (as can be seen in Fig. 6 of Zhou[17]), the delamination area of 8961 mm^2 was converted to a circle of 107 mm in diameter as shown in the inset of Fig. 5.22(a). Examining the 1/4 pair of strain gauges indicates that global buckling did not occur as the panel bending strain remained more or less zero until the ultimate failure was approached. Also, the fact that both panel bending and mean strains for the 2/5 pair were relatively large suggested that local buckling and delamination opening could have occurred simultaneously (case (2) in Fig. 5.21). The response of the 3/6 pair shows the similar behaviour to that of the 1/4 pair. The continuing local buckling eventually led to compression failure with a kink shear band as a photograph in Fig. 5.23 shows. This development must have been assisted

	Pair 1/4		Pair 2/5		Pair 3/6	
	Bending strain	Mean strain	Bending strain	Mean strain	Bending strain	Mean strain

(1) Euler buckling

Large Small   Large Small   Large Small

(2) Delamination opening

Small Large   Small Large   Small Large

(3) Global-local mechanism

Large Small   Large Small   Large Small

(4) Compression with kink shear band

Small Large   Small Large   Small Large

5.21 Illustration of failure mechanisms of damaged panels in CAI tests with back-to-back strain gauges.
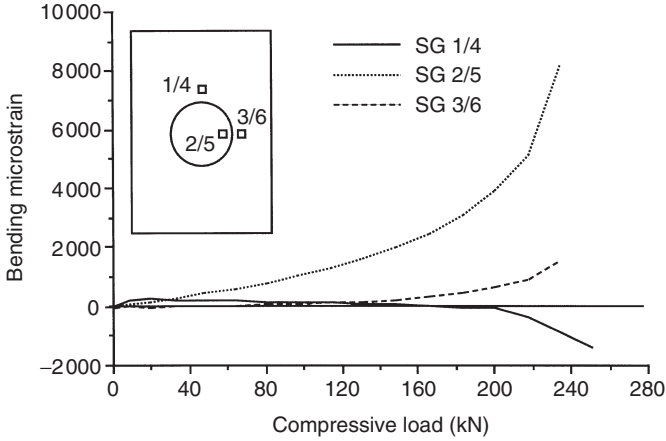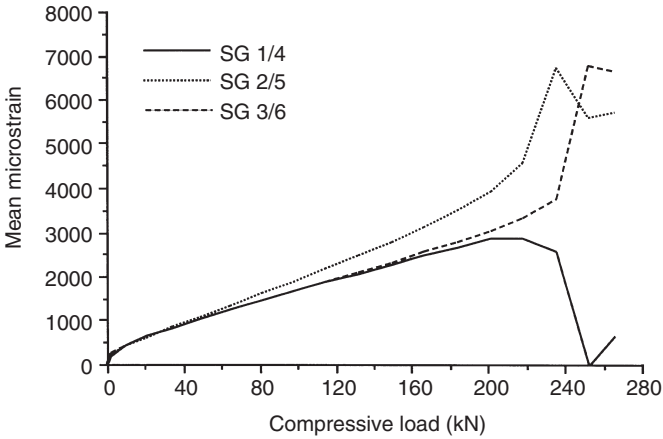
5.22 (a) Compressive load-bending strain curves of a 10 mm thick damaged E-glass/polyester panel. (b) Compressive load-mean strain curves of a 10 mm thick damaged E-glass/polyester panel.

by the presence of the increased curvature of local fibres which made the damaged panel unsymmetrical locally thereby favouring local buckling. Sideways propagation of delamination was not very noticeable, but this may have been due to the fact that the orientation of the 2/5 and 3/6 pairs of the strain gauges was in the loading direction. With the benefit of hindsight, it may be speculated that additional strain gauges in the direction of the panel width could have been more useful for detecting width-wise delamination growth.

In Fig. 5.24(a–b) from a damaged 14 mm thick S-glass/phenolic panel, some global buckling is visible though the response of all the strain gauges
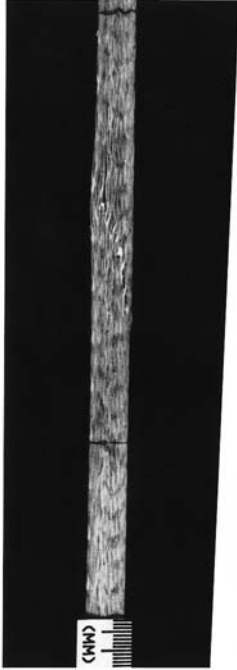
5.23 Compression failure with a kink shear band in a 10 mm thick E-glass/polyester CAI panel.

5.25 Compression failure with a kink shear band in a 14 mm thick S-glass/phenolic CAI panel.
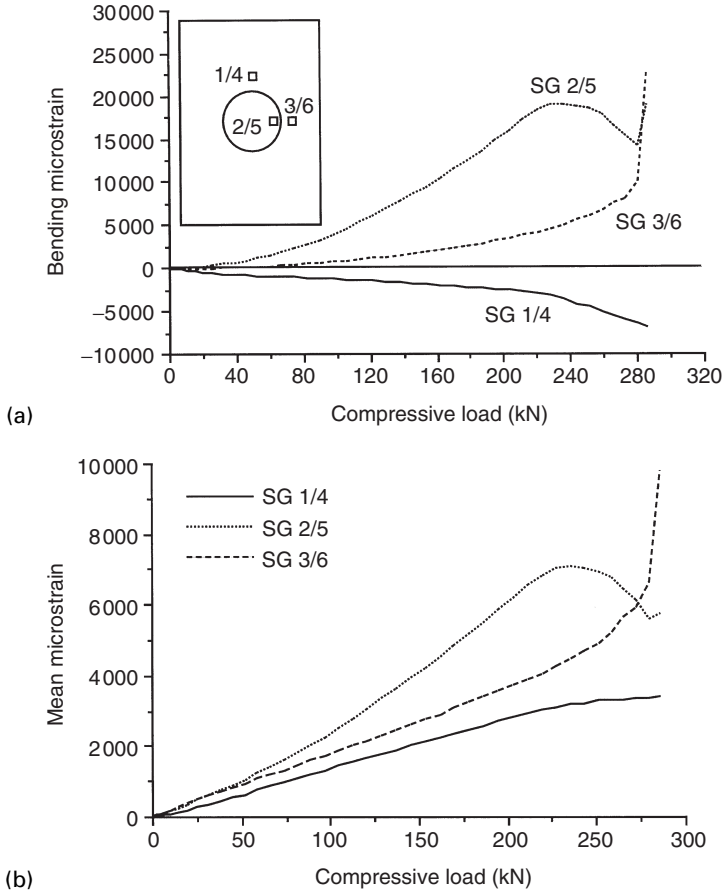
5.24 (a) Compressive load-bending strain curves of a 14 mm thick damaged S-glass/phenolic panel. (b) Compressive load-mean strain curves of a 14 mm thick damaged S-glass/phenolic panel.

was similar. Judging from the developing trend of the 2/5 and 3/6 pairs, local buckling and delamination opening again occurred simultaneously. The final panel failure is shown in Fig. 5.25 with a clear kink shear band. This in conjunction with all three pairs of strain gauge readings suggested that the damaged panel twisted during loading in the form of the second buckling mode.

Photographs in Fig. 5.26(a–b) show typical failed thicker damaged panels for both E-glass/polyester and S-glass/phenolic laminates. The only difference is that these thicker panels had multiple delaminations so that each sublaminate failed in compression through its own kink shear band. Therefore, the adjacent shear bands with often different orientations coalesced

(a)   (b)
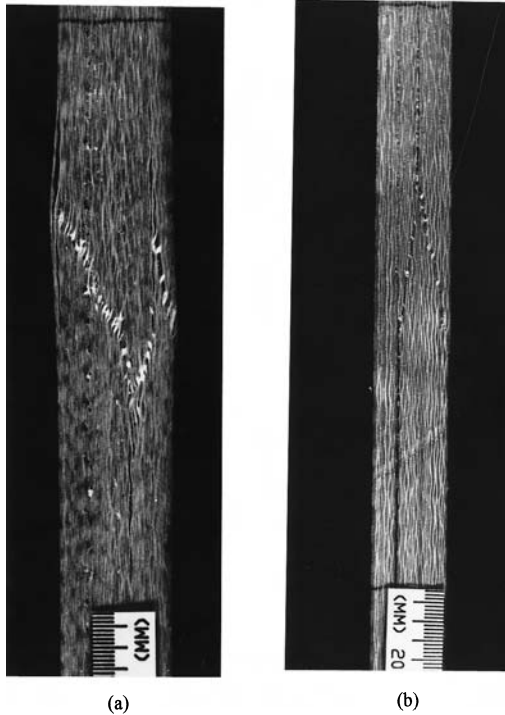
5.26 Compression failure with a kink shear band in (a) a 25 mm thick
     E-glass/polyester and (b) a 19 mm thick S-glass/phenolic CAI
     panels.

to form a saw-tooth shaped failure zone through the thickness. Other
noticeable features are that the E-glass/polyester panel had a much greater
shear angle formed between the loading direction and major kink band
than the S-glass/phenolic panel. Also that the kink band was more jagged
in the E-glass/polyester than in the S-glass/phenolic, possibly due to a
stronger fibre/matrix interfacial bonding. As a whole, it seemed that com-
pression failure with a kink shear band was predominant in the tests of the
damaged panels.

   Ideally, both the intact and damaged compressive strengths used to cal-
culate strength retention factor ought to be measured from panels which
fail by similar mechanisms or at least at the middle section. Although the
present damaged panels indeed failed consistently at the middle section
with the combined mechanism of local buckling and shear as demonstrated,
the intact panels always failed close to one end as shown in Fig. 5.27(a–b).
Therefore the use of the compressive strengths from the intact panels as a
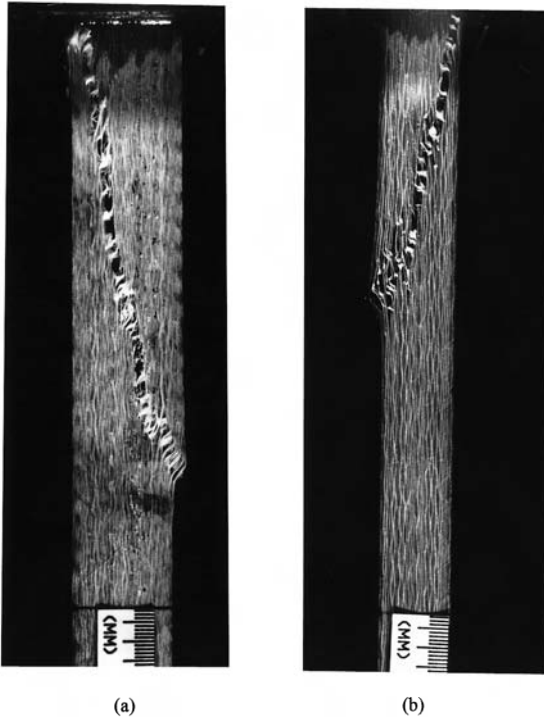
5.27 Compression failure with a kink shear band in (a) a 25 mm thick
     E-glass/polyester and (b) a 19 mm thick S-glass/phenolic intact
     panels.

reference was probably subject to a degree of systematic error. Neverthe-
less, this inherent feature is present in most of the published impact damage
tolerance research works.

Residual compressive stiffness could also be measured on the load-mean
strain curve. This is important not only for a stiffness-sensitive structural
component but also for its contribution to potential further propagation of
impact damage.

5.5.2 Factors affecting strength retention factor

Obviously, the strength retention factor decreased steadily as a severity of
impact damage increased. Less obvious was its possible dependence on the
panel geometry and local changes of fibre curvature in the vicinity of the
impact contact area. Very little information exists on the panel geometry
effect on residual and intact compressive strengths. In addition, an under-
standing of the contribution of local fibre curvature to a reduction of com-

pressive strength may shed light on the true nature of compressive strength degradation. For example, it may provide an interesting physical insight into why a panel with an open hole (indirect assessment of residual strength) provided greater compressive strength than the impact-damaged panel with delamination area identical to the hole.[39]

Impact damage induced in the large plates had both local and global effects.[40–41] Local damage consisted of matrix cracking, fibre/matrix debonding, surface microbuckling and fibre breakage (including both shear-out and tensile fracture for some plates), all surrounding the slightly dented impact contact area. Global damage refers to the extensive internal delamination or multiple delaminations, although, strictly, these are still local, but on a much larger scale. The local deformation (especially induced at relatively high IKE and involving ply shear-out) resulted in a local change in fibre curvature, which in turn acted as a pre-introduced misalignment, or region of fibre waviness, in the panel. In compressive loading this contributed to the initiation of local compression failure with a kink shear band. Another contribution to the loss in compressive strength was clearly the breakage of load-bearing fibres, but the failure mode is dominated by the impact-induced internal delamination.

The delamination effectively divided the laminate locally into two or more sublaminates so that local flexural stiffness of these sublaminates was significantly reduced. As a result, these sublaminates may buckle locally causing an overall failure of the panel at a load level considerably lower than that of the intact panel.[42] For thin damaged panels as demonstrated earlier, impact-induced delamination did not seem to propagate much in compressive loading. It is therefore thought that the large strains in the post-buckled part of the plate triggered in-plane compression failure. An increase of panel thickness by two and half times did not much alter either deformation mechanism or residual compressive strength as shown in Fig. 5.28(a–b). This finding is consistent with compression-after-impact (CAI) results of carbon/epoxy panels measured by Boeing method.[43–44]

Because failure is initiated locally, residual strength should not be affected by panel length. This was not investigated in the present study but work elsewhere on carbon/epoxy[45] found a reduction of the length of damaged panels by 17% did not result in any significant change in residual compressive strength determined by the NASA method. On the other hand, variation of the geometry of intact panels, especially length, can have a greater effect on compressive strength so as to significantly affect strength retention factor. This was found, for example in.[44] In the present investigation, the two-and-a-half-times increase of panel thickness between the two E-glass/polyester laminates led to a 12% decrease in undamaged compressive strength. This may partially account for the higher strength retention factors observed in the thicker plate.
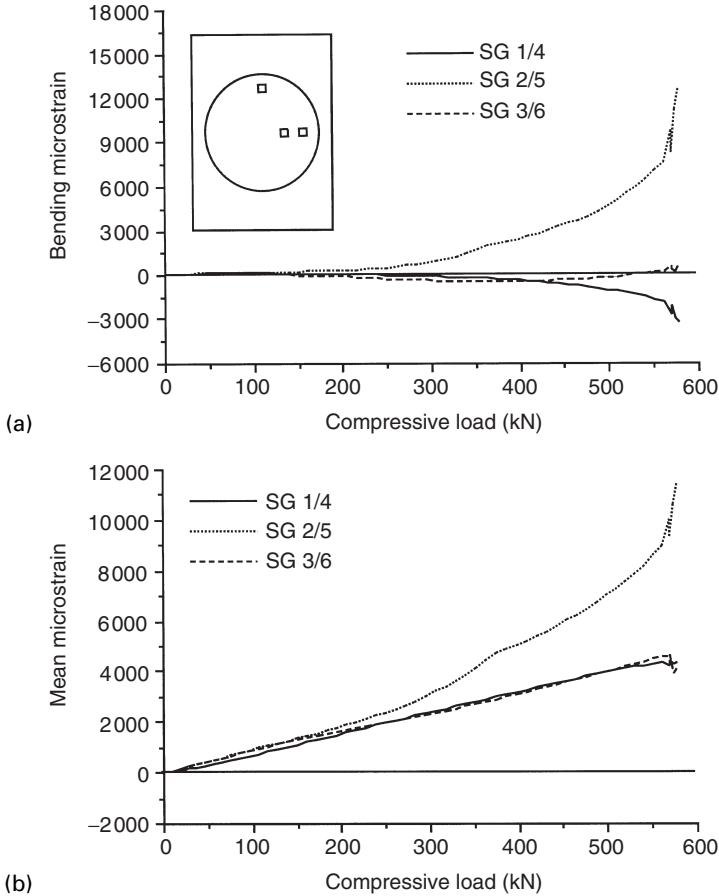
5.28 (a) Load-bending strain curves of a 25 mm thick damaged E-glass/polyester panel. (b) Load-mean strain curves of a 25 mm thick damaged E-glass/polyester panel.

5.5.3 Damage measures

IKE, delamination area and depth of surface indent have all been used as the measures of damage in the tolerance assessment of impact damage. While the depth of a surface indent has been proved[46] to bear no relation to the magnitude of interior damage and thus to a strength retention factor, IKE and delamination area also have inherent limitations, all involving the nature of impact damage. The only advantage of using IKE is its convenience as it can be readily defined to represent a degree of threat before an impact test is conducted. Disadvantages are that individual contributions

of impact velocity (including quasi-static case) and impactor mass to damage and thus to damage tolerance cannot easily be examined separately. Therefore, an impact energy value could potentially yield a range of different strength retention factors. As discussed earlier, combinations of low velocity with large mass and high velocity with small mass have proved to result in two different delamination areas. Different orientations with regard to the loading direction of a single irregular delamination area of a given size have also been demonstrated both experimentally[47] and numerically[48] to be responsible for different strength retention factors. For example, residual compressive strength was shown to be higher when an elliptical damage area had the major axis in the loading direction. The reliability of using delamination area to assess likely residual strength is therefore questionable. The use of absorbed energy was suggested as a more relevant measure of damage.[49]

Quite recently, the use of impact force was shown to be a useful additional measure of damage[17,40–41] as it brought out some features of the panel compressive behaviour, which were less obvious when the other measures of damage were used. In particular, the identifiable impact force thresholds on a force-time history curve could be not only related to the dominant damage mechanisms occurring in laminate during impact but also compared directly to the static ones for examining the effect of loading rate in damage tolerance assessment.

5.5.4 Conventional damage tolerance assessment

As described in Section 5.1, damage tolerance should embrace not only a load level or an IKE which a structure can sustain without suffering appreciable damage (IDR) but also a minimum level of residual load-bearing capability which the damaged structure can retain at the specified IKE or delamination area. The first part of the damage tolerance concept has already been established by the damage force and energy maps in the discussions of IDR (i.e. Figs 5.10(a–b), 5.17 and 5.28(a–b)). This is the idea of initial threshold force or IKE, below which there should be no damage. The estimated threshold will appear in the later diagrams as the end of the initial strength plateau on the grounds that if there is no damage, there should be no loss in residual compressive strength. The second part of the concept is addressed in the following through the variations of strength retention factor with IKE, delamination area and impact force.

Figures 5.29–31 show the variations of strength retention factor for all four laminates in terms of damage area, IKE and impact force. As can be seen, once damage area started to increase or the initial threshold value of IKE or impact force was exceeded, residual strength was reduced very rapidly due to the presence of extensive delamination or multiple
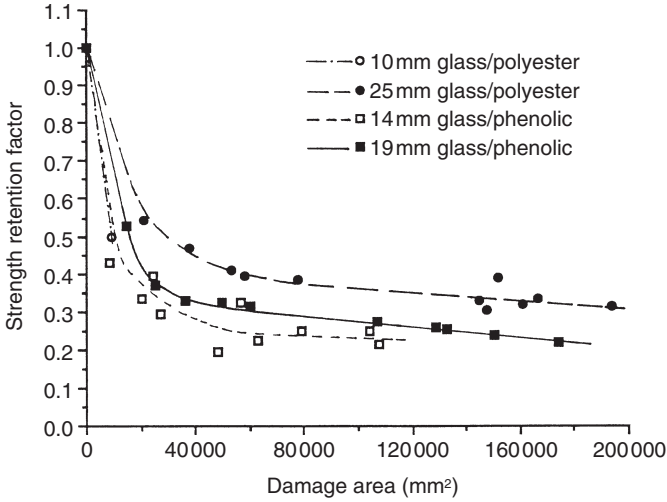
5.29 Compressive strength retention factors as a function of damage area for composite panels.
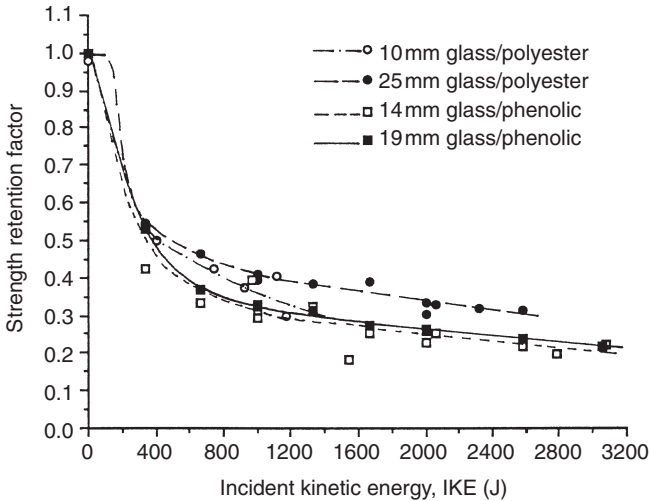
5.30 Compressive strength retention factors as a function of IKE for composite panels.

delaminations, prompting compression failure. It is noted that both types of the laminates could still retain 30% and 20% compressive strengths, respectively, even when they were completely delaminated. These asymptotes were largely due to the fact that the current panel width of 250 mm or the
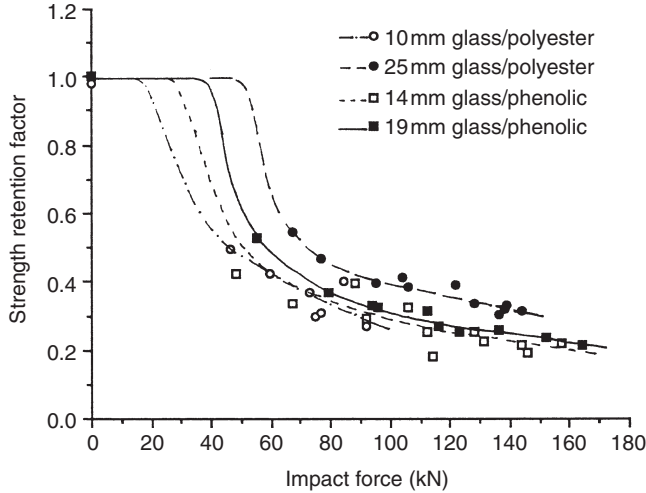
5.31 Compressive strength retention factors as a function of impact force for composite panels.

equivalent circular area of $49\,087\,mm^2$ was not capable of differentiating compressive strengths from the panels containing a delamination area greater than that. Thickness did not seem to have much effect on residual strengths plotted against damage area or IKE once damage occurred or the initial IKE threshold was exceeded. However, plotting against impact force did reveal an effect of thickness. Another advantage of using impact force is that the initial plateau established in the damage force maps is readily recognised in the retained strength plots.

The overall trends in degradation of residual strengths for the S-glass/phenolic laminates were similar to that of the E-glass/polyester laminates. The best performance from the 25 mm thick glass/polyester differed from the worst from the 14 mm thick glass/phenolic by less than 20%. For the same type of laminate, the thicker plates had fractionally higher residual strengths. The thickness effect on residual strength therefore did not seem to be significant on the basis of the present data.

Sometimes the residual far-field compressive strain rather than strength is favoured in the conventional assessment of impact damage tolerance. Thus, the far-field compressive strain data for all four laminates are presented in terms of IKE in Figs 5.32–33(a–b), which also include strength retention data for comparison. These results indicate that both the overall downward trends were similar in magnitude and that the residual far-field compressive strain data gave higher retention factors than the residual strength data (except for the 10 mm thick E-glass/polyester panels). This
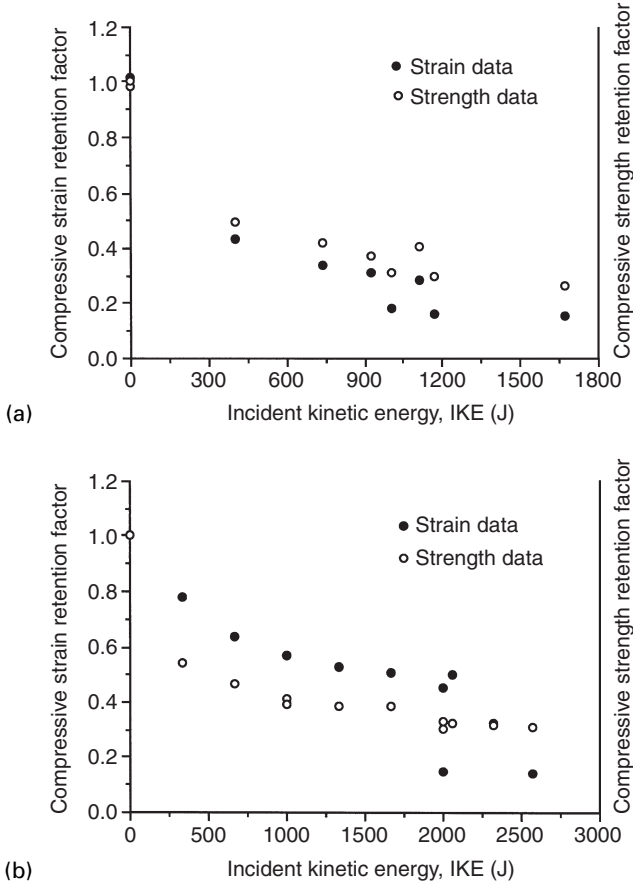
5.32 (a) Comparison of far-field strain and strength retention factor data for 10 mm thick E-glass/polyester panels. (b) Comparison of far-field strain and strength retention factor data for 25 mm thick E-glass/polyester panels.

would be expected if the damage caused a reduction in stiffness and may indicate that the gauges were not truly in the far field.

The impact damage did indeed cause a degradation in stiffness. For the present thick laminate panels, the reduction in compressive stiffness as shown in Figs 5.34–35 was much less severe than that in strength, as expected. The rate of degradation was nearly linear and the thicker panels suffered a lesser reduction. For example, the 25 mm thick E-glass/polyester panel suffered almost no loss in compressive stiffness after being impacted with an IKE of 334 J and having a delamination area of 163 mm in diameter, and lost only about 10% of stiffness at an IKE of 2000 J.
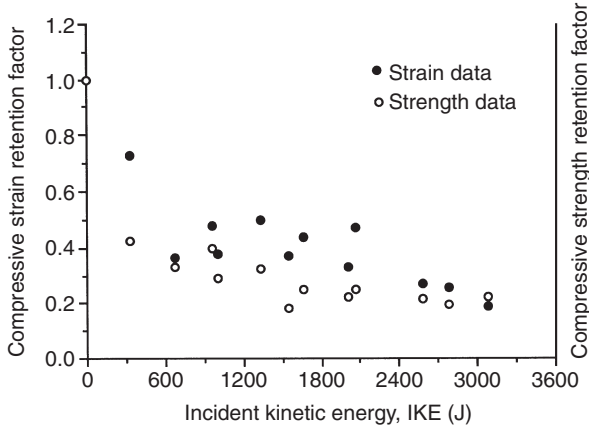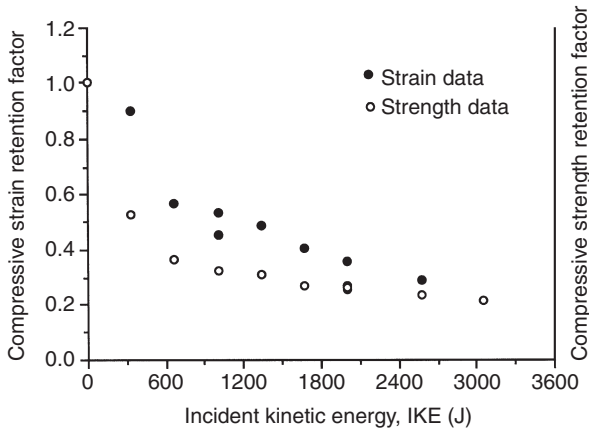
5.33 (a) Comparison of far-field strain and strength retention factor data for 14 mm thick S-glass/phenolic panels. (b) Comparison of far-field strain and strength retention factor data for 19 mm thick S-glass/phenolic panels.

5.5.5 Impact-force data based damage tolerance assessment

As discussed earlier, the conventional assessment of impact damage tolerance is a complex, costly and time-consuming process. The use of strength retention factor in this process has been shown to have several inherent limitations, for example, sensitivity to different local topographic features around the impact contact area and different failure characteristics in addition to the uncertain effect of anti-buckling support on residual compressive strength. Therefore, it seems necessary to seek a simpler and more cost-effective alternative on both cost and lead time grounds.
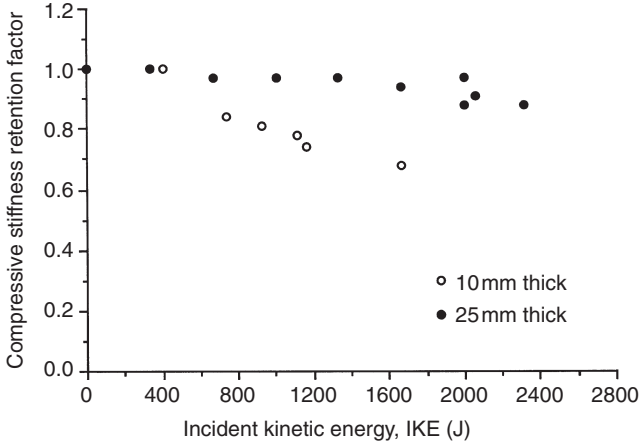
5.34 Stiffness retention factor as a function of IKE for E-glass/polyester panels.
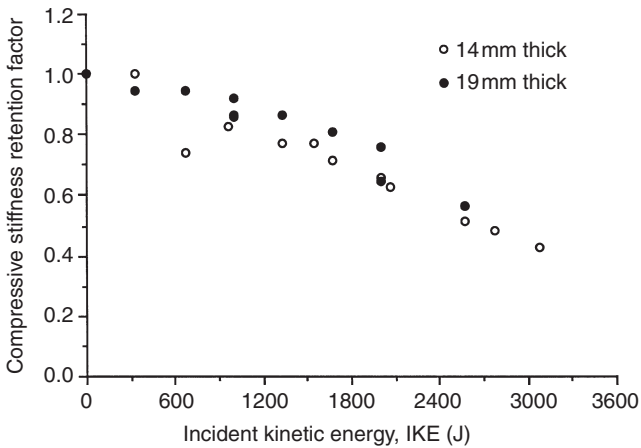
5.35 Stiffness retention factor as a function of IKE for S-glass/phenolic panels.

A novel method proposed recently[50–51] was to use the ratio of two impact force thresholds identified on the recorded impact force-time history curves. One was the initial threshold force corresponding to the onset of delamination whereas the other was a peak impact force. It is advantageous if the data from the impact tests can be used directly for a preliminary assessment of damage tolerance. This method was developed on the basis of the fact that the dominant damage mechanisms such as delamination and
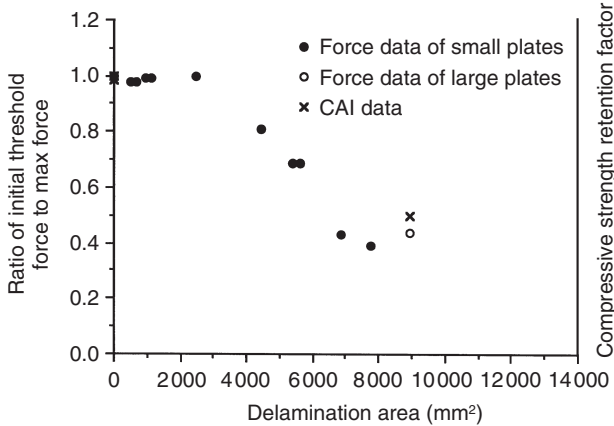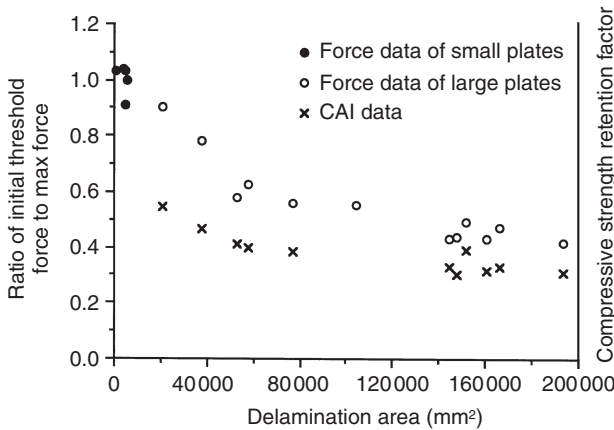
5.36 (a) Comparison of force ratio and strength retention factor data for 10 mm thick E-glass/polyester panels. (b) Comparison of force ratio and strength retention factor data for 25 mm thick E-glass/polyester panels. (c) Comparison of force ratio and strength retention factor data for 14 mm thick S-glass/phenolic panels. (d) Comparison of force ratio and strength retention factor data for 19 mm thick S-glass/phenolic panels.

fibre breakage took place at different stages of impact loading and could be identified easily as demonstrated in Section 5.4.1. Consequently, the impact force-time curves from either large or small plates could be used for this purpose. In addition, the quasi-static force data may also be used.

Figures 5.36–37(a–d) show impact force ratio data plotted against delamination area and IKE, respectively, for both large and small plates from all four laminates. Impact force ratio is defined here as initial damage

(c)

(d)
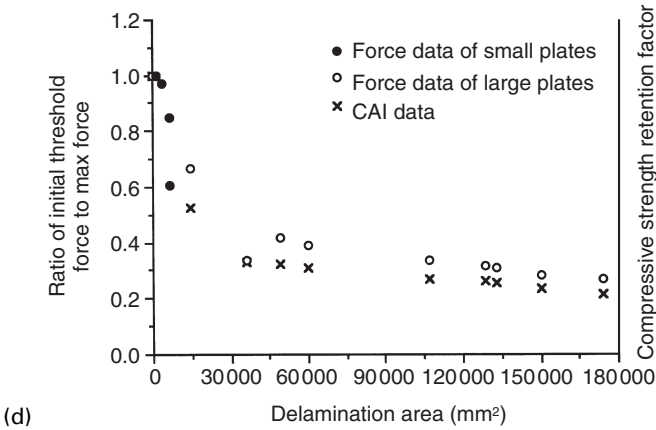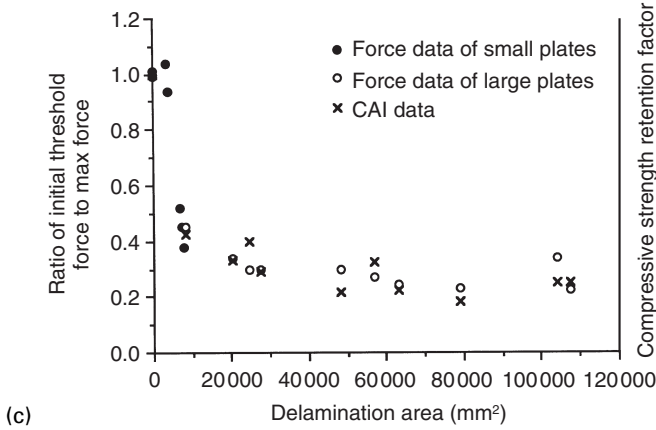
5.36 (cont.)

threshold divided by the maximum force that occurred during the impact, thus a low value of this ratio indicates a high maximum force. Compressive strength retention factor is also plotted on the same graphs. Two features can be readily observed from these diagrams. One is that the small plate data are in reasonably good agreement with the large plate data. The other is that impact force ratio and strength retention factor are approximately equal to each other for the 10 mm thick E-glass/polyester and both S-glass/phenolic panels. For the large 25 mm thick E-glass/polyester panels, the strength retention ratio is about 35% below the force ratio over the whole spectrum of damage. This difference is believed to be associated with the existence of a substantial amount of localised matrix cracking which contributed to a weakening of the panels.
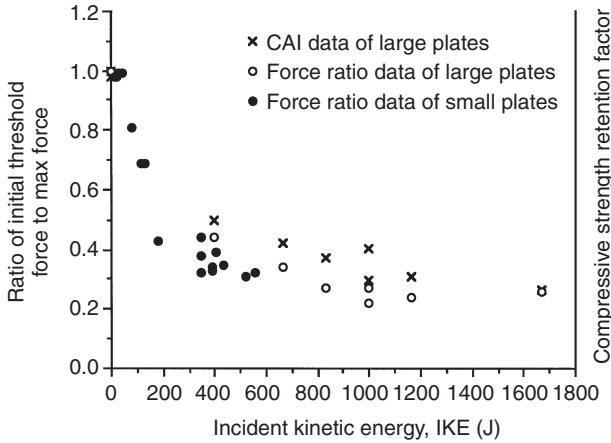
(a)
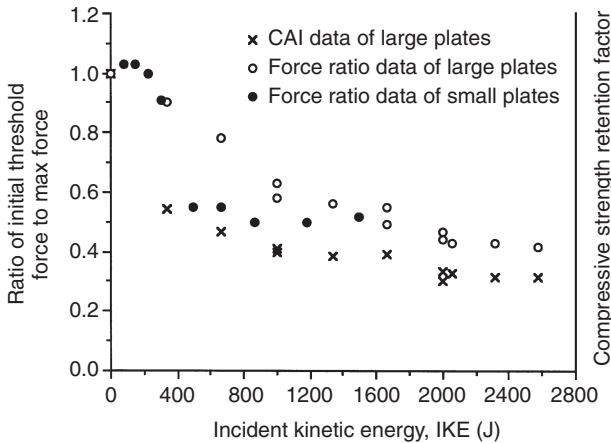
(b)

5.37 (a) Comparison of force ratio with strength retention factor in terms of IKE for 10 mm thick E-glass/polyester panels.
(b) Comparison of force ratio with strength retention factor in terms of IKE for 25 mm thick E-glass/polyester panels.
(c) Comparison of force ratio with strength retention factor in terms of IKE for 14 mm thick S-glass/phenolic panels.
(d) Comparison of force ratio with strength retention factor in terms of IKE for 19 mm thick S-glass/phenolic panels.

Alternatively, as mentioned earlier, impact damage tolerance can be assessed in terms of the residual far-field compressive strain rather than strength. Strain retention factor is compared with force ratio and strength retention factor, all plotted against IKE in Fig. 5.38(a–d). It is noticeable from these diagrams that the far-field compressive strain factors are close to, but generally higher than, the force ratios. Therefore to assume that the
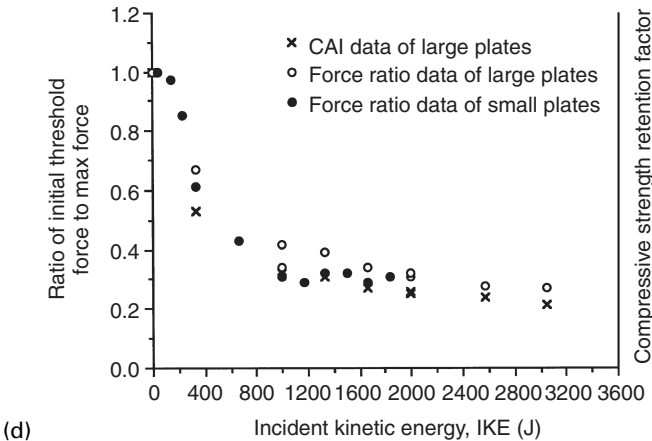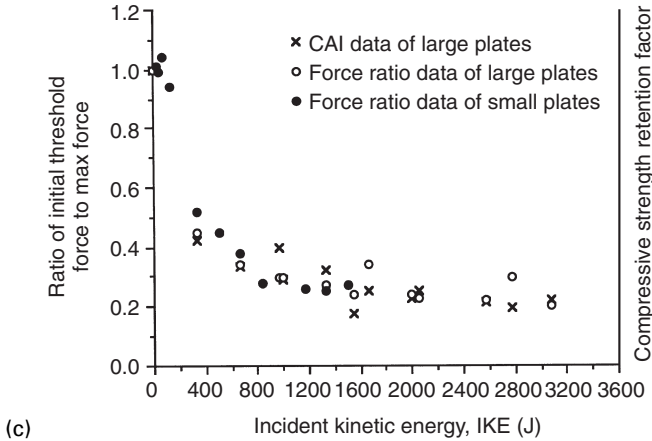
5.37 (cont.)

two were equal would normally give a conservative estimate of the strain retention factor. It should be noted that these results are based on only one size of CAI specimen, but the failure is thought to be controlled by the local damage and should therefore be independent of panel size.

This observation that impact force ratio can be used as an estimate of strength retention ratio could have significant practical implications such that damage tolerance could be assessed by using the impact response curves of small plates alone. It would be necessary neither to carry out impact tests on large plates, nor to resort to expensive CAI tests. In addition, the use of the impact force data can allow the development of a unified effective scheme to assess simultaneously both IDR for the development of composite materials and impact damage tolerance for structural
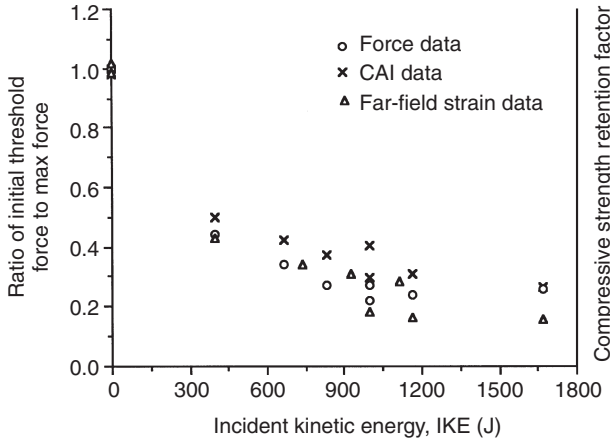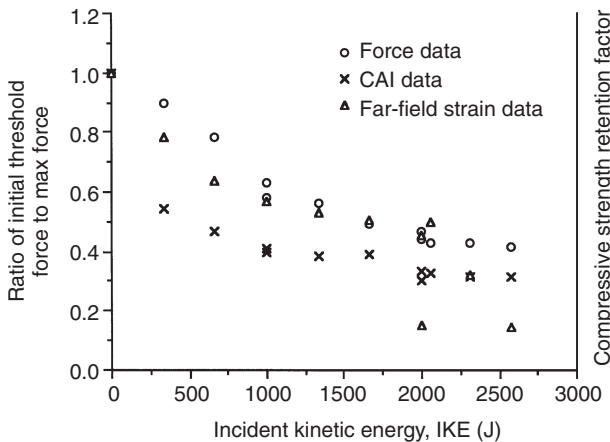
5.38 (a) Comparison of force ratio with strength and far-field strain
retention factors for 10 mm thick large E-glass/polyester panels.
(b) Comparison of force ratio with strength and far-field strain
retention factors for 25 mm thick large E-glass/polyester panels.
(c) Comparison of force ratio with strength and far-field strain
retention factors for 14 mm thick large S-glass/phenolic panels.
(d) Comparison of force ratio with strength and far-field strain
retention factors for 19 mm thick large S-glass/phenolic panels.

analysis and design. This could lead to a considerable further saving of both
time and experimentation cost. Further verification on different laminate
systems would, however, be necessary.

5.6   Conclusions

Thick woven roving glass fibre-reinforced laminated plates of various
dimensions were subjected to low-velocity and high-energy impact as well

(c)

(d)
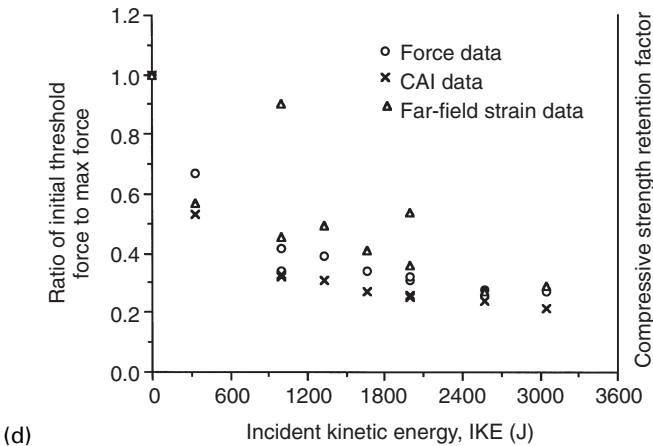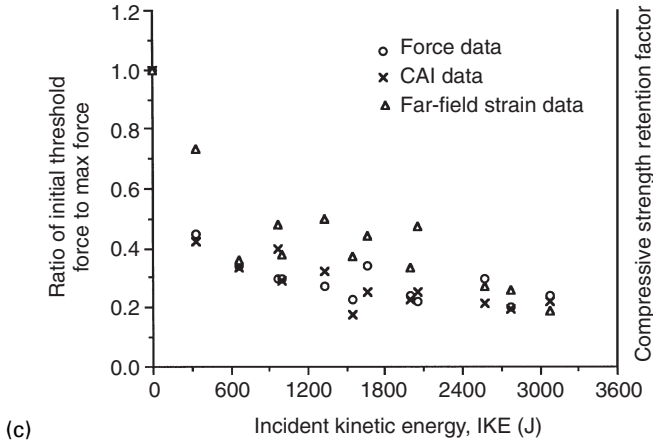
5.38 (cont.)

as quasi-static loading. Their resistance and tolerance to impact damage have been thoroughly investigated. Delamination and ply shear-out were found to be the dominant damage mechanisms. The effect of varying impact velocity, impactor mass, plate thickness and diameter on these damage mechanisms was examined by using the recorded impact response curves, ultrasonic C-scanning and cross-sectioning.

The resistance to (i.e. the threshold force for) the onset of delamination was shown to be insensitive to a change in either impactor mass or plate diameter for both E-glass/polyester and S-glass/phenolic systems. It was also insensitive to a change in velocity for the E-glass/polyester system but increased modestly with increasing velocity for the S-glass/phenolic system. Moreover, it was very sensitive to plate thickness and increased significantly for the thicker plates of the same diameter. The impact resistance to ply

shear-out was enhanced significantly by an increase of velocity for the E-glass/polyester and modestly for the S-glass/phenolic and was found to be significantly affected by the variation of geometry especially for the E-glass/polyester system. The plate diameter-related enhancement was due to a significant contribution from membrane stretching which diminished considerably with an increase of thickness.

It was demonstrated that an examination of the impact resistance to delamination propagation posed a very complex picture, being dependent on the parameter used to characterise the intensity of the impact. When impact force was used to characterise the impact, the resistance to delamination propagation was found to be insensitive to plate thickness for the S-glass/phenolic system, but it was much more sensitive for the thicker E-glass/polyester plates of the same diameter. When IKE was used, the thicker large plates had greater delamination areas. It was also found that the impacts of similar IKE gave similar amounts of delamination, regardless of whether the energy came from a high mass at low velocity or low mass at high velocity. Also, delamination propagation was found to be the primary energy-absorbing mechanism.

The residual compressive strength of impact-damaged panels was found to deteriorate very rapidly due to a combined effect of a change of local fibre curvature in the vicinity of the contact area and the presence of extensive delamination(s) once the initial threshold value of IKE or impact force was exceeded. It was not sensitive to either panel thickness or variations of impact velocity and impactor mass (at fixed IKE). In addition, strength suffered more than residual stiffness or residual far-field strains. It was also found that the characteristic failure mechanism of the damaged panels in the compression tests was different from that of the intact. The damaged panels failed by a combination of local delamination buckling and kink band formation, while a near-end compression failure with a shear mechanism was found for the intact panels.

The use of compressive strength retention factor along with IKE and delamination area in conventional impact damage tolerance assessment was reasonably satisfactory but was also complex, time-consuming and costly. In addition, strength retention factor, IKE and delamination area were all shown to have respective limitations. The novel alternative based on force data was demonstrated to be useful for the assessment of impact damage tolerance through direct comparisons with the conventional method in terms of both strength and far-field strain retention factors. In particular, it appeared possible to obtain a reasonable prediction of compression after impact performance using data from only impact tests on plates of an arbitrary size. If the composite system is not very strain rate sensitive, it should be possible to use quasi-static rather than impact loading. In addition, the use of impact force data can allow the development of a unified effective

scheme to assess simultaneously both IDR for the development of composite materials and impact damage tolerance for structural analysis and design. This could result in a considerable saving of both time and experimentation cost before resorting to the expensive conventional method.

Acknowledgements

References

1 Anon, 'Joint airworthiness requirements', JAR 25, ACJ 25.603, 1994.

2 Johnson A F and Marchant A, 'Design and analysis of composite structures', in *Polymers and Polymer Composites in Construction*, ed L C Hollaway, Thomas Telford, London, 1990.

3 Evans R E and Masters J E, 'A new generation of epoxy composites for primary structural applications: materials and mechanics', *ASTM*, 1985 **STP 876** 413–36.

4 Masters J E, 'Correlation of impact and delamination resistance in interleafed laminates', *6th ICCM/2nd ECCM*, London, **3**, 1987.

5 Mouritz A P, Leong K H and Herszberg I, 'A review of the effect of stitching on the in-plane mechanical properties of fibre-reinforced polymer composites', *Composites*, 1997 **28A** 979–91.

6 Freitas G, Magee C, Dardzinski P and Fusco T, 'Fiber insertion process for improved damage tolerance in aircraft laminates', *J Advan Mater*, 1994 **36**.

7 Dorey G, 'Damage tolerance and damage assessment in advanced composites', in *Advanced Composites*, ed I K Partridge, Elseview Applied Science Pub, **Chapter 11**, 369–98, 1989.

8 Abrate S, 'Impact on laminated composite materials', *Appl Mech Rev*, 1991 **44**(4) 155–90.

9 Cantwell W J and Morton J, 'The impact resistance of composite materials – a review', *Composites*, 1991 **22**(5) 347–62.

10 Abrate S, 'Impact on laminated composites – recent advances', *Appl Mech Rev*, 1994 **47**(11) 517–44.

11 Cantwell W J, Curtis P T and Morton J, 'Post impact fatigue performance of carbon fibre laminates with non woven and mixed woven layers', *Composites*, 1983 **14** 301–5.

12 Vedula M and Koczak M J, 'Impact resistance of cross-plied polyphenylene sulfide composites', *J Thermoplastic Composite Materials*, 1989 **2** 154–63.

13 Zhou G and Davies G A O, 'Experimental determination of interlaminar shear strengths of thick GFRPs', *6th ECCM–CTS2*, Hamburg, 1994.

14 Zhou G and Davies G A O, 'Characterisation of thick glass woven roving/ polyester laminates: Part I, tension, compression and shear', *Composites*, 1995 **26**(8) 579–86.

15 Zhou G and Davies G A O, 'Characterisation of thick glass woven roving/ polyester laminates: Part II, flexure and statistical consideration', *Composites*, 1995 **26**(8) 587–96.

16 Hodgkinson J M, Ayache S and Matthews F L, 'In-plane and out-of-plane property measurements on thick woven glass/polyester laminates', *5th ECCM-CTS 1*, Amsterdam, 1992.

17 Zhou G, 'Static behaviour and damage of thick composite plates', *Composite Struct*, 1996 **36**(1–2) 12–33.

18 Davies G A O, Hitchings D and Zhou G, 'Impact damage and residual strengths of woven fabric glass/polyester laminates', *Composites*, 1996 **27A**(8) 1147–56.

19 Zhou G and Davies G A O, 'Impact response of thick glass fibre reinforced polyester laminates', *Int J of Impact Eng*, 1995 **16**(3) 357–74.

20 Zhou G, 'Damage mechanisms in composite laminates impacted by a flat-ended impactor', *Composites Sci and Tech*, 1995 **54**(3) 267–73.

21 Zhou G, 'Prediction of Impact damage thresholds in glass fibre reinforced laminates', *Composite Struct*, 1995 **31** 185–93.

22 Sjoblom P, 'Simple design approach against low-velocity impact damage', *32nd Int SAMPE Symp*, Anaheim, 529–39, 1987.

23 Lagace P A, Williamson J E, Tsang P H W, Wolf E and Thomas S, 'The use of force as a (impact) damage resistance parameter', *7th Tech Conf of American Society of Composites*, PA, 1992.

24 Jakson W C and Poe Jr. C C, 'The use of impact force as a scale parameter for the impact response of composite laminates', *J Composite Technol Res*, 1993 **15** 282–9.

25 Lesser A J and Filippov A G, 'Mechanisms governing the damage resistance of laminated composites subjected to low-velocity impacts', *Int J Damage Mech*, 1994 **3** 408–32.

26 Rydin R W, Bushman M B and Karbhari V M, 'The influence of velocity in low-velocity impact testing of composites using the drop weight impact tower', *J Reinforced Plastics Composites*, 1995 **14** 113–27.

27 Delfosse D, Poursartip A, Coxon B R and Dost E F, 'Non-penetrating impact behaviour of CFRP at low and intermediate velocities', *ASTM*, 1995 **STP 1230** 333–50.

28 Liu D, 'Impact induced delamination – a view of bending stiffness mismatching', *J Composite Mater*, 1988 **22** 674–92.

29 Hull D and Shi Y B, 'Damage mechanism characterization in composite damage tolerance investigations', *Composite Struct*, 1993 **23** 99–120.

30 Davies G A O and Zhang X, 'Impact damage prediction in carbon composite structures', *Int J Impact Eng*, 1995 **15**(3) 357–74.

31 Zhou G, 'Impact velocity effect on damage in laminated composites', *7th ECCM – High Performance Composites*, London, **1,** 1996.

32 Zhou G, Impact damage resistance of thick glass woven roving fibre reinforced composites – geometric effects, *Int Conf on Advanced Materials*, Beijing, 1996.

33 Morton J, 'Scaling of impact-loaded carbon fiber composites', *AIAA Journal*, 1988 **26** 989–94.

34 Kwon Y S and Sankar B V, 'Indentation-flexure and low-velocity impact damage in graphite epoxy laminates', *J Composite Technol Res*, 1993 **15** 101.

35 Lee S W R and Sun C T, 'Dynamic penetration of graphite/epoxy laminates impacted by a blunted-ended projectile', *Composites Sci Technol*, 1993 **49** 369–80.

36 Zhou G, Lloyd J C and McGuirk, J J, 'Experimental evaluation of geometric factors affecting damage mechanisms in carbon/epoxy plates', accepted by *Composites* Part A.

37 Zhou G, 'Characteristics of impact energy absorption during damage development in laminated composites', *4th Int Conf Deformation and Fracture of Composites*, Manchester, 1997.

38 Zhou G, 'Compressive behaviour of large undamaged and damaged thick composite panels', *Composite Struct*, 1997 **38**(1–4) 589–97.

39 Horton R E and McCarty J E, 'Damage tolerance of composites', in *Engineering Materials Handbook*, T J Reinhart, Ohio, USA, **1**, ASM, 1987.

40 Zhou G and Davies G A O, 'Damage tolerance of thick glass fibre reinforced laminate structures subjected to low-velocity impact', *ASME-WAM*, Chicago, MD-vol. **51**, 1994.

41 Zhou G, 'Effect of impact damage on residual compressive strength of GFRP laminates', *Composite Struct*, 1996 **35**(2) 171–81.

42 Lagace P A, 'On delamination failures in composite laminates', in *Composite Structures Testing, Analysis, and Design*, eds J N Reddy and A V K Murty, New Delhi, Spinger-Verlag/Narosa Publications, 1992.

43 Manders P W and Harris W C, 'A parametric study of composite performance in compression-after-impact testing', *SAMPE J*, 1986 **Nov**. 47–51.

44 Vedula M, Lee W M, Benedetto E E and Groleau M R, 'Screening test for compression after impact strength evaluation of composites', *7th Tech Conf of American Society of Composites*, PA, 1992.

45 Ishikawa T, Sugimoto S, Matsushima M and Hayashi Y, 'Some experimental findings in compression-after-impact (CAI) tests of CF/PEEK (APC-2) and conventional CF/epoxy flat plates', *Composites Sci Technol*, 1995 **55** 349–63.

46 Wardle B L and Lagace P A, 'On the use of dent depth as an impact damage metric for thin composite structures', *J Reinforced Plastics Composites*, 1997 **16** 1093–110.

47 Lameris J, *BRITE-EURAM 3159 CR*, National Aerospace Lab., The Netherlands, 1993.

48 Xiong Y and Poon C, 'Prediction of residual compressive strength of impact-damaged composite laminates', *9th ICCM*, Madrid, 1993.

49 Pintado P, Vogler T J and Morton J, 'Impact damage tolerance of thick graphite-epoxy composite material systems', *8th ICCM*, Hawaii, 1993.

50 Zhou G, 'The use of experimentally-determined impact force as a damage measure in impact damage resistance and tolerance of composite structures', *Composite Struct*, 1998 **42**(4) 375–82.

51 Zhou G, 'Replacing residual compressive strengths by impact force data in the damage tolerance assessment of composite structures', *8th ECCM*, Naples, 1998.

6

Elastic impact stress analysis of composite plates and cylinders

S R SWANSON

6.1 Introduction

Impact is a complicated topic, involving both structural and material response and damage formation. However, the stress analysis of the impact is fundamental to understanding the entire problem. The analysis can take many forms, such as nonlinear numerical analysis or linear analysis with closed form solutions, as some examples show in Chapter 7. In the following, the fundamentals of primarily linear analysis of laminated plates and cylinders will be discussed, and examples of work in the literature on these topics will be presented.

6.2 Impact regimes

It is possible to classify impact into various categories, depending on the characteristics of the impactor and target. A major category is those impact events where through-the-thickness stress wave effects are important. In impact of a structure by a foreign body, a through-the-thickness compressive stress wave will be initiated. In some circumstances, this wave will be reflected as a tensile wave from the free surface on the back side, introducing the possibility of through-the-thickness tensile failure.[1] Calculation of the characteristics of the through-the-thickness wave may in general be difficult and require numerical treatment, however some limit cases will be informative. If the impactor is large with respect to the thickness of the target and both the target and impactor have parallel surfaces, the stress-state is that associated with one dimensional strain, and the wave speed will be in the order of

$$c = \sqrt{Q_{33}/\rho} \quad \text{and} \quad \sigma = -\alpha Q_{33} v/c \qquad [6.1]$$

where Q_{33} is the diagonal term of the three-dimensional stress–strain matrix for the composite in the through-the-thickness direction, α is a constant depending on the properties of the impactor and target, and v is the

impact velocity. For many composites Q_{33} is not greatly different from the through the thickness modulus, which is also comparable to the in-plane modulus E_{22} in a direction transverse to the fibers. The magnitude of the stress wave depends linearly on the ratio of the impactor velocity to the wave speed. Substituting values shows that through-the-thickness stress waves will be important in ballistic events and many simulations such as air-gun driven impactors, but are not likely to be significant in drop-weight impacts. However the impactor and target surfaces are often not parallel, and the impactor may not be large. In this case the indentation of the impactor into the target will smear out the transverse wave so that detailed numerical computation is required, e.g. as carried out by Joshi and Sun.[2]

For those impact events in which through-the-thickness stress waves are not considered to be important, a further division is possible. Events in which the distributed mass of the target is negligible relative to the impactor mass are termed quasi-static. This assumption greatly simplifies the analysis of the impact event, as the target can then be characterised only by its static stiffness properties. Impact events that do not fall into this category will respond in a much more complex fashion, that can be considered to be a synthesis of a large number of natural frequencies and mode shapes of the target. Because of the simplicity of the quasi-static analysis, it is important to be able to determine when this assumption is applicable, and this topic is addressed further in the following. Impacts in which the quasi-static assumption is assumed to hold are sometimes termed 'low-velocity' impacts, but this is questionable terminology as the division between the structural dynamic and the quasi-static regimes is completely independent of the impact velocity itself, but depends on other characteristics of the impact.

6.3   Analysis of impact

The analysis of the stresses and strains resulting from impacts on laminated plates, beams, and cylinders will be discussed in this section, for impacts in which the structural dynamics of the target are important, but through-the-thickness stress waves are not. The local deformations associated with the indentation of the target are first described, followed by several schemes for solving the dynamics problem of impact on plates and cylinders.

6.3.1   Contact stiffness and deformation

The projectile indents the target to a greater or lesser extent, and this additional compliance influences the response. The usual treatment follows that of Sun et al.,[3-5] who adapted the usual Hertz solution for contact between

two bodies to the impact problem. The contact force is assumed to be related to the contact indentation by the following equation

$$F = k\alpha^{3/2} \quad \text{with} \quad k = \frac{4}{3}\sqrt{R_s}\,E_{22} \qquad [6.2]$$

where F is the total contact force on the target, α is the local indentation, R_s is the radius of the spherical impactor, and E_{22} is the transverse Young's modulus of the laminated target. The contact force is then related to the motion of the projectile by assuming rigid body dynamics for the projectile, that is

$$F = -m\ddot{u} \qquad [6.3]$$

where m is the mass and u is the displacement of the projectile. The relationship between the local indentation, projectile displacement and plate displacement at impact center is expressed by

$$\alpha(t) = u(t) - w(t, \xi, \eta) \qquad [6.4]$$

where ξ and η give the location of the center of impact.

6.3.2 Structural dynamics of impact for plates

The analysis of static and dynamic loadings of laminated composite plates has seen considerable development recently. Lekhnitskii,[6] and Whitney and Leissa[7] have presented analyses with infinite transverse rigidity while Whitney and Pagano[8] have presented a theory including transverse shear deformations. The dynamic problems considered involved vibration of plates. Sun and Chattopadhyay[3] and Dobyns[9] used the plate equations developed by Whitney and Pagano[8] to analyse a simply supported orthotropic plate subject to center impact. Dobyns assumed that the lateral force history was known, while Sun and Chattopadhyay noted that in impact by a foreign body, the force history must be computed as part of the problem. Thus Sun and Chattopadhyay integrated the equations of motion numerically. Birman and Bert[10] obtained a closed-form solution for laminated angle-ply simply supported plates subject to blast loading, which again considers that the force history is known.

Solutions of the impact problem for plates have been displayed in the literature, that solve for the force history as well as the resulting stresses, strains, and deformation. An analytical solution is available for plates with simply supported boundary conditions, using Fourier series expansion techniques combined with Laplace transform techniques. However, the contact stiffness must be linearised to permit this analytical solution. The solution for other boundary conditions has been addressed using Ritz solutions,

combined with numerical time integration. These analysis techniques are illustrated in the following.

6.3.2.1   Equations of motion for plates

The plate equations of motion developed by Whitney and Pagano[8] reduced to specially orthotropic form ($B_{ij} = 0$, $A_{16} = A_{26} = D_{16} = D_{26} = 0$), are given by Dobyns[9] as

$$D_{11}\frac{\partial^2 \psi_x}{\partial x^2} + D_{66}\frac{\partial^2 \psi_x}{\partial y^2} + (D_{12} + D_{66})\frac{\partial^2 \psi_y}{\partial x \partial y} - kA_{55}\left(\psi_x + \frac{\partial w}{\partial x}\right) = \frac{\rho h^3}{12}\frac{\partial^2 \psi_x}{\partial t^2}$$

$$(D_{12} + D_{66})\frac{\partial^2 \psi_x}{\partial x \partial y} + D_{66}\frac{\partial^2 \psi_y}{\partial x^2} + D_{22}\frac{\partial^2 \psi_y}{\partial y^2} - kA_{44}\left(\psi_y + \frac{\partial w}{\partial y}\right) = \frac{\rho h^3}{12}\frac{\partial^2 \psi_y}{\partial t^2}$$

$$kA_{55}\left(\frac{\partial \psi_x}{\partial x} + \frac{\partial^2 w}{\partial x^2}\right) + kA_{44}\left(\frac{\partial \psi_y}{\partial y} + \frac{\partial^2 w}{\partial y^2}\right) + q(x,y,t) = \rho h \frac{\partial^2 w}{\partial t^2} \qquad [6.5]$$

where D_{ij} and A_{ij} are the stiffnesses, as defined by Whitney and Pagano,[8] h is the plate thickness, t is time, ρ is material density, w is the plate displacement in the z direction at the plate midplane, ψ_x and ψ_y are the rotations in the x and y directions and k is a shear correction factor that is often taken to be $\pi^2/12$.

6.3.2.2   Solution for simply-supported boundary conditions

For plates with boundary conditions of simple support on all four edges, it is possible to use standard Fourier series expansion techniques to determine the response. Christoforou and Swanson[11,12] have shown that it is possible to obtain an analytical solution to the impact problem by using Laplace transform techniques, if the nonlinear contact indentation is approximated by a linearised version.

The solution is based on expansions of the loads, displacements, and rotations in Fourier series which satisfy the end boundary conditions of simple support. Each expression is assumed to be separable into a function of time and a function of position. Furthermore, following Bert and Birman,[13] by neglecting in-plane and rotary inertia the problem becomes a second order ordinary differential equation in time for the Fourier coefficients of the lateral deflection. In the case of impact, the impact force is computed from the deceleration of the impactor mass. This involves the equilibrium equation between the impactor and the plate during contact.

For a given dynamic load, solutions of the governing equations [6.5] that satisfy the boundary conditions of simple support are given by
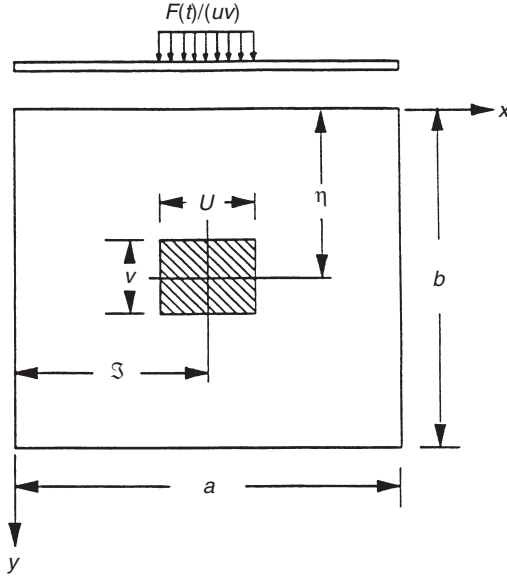
6.1 Illustration of plate geometry used for analysis of simply supported plates.

$$\psi_x = \sum_m \sum_n A_{mn}(t)\cos\frac{m\pi x}{a}\sin\frac{n\pi y}{b}$$

$$\psi_y = \sum_m \sum_n B_{mn}(t)\sin\frac{m\pi x}{a}\cos\frac{n\pi y}{b} \qquad\qquad [6.6]$$

$$w = \sum_m \sum_n W_{mn}(t)\sin\frac{m\pi x}{a}\sin\frac{n\pi y}{b}$$

with the load function represented by

$$q(x,y,t) = \sum_m \sum_n Q_{mn}(t)\sin\frac{m\pi x}{a}\sin\frac{n\pi y}{b} \qquad\qquad [6.7]$$

Equations [6.6] and [6.7] are the Fourier series representation of the rotations, lateral displacement and load. The coordinate system and geometry are illustrated in Fig. 6.1. The terms of the Fourier series representation for a uniform load over the rectangular area u, v with center at ζ, η is shown in Fig. 6.1 are Dobyns'.[9]

$$Q_{mn}(t) = \frac{16F(t)}{\pi^2 mn\,uv}\sin\frac{m\pi\zeta}{a}\sin\frac{n\pi\eta}{b}\sin\frac{m\pi u}{2a}\sin\frac{n\pi v}{2b} \qquad\qquad [6.8]$$

Following the results of Bert and Chen,[14] rotary inertia effects are neglected. Thus substituting equations [6.6] and [6.7] into equation [6.5]

results in the independent sets of three equations for each set of modal parameters m and n:

$$\begin{bmatrix} C_{11} & C_{12} & C_{13} \\ C_{12} & C_{22} & C_{23} \\ C_{13} & C_{23} & C_{33} \end{bmatrix} \begin{Bmatrix} A_{mn}(t) \\ B_{mn}(t) \\ W_{mn}(t) \end{Bmatrix} = \begin{Bmatrix} 0 \\ 0 \\ Q_{mn}(t) - \rho h \ddot{W}_{mn}(t) \end{Bmatrix}$$ [6.9]

where the elements of the symmetric matrix C_{ij} are

$$C_{11} = D_{11}\left(\frac{m\pi}{a}\right)^2 + D_{66}\left(\frac{n\pi}{b}\right)^2 + kA_{55}$$

$$C_{12} = (D_{12} + D_{66})\left(\frac{m\pi}{a}\right)\left(\frac{n\pi}{b}\right)$$

$$C_{13} = kA_{55}\left(\frac{m\pi}{a}\right)$$

$$C_{22} = D_{66}\left(\frac{m\pi}{a}\right)^2 + D_{22}\left(\frac{n\pi}{b}\right)^2 + kA_{44}$$ [6.10]

$$C_{23} = kA_{44}\left(\frac{n\pi}{b}\right)$$

$$C_{33} = kA_{55}\left(\frac{m\pi}{a}\right)^2 + kA_{44}\left(\frac{n\pi}{b}\right)^2$$

Following Bert and Birman,[13] equation [6.9] can be reduced to a single differential equation by the following transformation:

$$A_{mn}(t) = K_A W_{mn}(t); \quad B_{mn}(t) = K_B W_{mn}(t)$$ [6.11]

where

$$K_A = \frac{C_{12}C_{23} - C_{13}C_{22}}{C_{11}C_{22} - C_{12}^2}$$

$$K_B = \frac{C_{12}C_{13} - C_{11}C_{23}}{C_{11}C_{22} - C_{12}^2}$$ [6.12]

Substitution of equation [6.8] reduces the set [6.9] into the following:

$$\ddot{W}_{mn}(t) + \omega_{mn}^2 W_{mn}(t) = P_{mn}\frac{ab}{uv}\frac{F(t)}{m_1}$$ [6.13]

where $\omega_{mn}^2 = \dfrac{C_{13}K_A + C_{23}K_B + C_{33}}{\rho h}$ are the squared fundamental frequencies of the plate, and m_1 is its mass.

For zero initial displacement and velocity, the solution of equation [6.13] is obtained using the convolution integral:

$$W_{mn}(t) \frac{P_{mn}ab}{uvm_1\omega_{mn}} \int_0^t F(\tau)\sin\omega_{mn}(t-\tau)d\tau \qquad [6.14]$$

The deflection of the plate at any point is given by

$$w(x,y,t) = \frac{ab}{uvm_1} \sum_m \sum_n \frac{P_{mn}}{\omega_{mn}} \sin\frac{m\pi x}{a} \sin\frac{n\pi y}{b} \int_0^t F(\tau)\sin\omega_{mn}(t-\tau)d\tau \qquad [6.15]$$

The response of a plate to impact by a foreign object may be computed from the transient response, equation [6.15], by computing the impact force from the deceleration of the impactor mass. The integral equilibrium equation between the impactor and the plate during contact is given by

$$w\left(\frac{a}{2},\frac{b}{2},t\right) = V_0 t - \frac{1}{m_2}\int_0^t F(\tau)(t-\tau)d\tau - \frac{F(t)}{K_2} \qquad [6.16]$$

where V_0 is the initial velocity of the impactor with mass m_2, $w\left(\frac{a}{2},\frac{b}{2},t\right)$ is the lateral deflection of the plate evaluated at the impact point as a function of time, $F(t)$ is the impact force and K_2 is the linearised contact area stiffness.

As mentioned above, the contact problem must be linearised in order to be treated analytically using the present approach. This involves both replacing the nonlinear contact stiffness with an appropriate linearised value, as well as approximating the time varying contact area by a constant area.

Combining equations [6.15] and [6.16] yields

$$V_0 t - \frac{1}{m_2}\int_0^t F(\tau)(t-\tau)d\tau - \frac{F(t)}{K_2}$$
$$= \frac{ab}{uv\,m_1} \sum_m \sum_n \frac{P_{mn}}{\omega_{mn}} \sin\frac{m\pi}{2} \sin\frac{n\pi}{2} \int_0^t F(\tau)\sin\omega_{mn}(t-\tau)d\tau \qquad [6.17]$$

Taking the Laplace transform of equation [6.17] and after some rearranging yields

$$F(s) = \frac{m_2 V_0}{1 + \dfrac{m_2}{K_2}s^2 + \dfrac{abm_2}{uvm_1} \displaystyle\sum_m \sum_n P_{mn}\sin\dfrac{m\pi}{2}\sin\dfrac{n\pi}{2}\dfrac{s^2}{s^2+\omega_{mn}^2}} \qquad [6.18]$$

Using the inverse theorem for Laplace transforms and following the procedure of Christoforou and Swanson[11,12] yields
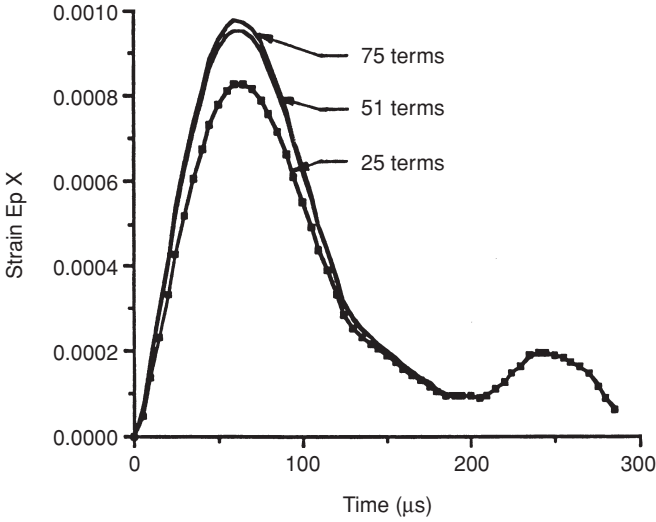
6.2 Convergence of solution for strain behind the impact point. (After Christoforou and Swanson[12].)

$$F(t) = \sum_j F_j \sin \omega_j t \qquad [6.19]$$

where ω_j are the response frequencies or poles of expression [6.18] and

$$F_j = \frac{m_2 V_0}{\omega_j \left[\dfrac{m_2}{K_2} + \dfrac{ab}{uv} \dfrac{m_2}{m_1} \sum_m \sum_n P_{mn} \sin \dfrac{m\pi}{2} \sin \dfrac{n\pi}{2} \dfrac{\omega_{mn}^2}{(\omega_{mn}^2 - \omega_j^2)^2} \right]} \qquad [6.20]$$

The impact response can be determined by combining the Laplace transforms of equations [6.14] and [6.19]

$$W_{mn}(s) = \frac{P_{mn} ab}{m_1 uv} \sum_j \frac{F_j \omega_j}{(s^2 + \omega_{mn}^2)(s^2 + \omega_j^2)} \qquad [6.21]$$

Inverting as above gives

$$W_{mn}(t) = \frac{P_{mn} ab}{m_1 uv} \sum_j \frac{F_j}{\omega_{mn}(\omega_j^2 - \omega_{mn}^2)} (\omega_j \sin \omega_{mn} t - \omega_{mn} \sin \omega_j t) \qquad [6.22]$$

The deflection and strain at any point can then be obtained by substituting [6.22] into equations [6.11] and [6.6]. An illustration of the convergence of the solution for strain is shown in Fig. 6.2, taken from Christoforou and Swanson.[12] Further results will be shown subsequently.

6.3.2.3 Plates with other boundary conditions

As is the case with the static analysis of plates, boundary conditions other than simple support require techniques other than the double Fourier series expansion. An approximate but general technique is to use a Ritz analysis, combined with a numerical integration of the time variable. It is possible to include the nonlinear contact stiffness with this approach. The analysis shown here has been displayed by Cairns and Lagace[15] and Qian and Swanson.[16]

The analysis is based on Lagrange's equation of motion with the Lagrangian function $L = T - V$:

$$\frac{d}{dt}\frac{\partial L}{\partial x} - \frac{\partial L}{\partial x} = 0 \qquad\qquad [6.23]$$

where x is the modal amplitude.

Consider a laminated plate under dynamic lateral loading. The potential energy is given as

$$V = \frac{1}{2}\int\int_A [\kappa]^T [D][\kappa]dA + \frac{1}{2}\int\int_A [\gamma]^T [A][\gamma]dA - \int\int_A p(t,x,y)\,w(t,x,y)dA \qquad [6.24]$$

where the first two terms are bending and transverse shear strain energy, respectively, and the third is the work done by the lateral load. The kinetic energy of the plate is given by

$$T = \frac{\rho h}{2}\int\int_A \dot{w}(t,x,y)^2 dA. \qquad\qquad [6.25]$$

Here again the in-plane and rotary inertia effects have been neglected, as suggested by Birman and Bert[10] and Dobyns.[9]

The problem considered in Qian and Swanson[16] has clamped boundary conditions on two opposing edges of the plate and free boundaries on the other two edges to correspond with experiments. The procedure followed is based on choosing two series of functions, or 'mode shapes', which satisfy the boundary conditions and give suitable expressions for deflection curves in x and y directions separately. The assumed deformed shape of the rectangular plate is then taken as a product of these functions. Therefore the series approximation for the planar rotations and transverse displacement can be taken as

$$\bar{\alpha}(t,x,y) = \sum_m \sum_n A_{mn}(t)X'_m(x)Y_n(y) \qquad\qquad [6.26]$$

$$\bar{\beta}(t,x,y) = \sum_m \sum_n B_{mn}(t)X_m(x)Y'_n(y) \qquad\qquad [6.27]$$

$$w(t,x,y) = \sum_m \sum_n C_{mn}(t)X_m(x)Y_n(y) \qquad\qquad [6.28]$$

where A_{mn}, B_{mn}, and C_{mn} are the modal amplitudes of the plate and are to be determined. Substituting the assumed mode shapes in the expressions for potential and kinetic energy, and then using Lagrange's equation [6.23] gives three sets of equations with unknowns A_{mn}, B_{mn}, and C_{mn}. Substituting A_{mn}, B_{mn} in terms of C_{mn} yields a system of second order ordinary differential equations for the modal amplitudes C_{mn}

$$[S]\{\ddot{C}\} + [T]\{C\} = \{P\}$$ [6.29]

In Qian and Swanson[16] the assumed mode shapes were taken as beam functions, which are solutions for mode shapes of beams under the appropriate boundary conditions.[17] The beam functions are orthogonal, permitting expansion of the load in terms of these functions. This expansion is of the form

$$p(t, x, y) = \sum_m \sum_n p_{mn}(t) X_m(x) Y_n(y)$$ [6.30]

with

$$p_{mn}(t) = \frac{\iint_A p(t, x, y) X_m(x) Y_n(y) dx dy}{\iint_A X_m^2(x) Y_n^2(y) dx dy}$$ [6.31]

The $\{P\}$ in the right hand of equation [6.29] is a force term, and each component comes from taking the derivative of the work done by the lateral load to the relative mode amplitude, that is

$$P_{mn} = \frac{\partial W}{\partial C_{mn}} = p_{mn} \iint_A X_m^2(x) Y_n^2(y) dx dy$$ [6.32]

The contact force is assumed to be related to the contact indentation using the relations given previously above. The contact pressure $p(t, x, y)$ is simply taken as the uniform distribution of the total contact force $F(t)$ over a square area A_c. This area is determined by

$$A_c = \pi \left[R_s^2 - (R_s - \alpha)^2 \right]$$ [6.33]

The equations above along with the contact laws were solved simultaneously. Due to the nonlinearity of the contact deformation relationship, the above equations were solved numerically, using the Newmark method with $\beta = 1/4$, which gives an unconditionally stable solution.

A typical comparison of calculation with experimentally measured strain is shown in Fig. 6.3, taken from Qian and Swanson.[16] It can be seen that the agreement is very reasonable.
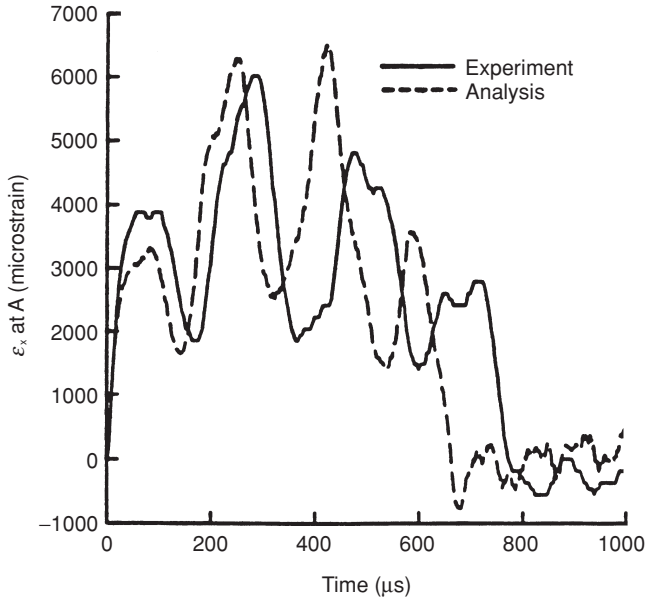
6.3 Comparison of Ritz analysis with experiment for strain in impact of plate. (After Qian and Swanson[16].)

6.3.2.4 Comparison of solution techniques

It is possible to apply the second solution technique described above, that of using a Ritz analysis in conjunction with numerical time integration, to the problem of impact of a plate with simply-supported boundary conditions, and thus permit a comparison with the first technique, which used Laplace transforms. This comparison of solution techniques has been carried out by Qian and Swanson,[18] and is reviewed in the following.

The basic problem chosen to illustrate the techniques is based on geometry and properties used previously by Sun and Chen,[19] and consists of center impact of a simply supported square composite plate. The material properties and geometry are given in Table 6.1. Analyses were also carried out on plates with two and four times the standard thickness. As mentioned above, the Rayleigh–Ritz technique used the Newmark method for time integration, and incorporated the nonlinear contact law with the contact area changing at each time step. The analytical solution with Laplace transforms was restricted to a linearisation of the contact law, with a constant contact area throughout the solution.

The results of the computations presented in Qian and Swanson[18] show the importance of using a sufficiently small time step in the numerical time integration used with the Ritz solution, and a time step of $0.1\,\mu s$ was

Table 6.1. Data for the plate impact problem used for comparison

Plate:	[0/90/0/90/0]$_s$ T300/934 carbon/epoxy plate, simply supported plate size: 200 mm by 200 mm

plate thickness: (a)   h = 2.69 mm (0.269 mm/layer)
(b)   2h = 5.38 mm (0.538 mm/layer)
(c)   4h = 10.76 mm (1.076 mm/layer)

E_{11} = 120 GPa E_{22} = 7.9 GPa
$G_{12} = G_{23}$ = 5.5 GPa $v_{12} = v_{23}$ = 0.30
ρ = 1580 kg m^{-3}

Impactor: 12.7 mm diameter steel ball, ρ = 7960 kg m^{-3}
mass = 8.537 g, impact velocity = 3.0 m s^{-1}

Hertzian contact stiffness k_h = 8.394 × 10^8 N m$^{-3/2}$
Linearised contact stiffness k_l = 5.866 × 10^6 N m^{-1}

Source: Qian and Swanson.[18]

employed. Comparisons of the contact force, and target displacement and strain between the two solution techniques were in general good. When the linearised contact law was used with both techniques, the agreement between the two methods was excellent. Using the nonlinear contact law with the Ritz technique and the linearised contact law with the Fourier series expansion technique gives results as shown in Fig. 6.4. Computations for the nominal plate thickness of the example problem showed reasonable agreement, but plates with thickness of two and four times this showed less good agreement, indicating the relative error involved in the linearisation of the contact law. A comparison with the dynamic finite element calculations of Sun and Chen[19] is shown in Fig. 6.5, which shows reasonable agreement for displacement.

6.3.3 Impact of a cylinder

Ramkumar and Thakar[20] have presented an analysis of the dynamic response of curved laminated plates subjected to low-velocity impact. They use Donnell's equations for thin shells, assume that the impact force varies linearly with time, and follow Dobyns's[9] procedure to solve for the response. Vinson and Chou[21] presented a double Fourier series solution of an orthotropic cylindrical shell subjected to a lateral concentrated static load.

A solution technique for impact of laminated cylinders has been presented by Christoforou and Swanson,[11] and a comparison with experimental data has been given by Swanson *et al.*[22] The solution uses Fourier series expansions and Laplace transform techniques, and requires linearisation of the contact stiffness. A review of this approach is given in the following.
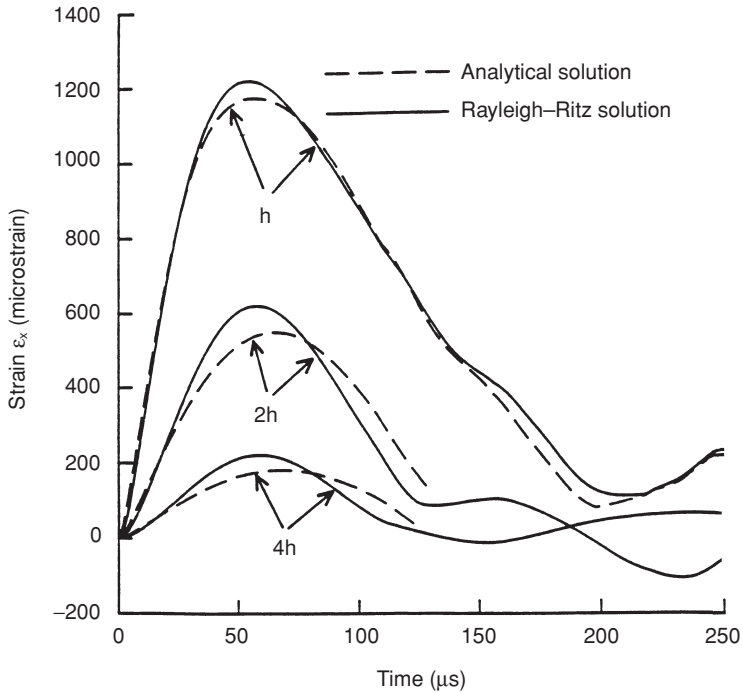
6.4 Comparison of Fourier series–Laplace transform solution with Ritz solution with numerical time integration, for strain behind the impact point in plate impact. (After Qian and Swanson[18].)

This analysis is based on an expansion of the load, displacements, and rotations in a double Fourier series that satisfies the end boundary conditions of simple support. Each expansion is assumed to be separable into a function of time and a function of position. Furthermore, by neglecting in-plane and rotary inertia the problem becomes a second order ordinary differential equation in time for the Fourier coefficients of the radial deflection. On the right hand side of the differential equation are the Fourier coefficients of the loading function. For a given loading impulse the solution can be found by invoking the convolution integral. In the case of impact, the impact force is computed from the deceleration of the impactor mass. This basically involves the equilibrium equation between the impactor and the shell during contact. By neglecting the local contact area deformation, the resulting integral equation can be solved algebraically for the impact force by using Laplace transforms. The expressions for the impact response and force in time are obtained by using the inversion theorem of the Laplace transforms in conjunction with the Cauchy residue theorem.
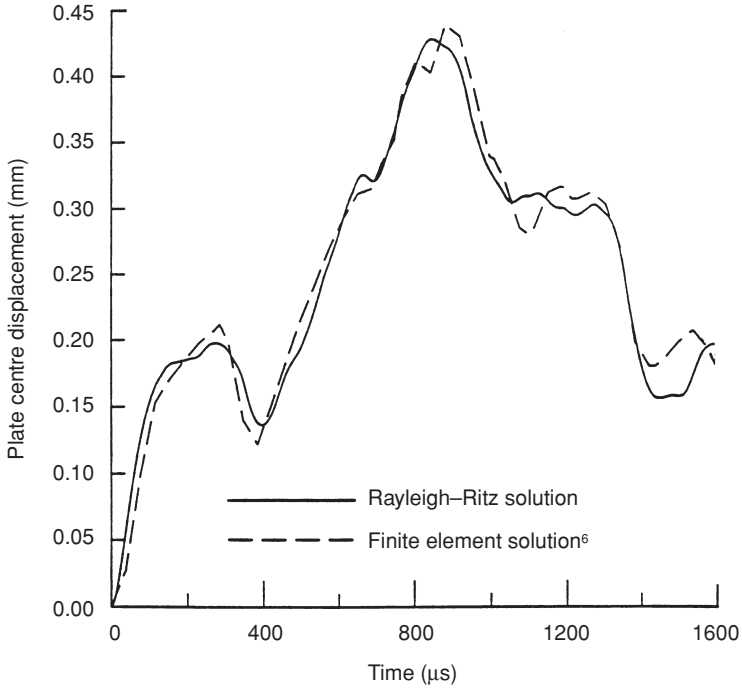
6.5 Comparison of Ritz solution with numerical time integration with dynamic finite solution,[19] for center displacement in plate impact. (After Qian and Swanson[18].)

6.3.3.1 Governing equations for cylinders

Love's equations of motion for a circular cylindrical shell of length L, radius R, and thickness h subject to lateral loads generalised to include shear deformations, combined with the constitutive equations for a specially orthotropic material, result in the equations given by Bert and Birman[13] as:

$$A_{11}u_{,xx} + \frac{A_{66}}{R^2}u_{,\theta\theta} + \left(\frac{A_{12}+A_{66}}{R}\right)v_{,x\theta} + \frac{A_{12}}{R}w_{,x} = \rho h \ddot{u}$$

$$\left(\frac{A_{12}+A_{66}}{R}\right)u_{,x\theta} + A_{66}v_{,xx} + \frac{A_{22}}{R^2}v_{,\theta\theta} - \frac{A_{44}}{R^2}v$$

$$+ \left(\frac{A_{22}+A_{44}}{R^2}\right)w_{,\theta} + \frac{A_{44}}{R}\beta_\theta = \rho h \ddot{v}$$

$$-\frac{A_{12}}{R}u_{,x} - \left(\frac{A_{44}+A_{22}}{R^2}\right)v_{,\theta} + A_{55}w_{,xx} + \frac{A_{44}}{R^2}w_{,\theta\theta} - \frac{A_{22}}{R^2}w$$

$$+ A_{55}\beta_{x,x} + \frac{A_{44}}{R}\beta_{\theta,\theta} + q(x,\theta,t) = \rho h \ddot{w}$$
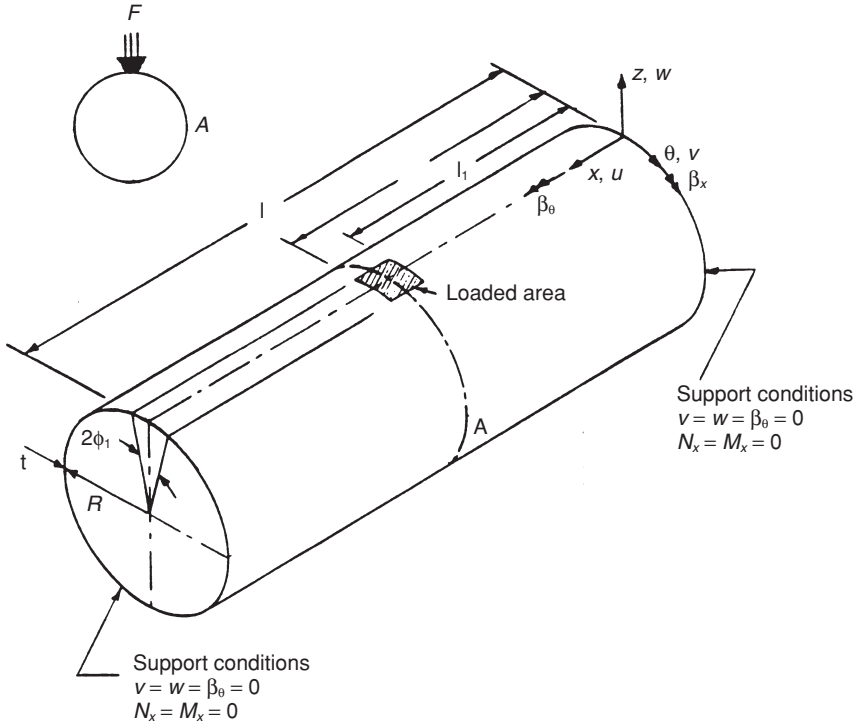
6.6 Geometry of cylinder under transverse impact. (After Christoforou and Swanson[11].)

$$-A_{55}w_{,x} + D_{11}\beta_{x,xx} + \frac{D_{66}}{R^2}\beta_{x,\theta\theta} - A_{55}\beta_x$$

$$+\left(\frac{D_{12} + D_{66}}{R}\right)\beta_{\theta,x\theta} = \frac{\rho h^3}{12}\ddot{\beta}_x$$

$$\frac{A_{44}}{R}v - \frac{A_{44}}{R}w_{,\theta} + \left(\frac{D_{12} + D_{66}}{R}\right)\beta_{x,x\theta} + D_{66}\beta_{\theta,xx}$$

$$+\frac{D_{22}}{R^2}\beta_{\theta,\theta\theta} - A_{44}\beta_\theta = \frac{\rho h^3}{12}\ddot{\beta}_\theta$$

[6.34]

where u, v, and w are the displacements along the axial x axis, circumferential θ axis and radial z axis, β_x and β_θ are bending slopes in the $x - z$ and $\theta - z$ planes, q is lateral pressure loading, ρ is the mass per unit area, A_{ij} and D_{ij} are the standard lamination theory constants, and t is time. A comma denotes differentiation with respect to the space variables, and a dot denotes differentiation with respect to time. The geometry considered is illustrated in Fig. 6.6. The constitutive equations for a specially orthotropic

material ($B_{ij} = 0$, $A_{16} = A_{26} = D_{16} = D_{26} = 0$) have been used to relate the stress, moment, and shear resultants to the midsurface strains ε_i^0, curvatures κ_i, and average transverse shear strains γ_{xz} and $\gamma_{\theta z}$.

6.3.3.2   Solution procedure for impact of cylinders

A closed-form solution of the governing equations is given as follows. The boundary conditions for a cylindrical shell that is freely supported (simply-supported without in-surface restraint) along its curved edges are given by

$$N_x(0, \theta, t) = N_x(L, \theta, t) = M_x(0, \theta, t) = M_x(L, \theta, t) = 0$$
$$w(0, \theta, t) = w(L, \theta, t) = v(0, \theta, t) = v(L, \theta, t) = 0 \qquad [6.35]$$
$$\beta_\theta(0, \theta, t) = \beta_\theta(L, \theta, t) = 0$$

For a given load, the solution to equation [6.34] that satisfies the boundary conditions, equation [6.35], can be separated into a function of time and a function of position as follows:

$$u = U_{mn}(t) \cos n\theta \cos \frac{m\pi x}{L}$$

$$v = V_{mn}(t) \sin n\theta \sin \frac{m\pi x}{L}$$

$$w = W_{mn}(t) \cos n\theta \sin \frac{m\pi x}{L} \qquad [6.36]$$

$$\beta_x = T_{mn}(t) \cos n\theta \cos \frac{m\pi x}{L}$$

$$\beta_\theta = B_{mn}(t) \sin n\theta \sin \frac{m\pi x}{L}$$

and the load as

$$q(x, \theta, t) = Q_{mn}(t) \cos n\theta \sin \frac{m\pi x}{L} \qquad [6.37]$$

Equations [6.36] and [6.37] are the double Fourier series expansions of the displacements, rotations and load, which are similar to the static case developed by Vinson and Chou.[21]

The effects of in-surface and rotary inertia will be assumed to be negligible. Bert and Birman[13] mentioned these effects to be negligible in dynamic stability studies, while Dobyns,[9] by referring to Mindlin's[23] finding made the same assumptions for the impact response of orthotropic plates. Thus, substituting equations [6.36] and [6.37] into equation [6.34] and neglecting in-surface and rotary inertia yields the following set of equations:

$$
\begin{bmatrix}
C_{11} & C_{12} & C_{13} & C_{14} & C_{15} \\
 & C_{22} & C_{23} & C_{24} & C_{25} \\
 & & C_{33} & C_{34} & C_{35} \\
 & sym & & C_{44} & C_{45} \\
 & & & & C_{55}
\end{bmatrix}
\begin{Bmatrix}
U_{mn}(t) \\
V_{mn}(t) \\
W_{mn}(t) \\
B_{mn}(t) \\
T_{mn}(t)
\end{Bmatrix}
=
\begin{Bmatrix}
0 \\
0 \\
\rho h \ddot{W}_{mn}(t) - Q_{mn}(t) \\
0 \\
0
\end{Bmatrix}
\qquad [6.38]
$$

where C_{ij} are given as

$$
C_{11} = -A_{11}\left(\frac{m\pi}{L}\right)^2 - A_{66}\left(\frac{n}{R}\right)^2
\qquad\qquad C_{25} = C_{52} = 0
$$

$$
C_{12} = C_{21} = (A_{12} + A_{66})\left(\frac{n}{R}\right)\left(\frac{m\pi}{L}\right)
\qquad C_{33} = -A_{55}\left(\frac{m\pi}{L}\right)^2 - A_{44}\left(\frac{n}{R}\right)^2 - \frac{A_{22}}{R^2}
$$

$$
C_{13} = C_{31} = \frac{A_{12}}{R}\left(\frac{m\pi}{L}\right)
\qquad\qquad\qquad C_{34} = C_{43} = A_{44}\left(\frac{n}{R}\right)
$$

$$
C_{14} = C_{15} = 0
\qquad\qquad\qquad\qquad\qquad C_{35} = -A_{55}\left(\frac{m\pi}{L}\right)
$$

$$
C_{22} = -A_{66}\left(\frac{m\pi}{L}\right)^2 - A_{22}\left(\frac{n}{R}\right)^2 - \frac{A_{44}}{R^2}
\quad C_{44} = -D_{66}\left(\frac{m\pi}{L}\right)^2 - D_{22}\left(\frac{n}{R}\right)^2 - A_{44}
$$

$$
C_{23} = -\left(\frac{A_{22} + A_{44}}{R}\right)\left(\frac{n}{R}\right)
\qquad\qquad C_{45} = -(D_{66} + D_{12})\left(\frac{n}{R}\right)\left(\frac{m\pi}{L}\right)
$$

$$
C_{24} = C_{42} = \frac{A_{44}}{R}
\qquad\qquad\qquad\qquad C_{55} = -D_{11}\left(\frac{m\pi}{L}\right)^2 - D_{66}\left(\frac{n}{R}\right)^2 - A_{55}
$$

$$
[6.39]
$$

Bert and Birman[13] obtained equations similar to [6.38] for a dynamic stability problem, and showed that they can be reduced to a single linear second-order differential equation by the following transformation:

$$
U_{mn}(t) = K_U W_{mn}(t); \quad V_{mn}(t) = K_V W_{mn}(t)
$$
$$
B_{mn}(t) = K_B W_{mn}(t); \quad T_{mn}(t) = K_T W_{mn}(t)
$$

$$
[6.40]
$$

where the coefficients K_i are given by Bert and Birman[13] as

$$
K_U = S_1 + S_2 K_B + S_3 K_T; \quad K_V = S_4 + S_5 K_B + S_6 K_T
$$
$$
K_B = \Delta_B/\Delta; \quad K_T = \Delta_T/\Delta
$$
$$
\Delta_B = (C_{35} + C_{15}S_1 + C_{25}S_4)(C_{45} + C_{14}S_3 + C_{24}S_6)
$$
$$
\quad - (C_{34} + C_{14}S_1 + C_{24}S_4)(C_{55} + C_{15}S_3 + C_{25}S_6)
$$
$$
\Delta_T = (C_{45} + C_{15}S_2 + C_{25}S_5)(C_{34} + C_{14}S_1 + C_{24}S_4)
$$
$$
\quad - (C_{44} + C_{14}S_2 + C_{24}S_5)(C_{35} + C_{15}S_1 + C_{25}S_4)
$$

$$\Delta = (C_{44} + C_{14}S_2 + C_{24}S_5)(C_{55} + C_{15}S_3 + C_{25}S_6)$$
$$- (C_{45} + C_{14}S_3 + C_{24}S_6)(C_{45} + C_{15}S_2 + C_{25}S_5)$$

$$S_1 = (C_{12}C_{23} - C_{22}C_{13})/S \qquad S_2 = (C_{12}C_{24} - C_{22}C_{14})/S$$
$$S_3 = (C_{12}C_{25} - C_{22}C_{15})/S \qquad S_4 = (C_{12}C_{13} - C_{11}C_{23})/S \qquad [6.41]$$
$$S_5 = (C_{12}C_{14} - C_{11}C_{24})/S \qquad S_6 = (C_{12}C_{15} - C_{11}C_{25})/S$$
$$S = C_{11}C_{22} - C_{12}^2$$

Substituting equation [6.40] into the third equation in [6.38] yields

$$\ddot{W}_{mn}(t) + \frac{K_{mn}}{\rho h} W_{mn}(t) = \frac{1}{\rho h} Q_{mn}(t) \qquad [6.42]$$

where the coefficients K_{mn} are given by

$$K_{mn} = -(C_{13}K_U + C_{23}K_V + C_{33} + C_{34}K_B + C_{35}K_T) \qquad [6.43]$$

The terms of the Fourier series representation for the load, applied uniformly over a small rectangular area, $2R\phi_1(l_2 - l_1)$, at the center of the cylindrical shell $(L/2, 0)$ are

$$Q_{mn}(t) = P_{mn} \frac{F(t)}{2R\phi_1(l_2 - l_1)} \qquad [6.44]$$

where

$$P_{mn} = \frac{8}{mn\pi^2} \sin\frac{m\pi}{2L}(l_2 + l_1)\sin\frac{m\pi}{2L}(l_2 - l_1)\sin n\phi_1 \qquad [6.45]$$

Substituting equation [6.44] into [6.42] and rearranging yields

$$\ddot{W}_{mn}(t) + \omega_{mn}^2 W_{mn}(t) = \frac{P_{mn}\pi RL}{R\phi_1(l_2 - l_1)} \frac{F(t)}{m_1} \qquad [6.46]$$

where $\omega_{mn}^2 = K_{mn}/\rho h$ are the fundamental frequencies of the shell and m_1 is the mass of the shell.

For zero initial displacement and velocity, the solution of equation [6.46] is

$$W_{mn}(t) = \frac{P_{mn}\pi RL}{R\phi_1(l_2 - l_1)m_1\omega_{mn}} \int_0^t F(\tau)\sin\omega_{mn}(t - \tau)d\tau \qquad [6.47]$$

Using equations [6.47] and [6.40] with [6.36] results in expressions for the deformations in a shell under transverse loading, for example, the transverse deflection at any point of the shell is given by

$$w(x,\theta,t) = \frac{\pi RL}{R\phi_1(l_2 - l_1)m_1} \sum_m \sum_n \frac{P_{mn}}{\omega_{mn}} \sin\frac{m\pi x}{L} \cos n\theta$$

$$\times \int_0^t F(\tau)\sin\omega_{mn}(t - \tau)d\tau \qquad [6.48]$$

6.3.3.3 Impact loading

The response of a cylindrical shell to impact loading may be computed from the transient response, equation [6.48], by computing the impact force from the deceleration of the impactor mass. This procedure parallels that given previously above for plates in Section 3.2.2.

The solution for the coefficients of the radial displacement are finally given by

$$W_{mn}(t) = \frac{P_{mn}\pi RL}{R\phi_1(l_2 - l_1)m_1} \sum_j \frac{F_j}{\omega_{mn}(\omega_j^2 - \omega_{mn}^2)}(\omega_j \sin\omega_{mn}t - \omega_{mn} \sin\omega_j t) \quad [6.49]$$

and by combining the above equations, the deflection and strain histories at any point of the shell can be evaluated.

A series of impact experiments with transverse impact of laminated cylinders has been reported by Swanson et al.[22] A typical comparison of a calculation made using the theory described above with three replicate experiments is shown in Fig. 6.7. It is seen that the comparison of calculated and measured strain is very reasonable.

6.4   The quasi-static approximation

The quasi-static calculation procedure involves treating the impact problem as an equivalent static problem with a static load applied to the impact site. By treating the impact mass and structure as a simple spring-mass system (neglecting the mass of the structure in comparison to the impact mass), the impact force can be obtained from the formula

$$F = v_i\sqrt{K_{st}M_i} \qquad [6.50]$$

where v_i and M_i are velocity and mass of the impactor, and K_{st} is the static stiffness of the structure. This formula can equivalently be obtained by equating the kinetic energy of the impactor to the strain energy of the structure. The stresses and strains in the structure are then obtained from the static solution, using the force from equation [6.50]. It is possible to include the Hertzian contact law as developed by Sun et al.[4,5] for anisotropic materials, to refine the above procedure.
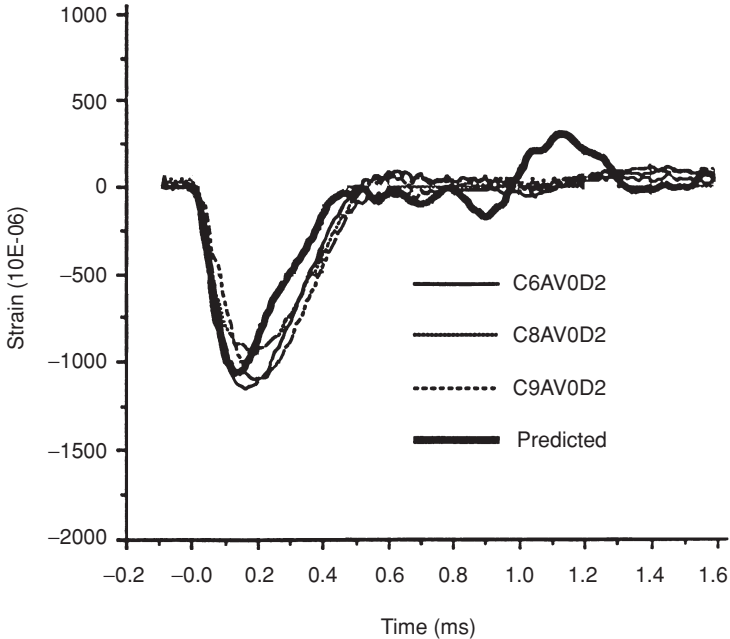
6.7 Comparison of analysis with strain gauge readings in impact of cylinders. The axial strains near the impact point in three separate experiments are shown. (After Swanson et al.[22])

Clearly the quasi-static solution is much simpler to use than the structural dynamics solution. The question that arises is whether it is possible to determine the limits of applicability of the quasi-static solution, without recourse to a more complicated dynamic solution. A dimensionless parameter consisting of the ratio of the mass of the impactor to the 'effective' structure mass has been developed[24] that permits identification of the range of applicability of the quasi-static solution. This procedure is briefly reviewed in the following.

6.4.1   Limits of quasi-static analysis

An often employed rule-of-thumb is that the quasi-static approximation is valid if the frequency of the impact (say as defined by the contact duration) is less than 1/3 the lowest natural frequency of the structure.[25] When dynamic effects in the structure do become important, the impact force and the resulting peak values of stresses and strains in the structure typically become larger than they would be for a given impact energy under quasi-static loading. This will be illustrated in calculations to be shown subsequently for impacts of plates and cylinders.

The rule-of-thumb cited above does seem to be a reasonable method of ascertaining the limit of the quasi-static solution. However, it entails knowing at least the lowest natural frequency of the structure. This may be a significant drawback in some cases, as the point of the quasi-static approximation is to be able to analyse the impact event without knowledge of the dynamic solution. While it is easier to get a natural frequency of the structure than the entire dynamic response, there is still motivation for developing an alternative rule for the limits of the quasi-static approximation without knowing the structure's natural frequency. This objective is pursued in the next section, following the work of Swanson.[24]

6.4.2 Alternative rule for limits of quasi-static approximation

Intuitively it can be seen that if the impact mass is large with respect to the structure mass, the impact event can be treated as quasi-static. This idea can be simply related to the conventional rule for the ratio of natural frequencies given above. The approach taken is to develop an expression for an equivalent lumped mass, that can be used in conjunction with the static stiffness to approximate the lowest natural frequency of the structure. The definition of the equivalent mass will be given subsequently. The first premise to be advanced is that the lowest natural frequency of the structure can be approximated as

$$\omega_n \approx \sqrt{\frac{K_{st}}{m_{eq}}} \qquad [6.51]$$

The impact frequency is given by

$$\omega_i \approx \sqrt{\frac{K_{st}}{m_{eq} + M_i}} \qquad [6.52]$$

Using the rule-of-thumb given above for the limits of quasi-static impact in terms of frequencies leads directly to the rule for the limits of validity of the quasi-static approximation as

$$M_i \geq 8m_{eq} \approx 10m_{eq} \qquad [6.53]$$

Thus a rule-of-thumb for the limits of the quasi-static approximation for impact problems has been formulated in terms of the ratio of impact mass to equivalent structure mass, which can be easily determined.

The equivalent structure mass is defined here implicitly by the following formula,

$$\frac{1}{2} m_{eq} v_c^2 = \frac{1}{2} \int_{Vol} \rho v^2 dVol \qquad [6.54]$$

where m_{eq} is the equivalent lumped mass of the structure, v_c is the peak velocity of the contact point for the impact, v is the peak velocity distribution throughout the impacted structure, and the integral is taken over the entire structure. The above expression is based on equating the energy of the equivalent lumped mass to the energy of the structure. If the assumption is made that the structure is undergoing motion in the mode determined by the quasi-static approximation, then the peak velocities are proportional to peak displacements, and the displacements are those calculated from a static application of load at the contact point. Thus, the above can be replaced by

$$\frac{1}{2} m_{eq} \delta_c^2 = \frac{1}{2} \int_{Vol} \rho w^2 dVol \qquad [6.55]$$

where here δ_c is the displacement at the point of impact, and w is the transverse displacement throughout the body as calculated by a static analysis. It is important to note that equation [6.55] enables the equivalent mass to be calculated from a knowledge of the static deformation of the body alone, without requiring access to a dynamic solution. The procedure given in [6.55] has been suggested for calculating lumped mass approximations, as presented by Steidel,[26] for example, as an approximate method of calculating natural frequencies for beams and rods.

The central issue at present is whether the equivalent lumped mass can be used to estimate the limits of suitability of a quasi-static solution for an impact problem. This is addressed in the following by comparing dynamic calculations with quasi-static calculations for various impact problems.

6.4.3 Comparison of dynamic and quasi-static impact response

The calculations shown in this section will use solutions for impact problems of orthotropic plates and cylinders with various boundary conditions. Various example solutions for the impact response of structures were calculated using the procedures described above, for various values of impact mass. The equivalent masses of the structures were calculated using static solutions.[55] The response quantities examined were the contact force, normal strains behind the impact point, and peak interlaminar shear stress values. In general, all of these response values start to increase relative to
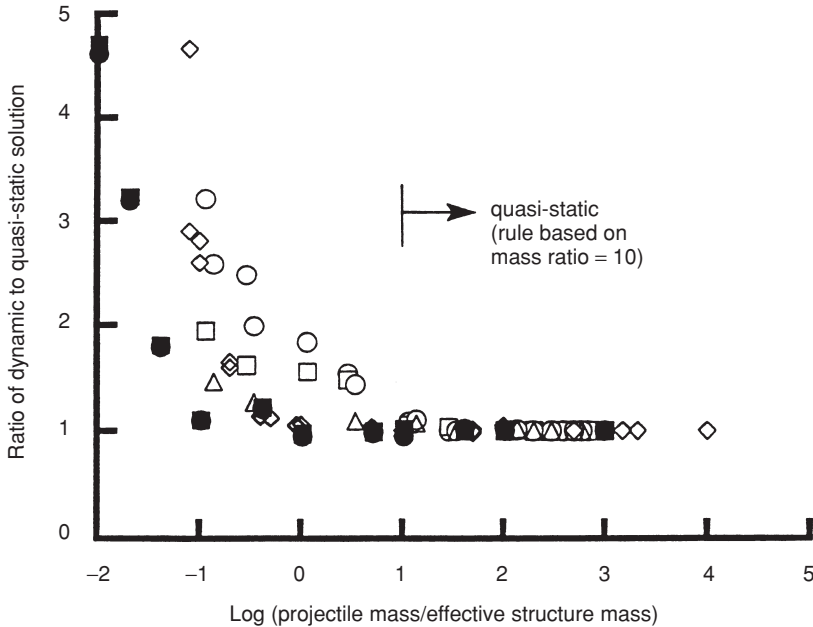
6.8 Transition from quasi-static to dynamic response in impact of composite plates and cylinders. The variables shown are peak contact force, strain behind the impact point, and interlaminar shear stress. Plates are both simply supported and clamped-clamped, free-free, and cylinders are of two lengths. (After Swanson[24].)

the quasi-static solution when impact energy is held constant, as dynamic effects in the structure start to become important.

A typical set of results for two different lengths of an orthotropic cylinder and plate solutions for two different sets of boundary conditions, using the calculational procedures discussed above, are shown in Fig. 6.8. These results have been normalised by dividing by the quasi-static solution, holding impact energy constant, and plotted as a function of the ratio of impact mass to equivalent structure mass as calculated by equation [6.55]. The critical ratio of impact mass to equivalent structure mass has been taken as 10 from [6.53], and is also shown. It can be seen that this rule is in fact a reasonable estimate of the limit of the validity of the quasi-static approximation.

Qualitatively the results are quite comparable, as the value of 10 for the ratio of impact mass to equivalent structure mass appears to represent the limit of the quasi-static approximation for both the plates and cylinders reasonably well.
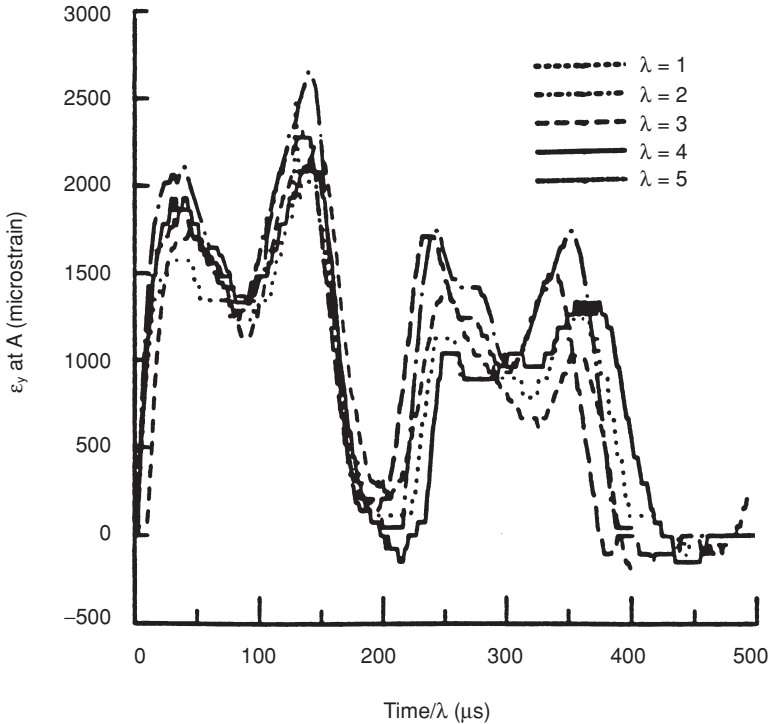
6.9 Comparison of strain response in impact tests on five different plate sizes. Plates are scaled geometrically by the parameter λ, and the analysis shows that time is also scaled by λ. (After Qian and Swanson[16].)

6.5   Issues of scaling in impact

The question of scaling, i.e. extrapolating from tests on small laboratory specimens to larger structures, is an important issue in impact. This issue has been addressed by a number of authors, including Morton,[27] Sankar,[28] Qian et al.,[29] Qian and Swanson,[16] Swanson et al.,[22] and others. Analytical solutions such as those discussed in the above are very helpful in understanding the issues of scaling, as the governing equations can be manipulated to reveal the dimensionless parameters involved. An approach taken[16,22,29] was to use geometric scaling, which also dictated the scaling of time. A typical result of scaled impact experiments on plates is shown in Fig. 6.9, where the linear response is found to scale within the basic reproducibility of the experiments for five sizes of plates. Scaling of the damage formation resulting from impact is more complicated. For example, Swanson[30] found that the scaling associated with delamination resulting from impact is that characteristic of fracture mechanics. Christoforou and Yigit[31,32] also address

scaling of impact, and in addition develop dimensionless numbers characterising impact with respect to the relative importance of indentation, and the conditions for quasi-static analysis to be applicable.

6.6   Summary and conclusions

The fundamental equations and some solution procedures have been presented for elastic impact of laminated plates and cylinders. Issues of convergence and accuracy have been addressed, and comparisons with experimental data have been given. The results show that the linear response of these fundamental structural elements is reasonably well understood.

References

1 Zukas J A, *et al.*, *Impact Dynamics*, New York, Wiley, 1982.
2 Joshi S P and Sun C T, 'Impact induced fracture in a laminated composite', *J Composite Mater*, 1985 **19** 51–66.
3 Sun C T and Chattopadhyay S, 'Dynamic response of anisotropic laminate plates under initial stress to impact of a mass', *J Appl Mech*, 1975 **42** 693–8.
4 Yang S H and Sun C T, 'Indentation law for composite laminates', *Composite Materials: Testing and Design (Sixth Conference), ASTM STP 787*, pp 425–49, 1982.
5 Tan T M and Sun C T, 'Use of statical indentation laws in the impact analysis of laminated composite plates', *J Appl Mech*, 1985 **52** 6–12.
6 Lekhnitskii S G *Anisotropic Plates*, transl S W Tsai and T Cheron, New York, Gordon and Breach Science, 1968.
7 Whitney J M and Leissa A W, 'Analysis of a simply-supported laminated anisotropic rectangular plate', *AIAA J*, 1970 **7** 28.
8 Whitney J M and Pagano N J, 'Shear deformation in heterogeneous anisotropic plates', *J Appl Mech*, 1970 **37** 1031.
9 Dobyns A L, 'Analysis of simply-supported orthotropic plates subject to static and dynamic loads', *AIAA J*, 1981 **19** 642.
10 Birman V and Bert C W, 'Response of composite plates to blast loading', in *Proc ICCM & ECCM Conf*, **5**, Imperial College of Science and Technology, London, July 20–24, 5.192, 1987.
11 Christoforou A P and Swanson S R, 'Analysis of simply-supported orthotropic cylindrical shells subject to lateral impact loads', *J Appl Mech*, 1990 **57** 376–82.
12 Christoforou A P and Swanson S R, 'Analysis of impact response in composite plates', *Intl J Solids Struct*, 1991 **27** 161–70.
13 Bert C W and Birman V, 'Dynamic stability of thick, orthotropic, circular cylindrical shells', in *Lecture Notes in Engineering: Refined Dynamic Theories of Beams, Plates and Shells and Their Applications*, Springer-Verlag, Berlin, 235, 1987.
14 Bert C W and Chen T L C, 'Effect of shear deformation on vibration of antisymmetric angle-ply laminated rectangular plates', *Int J Solid Struct*, 1978 **14** 465.

15 Cairns D S and Lagace P A, 'Transient response of graphite/epoxy and kevlar/epoxy laminates subjected to impact', presented at *29th Structures, Structural Dynamics and Materials Conference* (not published in Proceedings), 1988.

16 Qian Y and Swanson S R, 'Experimental measurement of impact response in carbon/epoxy plates', *AIAA J*, 1990 **28** 1069–74.

17 Timoshenko S and Young D H, *Vibration Problems in Engineering*, 3rd edn, Van Nostrand, New York, 1955.

18 Qian Y and Swanson S R, 'A comparison of solution techniques for impact response of composite plates', *Composite Struct*, 1990 **14** 177–92.

19 Sun C T and Chen J K, 'On the impact of initially stressed composite laminates', *J Composite Mater*, 1985 **19** 490.

20 Ramkumar R L and Thakar Y R, 'Dynamic response of curved laminated plates subjected to low velocity impact', *ASME J Eng Mater Technol*, 1987 **109** 67–71.

21 Vinson J R and Chou T W, *Composite Materials and Their Use in Structures*, Applied Science, London, 1975.

22 Swanson S R, Smith N L and Qian Y, 'Analytical and experimental strain response in impact of composite cylinders', *Composite Struct*, 1991 **18** 95–108.

23 Mindlin R D, 'Influence of rotary inertia and shear on flexural motions of isotropic elastic plates', *ASME J Appl Mech*, 1951 **18** 31–8.

24 Swanson S R, 'Limits of quasi-static solutions in impact of composite structures', *Composites Eng*, 1992 **2** 261–7.

25 Cook R D, Malkus D S and Plesha M E, *Concepts and Applications of Finite Element Analysis*, 3rd edn, New York, Wiley, 1989.

26 Steidel R F, *An Introduction to Mechanical Vibrations*, 3rd edn, New York, Wiley, 1989.

27 Morton J, 'Scaling of impact-loaded carbon-fiber composites', *AIAA J*, 1988 **26** 989–94.

28 Sankar B V, 'Scaling of low-velocity impact for symmetric composite laminates', *J Reinforced Plastics Composites*, 1992 **11** 296–309.

29 Qian Y, Swanson S R, Nuismer R J and Bucinell R B, 'An experimental study of scaling rules for impact damage in fiber composites', *J Composite Mater*, 1990 **24** 559–70.

30 Swanson S R, 'Scaling of impact damage in fiber composites from laboratory specimens to structures', *Composite Struct*, 1993 **25** 249–55.

31 Yigit A S and Christoforou A P, 'Impact dynamics of composite beams', *Composite Struct*, 1995 **32** 187–95.

32 Christoforou A P and Yigit A S, 'Characterization of impact in composite plates', *Composite Struct*, 1998 **43** 15–24.

Impact behaviour and analysis of CFRP laminated plates

ENBOA WU AND CHENG-ZORN TSAI

7.1   Introduction

The low-velocity impact behaviour of composite laminates has been studied extensively in recent decades. As described in two review papers,[1,2] experimental results reported in the literature have mainly focused on impact-induced damage mechanisms, such as matrix cracking, delamination and fiber breakage in different impact stages; on the other hand, most of the analytical methods have focused on elastic impact on laminates with perfect boundaries. Aside from direct investigation of the laminate damage using the naked eye, such as for glass/epoxy laminates that are partially light transparent,[3–5] C-scan or X-ray has mostly been employed in damage assessment.[6,7] A focused treatment of this topic is available in Chapter 2. The apparatus that has provided the impact energy has usually been a drop weight tower. Due to the limitation of the tower height, almost all the impact events have been conducted using a heavy impactor at a velocity of less than 10 m/s. The impact force has usually been recorded by a force transducer embedded in the impactor. The corresponding histories of energy, velocity, and displacement were then derived once the onset of contact between the impactor and the target was detected by Cantwell and Morton[8] and others in Chapters 5 and 8.

On the other hand, the higher-speed impact results published in the literature have been far fewer than those for lower-speed impact. One reason has been the need for a gas gun to provide the initial kinetic energy of the impactor. In this category, impact has generally been conducted using a lighter impactor, most of the time called a projectile, at a much higher initial velocity. Further, because it is very difficult to mount a sensor in a flying projectile,[9,10] the data recorded during such an impact event has usually been only the initial and the final states of the projectile and the target. The history of impact, even if a high-speed camera was employed, was very hard to record. For example, Gupta and Davids back in 1966[11] used a rifle to launch projectiles which struck glass/epoxy laminates at impact speeds from

305 to 387 m/s and found a linear relationship between the projectile energy loss and the target thickness. Takeda *et al.*[12,13] studied the delamination crack propagation phenomena of glass/epoxy laminates for projectiles at initial speeds up to 83 m/s. Cantwell and Morton investigated the effects of laminate thickness, dimensions, and stacking sequence on the penetration energy threshold.[14–16] Zhu *et al.* reported the impact phenomena for kevlar/polyester composites struck by cylindrically-conical projectiles.[17] The results of impact on graphite/epoxy laminates by blunt projectiles were reported by Lee and Sun.[18,19] The effect of the strain rate on the penetration behaviour was also uncovered by Jenq *et al.*[20] and Wu and Chang.[5] Other high-velocity impact studies can be found in Chapters 8 and 9.

Meanwhile, as the composite laminated structures used in modern industry have rapidly increased, the need to more accurately predict the impact response of such advanced structures has become inevitable. In the past, most of the studies focused on the development of analytical or numerical methods to predict the elastic response of laminated beams,[21] plates[22–25] and shells,[26] and the relationship between the impactor and the struck laminate was frequently modelled using the modified Hertz contact law,[27] which was verified experimentally[7,28] and analytically.[29,30] A further example is available in Chapter 6. On the other hand, the inverse method was found to be able to detect the impact force, location, impactor mass and velocity using the response, which sometimes was even incomplete, of the struck plate.[31–35] This method was also found to be able to reconstruct forces in bar-to-bar impact problems.[36]

However, most, if not all, of the experimental results reported in the literature for impact on graphite/epoxy composite laminates involving a gas gun, i.e. high-velocity impact, described only the final state, and in the analytical predictions, the laminates were all assumed to have perfect boundary conditions. In this chapter, the goal is to obtain the impact history of such advanced structures when they are struck by projectiles in a velocity range that is from very low to way above the ballistic limit of the targets, and to present an analytical method that can take boundary imperfection into consideration. In the experimental investigation, a gas gun was employed to launch a hemispherically tipped projectile to strike a 32-layered quasi-isotropic graphite/epoxy laminate. Transient laser Doppler anemometry (TLDA), which was developed at the National Taiwan University and is a noncontact measurement method having a 1.0 μs sampling rate, was employed to extract the velocity history of the projectile while it was striking the target. This excellent technique has been successfully employed to uncover the impact process of metallic targets,[37,38] glass/epoxy laminates[39,40] and honeycombs.[41] The force and the displacement histories were then subsequently derived. Thus, the terminal velocity, impact energy, absorbed energy, peak force and momentum change were obtained. The impact

response of this laminated structure will be discussed in detail using these data and the measured laminate damage area. On the other hand, the Ritz method along with the Mindlin plate theory was employed to construct the governing equations of a laminated plate under impact conditions. In order to predict the impact response of a laminate under 'imperfect' boundary conditions, two beam functions, one satisfying simply supported conditions and the other satisfying fixed conditions, were employed, and a non-dimensional constant that represents the rotational spring constant of the physical clamp was used. The actual value of the rotational spring constant was obtained from the quasi-static contact test result. The correlation between the prediction and the measured data will be used to verify the presented method.

7.2   Experimental set-up and procedure

7.2.1 Specimen

Fiberite Hy-E 1076E T300/976 graphite/epoxy prepregs were employed to fabricate the specimens using an autoclave. All the specimens were 32-ply $(0/45/90/-45)_{4S}$ quasi-isotropic laminates. The nominal thickness was $4.3 \pm 0.1\,mm$. The in-plane dimensions were $152.4\,mm$ by $101.6\,mm$. The $0°$ laminae were along the long dimension. Two types of boundary conditions were employed. In the first type, the plates were suspended by two light strings attached to two adjacent corners of the plate to simulate the free boundary condition, and was used for verification of the presented analytical method as the boundary can easily be made to be perfect. On the other hand, in most of the test runs, the laminates were tightly clamped on two opposite edges with the other two free of support, resulting in a clamped span of $101.6\,mm$ and leaving the original short dimension of $101.6\,mm$ as the free span. After the specimens were struck, they were C-scanned to uncover the delamination damage profile. In this study, the delamination area was defined as the area that was enclosed by the outermost crack fronts in all the interfaces along the thickness direction of the laminate.

7.2.2 Experimental procedure

The transient laser Doppler anemometer (TLDA), which was developed in the Impact and Precision Measurement Laboratory of National Taiwan University, was employed for extraction of the quickly changing velocity history of a projectile during impact and penetration.[38] This is a back-scattering arrangement. It allows the Doppler signals to scatter backward to the optical devices through which the laser beams originally passed.

The principle of laser Doppler anemometry is to intersect two coherent light beams to form a small measuring volume in an ellipsoidal shape, whose

size depends upon the beam diameter and the light intersection angle, 2κ, and is usually only a few mm in all three ellipsoidal axes. Because of light interference, fringes of spacing d_f are formed inside the measuring volume. When particles on the surface of a projectile travel across the fringes inside the measuring volume, light is scattered. By recording the history of this scattered light, the velocity history of the surface of the projectile can be obtained using the following equation:[42,43]

$$V = \frac{\lambda}{2 \sin \kappa} f_D \tag{7.1}$$

where λ is the wave length of the coherent light and f_D is the frequency of the Doppler signal. In this study, $\lambda = 632.8\,\text{nm}$ and $\kappa = \tan^{-1}(1/20)$. Thus, $d_f = \lambda/(2 \sin \kappa) = 6.336\,\mu\text{m}$ and $V = 6.336 \times 10^{-6} f_D\,\text{m/s}$. A detailed description of the LDA principle can be found in Durst et al.[42] and Drain.[43]

The experimental set-up for the impact test is schematically shown in Fig. 7.1. A gas gun was employed to launch a hemispherically tipped projectile, made of hard steel, of 12.7 mm diameter. The mass of the projectile was 35.6 g, and its length was 38.0 mm. The projectile was hardened to R_c60 to avoid possible plastic deformation during impact.

The transient laser Doppler anemometer (TLDA) system included a 35 mW He–Ne laser light source, a series of optical devices for passage of the laser light and the scattered Doppler signals, a photomultiplier for conversion of the scattered Doppler signals into electric current, and a band-passed filter for filtering out noises and pedestal signals carrying the Doppler signals. To simplify the process, the zero-crossing method was employed to extract the velocity history from the recorded Doppler signals. This was similar to the method used by Wu and Chang for impact on glass/epoxy laminates.[4,5] On the other hand, a complete description of the implementation procedure for TLDA can be found in Tsai and Wu.[38]

After the velocity data were obtained, the acceleration history could be retrieved, in principle, by means of differentiation. In order to avoid errors from being induced in the acceleration due to direct differentiation, the smoothing cubic-spline method was employed. This method was a modification of the cubic-spline interpolation method, in which a function, $f(x)$, in the following form is usually used:[44]

$$f(x) = a_i + b_i(x - x_i) + c_i(x - x_i)^2 + d_i(x - x_i)^3$$
$$x_i \le x \le x_{i+1} \quad i = 1, 2, \ldots, n-1 \tag{7.2}$$

where (x_i, y_i), $i = 1, 2, \ldots, n$; $n > 3$ are the recorded discrete data points set and $y_i = f(x_i)$. To suppress the noise, an objective function E is defined as

$$E(a_i, S) = \sum_{i=1}^{i=N} (y_i - a_i)^2 + S \int_{x_1}^{x_N} [f''(x)]^2 dx \tag{7.3}$$
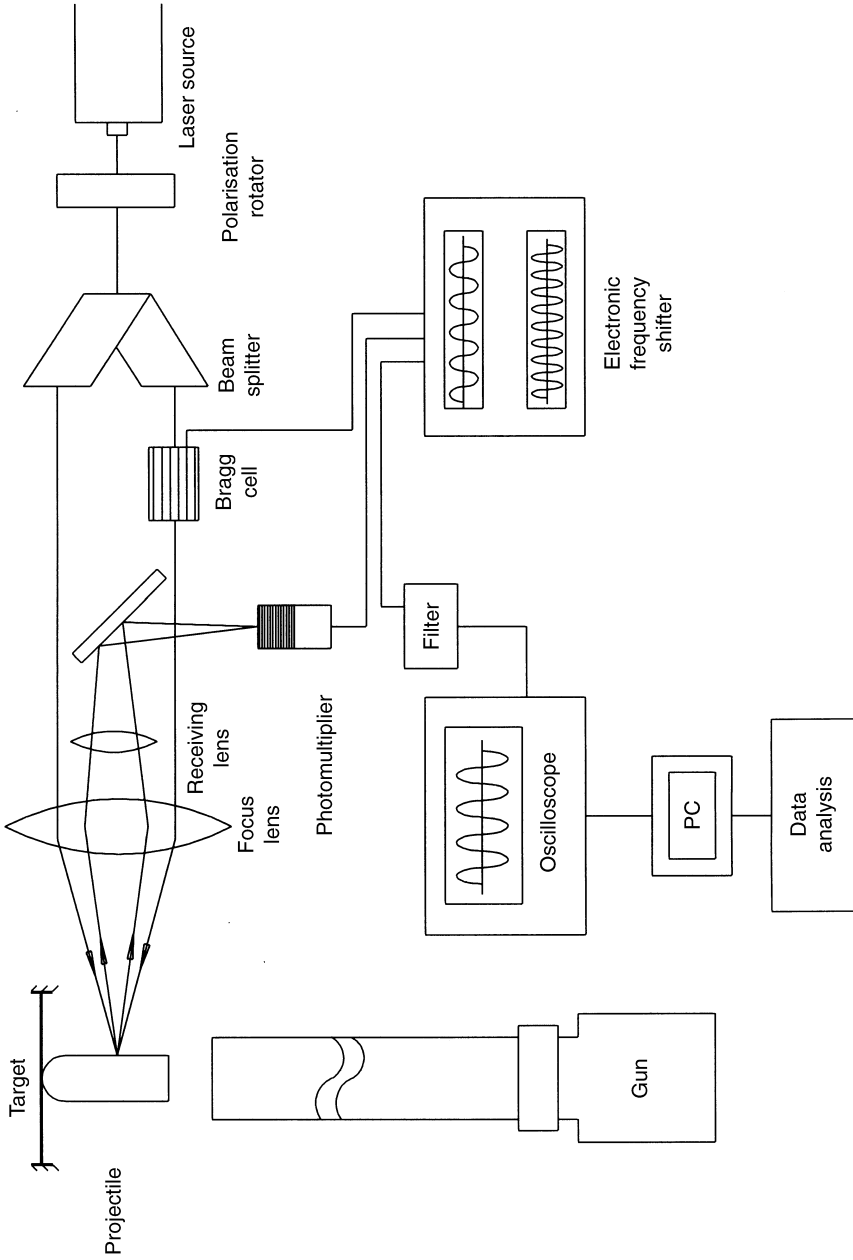
7.1 A schematic of the experimental set-up for impact on composite laminates.

where S is the smoothing parameter. The first term in [7.3] represents the deviation between f and the data point, and the second term is the smoothing level of f. A detailed description of the smoothing cubic-spline method can be found in de Boor.[44] This method acts as a low-pass filter to the velocity data extracted from Doppler signals. The acceleration history was then obtained by means of direct differentiation of the function f. A detailed description of the implementation procedure can also be found in Tsai[45] and examples shown in later sections. On the other hand, the displacement history was obtained by means of direct integration of the velocity data. The time for the onset of contact between the projectile and the target was precisely determined using a piezo-film attached at the center of the distal side of the laminated plate.[37]

7.3   Near-elastic impact behaviour

In this velocity range, no damage was found in laminates using both visual inspection by means of the naked eye and C-scan. The impact velocity of the projectile was lower than $20\,\mathrm{m\,s^{-1}}$. Typical velocity and force histories for the struck laminates in this category are shown in Fig. 7.2(a) and (b), which shows projectile impact results at 8.3 and $14.5\,\mathrm{m\,s^{-1}}$, respectively. Before the onset of contact, the velocity remained constant. This value dropped drastically once the projectile hit the target, and caused the projectile to indent the laminate in the contact region. The amount of indentation was equal to the difference of movement between the target and the projectile, and could be related to the impact force using the modified type of Hertz contact law.[7] Thus, this indentation caused the impact force to increase drastically. In the meantime, the impact neighbourhood of the target started to move forward owing to the action of the projectile. This movement immediately decreased the indentation value, and the force dropped almost as sharply as in the rising part, thus forming the first peak.

As impact proceeded, the velocity of the impact neighbourhood of the struck laminate was reduced due to the action of the bending stiffness of the laminate. As a result, the value of the indentation increased again. This resulted in a drastic increase of the force value. In this study, the second force peak was always observed when the laminate was not significantly damaged and occurred when the projectile velocity decreased to approximately zero, as typically shown in Fig. 7.2(a) and (b).

It is interesting to note that a third force peak was also observed, and that the projectile physically separated from the target before the third peak occurred. Further, this phenomenon occurred when the projectile velocity was negative. Apparently, the projectile was hit by the target when the target bounced back. Due to the force exerted by the bouncing target,
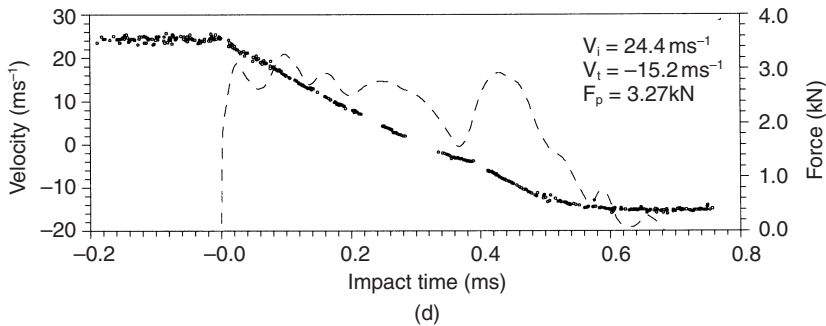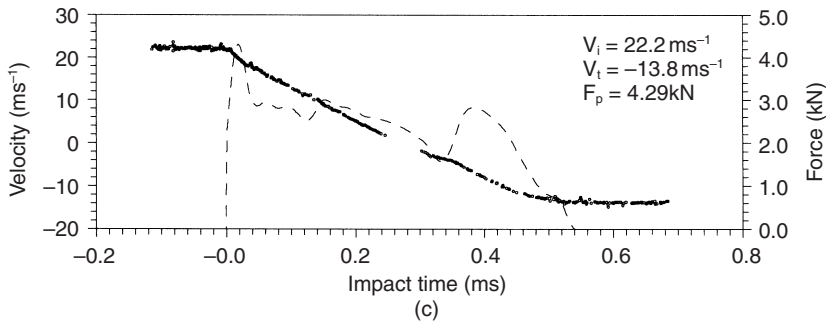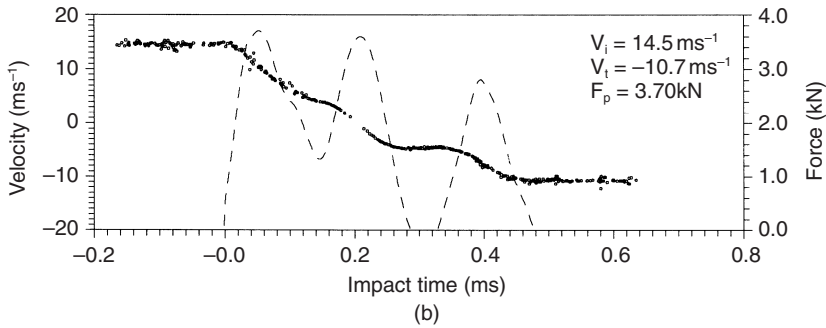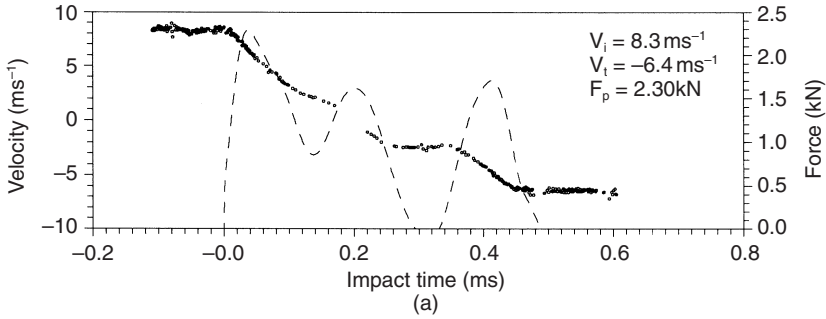
7.2 Velocity and force histories for laminates struck at (a) 8.3 m s⁻¹; (b) 14.5 m s⁻¹; (c) 22.2 m s⁻¹; (d) 24.4 m s⁻¹; (e) 31.8 m s⁻¹; and (f) 36.2 m s⁻¹.

$V_i = 31.8\,\text{ms}^{-1}$
$V_t = -5.1\,\text{ms}^{-1}$
$F_p = 4.23\,\text{kN}$

(e)

$V_i = 36.2\,\text{ms}^{-1}$
$V_t = 10.0\,\text{ms}^{-1}$
$F_p = 3.63\,\text{kN}$

(f)
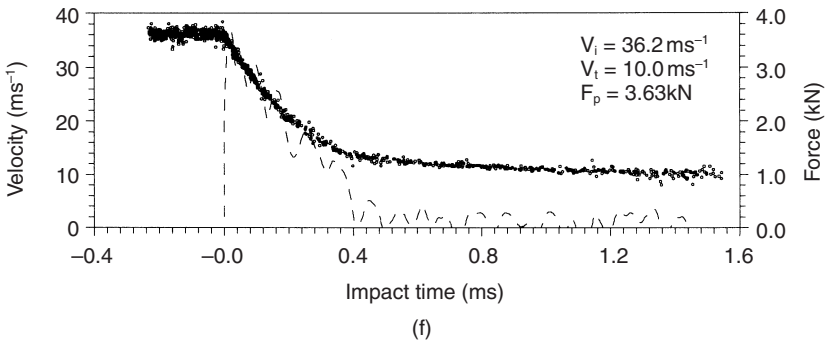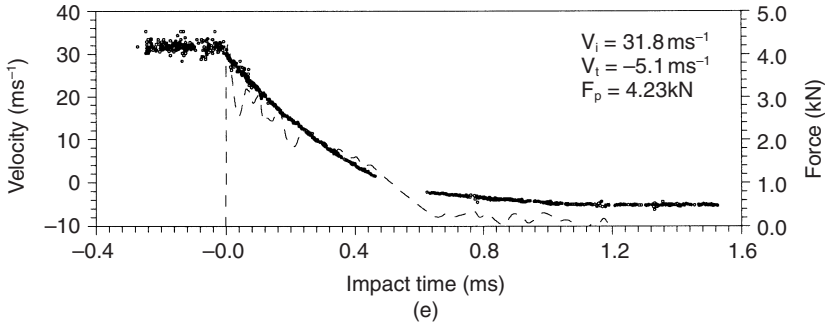
7.2 (cont.)

the absolute value of the projectile velocity increased again, but in the negative direction. The impact process terminated when the bouncing target was pulled again in the forward direction due to its bending stiffness, at which point the projectile gained enough momentum from the bounced target and started to separate permanently from the target.

The relationship between the impact and the terminal velocities for the event in which the struck laminates showed no delamination damage is illustrated in Fig. 7.3. A straight line was found to fit the relationship fairly well. Thus, the relationship between the absorbed energy, ΔE, and the impact velocity, V_i, was found to be quadratic, as shown in Fig. 7.4. On the other hand, a straight-line relationship is also observed in Fig. 7.5 between the impact velocity and the maximum force peak for each test run. Note that, in Fig. 7.2(a) and (b), the first peak in the multi-peak impact event always has the highest magnitude. This is because the largest indentation value between the projectile and the target always occurred very shortly after the onset of first contact. During this very short period the target did not deform extensively. As a result, the target response to impact was not similar to the target response to quasi-static loading because the peak force in the latter case always occurred when the deflection was largest.
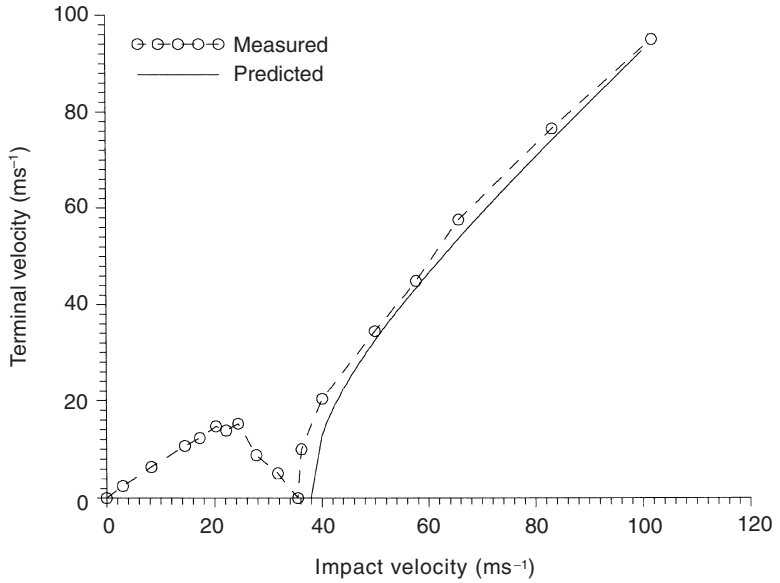
7.3 The relationship between the impact velocity, V_i and the terminal velocity, V_t of the projectile.
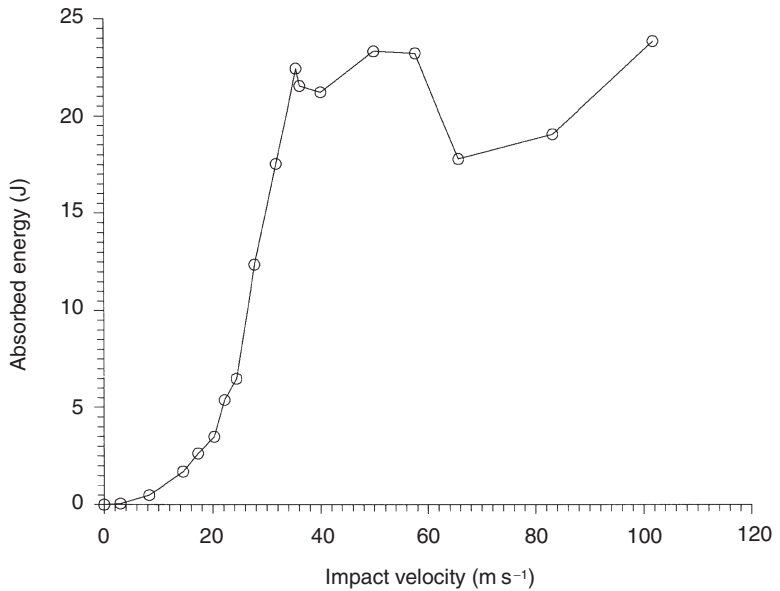
7.4 The relationship between the impact velocity, V_i of the projectile and the absorbed energy of the struck laminates.
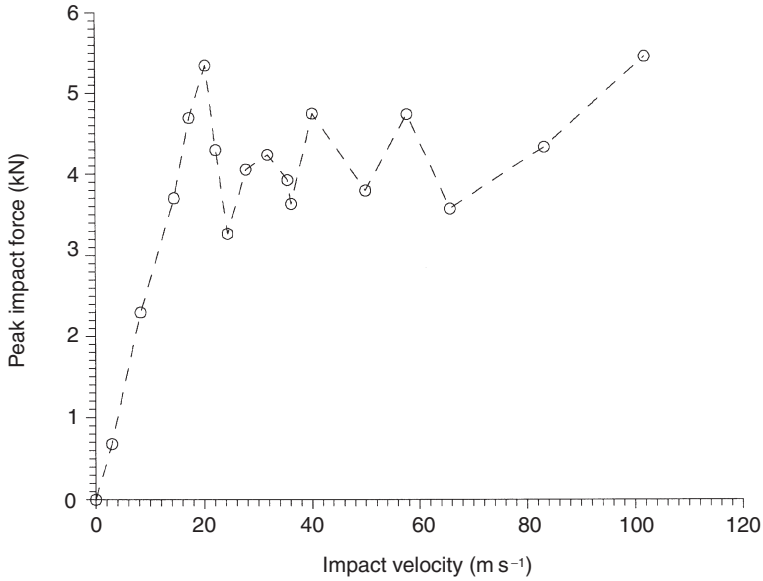
7.5 The relationship between the impact velocity, V_i and the peak impact force of the projectile.

7.4   Prediction of elastic impact response

7.4.1 Governing equations

The method presented in this section was derived using the Ritz method, and the Mindlin plate theory was adopted. The displacement field, by neglecting the in-plane deformation of the plate, reads

$$u_1(x, y, z, t) = z\overline{\alpha}(x, y, t)$$
$$u_2(x, y, z, t) = z\overline{\beta}(x, y, t) \tag{7.4}$$
$$u_3(x, y, z, t) = \omega(x, y, t)$$

where u_1, u_2 and u_3 are the displacements in the x, y and z directions of the plate; $\overline{\alpha}$ and $\overline{\beta}$ are the rotations of the plate in the x and y directions, respectively; and ω is the lateral deflection of the plate. The strain-displacement relations become

$$\begin{pmatrix} \varepsilon_{xx} \\ \varepsilon_{yy} \\ 2\varepsilon_{xy} \end{pmatrix} = \begin{pmatrix} \varepsilon_1 \\ \varepsilon_2 \\ \varepsilon_6 \end{pmatrix} = z \begin{pmatrix} \overline{\alpha}_{,x} \\ \overline{\beta}_{,y} \\ \overline{\alpha}_{,y} + \overline{\beta}_{,x} \end{pmatrix} \tag{7.5}$$

$$\begin{pmatrix} 2\varepsilon_{yz} \\ 2\varepsilon_{zx} \end{pmatrix} = \begin{pmatrix} \varepsilon_4 \\ \varepsilon_5 \end{pmatrix} = \begin{pmatrix} \overline{\beta} + \omega_{,y} \\ \overline{\alpha} + \omega_{,x} \end{pmatrix}$$

For each lamina, the constitutive relations are

$$
\begin{pmatrix} \sigma_{xx} \\ \sigma_{yy} \\ \tau_{xy} \end{pmatrix} = \begin{pmatrix} \sigma_1 \\ \sigma_2 \\ \sigma_6 \end{pmatrix} = \begin{bmatrix} Q_{11} & Q_{12} & Q_{16} \\ Q_{12} & Q_{22} & Q_{26} \\ Q_{16} & Q_{26} & Q_{66} \end{bmatrix} \begin{pmatrix} \varepsilon_1 \\ \varepsilon_2 \\ \varepsilon_6 \end{pmatrix}
\tag{7.6}
$$

$$
\begin{pmatrix} \tau_{yz} \\ \tau_{zx} \end{pmatrix} = \begin{pmatrix} \sigma_4 \\ \sigma_5 \end{pmatrix} = k \begin{bmatrix} Q_{44} & Q_{45} \\ Q_{45} & Q_{55} \end{bmatrix} \begin{pmatrix} \varepsilon_4 \\ \varepsilon_5 \end{pmatrix}
\tag{7.7}
$$

where Q_{ij} is the reduced elastic constant under the plane-stress conditions and k is the shear correction factor, whose value was taken to be 5/6.

The kinetic and strain energy for the laminate is, respectively,

$$
T = \frac{1}{2} \int_0^b \int_0^a \int_{-\frac{h}{2}}^{\frac{h}{2}} \rho(\dot{u}_1^2 + \dot{u}_2^2 + \dot{u}_3^2) dz dx dy
\tag{7.8}
$$

and

$$
V = \frac{1}{2} \int_0^b \int_0^a \int_{-\frac{h}{2}}^{\frac{h}{2}} (\sigma_1\varepsilon_1 + \sigma_2\varepsilon_2 + \sigma_6\varepsilon_6 + \sigma_4\varepsilon_4 + \sigma_5\varepsilon_5) dz dx dy
\tag{7.9}
$$

where ρ is the density of the laminate. On the other hand, the work done by the external force, $P(x, y, t)$, applied normally to the plate is

$$
W = \int_0^b \int_0^a P(x, y, t) u_3 dx dy.
\tag{7.10}
$$

In order to apply the Ritz method, beam functions that satisfy the geometric boundary conditions of the plate were adopted, and the three independent variables are expressed by the series expansion:

$$
\bar{\alpha}(x, y, t) = \sum_{ij} \alpha_{ij}(t) \xi_i'(x) \eta_j(y)
$$

$$
\bar{\beta}(x, y, t) = \sum_{ij} \beta_{ij}(t) \xi_i(x) \eta_j'(y)
\tag{7.11}
$$

$$
\omega(x, y, t) = \sum_{ij} \omega_{ij}(t) \xi_i(x) \eta_j(y)
$$

where $\xi(x)$ and $\eta(y)$ are beam functions in the x and y directions, respectively. Note also that $\xi'(x)$ and $\eta'(y)$ are included in the above equation in order to avoid the erroneous shear locking phenomenon when the plate becomes very thin.[31]

The governing equation in the form of

$$
[M]\{\ddot{q}\} + [K]\{q\} = \{P^*\}
\tag{7.12}
$$

can be derived by applying the Hamilton principle of

$$
\delta \int_{t_1}^{t_2} (T - V) dt = 0
\tag{7.13}
$$

where the generalised coordinates, q, are in the form of

$$\{q\}^T = \{\alpha_{11}, \alpha_{12}, \ldots, \alpha_{21}, \ldots; \beta_{11}, \beta_{12}, \ldots \beta_{21}, \ldots; \omega_{11}, \omega_{12}, \ldots, \omega_{21}, \ldots\}.$$
[7.14]

On the other hand, the generalised force, P^*, can be obtained from P. In this study, the area of contact between the projectile and the plate was small. Thus, a point load assumption is justified, and [7.10] is simplified as

$$W = \sum_{ij}\int_0^b\int_0^a P(t)\delta(x-x_0)\delta(y-y_0)\cdot\omega_{ij}(t)\xi_i(x)\eta_j(y)dxdy$$
$$= P(t)\left(\sum_{ij}\omega_{ij}(t)\xi_i(x_0)\eta_j(y_0)\right)$$
[7.15]
$$= P(t)\{q\}^T\{Y^*\} = \{q\}^T\{P^*\}$$

where

$$\{Y^*\}^T = \{0, 0, \ldots, 0, 0, \ldots, \xi_1\eta_1, \ldots, \xi_1\eta_2, \ldots, \xi_2\eta_1, \ldots\}_{(x_0,y_0)}.$$ [7.16]

Equation [7.12] can be further simplified by neglecting the effect of rotational inertia:[31]

$$\begin{bmatrix} 0 & 0 \\ 0 & M_{22} \end{bmatrix}\begin{pmatrix} \ddot{q}_1 \\ \ddot{q}_2 \end{pmatrix} + \begin{bmatrix} K_{11} & K_{12} \\ K_{21} & K_{22} \end{bmatrix}\begin{pmatrix} q_1 \\ q_2 \end{pmatrix} = \begin{pmatrix} 0 \\ P_2 \end{pmatrix}$$
[7.17]

$$[M_{22}]\{\ddot{q}_2\} + [K_{22}^*]\{q_2\} = \{P_2\}$$
[7.18]

where

$$[K_{22}^*] = [K_{22}] - [K_{12}]^T[K_{11}]^{-1}[K_{12}]$$
[7.19]

and

$$\{q_1\} = -[K_{11}]^{-1}[K_{12}]\{q_2\}$$
$$\{q_2\}^T = \{\alpha_{11}, \alpha_{12}, \ldots, \alpha_{21}, \ldots; \beta_{11}, \beta_{12}, \ldots, \beta_{21} \ldots\}$$
$$\{q_2\}^T = \{\omega_{11}, \omega_{12}, \ldots, \omega_{21}, \ldots\}$$
[7.20]
$$\{P_2\}^T = P(t)\{\xi_1\eta_1, \xi_1\eta_2, \ldots, \xi_2\eta_1, \ldots\}_{(x_0,y_0)} = P(t)\{Y\}^T$$

7.4.2 Solution scheme

The response of the projectile, on the other hand, is expressed in the form of

$$m\ddot{S}(t) = -P(t)$$
[7.21]

where m is the mass of the projectile and S is the projectile movement. The modified Hertz contact law, by assuming the projectile to be rigid, is then employed:[7,28]

$$f(\alpha) = \frac{4}{3}\sqrt{R}E_z(\alpha)^{3/2} \qquad\qquad [7.22]$$

where R is the radius of the projectile head and E_z is the Young's modulus of the laminate in the thickness direction. In this equation, the indentation, α, is defined as the difference between $s(t)$ and $\omega_0(t)$, and the impact force $P(t)$ is equal to $f(\alpha)$, where $\omega_0(t)$ is the laminate deformation in the thickness direction at the contact location. In this study, the central difference method was employed. Thus, equations [7.18] and [7.21] can be expressed in the following discrete forms:

$$\{q_2\}_{j+1} = P_j(\Delta t)^2[M_{22}]^{-1}\{Y\} - (\Delta t)^2(M_{22})^{-1}[K_{22}^*]\{q_2\}_j$$
$$+ 2\{q_2\}_j - \{q_2\}_{j-1} \qquad\qquad [7.23]$$

$$S_{j+1} = P_j(\Delta t)^2/m + 2S_j - S_{j-1} \qquad\qquad [7.24]$$

Comparisons between the prediction and the test results are shown in Fig. 7.6(a) and (b), in which the histories of the velocity and force are plotted. The initial striking velocity was $7.46\,\mathrm{m\,s^{-1}}$. The overall correlation is considered to be very satisfactory. Thus, the presented method has been demonstrated to be suitable for impact prediction of laminated structures.

7.4.3 Modeling of physically clamped boundaries

As stated in the Introduction, the boundary of a laminated plate, except for one under free-free boundary conditions, can hardly be considered as being perfect due to elastic deformation and material and geometric imperfection of both the laminate and the clamped pads. Figure 7.7(a) and (b) shows typical results for a laminate that was physically clamped on two opposite sides and struck by a 35.6 g projectile at an impact velocity of 4.3 m/s. Also shown in these figures are two predictions made under the assumption that the boundary was simply supported and fully clamped. It is found that neither correlates with the experimental data. Thus, it is essential to develop a method that takes the physical boundary condition into consideration. In order to model the boundary of a laminated plate that is physically clamped on its two opposite sides with the other two free of support, this near-perfect clamped boundary was modeled as a simple support with an elastic restrained edge; i.e. a finite rotational angle was allowed on the clamped sides. Thus, using the Ritz approach, where the displacement field was constructed by means of a series of orthogonal beam functions, the eigenfunction of such a beam can be derived from the following equation:

$$m\ddot{u} + EIu'''' = 0 \qquad\qquad [7.25]$$
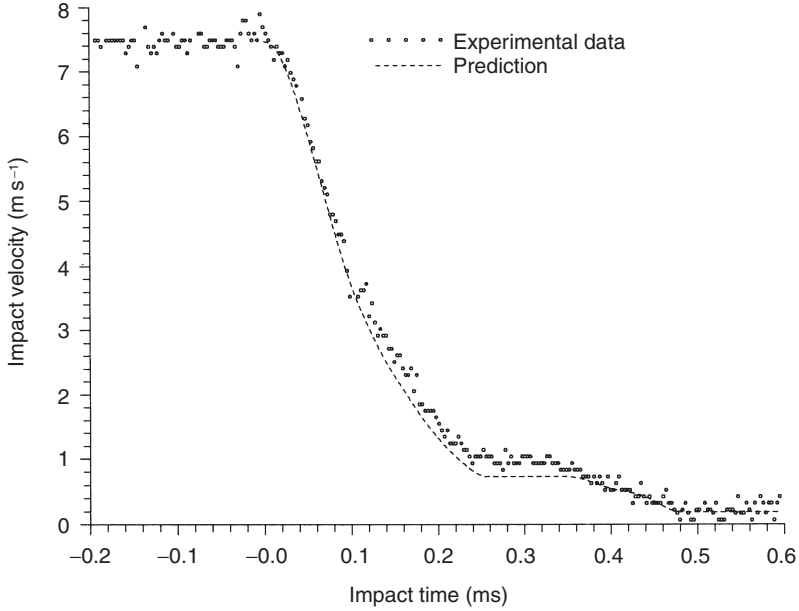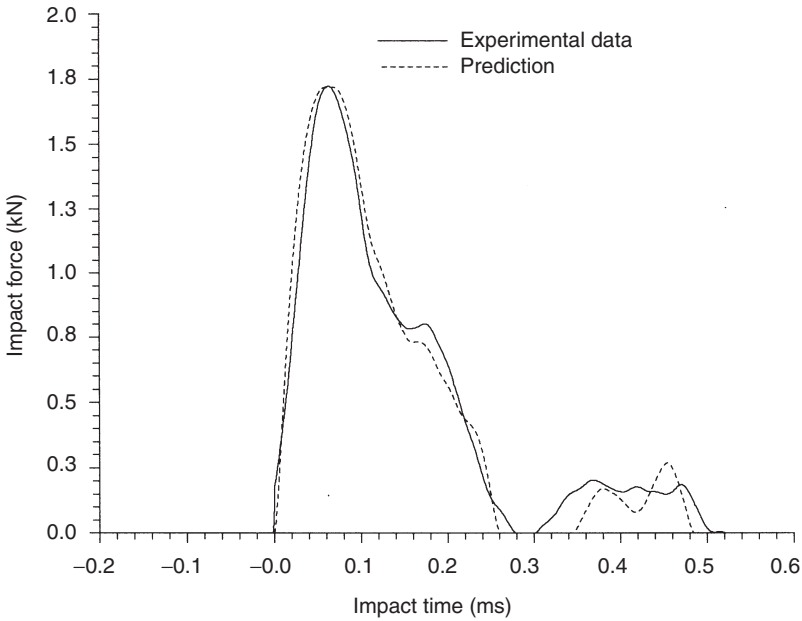
7.6 (a) The velocity history and (b) the force history for a 35.6 g
    projectile striking at 7.46 m s^{-1}. Both the measurement data and the
    prediction using the Ritz method are plotted.
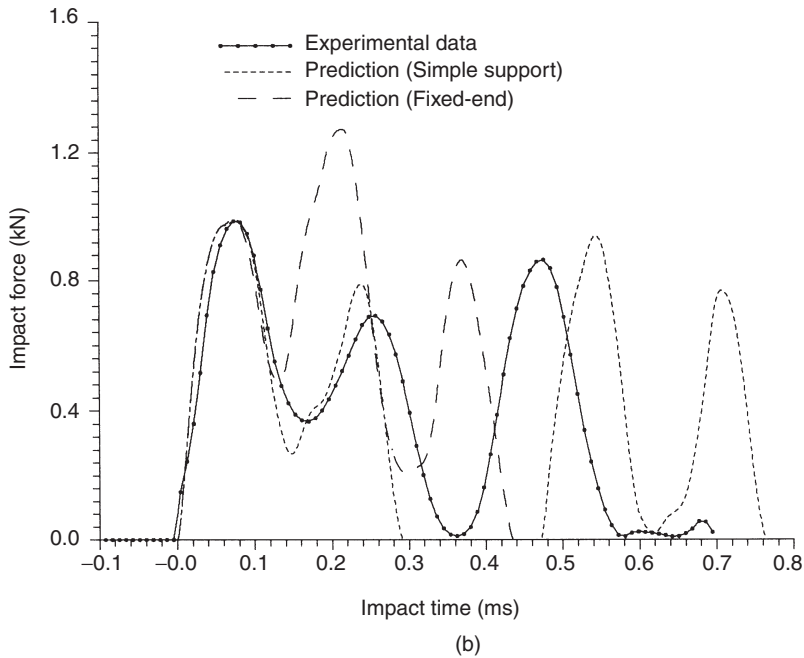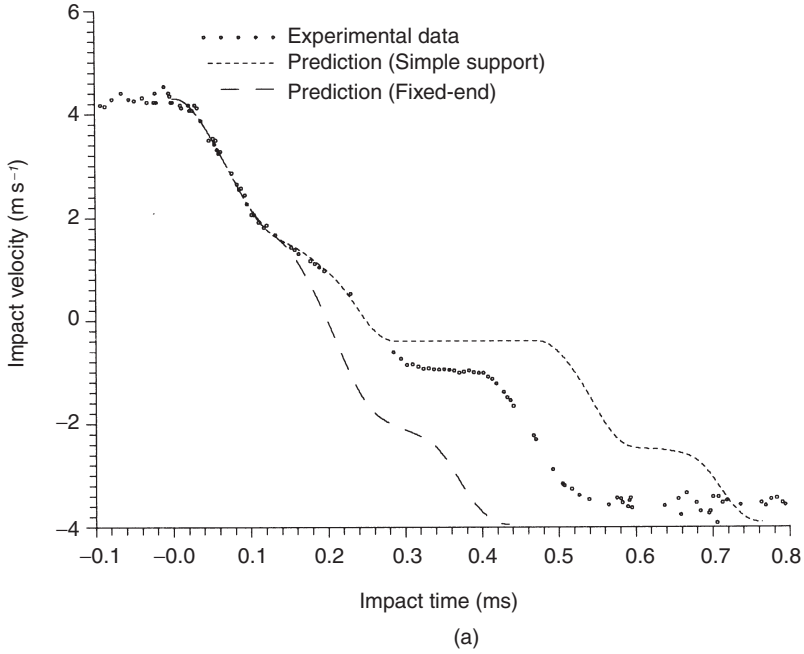
7.7 The measured (a) velocity and (b) force histories for a laminated plate that was struck by a 35.6 g projectile at 4.3 m s^{-1} and was physically clamped on two opposite sides with the other two sides free of support. Also shown are the Ritz predictions, which treat the boundary as being simply supported and fully clamped.

The corresponding boundary conditions are

$$u(0, t) = u(l, t) = 0$$

$$u''(0, t) = \frac{K}{EI} u'(0, t) \qquad\qquad\qquad [7.26]$$

$$u''(l, t) = -\frac{K}{EI} u'(l, t)$$

where m is the mass per unit length, $u(x, t)$ is the transverse displacement, and E and I are the Young's modulus and the moment of inertia, respectively, of such a beam. On the other hand, K is the stiffness of the rotational spring, and l is the length of the beam. The value of K represents the rotational stiffness of the boundary. In the two extreme cases when K reaches zero and infinity, the simply supported and the fixed end conditions are obtained, whose beam functions are

$$\phi_s(x) = \frac{2EI\alpha}{(\sinh\alpha l - \sin\alpha l)}(\sinh\alpha l \sin\alpha x - \sinh\alpha x \sin\alpha l) \qquad [7.27]$$

and

$$\phi_c(x) = (\cosh\alpha x - \cos\alpha x) - \frac{\cosh\alpha l - \cos\alpha l}{\sinh\alpha l - \sin\alpha l}(\sinh\alpha x - \sin\alpha x)$$

$$[7.28]$$

respectively. On the other hand, when the value of K falls in between the two extremes, the beam function becomes a combination having the following form:

$$\phi(x) = \phi_s(x)/K + \phi_c(x) \qquad\qquad\qquad [7.29]$$

and note that α must satisfy the following characteristic equation:

$$\left(\frac{K}{EI\alpha}\right)^2(\cosh\alpha l \cos\alpha l - 1) + 2\left(\frac{K}{EI\alpha}\right)^2(\cos\alpha l \sinh\alpha l - \sin\alpha l \cosh\alpha l)$$
$$- 2\sinh\alpha l \sin\alpha l = 0 \qquad\qquad [7.30]$$

By selecting a proper value of K, a real boundary condition that reflects the physically clamped condition can be obtained.

In this study, the K value was determined from a quasi-static test result, in which the boundary conditions, the shape of the indentor, and the laminate being tested remained identical to those tested under impact conditions. The optimal K, by which the correlation between the predicted Ritz

method and the experimental result was the best, was then searched. For analysis purposes, a non-dimensional value was employed:

$$\frac{S}{1-S} = \frac{Kl}{EI} \quad 0 \le S \le 1 \tag{7.31}$$

Note that S ranges between 0 and 1. In this study, $S = 0.93$ was found to be optimal.

The predictions obtained using $S = 0.93$ and the measured data are shown in Fig. 7.8(a) and (b). It is found that the correlation is much better. Other similar comparisons can be found in Tsai.[45] This demonstrates that the developed method is capable of predicting the impact response of a laminate under physically clamped boundaries. On the other hand, the deviation between the measurement and the prediction is more noticeable in Fig. 7.8(a) and (b) as compared with the example shown in Fig. 7.6(a) and (b), in which the plate is subject to free-free boundary conditions. This might to be due to the assumption of the uniform boundary condition along the clamped boundary. Other factors contributing to the deviation include the assumptions that the boundary behaviours due to the quasi-static and to the impact loads are identical, that S remains unchanged during loading and unloading processes, etc.

7.5   Impact beyond the delamination threshold

7.5.1   Delamination damage

Delamination damage was observed when the impact velocity increased to $20.3\,\mathrm{m\,s^{-1}}$, at which point the terminal velocity was $-13.8\,\mathrm{m\,s^{-1}}$ and the area calculated based on the C-scan run was $2.90\,\mathrm{cm^2}$. Under this impact condition, no damage was found on either the front or the distal surfaces of the struck laminate. Thus, delamination should be the only observed damage mechanism. However, because the absorbed energy ratio of $\Delta E/E_i = 0.48$ remained essentially identical to that for impact at $V_i = 14.5\,\mathrm{m\,s^{-1}}$, under which condition no delamination damage was observed, this damage alone did not absorb a significant amount of the impact energy. As a result, the impact histories of the force and velocity have profiles very similar to the results shown in Fig. 7.2(a) and (b) and, thus, are not plotted again. Similarly, the impact velocity versus the terminal velocity of the projectile, shown in Fig. 7.3, continuously follows the same linear relationship, and the absorbed energy, shown in Fig. 7.4, follows the same quadratic curve. From these revealed impact results, it is found that the responses of the projectile remained the same regardless of whether or not the impact was beyond the delamination threshold of the laminates.
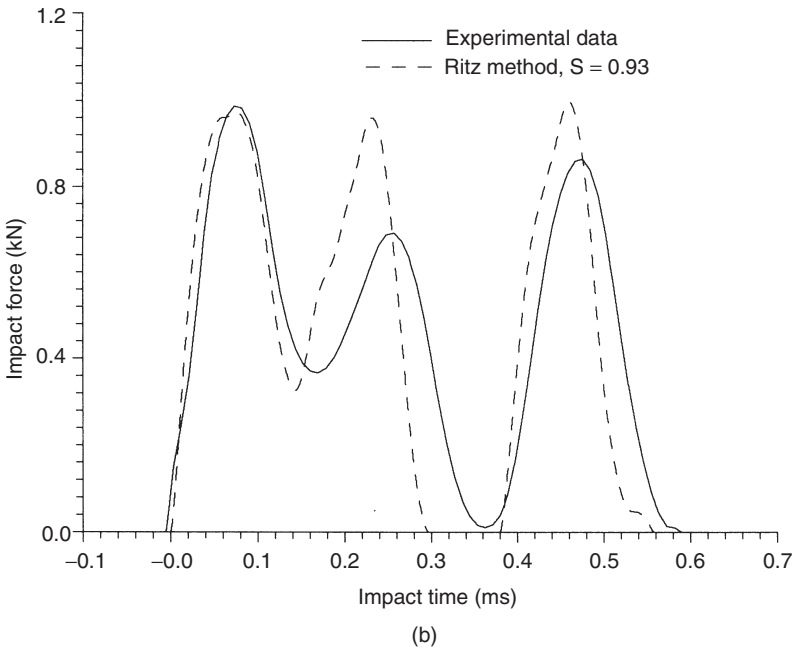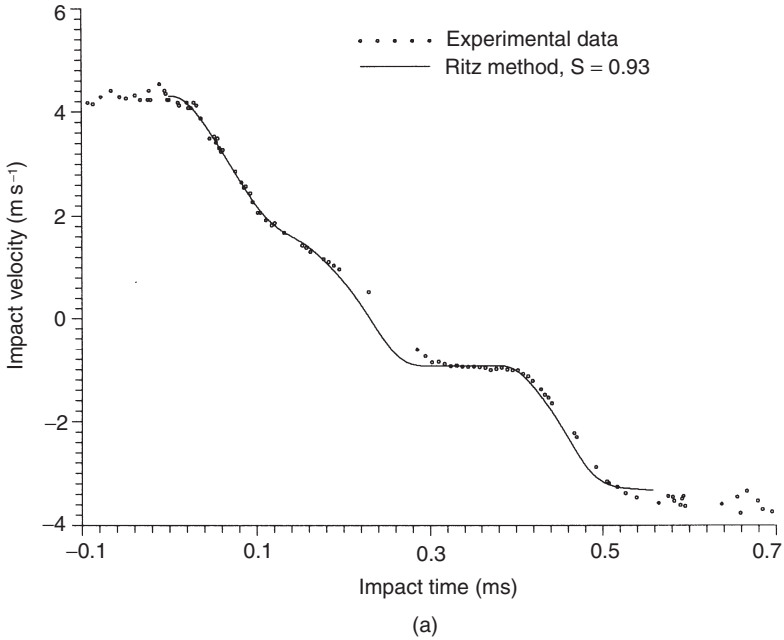
7.8 The (a) velocity and (b) force histories measured using the developed TLDA and predicted using the Ritz method with $S = 0.93$. The experimental data are identical to those shown in Fig. 7.7.
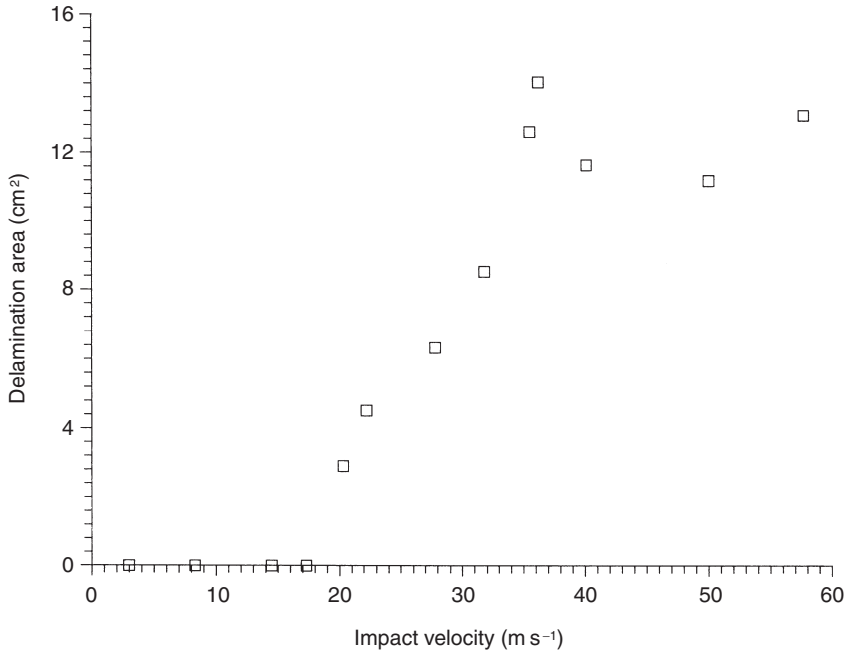
7.9 The relationship between the projectile initial velocity and the delamination damage area.

7.5.2 Spalling damage

When the impact velocity increased slightly to $22.2\,\mathrm{m\,s^{-1}}$, a patch of the lamina layers on the distal side of the struck specimen started to separate from the laminate. This phenomenon was different from that observed under the quasi-static loading condition. Thus, the damage was considered to have been induced by the reflected tensile waves that were induced by the dynamic loads applied by the striking projectile. This phenomenon, designated as spalling damage, was similarly observed for a brittle target, such as one made of concrete, under projectile impact.

In this test run, the delamination area was found to enlarge to $4.52\,\mathrm{cm^2}$, as plotted in Fig. 7.9. This shows that graphite/epoxy laminates are brittle, and that the difference in the thresholds between the delamination damage and the spalling damage of such a laminated specimen is not significant. On the other hand, the absorbed energy ratio, $\Delta E/E_i$, was found to jump significantly from 0.48 in a previous run to 0.61. This indicated that the spalling damage along with the enlargement of the delamination area consumed a significant amount of the impact energy. Still no damage was observed at the initial contact point between the projectile and the target.

The velocity and the force histories for impact at $22.2\,\mathrm{m\,s^{-1}}$ are shown in

Fig. 7.2(c). Compared to the results shown in Fig. 7.2(a) and (b) for the case that involved no impact-induced damage as revealed by both C-scan and visual inspection, the phenomenon is found to be significantly different. For example, the second force peak disappeared due to stiffness degradation of the struck laminate, which, in turn, was due to damage on the distal surface of the laminates. This degradation in laminate stiffness also prevented separation of the projectile from the struck target during impact. However, the residual stiffness of the struck laminate was still large enough to cause the laminate to strike the projectile when its velocity was close to zero during the impact process. This resulted in a peak force at around 0.4 ms after the onset of impact, and the projectile gained enough velocity in the negative direction to escape from contact with the struck target that bounced back due to the action of the residual stiffness. The terminal velocity was found to be $V_t = -13.8 \, \mathrm{ms^{-1}}$. Its absolute value, as expected, was found to be lower than that in the previous impact run of $V_t = -14.7 \, \mathrm{ms^{-1}}$ due to the more severe reduction of the stiffness in the struck laminate. Meanwhile, as shown in Fig. 7.3, the terminal velocity, V_t, was found to decrease as the impact velocity continuously increased. Thus, the spalling damage was considered to have caused significant degradation in laminate stiffness.

It is found from Fig. 7.5 that the maximum force peak was 5.34 kN when the impact velocity was $20.3 \, \mathrm{ms^{-1}}$. The force peak dropped and remained at a constant level as the impact velocity further increased. One possible explanation for this peculiar phenomenon was the occurrence of spallation, which reduced the stiffness of the laminate. Once spalling damage occurred on the distal side of the laminates, due to the sudden reduction of the laminate stiffness, the laminate moved much more easily with the projectile. As a result, the maximum indentation between the projectile and the laminate during the impact process, which corresponded to the maximum force peak, for the impact test run that involved spallation was smaller as compared to the test runs in which spallation was not observed.

7.5.3 Permanent indentation damage

Permanent indentation damage on the impact side of the struck laminates was observed when the impact velocities became higher, and layers on the distal side of the laminates broke more seriously and separated from the remainder of the laminate. Two typical velocity and force histories for $V_i = 24.4 \, \mathrm{ms^{-1}}$ and $V_i = 31.8 \, \mathrm{ms^{-1}}$ are shown in Fig. 7.2(d) and (e). Due to the higher impact velocity, such as in the test run conducted at $V_i = 31.8 \, \mathrm{ms^{-1}}$, the laminate was damaged more seriously. As a result, it was not able to vibrate effectively enough to push the projectile further back in the reverse direction. Thus, the previously observed multiple force peak phenomenon

was diminished, and there existed essentially only a single peak in the force history at the very beginning of the impact stage.

The terminal velocity, V_t, was found to decrease at an approximately constant rate as the impact velocity became higher, as shown in Fig. 7.3. This value dropped finally to zero at the ballistic limit. On the other hand, as shown in Fig. 7.4, the absorbed energy, ΔE, was found to continuously follow the quadratic relationship and to reach the highest value also at the ballistic limit.

Close investigation of the struck laminate reveals that the area of fiber bundle breakage increased when the impact velocity was slightly higher than the threshold, and that on the impact side of the fiber bundle, there was breakage due to permanent indentation of the laminate by the projectile. As the impact velocity became even higher, the fiber bundle breakage areas on both sides of the laminate remained approximately the same. However, comparing these areas with the delamination area, shown in Fig. 7.9, it was surprising to find that the delamination area was still proportional to the impact velocity even when the velocity was higher than the threshold corresponding to spalling damage. This demonstrates that it was not the delamination area that governed the residual stiffness of the struck laminate. Thus, the fiber bundle breakage associated with the spalling damage on the distal side of the laminate was considered to be the mechanism that affected the most of the residual stiffness of laminate.

7.6   Impact beyond the ballistic limit

7.6.1   Perforation

The ballistic limit occurred when the projectile was struck at the laminate after impact, at which point the terminal velocity was equal to zero, and the impact period lasted forever. The force and velocity histories at the ballistic limit were very similar to that shown in Fig. 7.2(e) for $V_i = 31.8\,\mathrm{m\,s^{-1}}$ except that the terminal velocity was equal to zero. When the impact velocity became higher than the ballistic limit, the terminal velocity was in the same direction as that of the impact velocity. Figure 7.2(f) shows a typical result for the case in which $V_i = 36.2\,\mathrm{m\,s^{-1}}$. The velocity and force profiles were very similar to those shown in Fig. 7.2(e). The single force peak occurred right after the onset of contact between the projectile and the target, as expected. As impact proceeded, the velocity dropped quickly, but its rate of decrease became slower. It was found that the rate of decrease of the projectile velocity could be divided into two portions. In the first portion of the impact process, during roughly the first 0.5 ms after the onset of contact, the rate of decrease was very sharp. As the hemispherical part of the projectile perforated the laminate, the rate of decrease became much smaller, and the corresponding force was only several hundred Newtons.

This force was considered to be the dynamic friction force between the projectile and the laminate, and was much smaller than the peak impact force. Meanwhile, the terminal velocity increased drastically again when the projectile velocity became even higher, as shown in Fig. 7.3.

A simple equation was adopted to predict the terminal velocity of the projectile, V_t, when the initial striking velocity, V_i, was higher than the ballistic limit:[19,20,46]

$$V_t = (V_0^2 - 2*E_s/m)^{0.5} \tag{7.32}$$

where E_s is the energy needed for an indentor to perforate a laminate under the quasi-static loading condition and m is the mass of the projectile. The predicted result is also plotted in Fig. 7.3. The correlation is considered to be satisfactory.

As shown in Fig. 7.8, the absorbed energy was found to remain approximately the same regardless of the increasing velocity of the projectile. Thus, the laminate did not absorb extra energy in a perforated test run even if it was struck at a higher velocity.

7.6.2 Comparison with the quasi-static results

To investigate the effect of the loading rate on the CFRP laminate when it is under lateral loading, results from both the impact test at the ballistic limit and the quasi-static contact test are plotted in Fig. 7.10. A similar comparison is also given in Fig. 8.5 of Chapter 8. A double peak phenomenon is observed in the quasi-static case. This is similar to the result observed by Lee and Sun and is attributed to delamination and the globally excessive deflection which occurred during the test.[19] In Fig. 7.10, there is only a single peak for the impact test, and it is seen that the force increased at a much faster displacement rate before it reached the peak value. This is because the laminate deflection was very local when the laminate was struck by a projectile at a much higher loading rate. On the other hand, the relatively lower force peak shown for the impact case, as compared to the quasi-static counterpart, was considered to be due to the occurrence of spallation damage that reduced the laminate stiffness. This damage was induced by stress waves that reflected back from the distal side of the struck laminate immediately after the onset of contact between the projectile and the target. Thus, the loading rate effect is also considered to be noticeable for graphite/epoxy laminates under laterally applied loading.

7.7   Conclusions

A general overview for the impact behaviour of a projectile striking on a graphite/epoxy composite laminate has been reported. The laminates used were 6 inch × 4 inch in their in-plane dimensions and 4.3 mm in thickness.
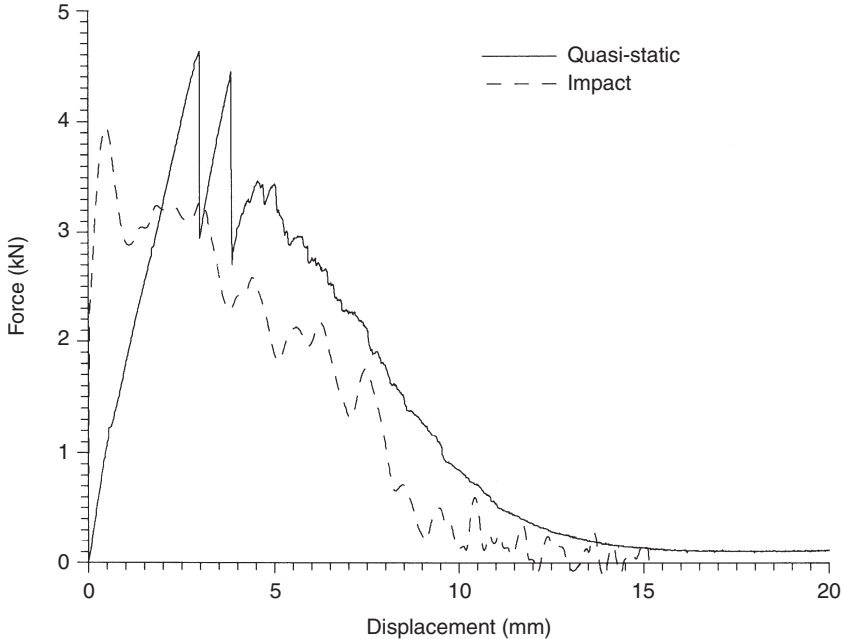
7.10 The force vs displacement relationships for laminates under impact at the ballistic limit and under quasi-static loading conditions.

The projectiles employed had a hemispherical tip weighing 35.6 g in mass. The impact speeds were from 3.0 to 101.8 m s^{-1}, where the ballistic limit of the laminates was found to be 35.5 m s^{-1}. The kinetic energy of the projectile was provided by a gas gun. Two different boundary conditions were employed. The first one, which is considered to be perfect, was a free-free boundary. On the other hand, the second was clamping on two opposite sides of the laminate with the other two sides left free of support. This physically clamped boundary only approximated the perfect fixed-end condition although the boundary had been tightly clamped. When the laminate was struck, the velocity signals were measured in a non-contact manner by a developed transient laser Doppler anemometer (TLDA) system. The force and displacement histories for each impact run were then derived from the recorded velocity history, from which the initial and terminal velocities, the initial and the absorbed energy, and the force peak of the projectile were obtained. The struck laminates were then C-scanned to measure the delamination area. On the other hand, an analytical model has been presented in this chapter to predict the impact response of the projectile, and the effect of boundary imperfection was accounted for. Following is a summary of the revealed impact phenomena:

1 *Near elastic impact.* When the impact velocity was low so that no damage was observed under visual inspection, even if a delamination damage area small in size was observed under C-scan when the velocity became higher, a multiple impact phenomenon was observed. The force history showed three peaks. The first had the highest value and occurred after the onset of contact between the projectile and the target, the second peak occurred when the projectile velocity reached zero, and the third peak happened when the laminate bounced back and struck the projectile. The terminal velocity of the projectile was linear to its impact velocity. Further, the maximum peak impact force in each test run also had a linear relationship with the impact velocity.

2 *Prediction of projectile response under an imperfect boundary.* An analytical method using the Ritz method along with the Mindlin plate theory was employed to predict the response of a laminated plate struck by projectiles at low velocities. The displacement field of the plate was represented by means of a series of beam functions that satisfied the boundary conditions of the plate. When the boundary conditions were perfect, such as a plate with a free boundary, the method could be experimentally verified, and the correlation was found to be very satisfactory. Then, when the laminated plate was physically clamped at two opposite sides, it has been found that the clamped boundary was neither fixed nor simply supported. To take this boundary imperfection into consideration, two beam functions corresponding to simple and fixed boundary conditions were combined, and a normalised rotational spring constant was employed to represent the actual rotational stiffness of the physically clamped boundary. In this study, this spring constant was obtained from the results of a quasi-static contact test. The satisfactory correlation between the prediction and the measured results demonstrates that the presented method is capable of predicting the impact response of a laminate with near-perfect boundaries.

3 *Impact beyond the spallation threshold.* When the impact velocity was higher than the spallation threshold, the laminae on the distal side of the struck laminates started to separate. This damage mechanism was considered to be due to stress waves reflected from the free surface on the distal side of the laminate, and was designated as spalling damage in this study. As the impact velocity continued to increase, a permanent indentation damage mechanism at the contact location was also observed in addition to spalling damage on the laminate distal side. A further increase of the impact velocity caused these two damage mechanisms to coincide, and the ballistic limit was observed at a speed of $35.5\,\mathrm{m\,s^{-1}}$.

   The three-force-peak phenomenon was found to gradually change to a single-force-peak impact phenomenon. This force peak occurred

immediately after the onset of contact between the projectile and the target. The friction force between the cylindrical portion of the projectile and the perforated laminate was found to be only a small fraction of the peak impact force. On the other hand, the terminal velocity gradually decreased to zero as the impact velocity increased to the ballistic limit, whereas the force peak was found to remain essentially unchanged, and a linear relationship was observed between the delamination area and the impact velocity.

4 *Perforated impact.* When the impact velocity became higher than the ballistic limit, perforation occurred. It was found that, whereas the terminal velocity increased drastically and approached the initial velocity of the projectile, other phenomena, such as the peak impact force and the delamination area, all remained the same regardless of the increase of the impact velocity. A simple equation was found to accurately predict the terminal velocity of the projectile.

In this study, the force versus the displacement relationships for laminates under impact and quasi-static loading conditions were also compared. The force peak for the laminate under impact occurred at a much lower displacement level. These different phenomena were considered to be mainly due to the more localised laminate response under impact conditions. Thus, the graphite/epoxy laminate was also sensitive to the rate of applied loading.

Acknowledgements

References

1 Abrate S, 'Impact on laminated composite materials', *ASME Appl Mech Rev*, 1991 **44**(2) 155–90.
2 Abrate S, 'Impact on laminated composites: recent advances', *ASME Appl Mech Rev*, 1994 **47**(11) 517–44.
3 Wu E and Liau J, 'Impact of unstitched and stitched laminates by line loading', *J Composite Mater*, 1994 **28**(17) 1640–58.

 4 Wu E and Wang J, 'Behavior of stitched laminates under in-plane tensile and transverse impact loading', *J Composite Mater*, 1995 **29**(11) 2254–79.
 5 Wu E and Chang L C, 'Loading rate effect on woven glass laminated plates by penetration force', *J Composite Mater*, 1998 **32**(8) 702–21.
 6 Liu D, 'Impact-induced delamination – a view of bending stiffness mismatching', *J Composite Mater*, 1988 **22** 674–92.
 7 Wu E and Shyu K, 'Response of composite laminates to contact loads and relationship to low-velocity impact', *J Composite Mater*, 1993 **27** 1443–64.
 8 Cantwell W J and Morton J, 'The impact resistance of composite materials – a review', *Composites*, 1991 **22**(5) 347–62.
 9 Virostek S P, Dual J and Goldsmith W, 'Direct force measurement in normal and oblique impact of plates by projectiles', *Int J Impact Eng*, 1987 **6** 247–69.
10 Delfosse D, Pageau G, Bennett R and Poursartip A, 'Instrumented impact testing at high velocities', *J Composites Technol Res*, 1993 **15**(1) 38–45.
11 Gupta B P and Davids N, 'Penetration experiments with fiberglass-reinforced plastic', *Exp Mech*, 1966 **6**(9) 445–50.
12 Takeda N, Sierakowski R L and Malvern L E, ' Wave propagation experiments on ballistically impacted composite laminates', *J Composite Mater*, 1981 **15** 157–74.
13 Takeda N, Sierakowski R L, Ross C A and Malvern L E, ' Delamination-crack propagation in ballistically impacted glass/epoxy composite laminates', *Exp Mech*, 1982 **22** 19–25.
14 Cantwell W J and Morton J, 'The influence of target geometry on the high velocity impact response of CFRP', *Composite Struct*, 1988 **10** 247–65.
15 Cantwell W J and Morton J, 'Comparison of the low and high velocity impact response of CFRP', *Composites*, 1989 **20**(6) 545–55.
16 Cantwell W J and Morton J, 'Impact perforation of carbon fibre-reinforced plastic', *Composites Sci Technol*, 1990 **38** 119–41.
17 Zhu G, Goldsmith W and Dharan C K H, 'Penetration of laminated kevlar by projectiles (I) experimental investigation', *Int J Solids Struct*, 1992 **29**(4) 399–420.
18 Lee S-W R and Sun C T, 'A quasi-static penetration model for composite laminates', *J Composite Mater*, 1993 **27** 251–71.
19 Lee S-W R and Sun C T, 'Dynamic penetration of graphite/epoxy laminates impacted by a blunt-ended projectile', *Composites Sci Technol*, 1994 **49** 369–80.
20 Jenq S T, Jing H S and Chung C, 'Prediction of the ballistic limit for plain woven glass/epoxy composite laminate', *Int J Impact Eng*, 1994 **15**(4) 451–64.
21 Schonberg W P, Keer L M and Woo T K, 'Low velocity impact of transversely isotropic beams and plates', *Int J Solids Struct*, 1987 **23**(7) 871–96.
22 Cairns D S and Lagace P A, 'Thick composite plates subjected to lateral loading', *ASME J Appl Mech*, 1987 **54** 611–16.
23 Cairns D S and Lagace P A, 'Transient response of graphite/epoxy and kevlar/epoxy laminates subjected to impact', *AIAA J*, 1989 **27**(11) 1590–6.
24 Chao C C, Tung T P, Sheu C C and Tseng J H, 'A consistent higher-order theory of lamimated plate with nonlinear impact modal analysis', *ASME J Vibrat Acoust*, 1994 **116** 371–8.
25 Wu H Y T and Chang F K, 'Transient dynamic analysis of laminate composite plates subjected to transverse impact', *Computer Struct*, 1989 **31**(3) 453–66.
26 Lin H J and Lee Y J, 'Impact-induced fracture in laminated plates and shells', *J Composite Mater*, 1990 **24** 1179–99.

27 Hertz H, 'Uber die Beruhrung fester Elastischer Korper', 1881 **92** 156–71, transl by Jones D E and Schott G A, London, MacMillan, 1896.

28 Tan T M and Sun C T, 'Use of statical indentation laws in the impact analysis of laminated composite plates', *J Appl Mech*, 1985 **52** 6–12.

29 Wu E, Chao J C and Yen C S, 'Smooth contact of orthotropic laminates by rigid cylinders', *AIAA J*, 1993 **31**(10) 1916–21.

30 Wu E and Yen C S, 'The contact behavior between laminated composite plates and rigid spheres', *ASME J Appl Mech*, 1994 **61** 60–6.

31 Yen C S and Wu E, 'On the inverse problems of rectangular plates subjected to elastic impact, part 1: method development and numerical verification', *ASME J Appl Mech*, 1995 **62** 692–8.

32 Yen C S and Wu E, 'On the inverse problems of rectangular plates subjected to elastic impact, part 2: experimental verification and further applications', *ASME J Appl Mech*, 1995 **62** 699–705.

33 Wu E, Yeh J C and Yen C S, 'Impact on composite laminated plates: an inverse method', *Int J Impact Eng*, 1994 **15**(4) 417–33.

34 Wu E, Yeh J C and Yen C S, 'Identification of impact forces at multiple locations on laminated plates', *AIAA J*, 1994 **34**(12) 2433–9.

35 Wu E, Tsai T D and Yen C S, 'Two method for determining impact force history on elastic plates', *Exp Mech*, 1995 **35**(1) 11–18.

36 Wu E, Tsai C Z and Tseng L H, 'A deconvolution method for force reconstruction in rods under axial impact', *J Acoust Soc Am*, 1998 **104**(3) 1418–26.

37 Wu E, Sheen H J, Chen Y C and Chang L C, 'Penetration force measurement of thin plates by laser Doppler anemometry', *Exp Mech*, 1994 **38** 93–9.

38 Tsai C Z and Wu E, 'A transient laser Doppler anemometry to measure rapidly changed velocities of solid bodies', *Exp Mech*, 1998 **38** 261–9.

39 Wu E, Tsai C Z and Chen Y C, 'Penetration into glass/epoxy composite laminates', *J Composite Mater*, 1994 **28**(18) 1783–802.

40 Wu E and Chang L C, 'Woven glass/epoxy laminates subject to projectile impact', *Int J Impact Eng*, 1995 **16**(4) 607–19.

41 Wu E and Jiang W S, 'Axial crush of metallic honeycombs', *Int J Impact Eng*, 1997 **19**(5–6) 439–56.

42 Durst F, Melling A and Whitelaw J M, *Principles and Practice of Laser Doppler Anemometry*, New York, Academic Press, 1976.

43 Drain L E, *The Laser Doppler Technique*, New York, Wiley, 1980.

44 de Boor C, *A Practical Guide to Splines*, Berlin, Springer, 1978.

45 Tsai C Z, 'Development of the transient laser Doppler anemometry and applications to impact force measurements', PhD dissertation, Institute of Applied Mechanics, National Taiwan University, Taiwan 1995.

46 Backman M E and Goldsmith W, 'The mechanics of penetration of projectiles into targets', *Int J Engng Sci*, 1978 **16** 1–99.

Perforation of FRP laminates and sandwich panels subjected to missile impact

S R REID AND H M WEN

8.1 Introduction

Composite structures such as fibre-reinforced plastic (FRP) laminates and sandwich panels made with such laminate skins and light-weight cores have great potential for use in aggressive environments. The high specific strength of composites can offer weight savings and their corrosion resistance gives advantage over traditional metallic materials. Such components, however, could be subjected to high speed impact by fragments resulting from the effects of the disintegration of nearby items of plant as well as low-velocity impact by dropped objects. Their response to such loading in the context of offshore applications has been studied extensively by the authors in recent years as part of the UK collaborative research programme on the Cost Effective Use of Fibre-Reinforced Composites Offshore. Most of this work has been summarised by the authors and their co-workers.[1–3]

Fibre-reinforced plastic laminates have also been considered for armour applications,[4,5] glass fibres being more popular than other types of fibre such as Kevlar due to their cost advantage. The mechanics of deformation and failure of FRP laminates subjected to local impact loads is understood only for a few cases of simple geometrical form.[4,5] Static indentation of thick composites with fibres in the form of woven fabrics by conical indenters has been modelled by Rutherford[6] (see Reid et al.[10]) who used an energy approach to relate the force at a certain level of indentation to two strength parameters representing the in-plane and through-thickness strengths of the composites, respectively. A similar problem was also examined by Zhao et al.[7] who employed transversely isotropic elastic analysis and rigid, perfectly-plastic material models. They showed that the latter led to a formula depending only on the in-plane strength of the material. This formula showed good agreement with tests on Scotch-ply laminates.

The deformation mechanisms which occur during dynamic penetration and perforation of laminates have been examined by a number of authors.[1–3,8–14] As indicated in Reid et al.,[10] Greaves[8,9] studied the deforma-

tion mechanisms during ballistic perforation of thick S-2 glass/phenolic laminates by flat-faced projectiles and found that the failure can be divided into two phases. Phase 1 involves compression, shear, indentation and expulsion of debris. In phase 2 the formation of a cone of delaminations, fibre stretching and fracture occur and the projectile exits the back face. It was noted that the phase 1 indentation mechanism, said to be dominated by the through-thickness compressive resistance of the material, absorbed most of the impact energy and was therefore worthy of more detailed study. To this end, an investigation into the impact force-indentation characteristics of laminates at velocities of up to 200 m/s has been carried out by Reid et al.[10]

Zhu et al.[11] investigated experimentally the penetration of laminated Kevlar29/polyester plates by conical-nosed projectiles and proposed a range of models for the various energy-absorbing mechanisms to estimate the target resistance to the projectile motion.[12] The event of ballistic impact was divided into three consecutive stages: indentation, perforation and exit. The global structural deformations were determined using laminated plate theory. Dissipative mechanisms including indentation of the projectile tip, bulging of the back surface of the laminate, fibre failure, delamination and friction were described utilising certain simplifying assumptions. Good agreement was obtained between the model predictions and the experimental results.

Lee and Sun[13] carried out a combined experimental and numerical study on the dynamic penetration of clamped circular CFRP laminates by a 30 g, 14.5 mm diameter flat-ended projectile in the velocity range 24–91 m/s. The composite material examined was Hercules AS4/3501-6 graphite/epoxy and the stacking sequence of all the laminates was based on a basic pattern, namely [0/90/45/-45]$_s$. Three types of impact tests were conducted on the graphite/epoxy laminates which had two thicknesses, 2 mm and 4 mm, and the ballistic limits were determined. The penetration process of composite laminates by a flat-ended missile consisted of three stages: pre-delamination, post-delamination before plugging and post-plugging. Based upon these three stages, a finite element model was established to simulate the static punch process. The material was modelled using effective moduli so that the details of the stacking sequence were not included in the model. The simulated static load-punch displacement curve was subsequently employed in the dynamic penetration analysis, and the displacements at certain specific checkpoints were adopted as the penetration criteria. It was shown that the computational results were in good agreement with the limited experimental data.

More recently, Mines et al.[14] conducted an experimental investigation into the high-velocity perforation behaviour of fully-clamped 200 mm × 200 mm polymeric composite laminates at impact velocities of up to 571 m/s. Woven

roving, z-stitched and through-thickness z-stitched glass polyester laminates for a number of laminate thicknesses (6, 12, 24 ply), three types of impactors (flat, hemispherical and conical), and two missile masses (6 g, 12 g) were examined. The results were presented in terms of static and impact perforation energies, and energy absorption mechanisms during high-velocity perforation were also discussed with a view to identifying improved combinations of materials. It was found that all types of construction behave in a similar manner.

As far as sandwich structures are concerned, Moriarty and Goldsmith[15] have recently conducted an experimental investigation into the dynamic energy absorption characteristics of sandwich shells, this work representing an extension of earlier work on flat sandwich panels.[16] Aluminium or ABS (acrylonitrile–butadiene–styrene) were used for the skins and a variety of honeycomb materials for the cores of the sandwich constructions. The specimens were subjected to non-perforating impact by a 0.7045 kg, 76.2 mm diameter projectile with a slightly curved impact surface. The projectiles were fired pneumatically at speeds ranging from 16.5 to 19.05 m/s. At these low velocities, it was found that the core material dominates the response in the case of fully-clamped specimens. For the simply-supported samples, the skins (faceplates) dominated the performance characteristics, with the thicker aluminium skin giving significantly poorer results than either the thinner metal or the ABS facing. The effect of the core was more diffuse and was coupled more to the nature of the skin than for fully-clamped specimens. Other relevant investigations have been concerned primarily with the analysis and design of sandwich structures for quasi-static loading[17–19] although Bernard and Lagace[20] examined the impact resistance of composite sandwich panels and Kosza and Sayir[21] studied failure patterns in the cores of sandwich beams and plates under impact loading. It is noted however that all of these studies of sandwich panels and components relate to relatively low impact velocities.

This chapter presents some of the results of our own detailed study on the penetration and perforation of sandwich panels made of composite material skins with polymeric foam cores. Emphasis is placed on ballistic test results and associated deformation mechanisms are contrasted with those found in quasi-static penetration. General empirical models are given that provide the perforation energies of FRP laminates and sandwich panels consisting of FRP laminate skins and foam cores under low-velocity impact by flat-faced, hemispherical-ended and conical-nosed indenters. A new model is developed for the so-called wave-dominated response/perforation of FRP laminates and sandwich panels with such laminates as skins and foam cores subjected to high-velocity impact by the three types of missile (flat, hemispherical and conical). The model predictions and the available test data are compared and discussed. The development

of the high velocity perforation model complements and extends the discussion on the ballistic impact on FRP laminates and sandwich panels given recently in references.[1–3]

8.2   Experimental procedure

8.2.1   Materials and specimens

E-glass woven roving (WR) cloth of $600\,g/m^2$ area density with polyester resin (Crystic 491PA and Butanox M50 (1%) hardener) were chosen for the skins and expanded polymeric foam (e.g. PVC) cores were used, these being purchased in slab/sheet form. The manufacture of panels and preparation of specimens by hand lay-up and assembly are described in Wen *et al.*[1]

Square laminates and sandwich panels with side lengths of 0.9 m were prepared and some smaller panels of 0.3 m × 0.3 m were cut from the larger panels for testing. Several triple-skinned (i.e. with a central laminate as well as the other skins) panels were manufactured using the same procedures. The behaviour of these latter panels is not discussed extensively herein (see Wen *et al.*[1]) but some of the test data will be included in the appropriate figures.

Some of the properties of the materials used are given in Table 8.1 in which σ_u, E_{s1}, σ_e and τ_{13} are the tensile strength, Young's modulus for in-plane tension, the elastic limit for through-thickness compression and the transverse shear strength of the laminates, respectively, and σ_c, E_c, G_c and τ are the compressive strength, Young's modulus in compression, shear modulus and shear strength of the core materials, respectively. Typical nominal stress-strain curves for both GRP laminates and foam core are given in Fig. 8.1.

8.2.2   Loading and data recording

In all the tests, panels were supported in specially designed frames, one with a 0.85 m square aperture (for the larger 0.9 m square panels) and the other with a 0.2 m square window (for smaller 0.3 m square panels). The supports were such that the out-of-plane movement of the edges of the panels was restrained but their in-plane movement was allowed (see Wen *et al.*[1]).

Quasi-static indentation tests were conducted on a screw driven (RDP) testing machine operating under displacement control. Flat-ended, hemispherical-ended and conical-nosed indenters with different diameters (ranging from 5.25 mm up to 150 mm) were used in the experiments. All the indenters were case-hardened. The panels were loaded normal to their planes at the centre and the load versus punch displacement curves were

Table 8.1. Materials for sandwich panels

Resins	*Source*	*Type*	*Catalyst/hardener*
Isopthalic polyester	Scott Bader	Crystic 491 PA	Butanox M50 (1%)
Reinforcement	*Source*	*Weight*	*Cloth*
E-Glass WR	Strand	$600\,g\,m^{-2}$	Woven roving
Core material	*Source*	*Density, thickness*	σ_c	E_c	G_c
Divinycell H130	Barracuda	$130\,kg\,m^{-3}$, 25 mm	2.5 MPa	175 MPa	50 MPa
Divinycell HCP100	Barracuda	$400\,kg\,m^{-3}$, 20 mm	10.4 MPa	340 MPa	180 MPa
GRP skins	Tensile tests	Average volume fraction = 43%	$\sigma_u = 345\,MPa$	$E_{s1} = 24\,GPa$	$\tau_{13} = 45\,MPa$
			$\sigma_e = 225\,MPa$		

Core material extra column: τ: 2 MPa, 7.4 MPa
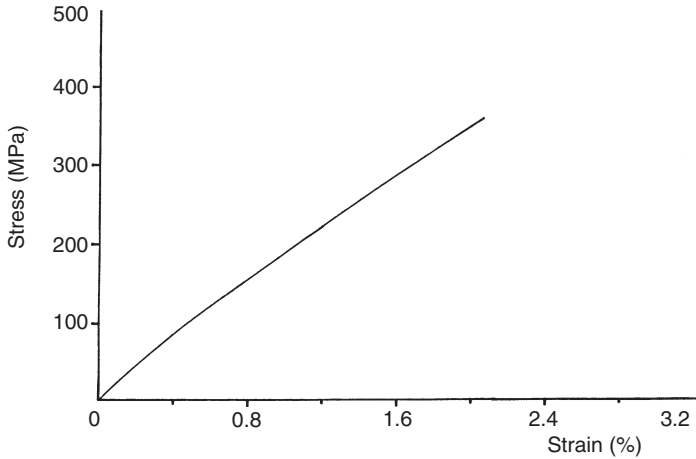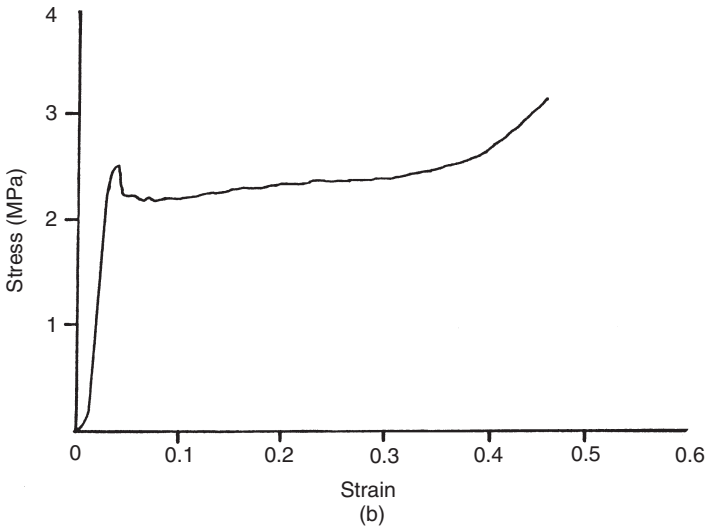
8.1 Nominal stress-strain curves: (a) GRP laminates in tension; (b) Divinycell H130 foam in compression; (c) GRP laminates in through-thickness compression.

recorded. The movements of the centres of the lower skins were also recorded on the larger panels during the tests using a suitable arrangement with an LVDT. The cross-head speed was 3 mm/minute for all the tests.

Low-velocity impact tests were carried out using a drop weight apparatus. The tup was instrumented with an accelerometer (Bruel and Kjaer, type 4382) and the deceleration-time history was recorded using a Kontron digital event recorder (WW700) operating at a sampling rate of 10^6 samples

Strain (mm/mm)
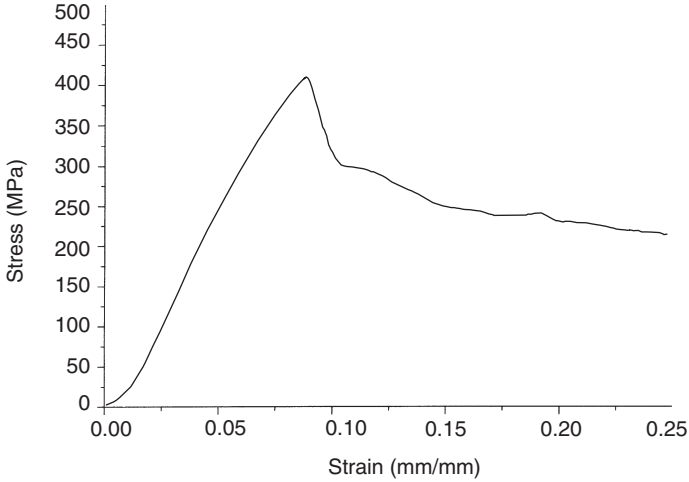
(c)

8.1 (cont.)
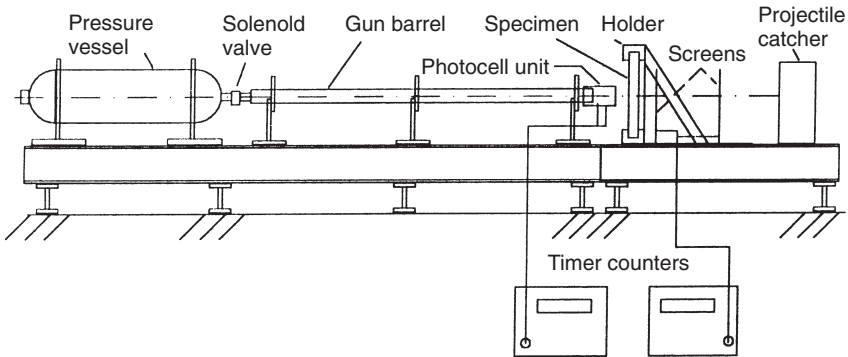
8.2 Schematic diagram of the pneumatic gun facility.

per second. The direction of motion of the tup was controlled by pre-tensioned vertical guide ropes. The initial impact velocity was measured by means of a photocell system. Details of the results of these tests have been described elsewhere[1] but some of the data are included in the relevant graphs to indicate the consistency in the behaviour of panels over a wide range of impact velocities.

The fixtures for high speed ballistic impact tests and the pneumatic gun facility for firing the projectiles are shown schematically in Fig. 8.2. Three types of projectile end geometries referred to above were used but only two projectile diameters (10.5 mm and 45 mm) were chosen, the projectiles

weighing approximately 18.0 g and 1.30 kg, respectively (see Wen *et al.*[1] and Reddy *et al.*[2] for details).

8.3   Experimental results

8.3.1   Quasi-static tests

8.3.1.1   *Range of tests and general observations*

Details of the results of the quasi-static indentation experiments are given by Wen *et al.*[1] It was found that most of the specimens failed by local indentation, penetration and perforation under the punches. One exception was the case of larger (0.9 m square) sandwich panels with 3.25 mm thick GRP skins and higher density foam core (Divinycell H100, density 400 kg/m³) loaded by 50 mm diameter flat or hemispherical indenters and those loaded by larger (150 mm) diameter indenters, all of which failed in a global bending mode. The other exception was the case of smaller (0.3 m square) sandwich panels with 3.25 mm thick GRP skins and higher density foam core (HCP100) loaded by a 20 mm flat-faced punch which failed by core shear.

It was also found that sandwich panels loaded quasi-statically by hemispherical-ended indenters with radii equal to or greater than the thickness of the core required the least energy for complete penetration and for this reason particular emphasis was placed upon the results for this nose geometry.[2] The details of the response to flat-ended indenters/projectiles are sufficiently different to warrant separate discussion and this has been given elsewhere.[1,3] When the radii of the indenters were smaller than the core thickness, the energies for perforation by hemispherical, flat and conical punches were approximately the same.

Flat-faced indenters

Figure 8.3(a) shows typical quasi-static load-displacement characteristics for a 0.9 m square sandwich panel with 3.25 mm thick GRP skins and 25 mm thick Divinycell H130 foam core loaded centrally by a 50 mm diameter flat-faced indenter, which first failed by indentation. The load-punch displacement curve and the vertical moment of the bottom skin of the panel are indicated in the figure. The first part of the load-punch displacement trace (up to the top skin failure at the first peak load) is bilinear. Core crushing as evidenced by the difference between the punch and the bottom skin displacement starts just after the knee of this bilinear part. After top skin failure (by shear along the periphery of the punch) at the peak load, the load drops to about a third of its peak value, there was considerable further
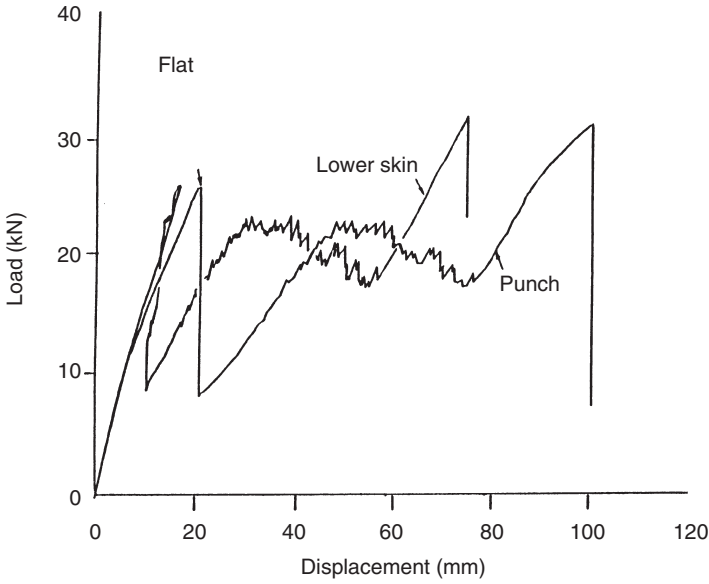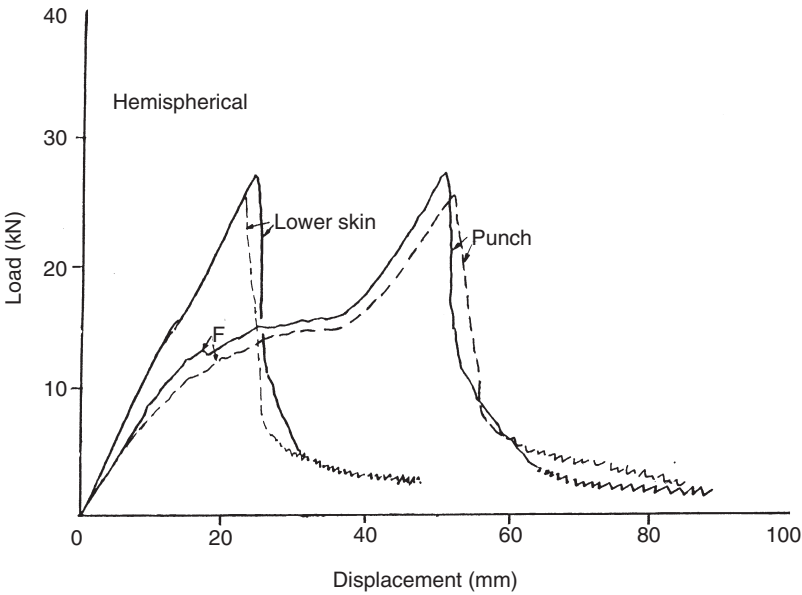
8.3 Load-displacement characteristics for 0.9 m square 3.25 mm thick GRP skin sandwich panels loaded quasi-statically by 50 mm diameter indenters: (a) Twin-skinned panel with 25 mm thick H130 foam core; (b) twin-skinned panel with 25 mm thick H130 foam core; (c) twin-skinned panel with 50 mm thick H130 foam core; (d) triple-skinned panel with 25 mm thick H130 foam cores; (e) twin-skinned panel with 25 mm thick H130 foam core; (f) cross-sectional view of identical panels loaded by flat-faced, hemispherical-ended and conical-nosed indenters (from bottom to top).
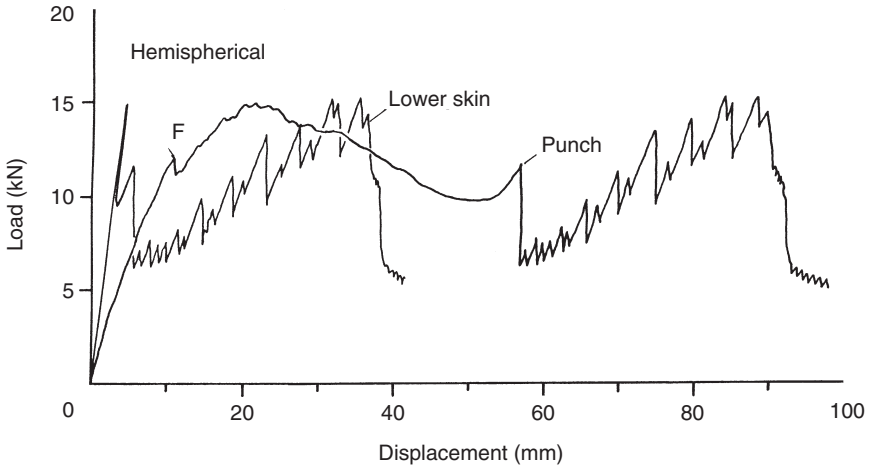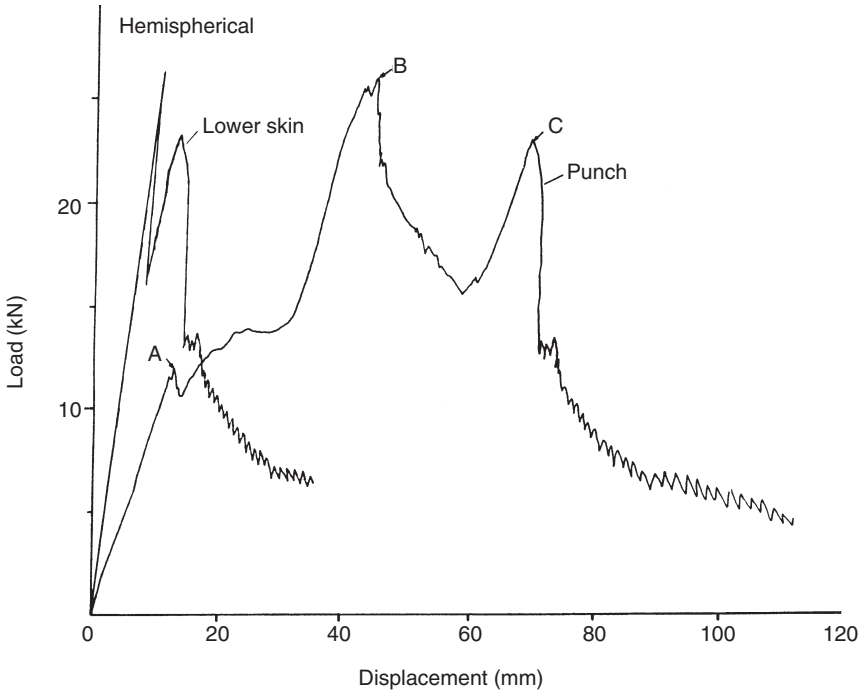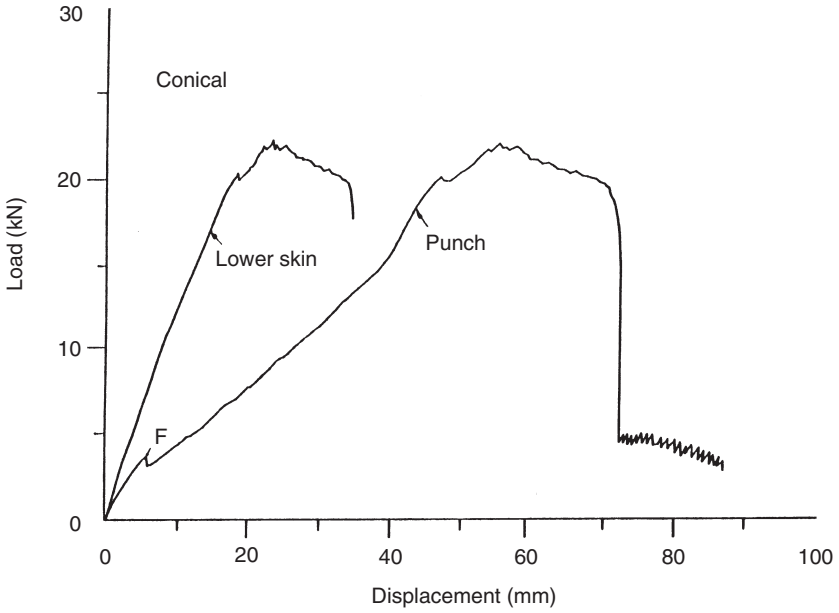
8.3 (cont.)

(e)

(f)

8.3 (cont.)

deformation characterised by progressive core crushing, lower skin debonding and bending. The lower skin of the panel debonded gradually from the core and failed by fracturing due to bending of the debonded skin.

Hemispherical-ended indenters

Typical load-displacement characteristics for 0.9 m square sandwich panels with 3.25 mm thick GRP skins and 25 mm and 50 mm thick H130 foam cores loaded quasi-statically by a 50 mm diameter hemispherical-ended indenter are presented in Fig. 8.3(b) and (c), respectively. It can be seen that core crushing starts very soon after loading begins. The top skins failed by a central puncture causing four cruciform cracks, at points indicated by F in these two load-displacement curves. It is clear that the load-punch displacement responses are different. In Fig. 8.3(b) after the top skin failure, the load did not fall but rather increased steadily. This corresponded to the crushing of the core material, the lengthening of cracks in the top skin as well as bending of the flaps resulting from cracks. This was then followed by a more rapid rise in load until the bottom skin failed in bending. It should be noted here that in this test the core thickness was equal to the radius of the indenter so that the applied force directly acted on the lower skin before the indenter had completely penetrated the upper skin. By contrast the load-displacement curve in Fig. 8.3(c) shows double hump response. This response is associated with the larger ratios of core thickness, c, to punch diameter, D, ($c/D > 0.5$) which allows the top skin penetration to be completed before the bottom skin is loaded directly by the indenter through a layer of densified foam (Reddy *et al.*[2]). Good repeatability was observed for identical sandwich panels in terms of their load-displacement response. A typical example is shown in Fig. 8.3(b) in which the solid and broken lines represent the load versus punch displacement characteristics of two nominally identical panel tests.

Figure 8.3(d) shows the load-displacement curve for a triple-skinned sandwich panel with three six-layer laminate skins of E-glass WR cloth reinforced polyester resin and two 25 mm thick H130 foam cores, loaded quasi-statically by the 50 mm diameter hemispherical-ended indenter. Like the twin-skinned sandwich panels described above, core crushing occurs from the beginning of the loading process as can be seen from Fig. 8.3(d). The top skin failed by a central puncture causing four cruciform cracks at point A in the curve. After the top skin failure, the load dropped slightly and then increased steadily which corresponded to the crushing of the core, the lengthening of the cracks as well as the bending of the resulting petals in the top skin. This was then followed by a more rapid rise in load until the middle skin failed at point B. It is interesting to note here that up to the middle skin failure the load-displacement response of the triple-skinned

panel was very similar to that of the double-skinned panel as shown in Fig. 8.3(c). After the middle skin failure, there was considerable further deformation which was characterised by progressive core crushing and the lower skin bending. At point C the lower skin fractured with the formation of four major cruciform cracks and perforation ensued.

Conical-nosed punches

Figure 8.3(e) shows typical load-displacement characteristics for a 0.9 m square sandwich panel with 3.25 mm thick GRP skins and 25 mm thick H130 foam core loaded quasi-statically by a 50 mm diameter conical-nosed indenter. After top skin failure just underneath the 2 mm radius nose tip (denoted by F in the figure), the load dropped slightly and then increased steadily to the maximum value. This second region was associated with the formation of major cruciform cracks and bending of the resulting flaps with bending hinges moving away from the loading point through the propagation of fractures and also overcoming the friction between the panel and the conical punch, all of which dissipated energy at an increasing rate. The bottom skin failed in bending accompanied by a small area of debonding.

Figure 8.3(f) shows photographs of the cross-sectional views of the three identical 0.9 m square sandwich panels with 3.25 mm thick GRP skins and 25 mm thick H130 foam cores loaded quasi-statically by 50 mm diameter flat-faced, hemispherical-ended and conical-nosed indenters (from bottom to top). The top skin shear plugging and core crushing are evident with a flat punch, the other two look very similar to each other. All these cases are categorised as indentation failures.

8.3.1.2 Discussion

Energies associated with three critical events in the penetration process of a twin-skinned sandwich panel loaded by flat-faced, hemispherical-ended and conical-nosed indenters can be found from the load-displacement curves as shown in Fig. 8.3(a), (b,c) and (e). These critical events are: (i) the energy to penetrate the top skin; (ii) the energy to penetrate (fracture) the bottom skin; and (iii) the energy to perforate the whole panel. It was found (Wen *et al.*[1]) that both the peak load at the failure of the top skin and the corresponding energy absorbed are approximately proportional to the weight of glass fibres in a skin, or equivalently, the thickness of the skin if the volume fraction is maintained the same. Similarly, the energies absorbed up to the failure (fracture) of the bottom skins of sandwich panels which fall into the same category (defined below) were also found to be linearly related to the weight of fibres or the thickness of skin (Wen *et al.*[1] and

Reddy *et al.*[2]). These observations indicate that laminate skins play a very important role in the failure and energy absorption of GRP skinned sandwich panels with foam cores, whilst the core thickness controls which category of behaviour occurs.

The experimental results obtained for sandwich panels loaded quasi-statically by hemispherical-ended indenters are presented in Fig. 8.4(a), which shows the plot of the non-dimensional penetration energy $(E_f/\sigma_u TD^2)$ versus the non-dimensional geometric property (L/D). It is clear from Fig. 8.4(a) that, irrespective of panel side length (L), the quasi-static tests conducted on the sandwich panels using hemispherical-ended punches may be categorised into two groups, one group with $H/D > 2$, the other with $H/D < 2$, here H and D are the total panel thickness and the punch diameter, respectively. In the former case considerably more energy was absorbed as can be seen from Fig. 8.4(a). In order to dilineate the difference, panels were sectioned to study the mechanisms. The only obvious difference appeared to be that for the panels with $H/D > 2$ relatively more debonding between the lower skin and the foam core had occurred. This was found (Wen *et al.*[1]) generally to be one of the mechanisms enhancing the quasi-static energy absorbing capacity.

On the other hand, the experimental data obtained for sandwich panels loaded quasi-statically by flat-faced punches are given in Fig. 8.4(b), which shows the plot of the non-dimensional global energy $(E_g/\sigma_u TD^2)$ against the non-dimensional geometric property (L/D). It can be seen from Fig. 8.4(b) that all the data points follow the same trend irrespective of the ratios of H/D. Closer examination reveals that the plots of the non-dimensional global energy $(E_g/\sigma_u TD^2)$ against the non-dimensional geometric property (L/D) for sandwich panels loaded quasi-statically by both flat-faced punches and hemispherical-ended indenters with $H/D > 2$ are almost identical, as can be deduced from Fig. 8.4(a) and (b). It may also be inferred from Fig. 8.4(b) that the energy absorbed by the global deformations of panels loaded by flat-faced punches is also approximately proportional to the thickness of the skin laminates. It should be mentioned here that the experimental results obtained for sandwich panels loaded quasi-statically by hemispherical-ended indenters can also be presented in terms of the plot of the non-dimensional global energy $(E_g/\sigma_u TD^2)$ against the non-dimensional geometric property (L/D), which is very similar to that given in Fig. 8.4(a). How to distinguish the global energy from the total penetration energy is discussed in Section 8.4.

8.3.2   Low-velocity impact tests

Low-velocity tests will not be described or discussed in detail in this chapter (for details, see Wen *et al.*[1]). However, Fig. 8.5 shows a typical low-velocity
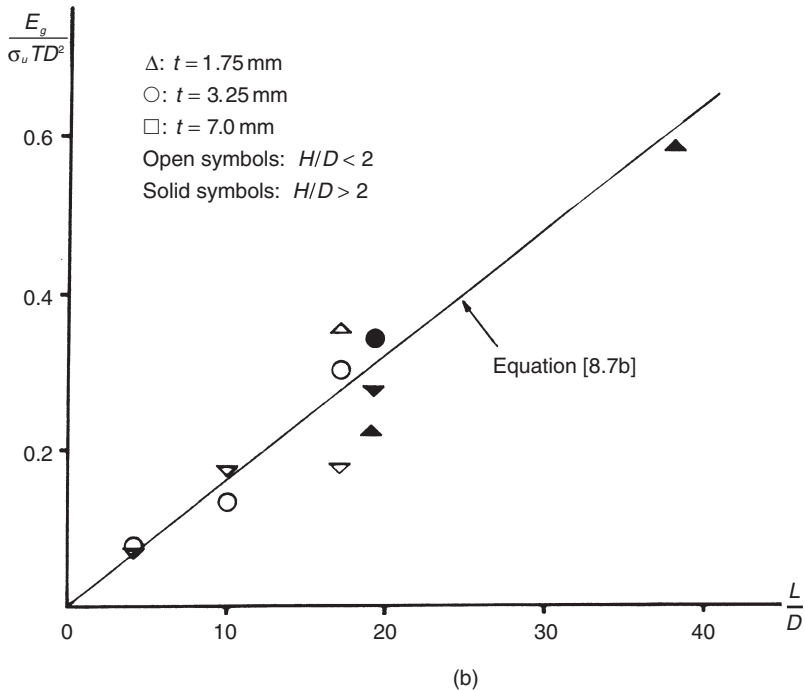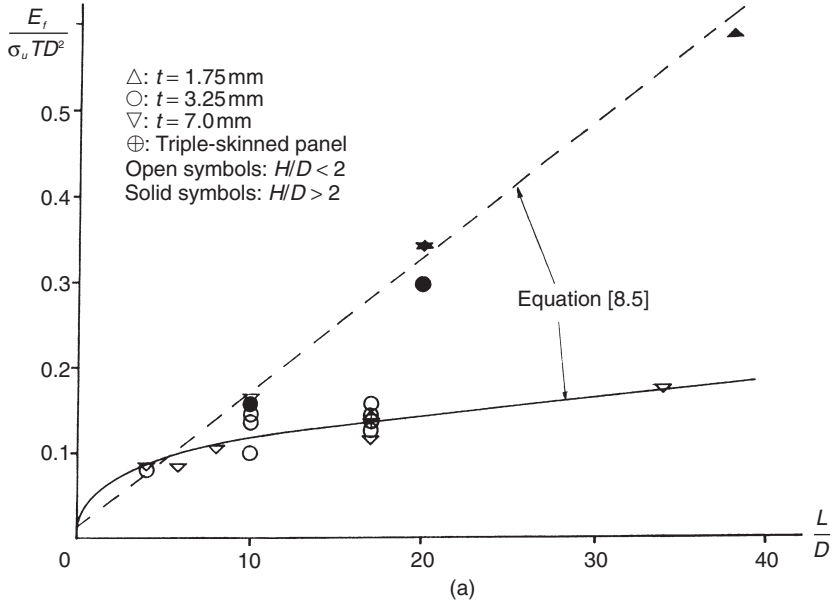
8.4 Variation of the non-dimensional penetration/global energies with the ratio of panel span to indenter diameter for sandwich panels loaded quasi-statically at the centre: (a) hemispherical-ended indenters; (b) flat-faced punches.
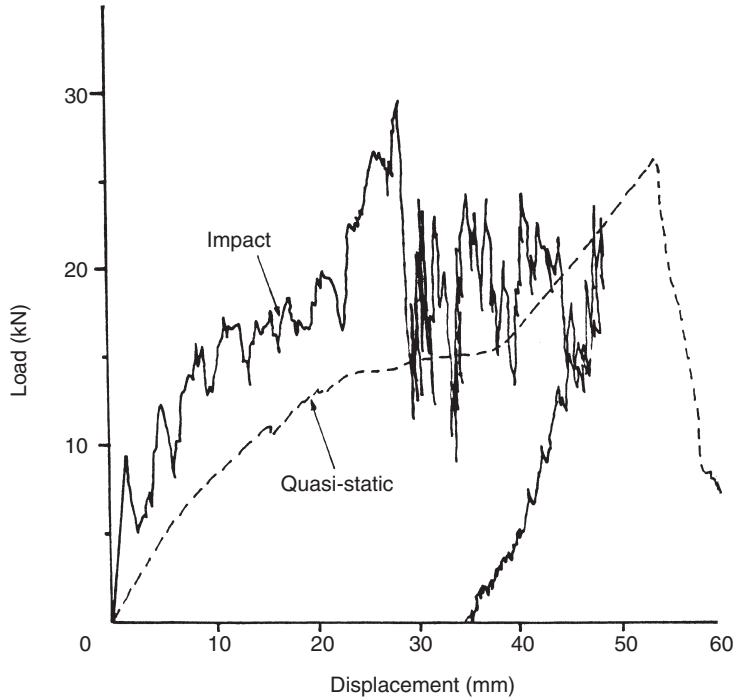
8.5 Comparison between quasi-static and impact load-displacement characteristics for 0.9 m square sandwich panels with 3.25 mm thick GRP skins and 25 mm thick H130 foam core loaded by a 50 mm diameter hemispherical-ended punch.

impact load-displacement curve for a 3.25 mm thick GRP skin sandwich panel with 25 mm thick H130 foam core struck at 6.23 m/s by a 42.5 kg tup mass with an attached 50 mm diameter hemispherical indenter.[1] Also shown in the figure is the corresponding quasi-static load-displacement curve for an identical panel. The lower skin of the panel subjected to dropped object loading fractured but was not completely penetrated. It was found that the fracture patterns as well as the load-deflection characteristics of the GRP skin sandwich panels loaded dynamically were similar to those observed in the corresponding quasi-static cases. It was also found that the extent of damage (judged by the extent of lower skin perforation) under dropped object loading was less than that observed in the identical panel under quasi-static loading even though the impact energy was about 20% higher than the corresponding quasi-static perforation energy. However, the extent of debonding between the lower skin and the core was larger in the impact tests. The dynamic load required to cause a given deflection is higher than the load required to cause the same deformation under quasi-static loading

conditions (see Fig. 8.5). The changes are presumably the result of enhanced strengths and stiffnesses of the components due to rate-dependent material properties and inertia effects. The interplay between these and the core-skin bond strength will influence the balance between the various failure mechanisms in the panel and their respective contributions to energy absorption.

8.3.3 Ballistic impact tests

8.3.3.1 *Range of tests and observations*

Ballistic impact tests were performed on 0.3 m square GRP laminates as well as sandwich panels with H130 foam core using 10.5 mm diameter projectiles with masses of approximately 19.0 g at impact velocities up to 305 m/s. Ballistic impact tests were also carried out on 0.9 m square twin-skinned (as well as triple-skinned) panels using projectiles with a 45 mm diameter and masses of approximately 1.3 kg at impact velocities up to 102 m/s.

Many tests were performed. Here we concentrate on presenting data for the critical impact conditions associated with the ballistic limit (velocity for full perforation of the projectile nose through the panel) for flat-faced, hemispherical-ended and conical-tipped projectiles. Figure 8.6(a) and (b) shows respectively the effects of total laminate skin thickness on the ballistic limits for 0.3 m and 0.9 m square sandwich panels struck by hemispherical-ended and conical-nosed missiles while Fig. 8.6(c) and (d) show respectively the same effects for 0.3 m and 0.9 m square sandwich panels struck by flat-faced projectiles. Plots of the variation in the residual velocity with impact velocity for 0.3 m square sandwich panels struck by hemispherical-ended conical-nosed projectiles are given in Fig. 8.6(e). It is seen from Fig. 8.6(a) to (d) that the ballistic limit is an increasing function of the total laminate thickness. Figure 8.6(a), (b) and (e) illustrates that the perforation processes for the hemispherical-ended and the conical-tipped projectiles used in the study are essentially the same in terms of ballistic limits and residual velocities.

In order to observe the influence of skin thickness on the ballistic performance of sandwich panels, panels were sectioned. Figure 8.7(a) shows the cross-sectional view of 0.3 m square sandwich panels with 1.75 mm, 3.25 mm and 7.0 mm thick GRP skins and 25 mm thick H130 foam core, perforated by the 10.5 mm diameter hemispherical-ended missile at initial velocities well above their ballistic limits. It is evident from this figure that debonding between the lower skins and the core decreases with an increase in laminate thickness while delamination in the lower skins in particular increased with increasing laminate thickness. This is the reverse of the
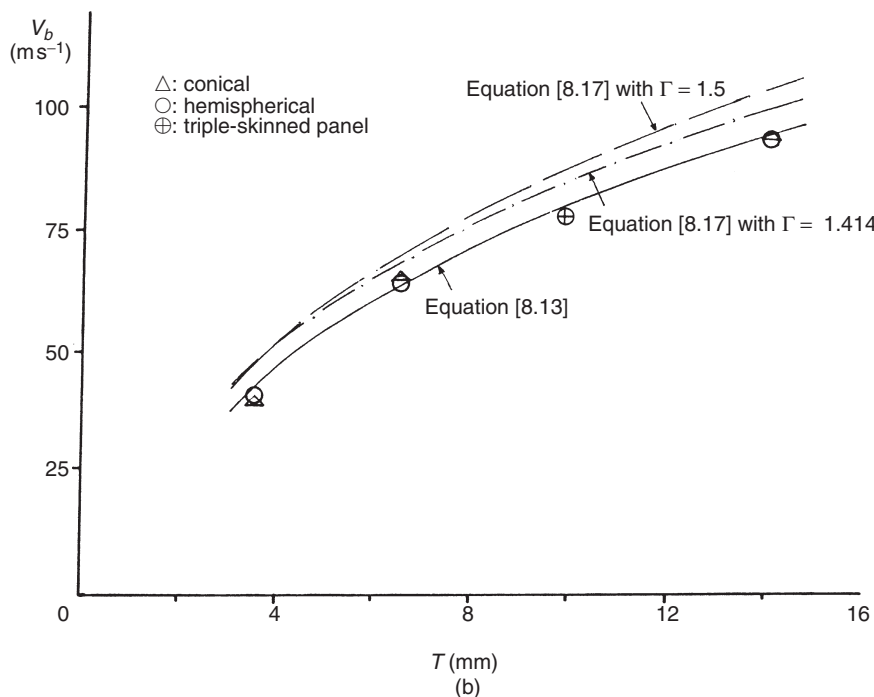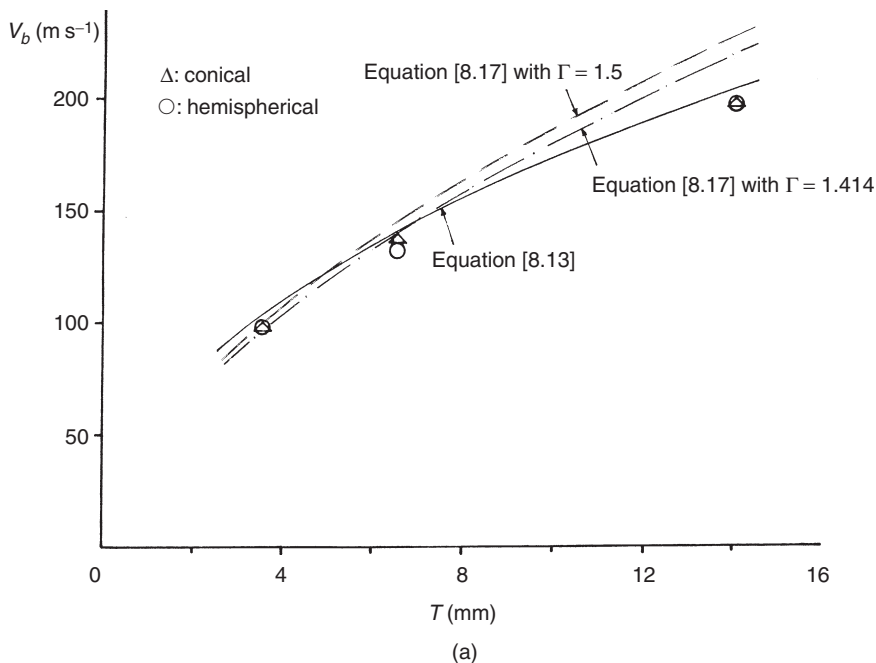
8.6 (a) Effects of total laminate thickness on the ballistic limits for 0.3 m square sandwich panels with GRP skins and 25 mm thick H130 foam core struck by 10.5 mm diameter hemispherical-ended and conical-nosed missiles. (b) Effects of total laminate thickness on the ballistic limits for 0.9 m square sandwich panels with GRP skins and 25 mm thick H130 foam core (two in the case of triple-skinned panel) struck by 10.5 mm diameter hemispherical-ended and conical-nosed missiles.
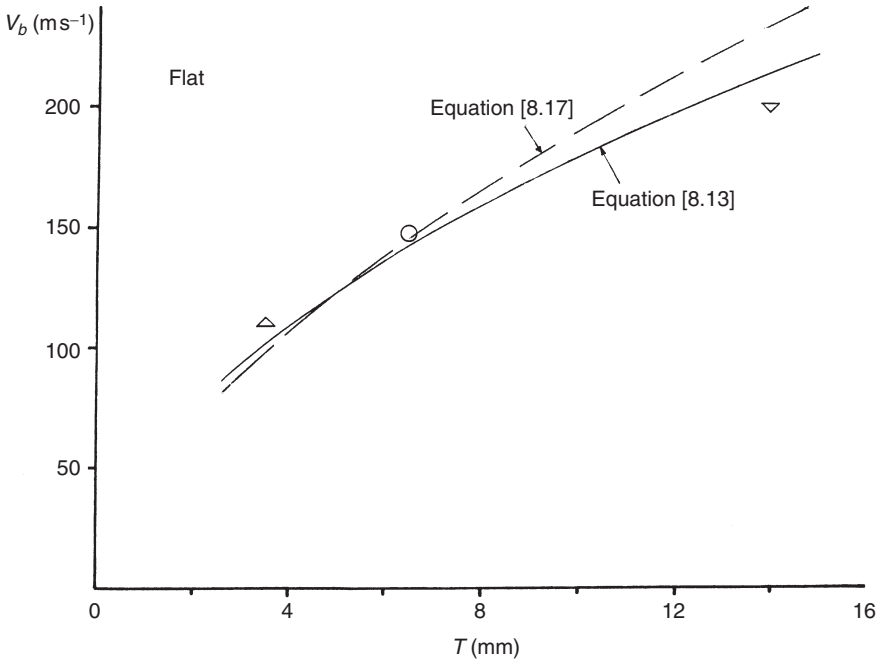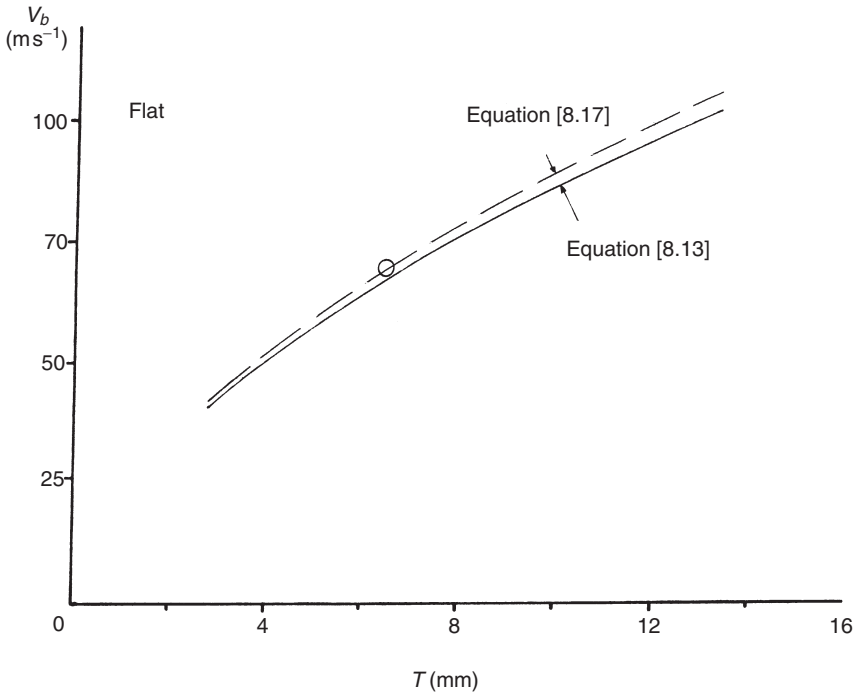
8.6 (cont.) (c) Effects of total laminate thickness on the ballistic limits for 0.3 m square sandwich panels with GRP skins and 25 mm thick H130 foam core struck by a 10.5 mm diameter flat-faced projectile. (d) Effects of total laminate thickness on the ballistic limits for 0.9 m square sandwich panels with GRP skins and 25 mm thick H130 foam core struck by a 45 mm diameter flat-faced missile.

V_r (ms^{-1})

Δ: $t = 1.75$ mm
○: $t = 3.25$ mm
□: $t = 7.0$ mm
Open symbols: hemispherical
Solid symbols: conical

V_i (ms^{-1})

(e)
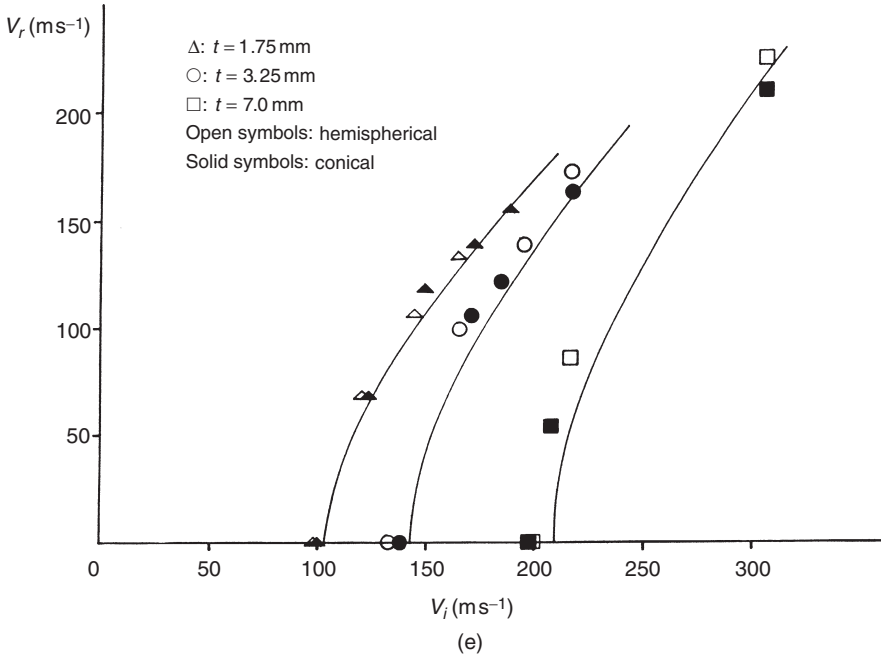
8.6 (cont.) (e) Variation of the residual velocity with the initial impact velocity for 0.3 m square sandwich panels with GRP skins and 25 mm thick H130 foam core struck by 10.5 mm diameter hemispherical-ended and conical-nosed missiles.

behaviour of identical panels loaded quasi-statically by the same diameter punch, as shown in Fig. 8.7(b).

The photographs in Fig. 8.8 show the effects of initial impact velocity on the behaviour of 0.3 m square sandwich panels with 1.75 mm thick GRP skins and 25 mm thick H130 foam core tested using the 10.5 mm diameter hemispherical-ended missile with impact velocities at and above the ballistic limit (approximately 100 m/s), as indicated in the figure. It is clear from this figure that debonding between the lower skins and the core decreased with increasing impact velocity whereas delamination within the lower skins increased with an increase in impact velocity. At an impact velocity of 163.9 m/s the delamination area was roughly circular in shape and its diameter was about eight times that of the missile, as can be seen from Fig. 8.8(d).

8.3.3.2   Discussion

It was observed from the experiments described briefly in the previous sections that the dynamic perforation energies are higher than those under
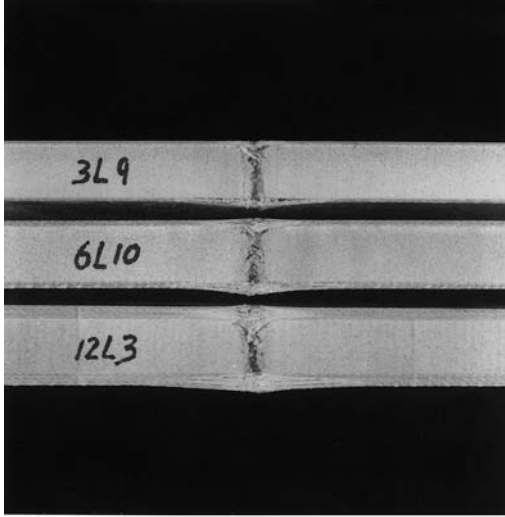
(a)
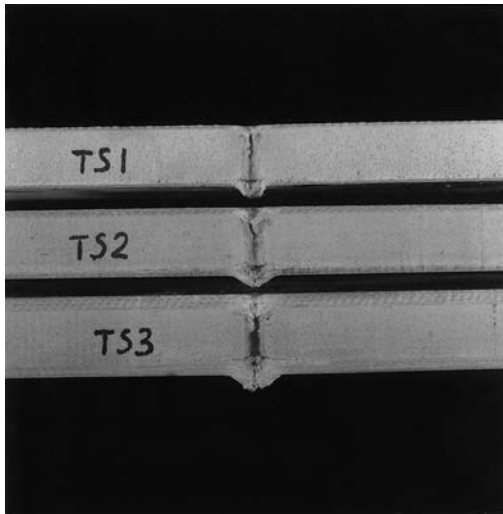
(b)

8.7 Cross-sectional views of 0.3 m square sandwich panels with GRP skins and 25 mm thick H130 foam core tested with a 10.5 mm diameter hemispherical-ended punch: (a) ballistic loading; (b) quasi-static loading, indicating the extent of delamination in the skins and debonding between the core and the bottom skin.

(a)　　　　　　　　　　　　(b)

(c)　　　　　　　　　　　　(d)
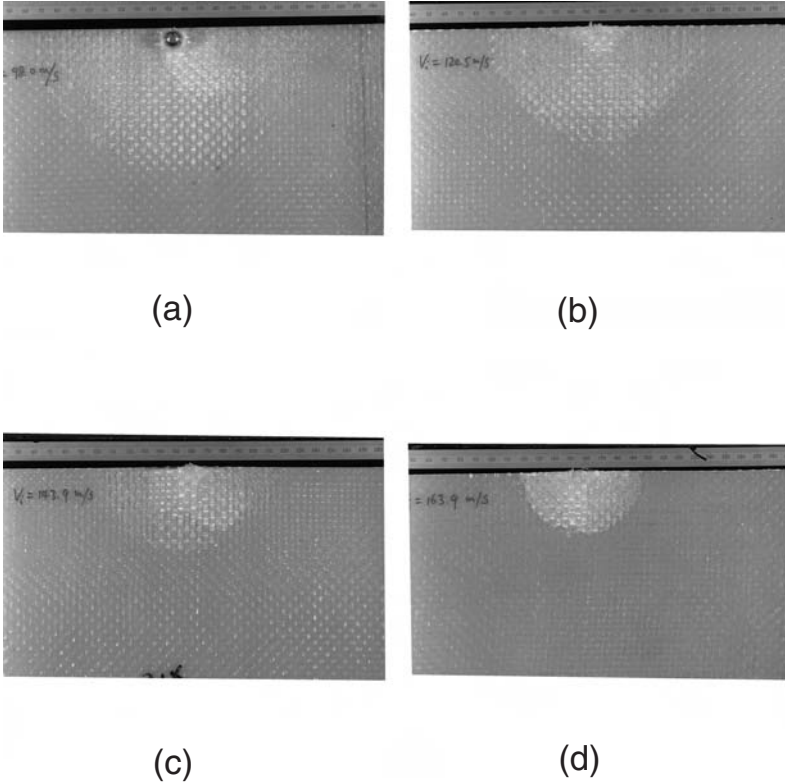
8.8 Photographs of 0.3 m square sandwich panels with 1.75 mm thick
GRP skins and 25 mm thick H130 foam core struck by a 10.5 mm
diameter hemispherical-ended missile at different velocities.
(a) $V_i = 98\,\text{m s}^{-1}$; (b) $V_i = 120.5\,\text{m s}^{-1}$; (c) $V_i = 143.9\,\text{m s}^{-1}$;
(d) $V_i = 163.9\,\text{m s}^{-1}$.

quasi-static loading conditions. Figure 8.9(a), (b) and (c) shows plots of the
dynamic enhancement factor, ϕ, against impact velocity, V_i, for sandwich
panels struck by hemispherical-ended projectiles for H/D ratios less than
and greater than 2, and by flat-faced missiles (irrespective of the ratios of
H/D), respectively. ϕ is defined here as the ratio of the dynamic perforation
energy for a panel to the energy absorbed up to the fracture of the lower
skin of an identical panel under quasi-static loading. What it reflects is
changes in energy absorbing mechanisms due to dynamic effects including
inertia. Closer examination of Fig. 8.4(a) and Fig. 8.9(a) and (b) reveals that
the products of the quasi-static penetration energy and the dynamic
enhancement factor are nearly the same for sandwich panels with $H/D > 2$
and $H/D < 2$ especially at higher impact velocities. This means that at higher
impact velocities the energy absorbing mechanisms are the same for sand-
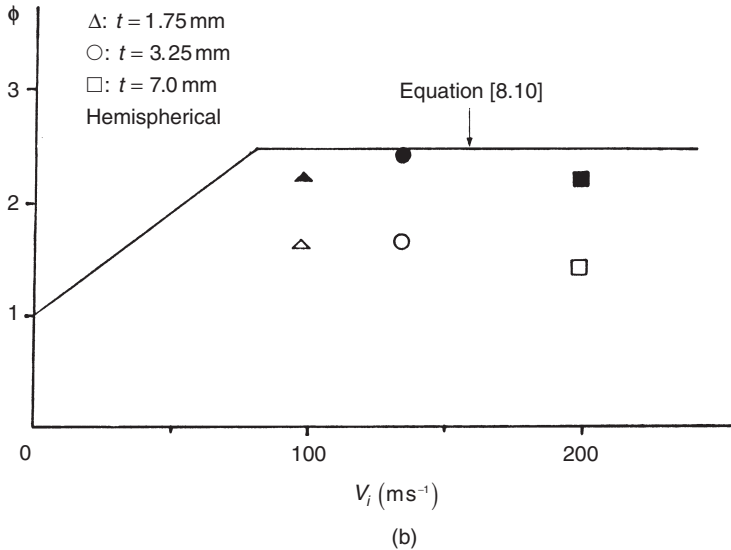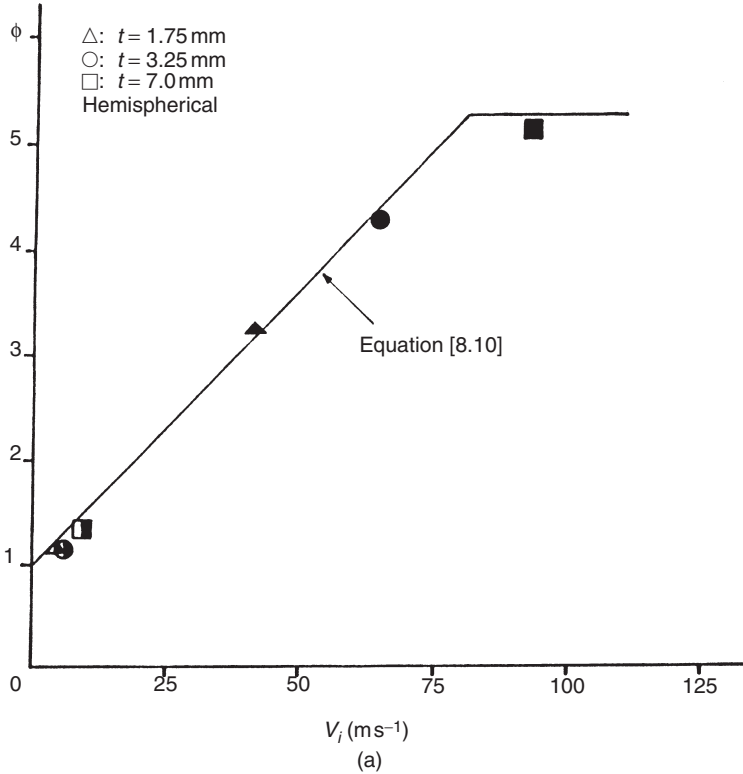
8.9 Variation of the dynamic enhancement factors, ϕ, with the initial impact velocity, V_i for sandwich panels. (a) Hemispherical-ended projectiles with $H/D < 2$; (b) hemispherical-ended projectiles with $H/D > 2$; (c) flat-faced missiles.
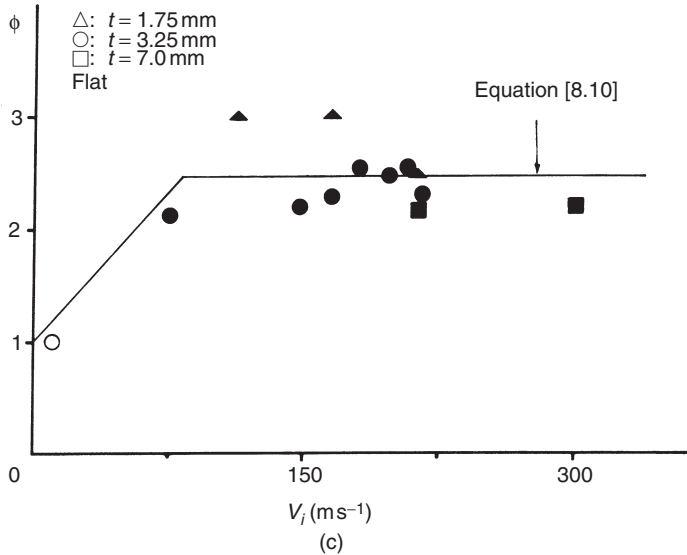
8.9 (cont.)

wich panels irrespective of the H/D ratios and that the kinetic energy is mainly dissipated by the FRP laminate skins. The ratios of dynamic to quasi-static perforation energies versus impact velocity (in this case for 0.3 m square sandwich panels as noted above) are also given in Fig. 8.9(b) as open symbols. The latter illustrates the difference in the fracture and perforation energies for the smaller panels struck by hemispherical-ended projectiles when $H/D > 2$ which is why the fracture energies are used. It should be noted that for all the 0.9 m square panels loaded quasi-statically by a 50 mm diameter hemispherical-headed indenter the perforation energy and the energy absorbed up to the fracture of the lower skin of the panels are almost identical (Wen et al.[1]). Therefore, these two ratios are equivalent to each other in Fig. 8.9(a) as designated by the solid symbols. The half-solid symbols in this figure represent the experimental data for the 0.9 m square sandwich panels subjected to low speed impact (dropped object) loading, where the panels were not totally perforated, while the open symbol in Fig. 8.9(c) represent the test result for a 0.9 m square sandwich panel under dropped object loading, where the lower skin of the panel was not penetrated but debonded from the core in a large area (Wen et al.[1]).

It is apparent from Fig. 8.9(a) and (c) that initially the dynamic enhancement factor increases with increasing impact velocities, while it is seen from Fig. 8.9(b) (where only the results of higher velocity impact tests are shown) that the dynamic enhancement factor is independent of the impact veloci-

ties. These results imply that there exists a transition velocity below which the dynamic enhancement factor is linearly related to initial impact velocity and above which it is a constant. For the tests performed this velocity is approximately 80 m/s. It should be mentioned here that similar observations can be made for conical-nosed projectiles.

8.4   Model development

Based on the experimental observations and discussions made in the previous sections and elsewhere,[1–3] ballistic impact on fibre-reinforced polymer laminates and sandwich panels with such laminates as skins and foam cores may be categorised into two regimes, namely, low velocity impact and wave-dominated response. In the former case global response as well as local deformations/failure are simultaneously present while in the latter case local deformations/failure dominate. Two semi-empirical modelling methods are described. One uses the dynamic enhancement factor to scale the quasi-static behaviour and encompass the whole range of perforation/ballistic data. The other (wave-dominated) model is based upon a local mechanism alone and incorporates inertial effects in a simplified manner.

8.4.1   Low-velocity impact

8.4.1.1   Empirical formulas for quasi-static penetration energy

The principle of dimensional analysis is used here to derive the empirical formulas for quasi-static penetration energies. Based on the observations made on the experimental data, it is reasonable to assume that the energy absorbed up to the fracture (penetration) of the lower skin by a sandwich panel with FRP laminate skins and foam core loaded quasi-statically by an indenter can be divided into two parts, in a similar manner to the procedure suggested by Wen and Jones.[22] One part is associated with the energy absorbed by local deformations, E_l, and the other, E_g, is related to the energy dissipated by global deformations of the panel. Thus[1–3]

$$E_f = E_l + E_g \qquad\qquad [8.1]$$

where E_f is the energy absorbed up to the fracture (penetration) of the lower skin of the sandwich panel.

Hemispherical-ended indenters

It is assumed that, in the case of a sandwich panel loaded by a hemispherical-ended indenter, the local energy, E_l, can be estimated by the fragmentation energy given by

$$E_1 = \frac{\pi D^2 T \sigma_u \varepsilon_f}{8}$$

[8.2]

in which σ_u, ε_f, D and T are the failure stress (UTS) and the fracture strain of the laminates in tension, indenter diameter and total laminate thickness, respectively. If the indenter diameter, D, is taken as a characteristic length, then standard techniques of dimensional analysis indicate that the energy absorbed by global structural response, E_g, when normalized with respect to $\sigma_u D^3$ can be related to the geometric properties of the punch and the panel by a relationship of the following form[1–3]

$$\frac{E_g}{\sigma_u D^3} = A\left(\frac{L}{D}\right)^{\beta_1}\left(\frac{T}{D}\right)^{\beta_2}$$

[8.3]

Substituting E_l and E_g in equations [8.2] and [8.3] into equation [8.1] and rearranging gives

$$\frac{E_f}{\sigma_u D^3} = \frac{\pi \varepsilon_f}{8}\left(\frac{T}{D}\right) + A\left(\frac{L}{D}\right)^{\beta_1}\left(\frac{T}{D}\right)^{\beta_2}$$

[8.4]

here A, β_1 and β_2 are constants which are to be determined from experiments.

For FRP skin sandwich panels with foam cores loaded quasi-statically by hemispherical-ended indenters it is found (Wen et al.,[1] also see discussion in Section 8.3.1.2) that E_f is linearly related to the thickness of the skin laminates. Hence, β_2 in equation [8.4] can be taken as unity. Equation [8.4] can thus be rewritten in the following form

$$\frac{E_f}{\sigma_u T D^2} = \frac{\pi \varepsilon_f}{8} + A\left(\frac{L}{D}\right)^{\beta_1}$$

[8.5]

Flat-faced punches

It is assumed that, in the case of a sandwich panel loaded by a flat-faced punch, the local energy, viz. the first term on the right hand side of equation [8.1], can be estimated by the following expression

$$\frac{E_1}{\sigma_u T D^2} = \frac{\pi}{4}\left(\frac{K\sigma_c}{\sigma_u}\right)\left(\frac{c}{T}\right)\varepsilon_d + \frac{\pi}{2}\left(\frac{\tau_{13}}{\sigma_u}\right)\left(\frac{T}{D}\right)\left(\frac{t}{T}\right)^2 + \frac{\pi \varepsilon_f}{8}\left(\frac{t}{T}\right)$$

[8.6]

in which the first, second and last terms on the right hand side of equation [8.6] represent the energies dissipated by the core crushing, the upper skin shear plugging and the fragmentation energy of the lower skin of the panel, respectively. K is the constraint factor usually taken to be 2 (Wen et al.[1]) and τ_{13} and σ_c are the transverse shear strength of the skin laminates and

the compressive strength of the core, respectively. ε_d is a measure of densification of the foam core, which may be determined experimentally, as discussed in Section 8.5.

The energy dissipated by the global deformations of the panel may be estimated in a similar manner to that described above for a hemispherical-ended indenter. Thus,

$$\frac{E_g}{\sigma_u D^3} = B\left(\frac{L}{D}\right)^{\beta_3}\left(\frac{T}{D}\right)^{\beta_4} \qquad [8.7a]$$

here B, β_3 and β_4 are constants which are to be determined from experiments.

For FRP skin sandwich panels with foam cores loaded quasi-statically by flat-faced punches it is found (see discussion in Section 8.3.1.2) that E_g is approximately proportional to the thickness of the skin laminates. Therefore, β_4 in equation [8.7a] can be taken as unity. Equation [8.7a] can thus be recast into the following form

$$\frac{E_g}{\sigma_u T D^2} = B\left(\frac{L}{D}\right)^{\beta_3} \qquad [8.7b]$$

Substituting equations [8.6] and [8.7b] into equation [8.1] yields

$$\frac{E_f}{\sigma_u T D^2} = \frac{\pi}{4}\left(\frac{K\sigma_c}{\sigma_u}\right)\left(\frac{c}{T}\right)\varepsilon_d + \frac{\pi}{2}\left(\frac{\tau_{13}}{\sigma_u}\right)\left(\frac{T}{D}\right)\left(\frac{t}{T}\right)^2$$
$$+ \frac{\pi\varepsilon_f}{8}\left(\frac{t}{T}\right) + B\left(\frac{L}{D}\right)^{\beta_3} \qquad [8.8]$$

8.4.1.2 Dynamic enhancement factor

On the basis of the observations made regarding the experimental results (Section 8.3.3.2), the impact perforation energy, E_{pi}, of a sandwich panel struck transversely by a projectile may be written as

$$E_{pi} = \phi E_f \qquad [8.9]$$

where ϕ is the dynamic enhancement factor which may be expressed in the following form

$$\phi = 1 + \beta\left(\frac{V_i}{V_o}\right) \quad (V_i < V_o) \qquad [8.10a]$$

$$\phi = 1 + \beta \qquad (V_i > V_o) \qquad [8.10b]$$

where β is an empirical constant. Here, V_o is the transition velocity. The data acquired in the test programme suggest that this is given by

$$V_o = C\varepsilon_f = \sqrt{\frac{E_{s1}}{\rho_t}}\varepsilon_f \qquad\qquad [8.10c]$$

in which C is the speed of sound in the laminates along the fibre direction; ρ_t and E_{s1} are the density and the in-plane Young's modulus of the laminates, respectively. Equation [8.10c] is the Karman critical velocity, the uniaxial impact velocity above which tensile deformation cannot be transmitted away from the loading point because the material has fractured and, perhaps coincidentally, is approximately 80 m/s for the material properties of the laminates used. The rationale for using this critical velocity for transverse impacts needs to be explored further.

Combining equations [8.5], [8.8] and equation [8.9] yields

$$\frac{E_{pi}}{\phi\sigma_u TD^2} = \frac{\pi}{8}\varepsilon_f + A\left(\frac{L}{D}\right)^{\beta_1} \qquad\qquad [8.11]$$

for hemispherical-ended projectiles, and

$$\frac{E_{pi}}{\phi\sigma_u TD^2} = \frac{\pi}{4}\left(\frac{K\sigma_c}{\sigma_u}\right)\left(\frac{c}{T}\right)\varepsilon_d + \frac{\pi}{2}\left(\frac{\tau_{13}}{\sigma_u}\right)\left(\frac{T}{D}\right)\left(\frac{t}{T}\right)^2$$
$$+ \frac{\pi\varepsilon_f}{8}\left(\frac{t}{T}\right) + B\left(\frac{L}{D}\right)^{\beta_3} \qquad\qquad [8.12]$$

for flat-faced missiles.

Finally, from the above equations an approximate expression can be obtained for the ballistic limit, V_b, by assuming that the critical projectile kinetic energy is equal to E_{pi}, the energy for perforation. Thus,

$$V_b = \left(\frac{2E_{pi}}{G}\right)^{\frac{1}{2}} \qquad\qquad [8.13]$$

where G is the projectile mass.

8.4.2   Wave-dominated response

8.4.2.1   Assumption about the resistive pressure

As discussed previously, for the wave-dominated response the deformations will be localised and the through-thickness strength of the FRP laminates will be enhanced by dynamic effects such as inertia and wave propagation. The nose shape of missiles also has an effect on the ballistic perforation process. In the following, a simple model is proposed for the high speed perforation of FRP laminates by missiles with different nose shapes. It is assumed that the mean pressure (σ) applied normally to the surface of the missile provided by an FRP laminate target material to resist penetration

and perforation by a missile can be decomposed into two parts, one part is the cohesive static resistive pressure (σ_s) due to the elastic-plastic deformations of the laminate material and the other is the dynamic resistive pressure (σ_d) arising from velocity effects. Thus[23]

$$\sigma = \sigma_s + \sigma_d \qquad [8.14]$$

If it is further assumed that the cohesive static resistive pressure is equal to the static linear elastic limit (σ_e) in through-thickness compression of the FRP laminates,[1,10] i.e. $\sigma_s = \sigma_e$, and that the dynamic resistive pressure (σ_d) is a function of the parameter $(\rho_t/\sigma_e)^{1/2}V_i$ and is taken to be $\sigma_d = \Gamma(\rho_t/\sigma_e)^{1/2}V_i\sigma_e$,[23] then equation [8.14] can be rewritten as

$$\sigma = \left[1 + \Gamma\sqrt{\frac{\rho_t}{\sigma_e}}V_i\right]\sigma_e \qquad [8.15]$$

Here ρ_t and V_i are the density of the FRP laminates and the initial impact velocity of the missile, respectively. Γ is a constant which is determined empirically. In Wen,[23] by curve-fitting the perforation data, Γ has been evaluated to be 2, 1.5 and $2\sin(\theta/2)$ for flat-faced, hemispherical-ended and conical-nosed missiles, respectively. Here θ is the cone angle of a conical-nosed projectile.

8.4.2.2 Perforation of FRP laminates/sandwich panels

The ballistic limit condition for FRP laminates and sandwich panels with such laminates as skins and with foam core struck transversely by a rigid missile with different nose shapes can be estimated from energy consideration. It is easy to show that

$$E_k = \frac{\pi D^2 T\sigma}{4} = \frac{\pi D^2 T}{4}\left[1 + \Gamma\sqrt{\frac{\rho_t}{\sigma_e}}V_b\right]\sigma_e \qquad [8.16]$$

Substituting $E_k = (1/2)GV_b^2$ into the above equation and rearranging yields

$$V_b = \frac{\pi\Gamma\sqrt{\rho_t\sigma_e}\,D^2T}{4G}\left[1 + \sqrt{1 + \frac{8G}{\pi\Gamma^2\rho_t D^2T}}\right] \qquad [8.17]$$

where V_b is the critical impact velocity or ballistic limit.

8.5   Comparisons and discussion

The four constants, viz. A, β_1 in equation [8.5] and B, β_3 in equation [8.7] are determined by a curve-fitting technique using the test data obtained from the experimental programmes. As noted earlier in Section 8.3.1, all the quasi-static tests performed on sandwich panels by hemispherical-

ended indenters thus far can be classed into two groups (see Fig. 8.4(a)) depending upon the ratio of the total panel thickness to punch diameter, H/D. ε_f in equation [8.5] is taken to be 0.021.[1] For $H/D < 2$, $A = 0.05$, $\beta_1 = 1/3$; for $H/D > 2$, $A = 0.016$, $\beta_1 = 1$. Figure 4(a) shows how equation [8.5] correlates with the experimental data with these values of A and β_1.

On the other hand, all the quasi-static tests conducted on sandwich panels by flat-faced punches, as shown in Fig. 8.4(b), followed the same trend irrespective of the ratios of H/D. The data points for the global energy (E_g) presented in Fig. 8.4(b) are calculated using equation [8.1] and equation [8.6]. ε_d in equation [8.6] is taken to be 0.8 for H130 foam core employed in the tests, which may be estimated from the load-displacement characteristics as shown in Fig. 8.3(a) (from which it can be seen that the 25 mm thick foam core crushed about 20 mm when the bottom skin of the sandwich panel failed. Hence, $\varepsilon_d = 20/25 = 0.8$). It can be shown that the two constants, namely, B and β_3 in equation [8.7] can be estimated to be $B = 0.016$ and $\beta_3 = 1$. It should be noted here that these two values are the same as those for sandwich panels loaded by hemispherical-ended indenters with $H/D > 2$. It is seen from Fig. 8.4(b) that equation [8.7] with these two values is in good correlation with the experimental data.

Equation [8.10] has been fitted to the available experimental results presented in Fig. 9(a), (b) and (c). ρ_t and E_{s1} in equation [8.10c] are taken to be 1650 kg/m^3 and 24 GPa, respectively (Wen et al.[1]). Substituting these values and $\varepsilon_f = 0.021$ into equation [8.10c] gives $V_o = 80$ m/s. The empirical constant, β, in the equation has been evaluated to be $\beta = 4.5$ and 1.5 for sandwich panels struck by hemispherical-ended projectiles with $H/D < 2$ and $H/D > 2$, respectively. For sandwich panels impacted by flat-faced missiles β has been evaluated to be $\beta = 1.5$. As can be seen from Fig. 8.9, with these values for β, there is good correspondence between equation [8.10] and the test data.

Comparisons are made in Fig. 8.6(a) and (b) between the model predictions (equations [8.13 and [8.11]) and the experimental results obtained for GRP skin sandwich panels with $H/D > 2$ and $H/D < 2$ struck normally by hemispherical-ended projectiles. In Fig. 8.6(a) the solid line is the predictions of equation [8.13] with $A = 0.016$, $\beta_1 = 1$ and $\beta = 1.5$, whilst in Fig. 8.6(b) the solid line represents equation [8.13] with $A = 0.05$, $\beta_1 = 1/3$ and $\beta = 4.5$. It is clear from these two figures that the model predictions (equations [8.13] and [8.11]) fit the experimental results with good accuracy.

Comparisons are also made in Fig. 8.6(c) and (d) between the model predictions (equations [8.13] and [8.12]) and the test data obtained for sandwich panels impacted by flat-faced missiles. The solid lines are the predictions of equation [8.13] with $B = 0.016$, $\beta_3 = 1$ and $\beta = 1.5$. It is seen

from Figs. 8.6(c) and (d) that the model (equations [8.13] and [8.12]) fits well with the experimental data.

Figure 8.6(e) shows the experimental plots of the residual velocity versus impact velocity for 0.3 m square sandwich panels with H130 foam core impacted by a 10.5 mm diameter hemispherical-headed missile with a mass of 17.9 g at velocities up to 305 m/s. Also shown in Fig. 8.6(e) as solid lines are predictions based upon

$$V_r = (V_i^2 - V_b^2)^{\frac{1}{2}} \tag{8.18}$$

where V_r and V_i are the residual and incident impact velocities of the missile, respectively and V_b is the ballistic limit which is determined by equation [8.13]. It is evident from Fig. 8.6(e) that the model predictions are in good accord with the experimental observations.

As noted earlier, the difference of the energies absorbed by identical sandwich panels loaded by hemispherical-ended indenters and conical-nosed punches are negligibly small and therefore the equations derived above for hemispherical indenters may also be applicable for conical punches. Indeed, as can be seen from Fig. 8.6(a), (b) and (e), good agreement is also obtained between the model predictions and the experimental data for sandwich panels struck by conical-nosed projectiles which are represented by the triangle (Δ) in Fig. 8.6(a) and (b) and the solid symbols in Fig. 8.6(e). Figures 8.10(a) and (b) show photographs of two identical panels with 7.0 mm thick GRP skins and 25 mm thick H130 foam core tested with 10.5 mm diameter hemispherical-ended and conical-nosed missiles at impact velocities of 199 m/s and 197 m/s, respectively which lend further support to the above argument.

To a first approximation, the equations developed above may also be applied or adapted to monolithic FRP laminates subjected to missile impact and have been checked against published data on FRP laminates.

For hemispherical-ended and conical-nosed projectiles the empirical constants in the appropriate equations are found to be $A = 0.05$, $\beta_1 = 1/3$, $\beta = 4.5$ for simply-supported single laminates using the data presented above for panels with $H/D < 2$ and $A = 0.016$, $\beta_1 = 1$, $\beta = 4.5$ for fully-clamped monolithic laminates using the data reported by Zhu et al.[11]

Figure 8.11(a) shows comparisons between equation [8.13] (solid line) and the test data for simply-supported GRP single laminates struck transversely by the 10.5 mm diameter hemispherical-ended projectile of 17.9 g mass. It is evident from Fig. 8.11(a) that the model predictions are in good agreement with the experimental data. Figure 8.11(b) demonstrates the comparison between equation [8.13] (solid line) and the experimental results for fully-clamped KFRP single laminates subjected to impact by a 12.7 mm diameter conical-nosed missile with a mass of 28.9 g, reported by
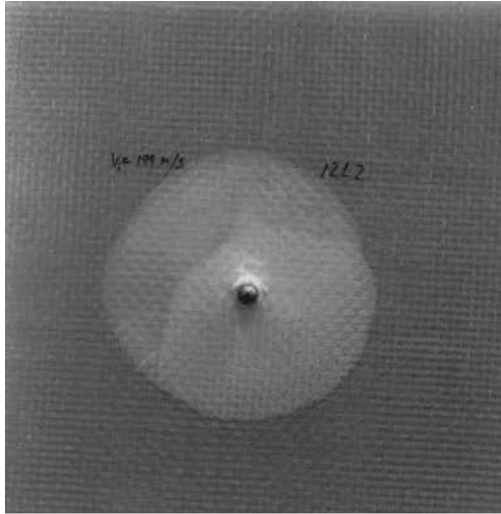
(a)
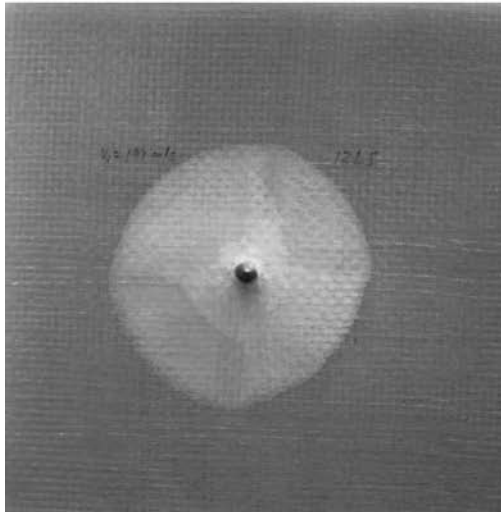
(b)

8.10 Photographs of two 0.3 m square sandwich panels with 7.0 mm thick GRP skins and 25 mm thick H130 foam core tested with 10.5 mm diameter projectiles. (a) hemispherical-ended projectile at an impact velocity of 199 m s^{-1}; (b) conical-nosed missile at an impact velocity of 197 m s^{-1}.
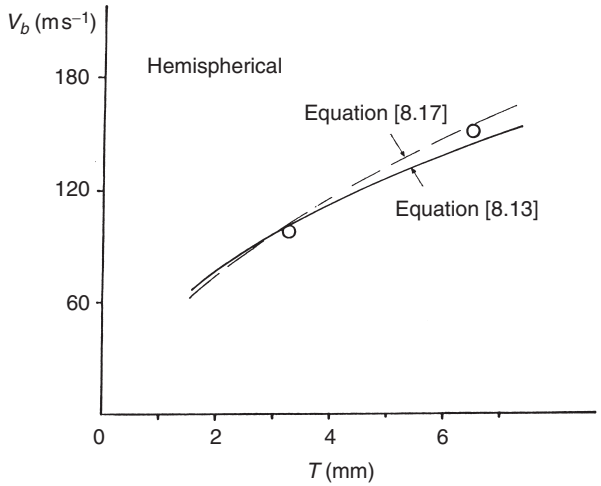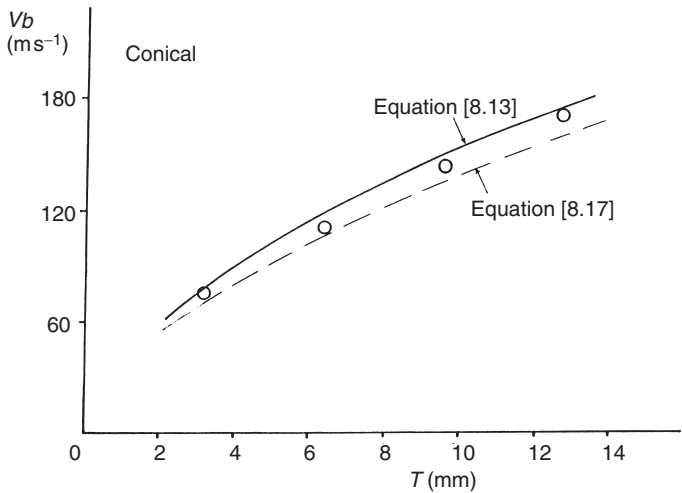
8.11 (a) Comparison of the model predictions with the experimental results for simply-supported GRP single laminates struck by a 17.9 g, 10.5 mm diameter hemispherical-ended missile.
(b) Comparison of the model predictions with the test data for fully-clamped KFRP monolithic laminates impacted by a 28.9 g, 12.7 mm diameter conical-nosed missile. (After Zhu et al.[11])
(c) Comparison of the model predictions with the experimental data for simply-supported GRP single laminates struck by a 20.4 g, 10.5 mm diameter flat-faced missile.
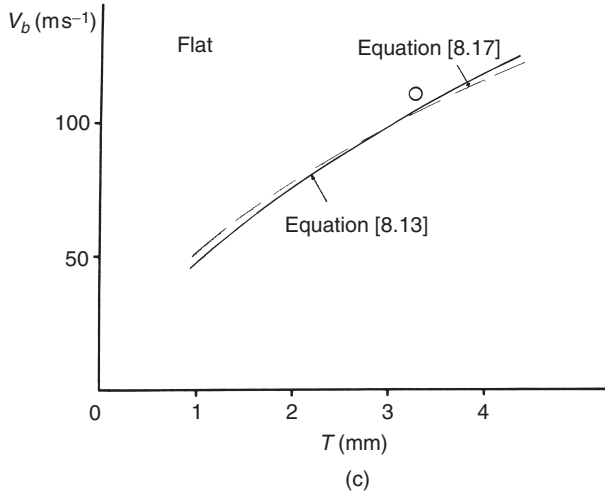
8.11 (cont.)

Zhu et al.[11,12] It is seen from Fig. 8.11(b) that equation [8.13] gives a good fit to the test data reported by those authors when $A = 0.016$, $\beta_1 = 1$ and $\beta = 4.5$ are used.

For flat-faced missiles the appropriate equations developed previously for sandwich panels may be adapted directly to single FRP laminates. It has been observed experimentally that, depending upon the ratio of laminate thickness to missile diameter, either shear plugging (plus delamination) or shear plus tensile fracture (plus delamination) are the predominant failure mechanisms in the perforation of monolithic FRP laminates subjected to impact by flat-ended projectiles. It is further assumed that this critical value for T/D is to be determined empirically and may be taken as $\frac{1}{4}$. Thus, one obtains

$$\frac{E_{pi}}{\phi \sigma_u TD^2} = \frac{\pi}{2}\left(\frac{\tau_{13}}{\sigma_u}\right)\left(\frac{T}{D}\right) + 0.016\left(\frac{L}{D}\right) \qquad [8.19]$$

for $T/D \leq 1/4$ (i.e. thin single FRP laminates), and

$$\frac{E_{pi}}{\phi \sigma_u TD^2} = \frac{\pi}{2}\left(\frac{\tau_{13}}{\sigma_u}\right)\left[\frac{1}{2} - \frac{1}{16}\left(\frac{D}{T}\right)\right] + \frac{\pi \varepsilon_f}{8}\left[1 - \frac{1}{4}\left(\frac{D}{T}\right)\right] + 0.016\left(\frac{L}{D}\right) \qquad [8.20]$$

for $T/D > 1/4$ (viz. thick monolithic FRP laminates).

Figure 8.11(c) shows the comparison of equation [8.13] which incorporates equation [8.19] (solid line) with the limited test data obtained for simply-supported single GRP laminates struck by a 20.4 g, 10.5 mm diame-

ter flat-faced projectile. It is seen from Fig. 8.11(c) that the model predictions are in good agreement with the limited experimental data.

Figures 8.12–8.14 show comparisons of equation [8.13] with the recently obtained high velocity perforation data for glass fibre-reinforced polymeric laminates struck transversely by flat-faced, hemispherical-ended and conical-nosed (90° cone) missiles, respectively. It is seen from Fig. 8.12 that equation [8.13] incorporating equation [8.20] (solid line) predicts well the ballistic limits at relatively low velocities but underpredicts the ballistic limits at higher velocities for the GRP laminates subjected to impact by flat-faced missiles. It is also seen from Fig. 8.13 and 8.14 that equation [8.13] incorporating equation [8.11] (solid line) overpredicts the ballistic limits compared to the experimentally obtained values for the GRP laminates when struck by hemispherical-ended and conical-nosed projectiles.

The predictions by the newly developed wave-dominated model for high velocity perforation of FRP laminates/sandwich panels are also presented in Fig. 8.6(a–d), Fig. 8.11(a) and (c) and Figs. 8.12–8.14. In the theoretical calculation,[1] $\rho_t = 1650\,\text{kg/m}^3$, $\sigma_e = 225\,\text{MPa}$ and Γ has been evaluated to be $\Gamma = 2$, 1.5 and $2\sin(\theta/2)$ for flat-faced, hemispherical-ended and conical-nosed missiles, respectively.[23] Here θ is the cone angle of a conical-nosed missile. It is clear from Fig. 8.5(a–d) and Fig. 11(a) and (c) that the high velocity perforation model, equation [8.17], is in reasonable agreement with the experimental data.[1] It is also clear from Fig. 8.12–8.14 that equation [8.17] predicts well the high velocity perforation of the GRP laminates examined in Mines et al.[14]

The high velocity perforation model is also compared in Fig. 8.11(b) with the ballistic perforation of KFRP laminates impacted by a 28.9 g, 12.7 mm diameter conical-nosed missile investigated in Zhu et al.[11] In the theoretical calculation, $\rho_t = 1231\,\text{kg/m}^3$, $\sigma_e = 145\,\text{MPa}$ and $\theta = 60°$.[11] It is seen from Fig. 8.11(b) that the model predictions (equation [8.17]) are in good agreement with the test results.

The applicability of the models is dictated by the range of impact parameters examined in the present investigations. For example, the range of impact velocities studied lies between 0 and 305 m/s from which the empirical models have been derived. Furthermore, the empirical constants in the models have mainly been determined from the present experiments conducted on GRP laminates and sandwich panels with such laminates as skins and with foam cores and, strictly speaking, these constants are valid only for the material systems investigated. Therefore, care should be exercised when the model with these empirical constants is applied to other material systems though it has been shown to give good representation for KFRP laminates.

From the comparisons between the empirical models and the high veloc-
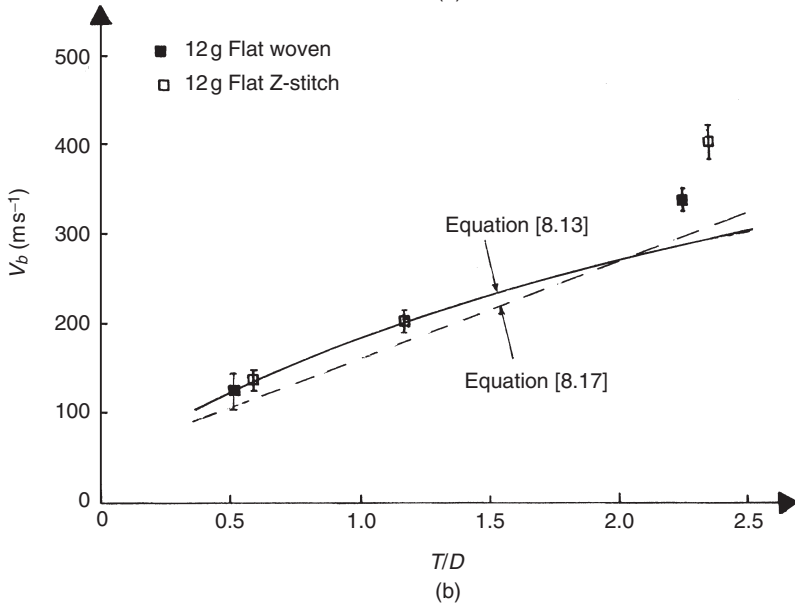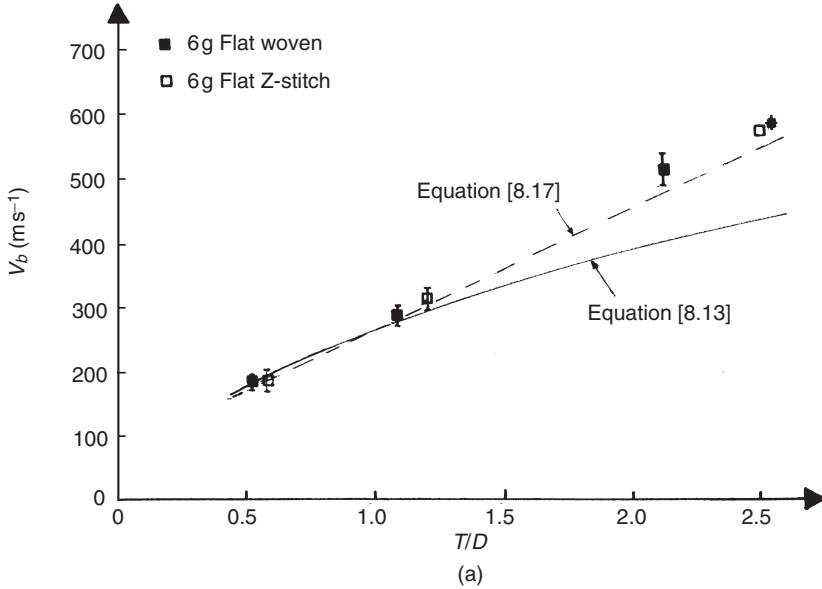
8.12 Comparison of the model predictions with the experimental data for fully-clamped GRP single laminates struck by a 7.6mm diameter flat-faced missile. (a) G = 6g; (b) G = 12 g. (After Mines et al.[14])
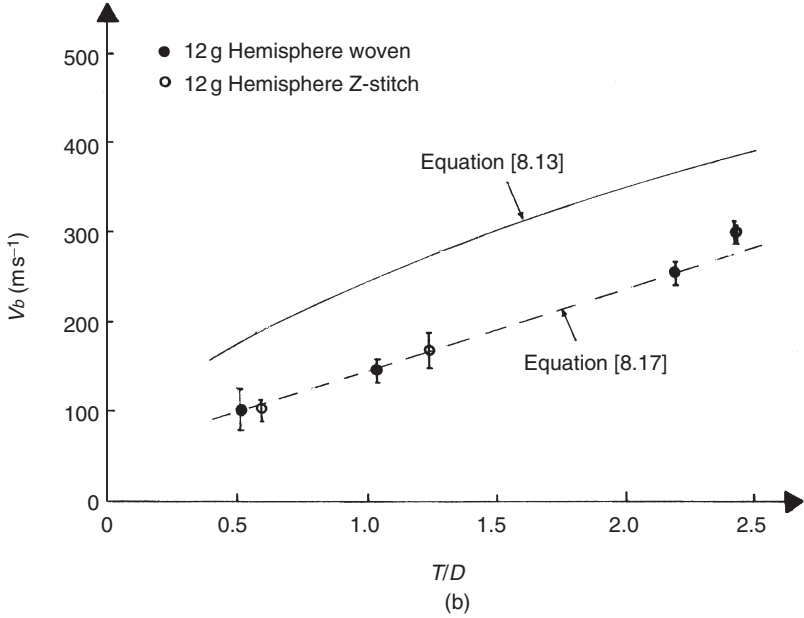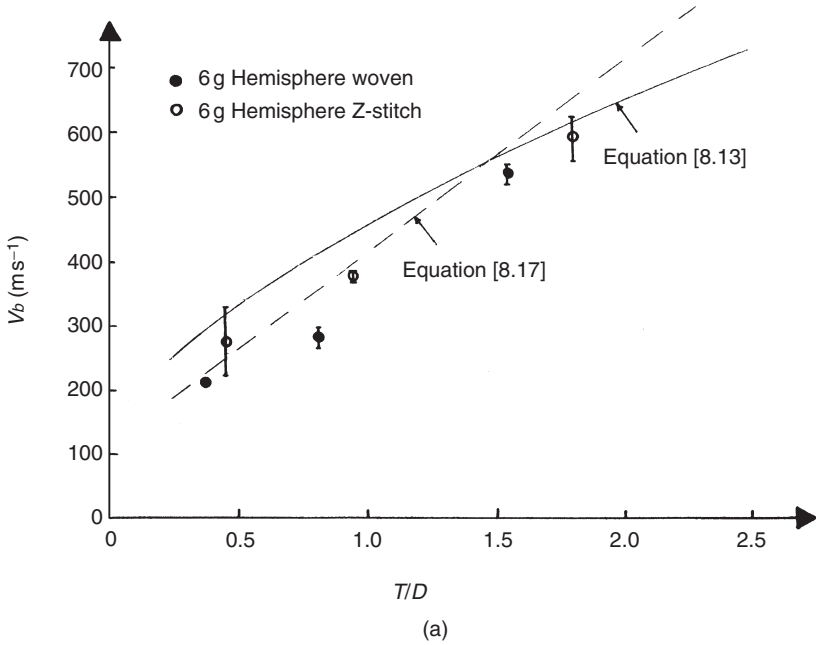
8.13 Comparison of the model prediction with the experimental data for fully-clamped GRP single laminates struck by hemispherical missiles. (a) D = 10 mm; G = 6 g; (b) D = 7.6 mm, G = 12 g. (After Mines *et al.*[14])
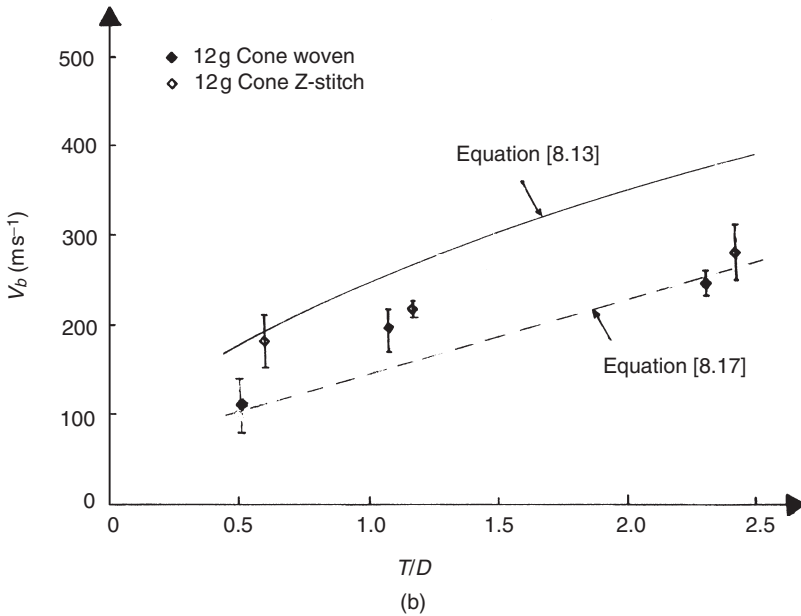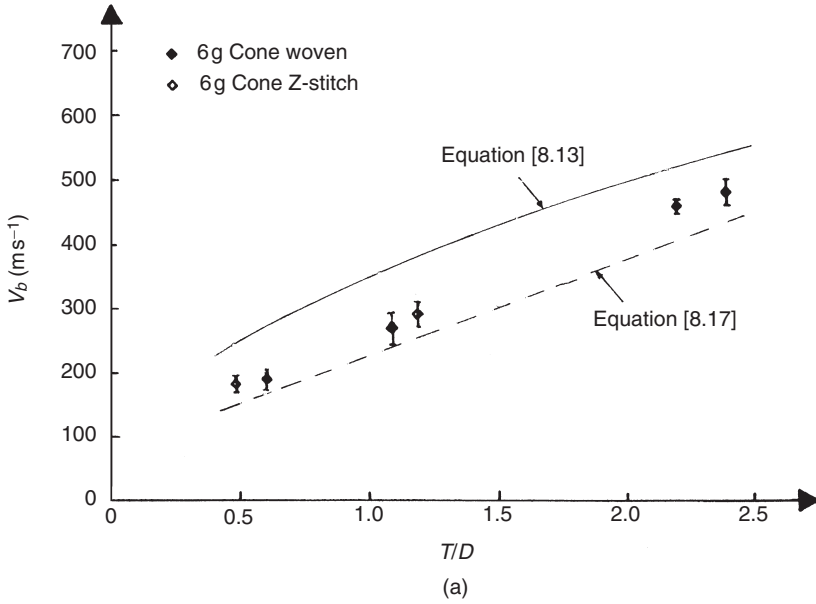
8.14 Comparison of the model predictions with the experimental data for fully-clamped GRP single laminates struck by a 7.6 mm diameter conical-nosed missile. (a) $G = 6$ g; (b) $G = 12$ g. (After Mines *et al.*[14])

ity perforation model and the available experimental data there exists a critical condition at which a change takes place in the mode of deformation from global response (low velocity impact) to localized deformation (wave-dominated response). It is very difficult to determine the critical condition either theoretically or experimentally, and this needs to be further investigated in a future study.

8.6   Conclusions

The results of quasi-static, drop-weight and ballistic impact tests performed on triple- as well as twin-skinned sandwich panels and single laminate skins using flat-faced, hemispherical-ended and conical-nosed indenters/projectiles with initial impact velocities up to 305 m/s have been briefly reported and discussed. Typical load-displacement characteristics under quasi-static and dropped object loading have been presented. Ballistic limits (perforation energies) have been determined and a classification of the responses deduced from the test data obtained.

Experimental evidence has shown that ballistic impact on FRP laminates and sandwich panels with such laminates as skins and with foam cores may be categorized into two regimes, viz. low velocity impact and wave-dominated response.

Based on the experimental observations, dimensional analysis has been used to derive empirical equations that predict the penetration and perforation energies of fibre-reinforced plastic (FRP) laminates and sandwich panels with such laminates as skins and with foam cores subjected to quasi-static and impact loading by flat-faced and hemispherical-ended indenters. It is shown that the empirical formulas correlate well with the available data from experiments carried out by the authors and others. It is also shown that, to a first approximation, the formula obtained for hemispherical-tipped indenters is applicable to conical-nosed punches.

A new model has also been developed for the high velocity perforation of FRP laminates and sandwich panels struck transversely by flat-faced, hemispherical-ended and conical-nosed missiles. It is found that the model predictions are in good agreement with the recently published[14] high velocity perforation data.

Future investigation should be directed towards clearly defining the respective ranges of impact parameters for which the models developed in Sections 8.4.1 (i.e. low velocity impact) and 8.4.2 (wave-dominated response/high velocity perforation) apply and engaging in detailed modelling of the range of failure mechanisms which control the failure of the laminates. Such investigation should lead to a methodology for optimising the design of FRP laminates and sandwich panels against impact loading.

References

1 Wen H M, Reddy T Y, Reid S R and Soden P D, 'Indentation penetration and perforation of composite laminates and sandwich panels under quasi-static and projectile loading', *Key Eng Mater*, 1988 **141–143** 501–52.

2 Reddy T Y, Wen H M, Reid S R and Soden P D, 'Penetration and perforation of composite sandwich panels by hemispherical and conical projectiles', *Trans ASME, J Pres Ves Technol*, 1988 **120** 186–94.

3 Reid S R, Wen H M, Soden P D and Reddy T Y, 'Response of single skin laminates and sandwich panels to projectile impact', in *Composite Materials for Offshore Operation – 2*, (S S Wang, J J Williams and K H Lo, eds), pp 593–617. American Bureau of Shipping, 1999.

4 Abrate S, 'Impact on laminated composite materials', *Appl Mech Rev*, 1991 **44**(4) 155–90.

5 Abrate S, 'Impact on laminated composites: recent advances', *Appl Mech Rev*, 1994 **47**(11) 517–43.

6 Rutherford K L, 'Indentation and penetration resistance of composite materials to pointed projectiles', unpublished UK DRA Report, 1992.

7 Zhao Y, Pang S S and Griffin S A, 'Force-indentation study of transversely isotropic composite materials using a conical-tip indenter', *Composites Eng*, 1991 **1**(6) 393–402.

8 Greaves L J, 'Failure mechanisms in GFRP armour', unpublished UK DRA Report, 1992.

9 Greaves L J, 'Progress in modelling the perforation of GFRP by ballistic projectiles', unpublished UK DRA Report, 1994.

10 Reid S R, Reddy T Y, Ho H M, Crouch I G and Greaves L J, 'Dynamic indentation of thick fibre-reinforced composites', in *High Rate Effects on Polymer, Metal and Ceramic Matrix Composites and Other Advanced Materials* (Y D S Rajapakse and J R Vinson, eds), AD-Vol **48** ASME, 71–9, 1995.

11 Zhu G, Goldsmith W and Dharan C K H, 'Penetration of laminated Kevlar by projectiles – I. Experimental investigation', *Int J Solids Struct*, 1992 **29**(4) 399–420.

12 Zhu G, Goldsmith W and Dharan C K H, 'Penetration of laminated Kevlar by projectiles – II. Analytical model', *Int J Solids Struct*, 1992 **29**(4) 421–36.

13 Lee S-W R and Sun C T, 'Dynamic penetration of graphite/epoxy laminates impacted by a blunt-ended projectile', *Composites Sci Technol*, 1993 **49** 369–80.

14 Mines R A W, Roach A M and Jones N, 'High velocity perforation behaviour of polymer composite laminates', *Int J Impact Eng*, 1999 **22** 561–88.

15 Moriarty K and Goldsmith W, 'Dynamic energy absorption characteristics of sandwich shells', *Int J Impact Eng*, 1993 **13**(2) 293–317.

16 Goldsmith W and Sackman J L, 'An experimental study of energy absorption in impact on sandwich plates', *Int J Impact Eng*, 1992 **12** 241–61.

17 Evans K E, 'Design of doubly curved sandwich panels with honeycomb cores', *Composite Struct*, 1990 **17** 95–111.

18 Allen H G, *Analysis and Design of Sandwich Structures*, Oxford, Pergamon Press, 1969.

19 Vinson J R, 'Optimum design of composite sandwich panels subjected to uni-axial compression', *AIAA J*, 1988 **24** 1690–6.

20 Bernard M L and Lagace PA, 'Impact resistance of composite sandwich panels', *J Reinforced Plastic Composites*, 1989 **8** 432–45.

21 Kosza P and Sayir M B, 'Failure patterns in the core of sandwich structures under impact loading', *Int J Impact Eng*, 1994 **15**(4) 501–17.

22 Wen H M and Jones N, 'Semi-empirical equations for the perforation of plates by a mass', in *Structures Under Shock and Impact – II*, (P S Bulson, ed), pp 369–80. Computational Mechanics Publications, Southampton and Boston, Thomas Telford, London, 1992.

23 Wen H M, 'Predicting the penetration and perforation of FRP laminates struck normally by a projectile with different noseshapes', *Composite Structures*, 2000 **49** 321–9.

High-velocity impact damage to polymer matrix composites

R C TENNYSON AND C G LAMONTAGNE

9.1   Introduction

One of the major concerns involving the use of light-weight fibre-reinforced composites is their susceptibility to impact damage. Delamination (or inter-laminar fracture), surface spallation and laminate penetration constitute various modes of failure resulting from impact loads. Low-velocity impacts are associated with delamination damage, especially that caused by blunt-headed projectiles. This inter-laminar debonding primarily reduces the local bending stiffness and thus can affect the bending and buckling behaviour of the structure. In the latter case, local buckling can induce further delamination growth which can lead to overall global weakening of the structure. Such damage has been reported to cause as much as a 40% reduction in static and fatigue strength.[1,2] Low-velocity impacts have also been shown to reduce cylindrical shell buckling strengths by as much as 25 ~ 35%.[3]

As impact energy is increased, delamination coupled with surface spallation can occur, followed by penetration of the laminate. Figure 9.1 shows photomicrographs of front and rear face spallation damage to a graphite/PEEK laminate. An enlarged view of the damage associated with surface spallation and through-thickness delamination can be seen in Fig. 9.2. The 'ballistic limit' defines that energy which is required for a projectile to penetrate to the rear face of the laminate. Such cases are characterised by front face spallation, localised delamination below the surface (easily detected by ultrasonic C-scan) and an 'impact hole' just reaching the rear face. Beyond the ballistic limit, higher energy impacts produce all of the above features coupled with a crater hole, rear face spallation and ejecta plumes emanating from both sides of the laminate. Figure 9.3 presents photomicrographs of a crater hole viewed from the front and rear faces of a graphite/epoxy tube due to an actual micrometeoroid hypervelocity impact recorded on an experiment aboard a NASA satellite (LDEF, 1984–1990). Again, spallation damage is visible.
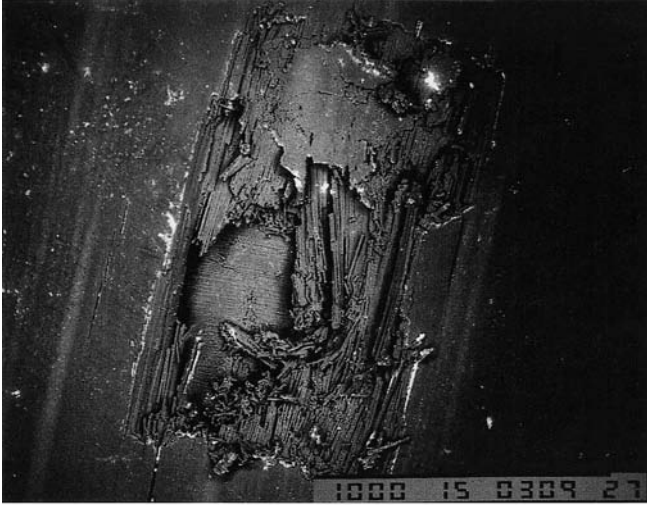
Front (x50)
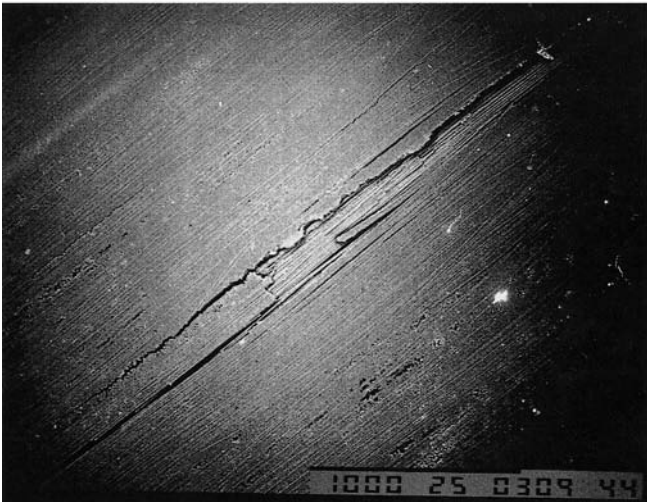
Back (x35)

9.1 Impact damage on front/back faces.
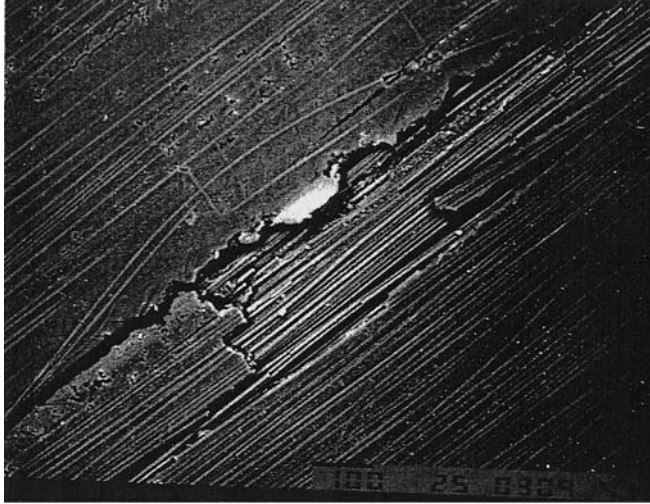
Back (x 100)
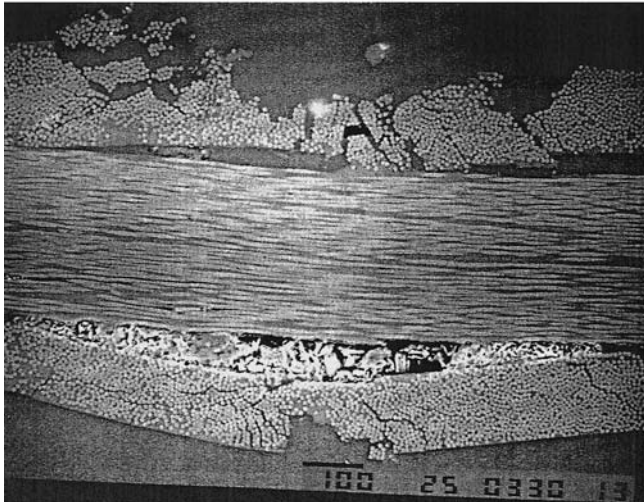
Cross-section (x 100)

9.2 Impact damage on back face and through-thickness of graphite/epoxy laminate.

Front (x 35)

Back (x 35)

9.3 SEM Photographs of micrometeoroid/debris impact/exit holes for graphite/epoxy tube (SP-288/T300, $[\pm 43°]_{4s}$).

One of the dangerous features of hypervelocity impact is the debris plume emanating from the rear face. These ejecta particles can impact adjacent structures and components within the interior of the impacted structure. This of course includes human occupants residing inside a containment vessel such as the cylindrical habitat structures of the International Space Station (ISS), presently being deployed over the next several years. The ejecta from such hypervelocity impacts (i.e. at typical orbital velocities ≥7 km s^{-1}) also travel at comparable speeds and can thus penetrate other structures causing much enhanced damage.[4] Whereas the hypervelocity impacting particle produces an irregular shaped 'hole' or crater (typically 2.5–3 times larger than the particle diameter) on first hitting a laminate, the subsequent fracture of the particle and composite material at the impact site results in a debris plume containing 10–100 fold more particles that spread in a spherical or tear-drop pattern. Depending on the distance traveled and 'cone' angle, these particles produce an impact pattern and damage zone many times larger than the original crater. For composite shell structures, this secondary damage from the debris plume can lead to major structural failure.[4]

Hypervelocity impact conditions are most likely to occur on spacecraft in low earth orbit (LEO, 200–1000 km altitude). They are vulnerable to impact damage resulting from collisions with natural micrometeoroids (≤1 cm diameter) and orbital debris (known as the MOD environment). Micrometeoroids originate from planetary or asteroidal collisions and cometary ejecta. Artificial space debris consists of everything from spent satellites and rockets to aluminum oxide fuel particles, paint chips and fragmentation objects from collisions of these bodies in orbit. A plot of the MOD environment as a function of altitude and particle size is presented in Fig. 9.4. This chart does not depict the enhanced micrometeoroid fluxes that occur when the earth passes through periodic 'showers' that can produce flux increases of 5–10 times that of the 'natural' background. In some isolated cases, these fluxes can reach as high as 10^5 times the background (such as the Leonid meteor storms in November 1998 and 1999).

Fibre-reinforced polymer matrix composites are used extensively in spacecraft structures and satellite components such as antenna struts, panels and low distortion frames. The largest composite structure in space is the Canadian robot arm mounted on all of the Space Shuttles. A much more complex robot consisting of graphite IM7/PEEK cylinders has been assembled for the ISS Remote Manipulator System. Perhaps the greatest spacecraft application of composites is the Iridium telecommunications satellite constellation currently in orbit (~66 satellites) which employs carbon/epoxy laminates on the satellite exterior panels. Clearly, with the high cost of replacement of spacecraft, and particularly with the presence of humans in
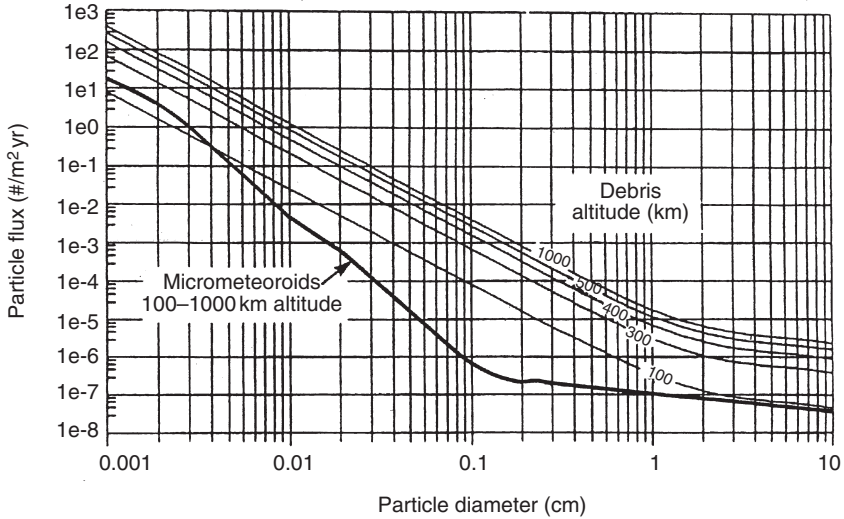
9.4 Micrometeoroid and orbital debris flux as a function of altitude (NASA CR # BB000883A, January 1991).

some cases, it is essential that the effects of hypervelocity impacts on materials and structures must be understood in order to evaluate risks and provide for the safe and reliable design of these systems. This is particularly true for composite materials where the data base is scarce and their utilisation is increasing. This chapter reviews hypervelocity impact damage to composites, with special emphasis on test data obtained on graphite epoxy and PEEK laminates. Sufficient data have been obtained to provide some insight on the major parameters governing the initial impact and debris damage that occurs.

9.2   Hypervelocity impact (HVI) tests on composites

Studies of HVI damage to composite materials and structures can be classified into three categories: flat plate laminates, tubes/cylinders, and composite laminate/sandwich structures.

In the first category, a large number of graphite/epoxy, graphite/PEEK and Kevlar®/epoxy laminates have been investigated.[5–13] Early work by Yew et al.[5,6] on graphite/epoxy plates was done at the NASA Johnson Space Center (JSC), USA using their light gas gun facilities. A wide range of plate thicknesses was studied, including quasi-isotropic configurations. Later, Christiansen[13] reported on a more detailed series of tests in which both high and low modulus graphite/epoxy laminates were tested, including tubes. Again, various target thicknesses were used and different impact angles

employed. It was found that fibre modulus has a greater effect than lay-up. Lower energy impact tests were conducted on both graphite/epoxy and PEEK laminates,[8] but the parametric range was small. A subsequent study focusing on PEEK/IM7 and AS-4 flat plates was reported,[9] where varying thickness laminates of different lay-ups were tested. These experiments were conducted at JSC covering a wide range of projectile energies, including some cylinder tests as well. Most of the data reported to-date are for normal impact conditions, although some results have been obtained for oblique angles.[12,13] In Lamontagne et al.,[12] the experiments were undertaken at the University of Kent, UK using their light gas gun. It was observed that for oblique angle impacts, the debris cloud does not follow the line of flight of the projectile. Moreover, the cone angle associated with the debris cloud is not symmetric about the projectile impact velocity vector. Design charts derived from much of the test data reported in the above references will be described later.

In comparison, HVI tests on composite tubes and cylinders are few in number.[13–16] Of particular interest in these studies is the effect of the debris plume on the damage to the opposing wall. As noted earlier, the energy associated with the ejecta particles at orbital impact velocities is sufficiently high that structural failure of a cylinder under compressive loading can occur when the damage zone is large enough.[4]

Studies of HVI damage to composite laminate/sandwich panels have been reported for honeycomb[17–20] and various heat shield materials.[21] An extensive data base has been compiled for normal and oblique impacts on honeycomb/woven carbon fibre/epoxy structures.[20] This data has been used to determine the ballistic limit which showed a strong dependence on impact angle. Additional data were published[21] for graphite/epoxy laminates bonded to different types of heat shield material combinations subjected to normal hypervelocity impact conditions. Substantial data were obtained on the correlation of entry hole size and impactor energy.

This chapter focuses on HVI damage to composite laminates only, with special emphasis on graphite/epoxy and PEEK materials.

9.3   Entry impact damage

The entry crater or hole size produced by the impact of a particle with a composite laminate can be correlated with the parameter (as suggested by Christiansen[13]) $[Et\rho_t/D_p\rho_p]^{1/3}$ where E is the projectile's energy (J), t is the target thickness (mm), D_p is the projectile diameter (mm), ρ_t and ρ_p are the densities of the target and projectile, respectively. The entry crater is defined as D_c which is the equivalent diameter of a circle that encompasses the same area as the irregularly shaped hole. The projectile energy E is calculated as $\frac{1}{2} m\, V_n^2$ where V_n is the normal velocity component of the projectile

▽ Auburn GRE (SiC)	▽ Auburn PEEK (SiC)	■ JSC PEEK (Al)
● SwRI PEEK (Al)	⊞ USAF #1 PEEK (Al/Nylon)	▫ Austin GRE (Al)
▲ Eagle GRE (low E & Al)	✕ USAF PEEK #2 (steel)	△ MSFC PEEK (Al)
+ SSRMS PEEK (Al)	⊠ UKC PEEK (Al)	—— Regression

$$D_c = 1.05 \sqrt[3]{E \frac{t}{D_p} \frac{\rho_t}{\rho_p}}$$

Crater diameter (mm)

$$\sqrt[3]{E \frac{t}{D_p} \frac{\rho_t}{\rho_p}} \ [\sqrt[3]{J}]$$
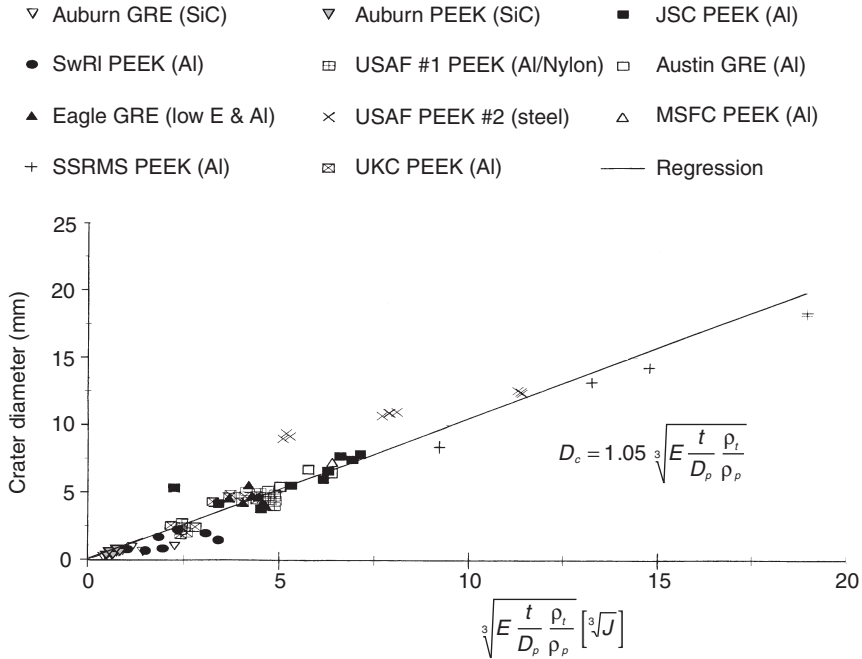
9.5 Equivalent crater diameter as a function of impact energy
parameter.

velocity V and is given by $V \cos \theta$, where θ is the angle of V relative to the surface normal. Based on the AS-4 and IM7graphite/PEEK laminate test data described in Tennyson and Shortliffe,[4,11] Fig. 9.5 illustrates the correlation between D_c and the energy parameter using a regression line forced to pass through zero. A variety of laminate lay-ups and thicknesses were tested under normal impact conditions using aluminum spheres of different diameters. Included in this plot are test results on AS-4graphite/PEEK cylinders[16] and graphite/epoxy plates.[13,8,5] In the latter case, some data from unpublished contract reports are also included. These results were obtained for a broad range of projectile diameters (0.4–9.13 mm), travelling at velocities from 4 to 7.5 km/s, for a variety of materials including glass, nylon, steel and SiC.

More recent oblique angle impact tests were conducted on AS-4 graphite/PEEK flat plate laminates[12] of different thicknesses using aluminum spheres of diameter 1–2 mm over a velocity range of 4.5–5.5 km/s. Impact angles of 0°, 30° and 45° were investigated. These results (UKC) are also plotted in Fig. 9.5 where it can be seen that reasonable correlation with normal impact data was found based on the normal velocity component.

NASA JSC HIT-F shot #A2704
Target: SSRMS boom #1
Projectile diameter: 3.2 mm
Velocity: 6.4 km s^{-1}
Impact angle: 0°
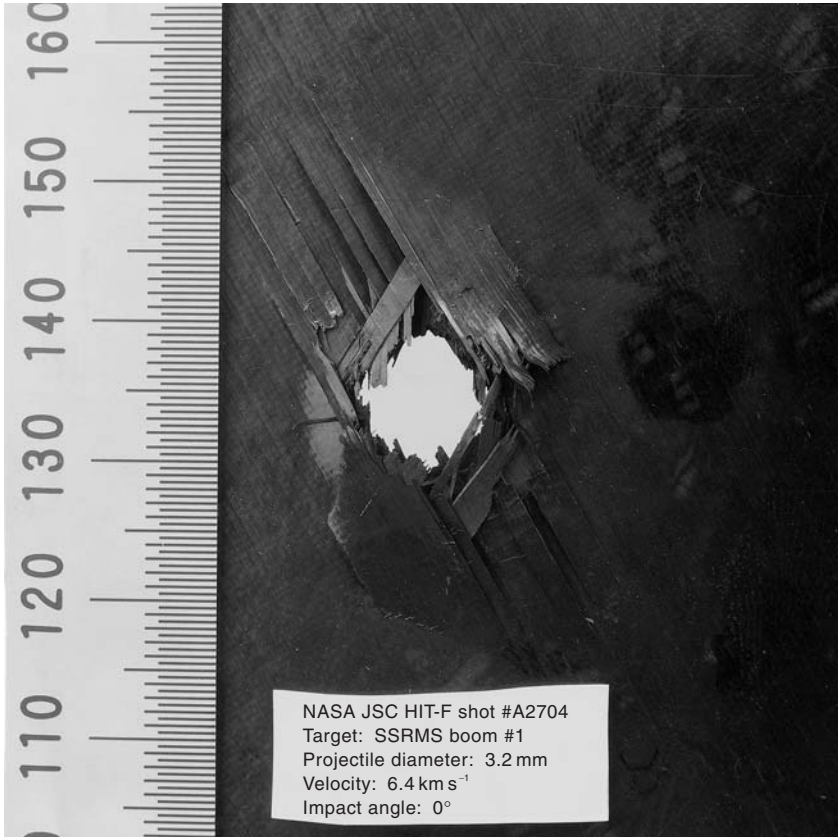
9.6 Photograph of crater and front face spallation damage due to hypervelocity impact on graphite/PEEK laminate.

From a structural design point of view, the entry damage on the front face is an important parameter for assessing the overall reduction in stiffness, strength or long-term fatigue life due to crack propagation from this damaged region. The entry damage zone includes the crater hole and associated delamination/surface cracking area, as can be seen in the photograph shown in Fig. 9.6. As in the case of the hole diameter calculation, this region can also be defined by an 'equivalent entry damage diameter' parameter. Using earlier data,[4,8,11] the entry damage diameter is plotted as a function of a reduced energy parameter in Fig. 9.7. Included in this graph is the regression curve based on C-scan measurements of the sub-surface damage zones. It can be seen that even though the delamination lies below the surface, the enhanced area is only about 20% greater than the visible surface area.

To estimate probable damage for a given projectile impactor size, it is

▽ Auburn GRE (SiC)   ▽ Auburn PEEK (SiC)   ■ JSC PEEK (Al)

● SwRI PEEK (Al)   × USAF #1 PEEK (Al/SiC) —— Regression

—— C-Scan regression   △ UKC PEEK (Al)

$$D_{C\text{-}scan} = 4.04^3 \sqrt{E \frac{t}{D_p}}$$

$$D_{entry\ damage} = 3.73^3 \sqrt{E \frac{t}{D_p}}$$

$$\sqrt[3]{E \frac{t}{D_p}} \quad \left[\sqrt[3]{J}\right]$$
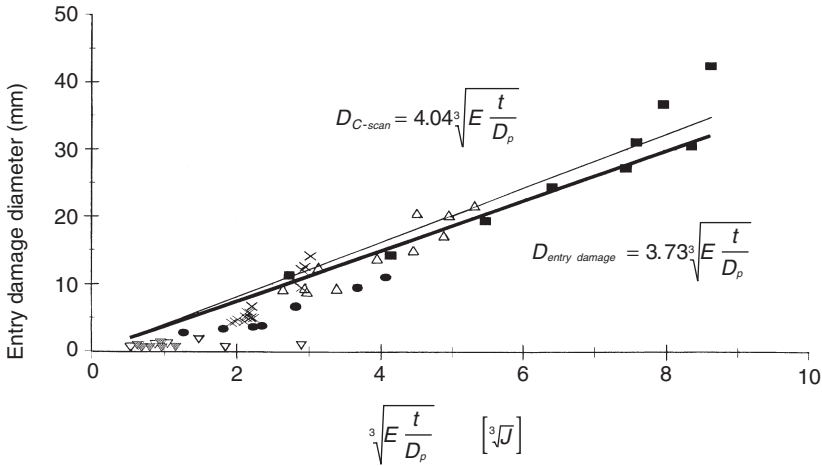
9.7 Equivalent entry damage diameter as a function of impact energy parameter (visible and C-Scan).

useful to correlate the measured crater diameters with the known impactor diameters. Figure 9.8 presents this plot based on the above experiments. The regression curve was constructed only through the PEEK data. There appears to be no energy dependence when one considers complete penetration tests. However, for projectile diameters below 1 mm, it is apparent that the hole diameter can be taken as equal to the particle diameter.

Rear face spallation damage on the impacted laminate is also an important parameter for assessing overall entry damage. Using the same data base, Fig. 9.9 illustrates the correlation of the equivalent damage diameter with the reduced energy parameter. The regression analysis indicates that this damage area is comparable to that observed on the front face for a given energy parameter.

9.4   Secondary debris cloud

Once the projectile has impacted and penetrated the laminate, two debris clouds are formed. These clouds or plumes of ejecta, formed by the disintegration of the wall material and the projectile, emanate from both the front and rear faces of the laminate. For high-velocity impacts, it has been found that the velocity of the ejecta is comparable to that of the impactor

▽ Auburn GRE (SiC)   ▼ Auburn PEEK (SiC)   ■ JSC PEEK (Al)

● SwRI PEEK (Al)   × USAF #1 PEEK (Al/nylon) □ Austin GRE (Al)

▲ Eagle GRE (low E & Al)   —— Regression   △ UKC PEEK (Al)
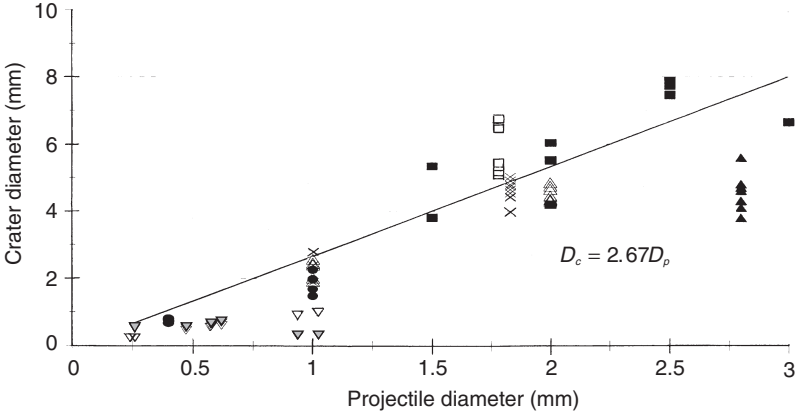
9.8 Equivalent crater diameter as a function of projectile diameter.

■ JSC PEEK (Al)   ● SwRI PEEK (Al)   × USAF #1 PEEK (Al/SiC)

—— Regression   △ UKC PEEK (Al)
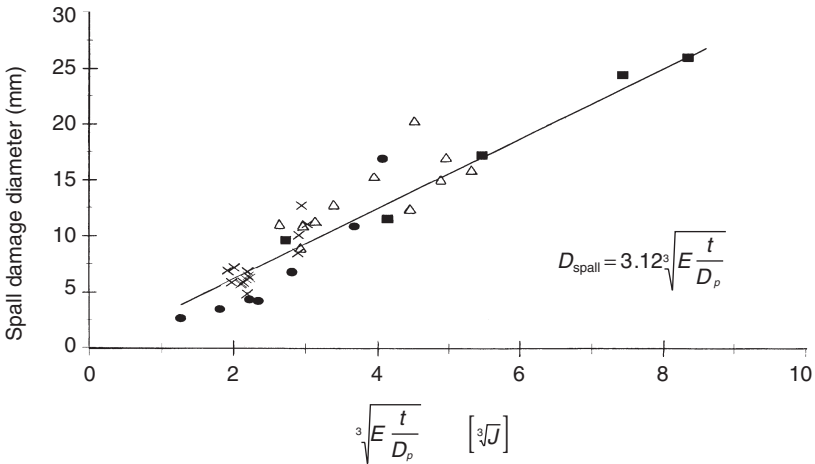
9.9 Equivalent rear face spall diameter as a function of impact energy
    parameter.

for the range of parameters studied.[16] Consequently, the ejecta energy in the secondary debris cloud emanating from the rear face can be sufficiently high as to penetrate another adjacent composite laminate. Depending on the separation distance and the plume cone angle, damage areas much larger than the impact crater hole can occur.

To demonstrate this process, consider the high speed photographs (Fig. 9.10) of an aluminum projectile (~9 mm diameter) impacting a composite cylindrical shell constructed of IM7/PEEK material, 19 plies thick (~2.7 mm) and 33 cm in diameter. The cylinder is a symmetric, balanced laminate (+/–43° with a single 0° centre ply). A Cordin high speed camera capable of snapping 80 frames over an elapsed time of 100 μs was used to record this impact.[16] These frames show the early formation of the debris cloud and the subsequent growth of the spherical shaped plume of ejecta. Impact of the debris cloud with the rear wall of the cylinder results in the large damage area visible in the photograph of Fig. 9.11. Analysis of the debris plume velocity reveals that the cloud tip travelled at approximately the same velocity as the projectile. The damage resulting from this debris cloud impact (Fig. 9.11) contains many holes in the rear wall. This region is defined by a 200 mm diameter circle, thus yielding a damage cone angle of ~69.5°. Because of the multiple penetrations, cracks and spallation damage, the cylinder can be regarded as having a circular 'cutout' for structural analysis purposes. Analysis performed[4] showed a compressive buckling strength loss for this cylinder of over 50%.

Similar results were found in the flat plate IM7/PEEK tests.[11] Using composite witness plates located 330 mm behind the primary impact sites, detailed mapping of the major debris impacts was performed to evaluate the ejecta plume damage and cone angles associated with the various laminate configurations tested. A plot of the semi-angles is presented in Fig. 9.12 as a function of the energy parameter. It is apparent that an average semi-cone angle of ~12.3° can be attributed to these experiments. Figure 9.13 depicts a schematic of one such plume impact where 87 craters were counted within a 120 mm diameter circle. The fact that these craters define holes in the laminate with associated spallation damage testifies to the ejecta energy. The typical projectile used in these tests was 2 mm in diameter and traveled at 6–7 km s^{-1}.

A series of oblique angle impact tests were conducted on 16 and 24-ply AS-4/PEEK plates[12] to investigate plume damage using aluminum projectiles (1 and 2 mm in diameter) at velocities of 4.5–5.5 km/s. Analysis of the debris cloud impacts on adjacent aluminum witness plates showed that in fact there are two classes of damage. A primary damage zone was identified by large craters associated with projectile fragments, with a secondary area containing a larger number of smaller craters having carbon fibres imbedded in the aluminum plate. Figures 9.14 and 9.15 illustrate the
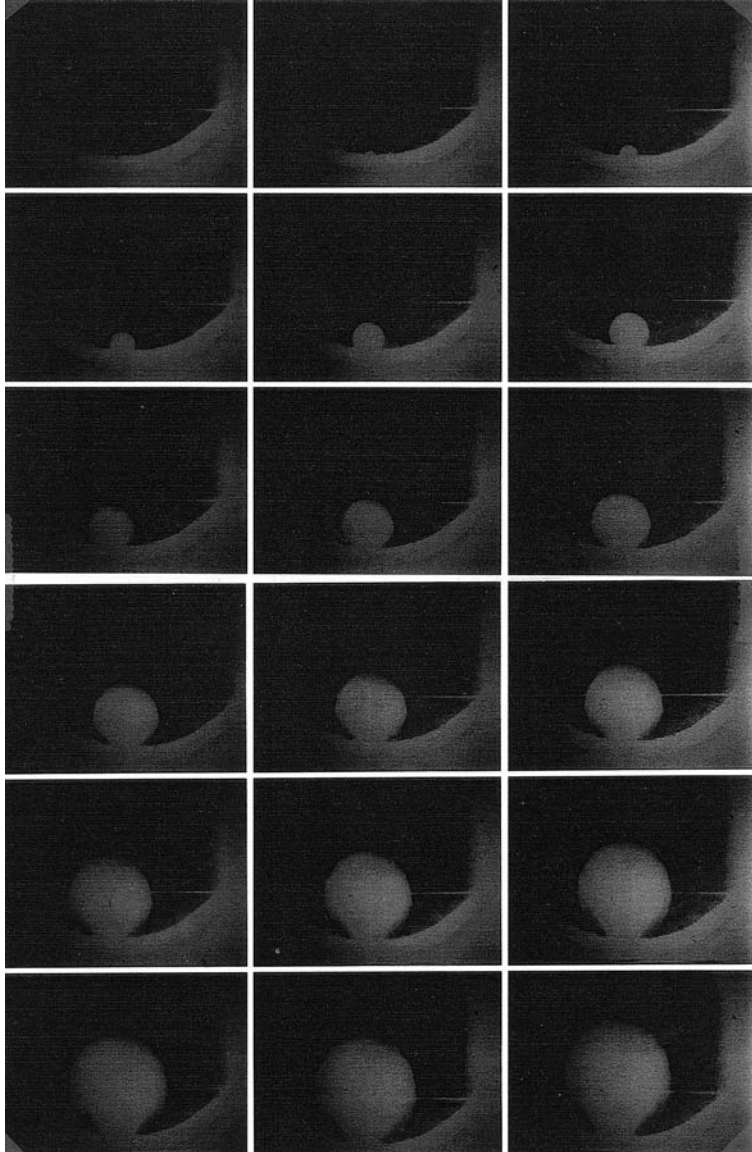
9.10 High speed photographs of debris plume from hypervelocity impact on graphite/PEEK cylinder.

primary (α) and secondary (β) damage cone angles for normal and oblique impacts, respectively. In the latter case, the debris cloud exiting from the rear face of the laminates does not follow the line of flight of the projectile. Thus, a 'turning' angle (ε) was defined as the angle between the initial

9.11 Photograph of crater, front face spallation and debris plume
damage to rear wall due to hypervelocity impact on
graphite/PEEK cylinder.

projectile velocity vector and the centre of mass of the primary damage
zone (see Fig. 9.15). Furthermore, it was also observed that the primary and
secondary cone angles for the oblique tests were not symmetric about the
projectile flight line, thus accounting for the introduction of angles γ and δ
in Fig. 9.15.

Based on these experiments, a plot of the cone angles α and β are pre-
sented in Fig. 9.16 as a function of projectile impact angle. In addition, the
cylinder secondary cone angle results are included for the normal impact
case (~69.5°). In those experiments, one could not identify primary from
secondary impacts. However, using the flat plate results from Fig. 9.12 for
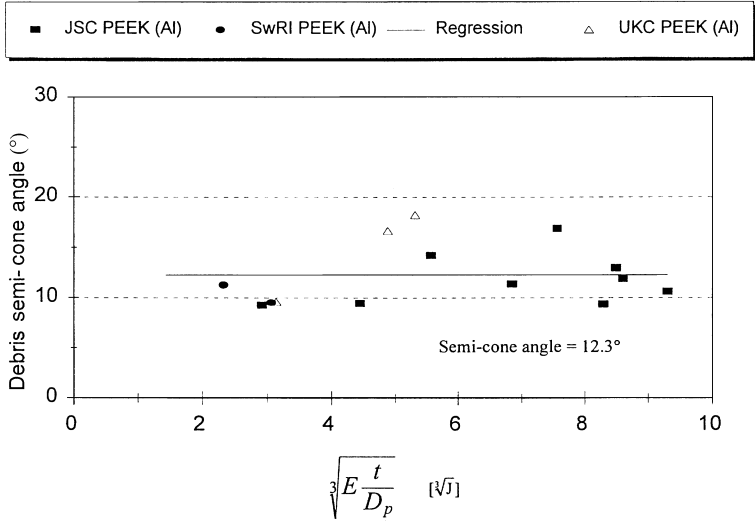
9.12 Plot of semi-cone angle of debris plume as a function of impact energy parameter.
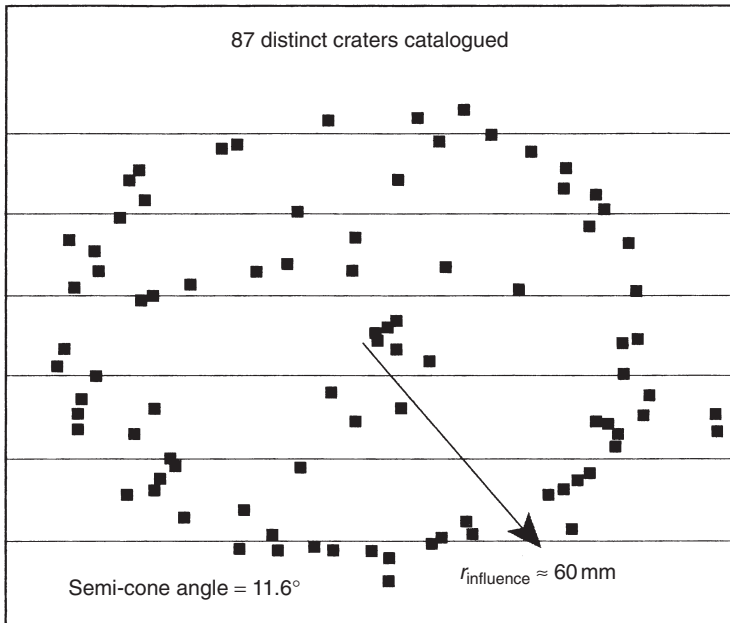
9.13 Plot of secondary debris impact sites on flat plate.
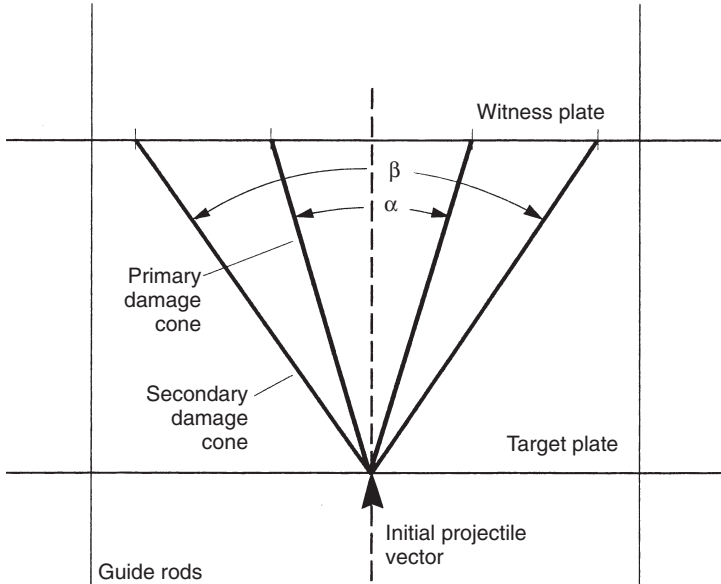
9.14 Schematic defining primary and secondary cone angles for debris plume (normal impact).

primary normal impacts (i.e. only those full penetration cases were plotted), an average primary cone angle of ~23.2° was also plotted. Thus, within the scatter indicated, all normal impact tests correlate reasonably well. Note that for the oblique tests on the 16-ply laminates using a 1 mm projectile, no evidence of primary impact debris was found. Figure 9.17 illustrates the variation of cone angles with the energy parameter using the normal projectile velocity component.

Figure 9.18 presents a plot of the turning angle (ε) as a function of the impact angle. For the limited data available, it appears that ε is independent of ply thickness. This 'turning' effect, although small in magnitude, may well be important in predicting major impact damage relative to the location of critical spacecraft components and determining what protective measures it is necessary to implement.

9.5   Conclusions

This chapter presents an overview of high-velocity impact damage to composite laminates, with specific reference to test data obtained by UTIAS researchers using gun facilities at various laboratories in the USA and UK. Emphasis is placed on graphite/carbon fibre-reinforced epoxy/PEEK laminates of varying thickness and ply orientations. Where possible, pub-
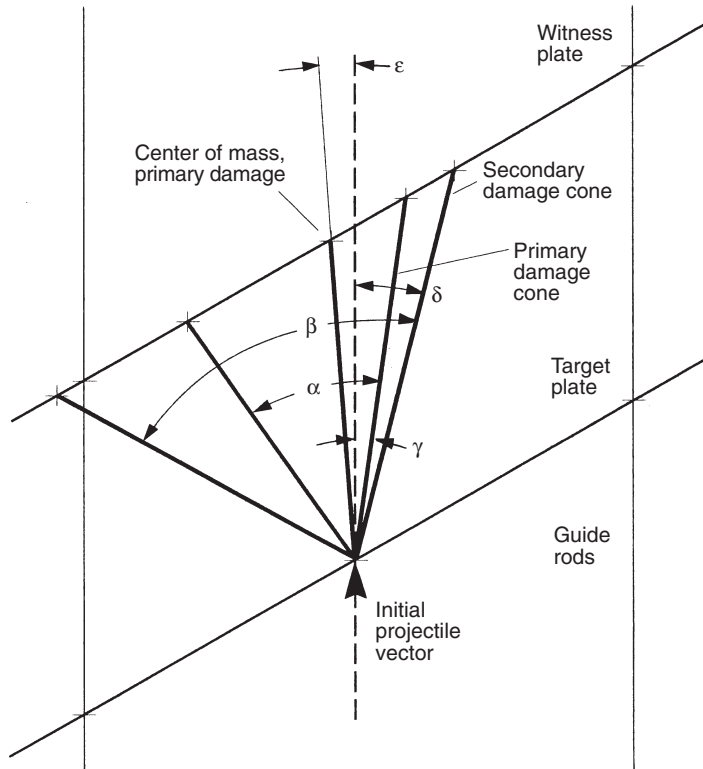
9.15 Schematic defining oblique angle impact geometry associated with debris plume damage.
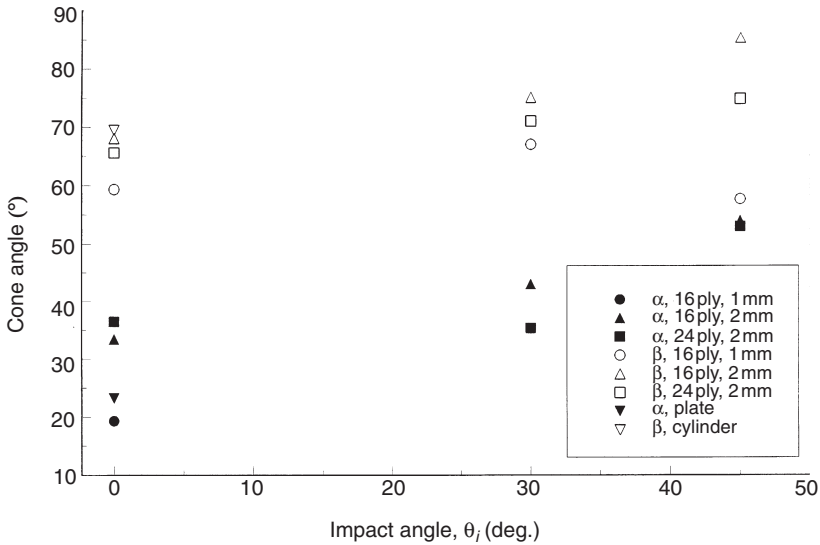
9.16 Plot of primary and secondary debris cone angles for normal and oblique impacts on graphite/PEEK laminates.
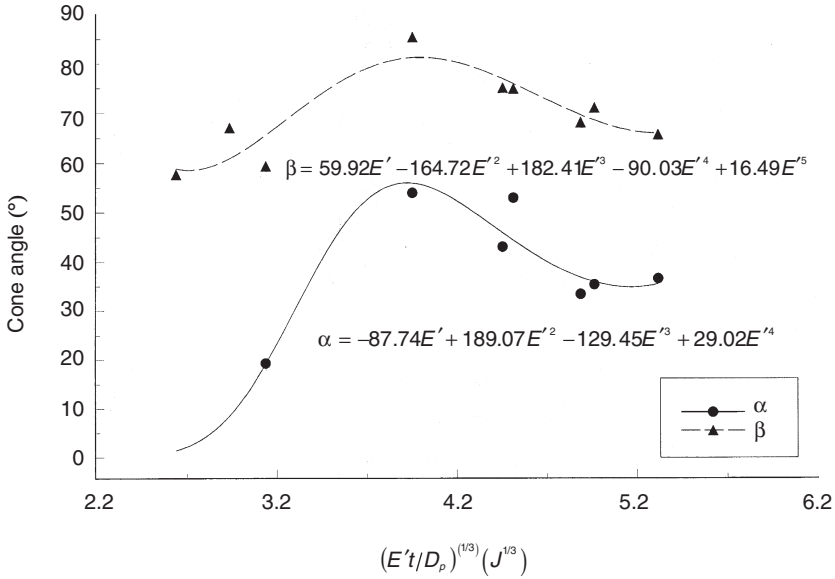
9.17 Plot of primary and secondary debris cone angles as a function of impact energy parameter.
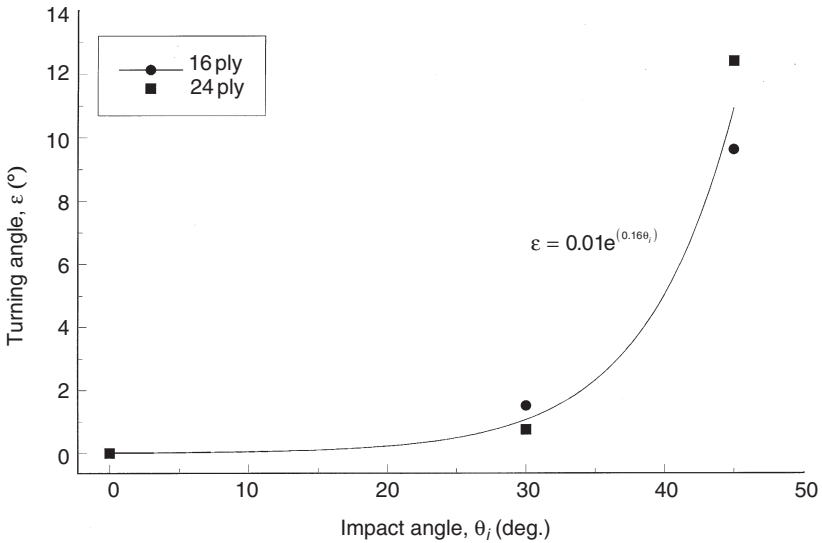
9.18 Plot of primary turning angle as a function of impact angle.

lished data from other researchers are included, although no results are presented on composite/sandwich construction. A variety of projectile materials are noted in the studies, but the bulk of the test data presented is based on aluminum spheres covering a wide range of impact energies. Most of the test results are derived from normal impact experiments, with a limited number of oblique tests also included. Despite the data base available from these studies, no predictive models are proposed. However, a number of observations can be made which might prove useful in the design of composite structures subject to hypervelocity impacts.

First, a linear correlation of crater size and entry damage with an energy parameter has been established, which appears to be independent of laminate lay-up and valid for graphite/epoxy/PEEK materials.

The damage resulting from secondary debris clouds has been amply demonstrated when the ejecta impact another laminate structure. Primary and secondary cone angles describing this debris plume have been identified for both normal and oblique angle impacts. Knowledge of the cone angles is essential in predicting the size of the plume impact area on adjacent structures. It has been shown that the energy of the debris particles can be sufficiently high as to result in major structural damage.

Future research is necessary to enhance the data base, particularly for oblique impacts, and to develop predictive models capable of analysing the damage resulting from hypervelocity impacts on composite structures.

Acknowledgements

References

1 Christoforou A P and Swanson S R, 'Strength loss in composite cylinders under impact', *Trans ASME*, 1988 **110**(2) 180–4.

2 Poe C C and Illg W, 'Strength of a thick graphite/epoxy rocket motor case after impact by a blunt object', 1987, *NASA TM 89099*.

3 Tennyson R C and Krishna Kumar S, 'Delamination damage and its effect on buckling of laminated cylindrical shells', *AGARD Conf. Proc 530, Debonding/Delamination of Composites*, 1989.

4 Tennyson R C and Shortliffe G, 'MOD impact damage on composite materials in space', *Proc 7th Inter Symp, SP-399, Materials in Space Environment*, 1997.

5 Yew C H, Yang C Y and Crews J, 'A phenomenological study of the effect of hypervelocity impacts on graphite/epoxy plates', *Engineering Mechanics, University of Texas at Austin, and NASA JSC*, 1986.

6 Yew C H and Kendrick R B, 'A study of damage in composite panels produced by hypervelocity impact', *Int J Impact Eng*, 1987.

7 Schonberg W P, 'Hypervelocity impact response of spaced composite material structures', *Int J Impact Eng*, 1990.

8 Tennyson R C, Manuelpillai G and Zimcik D G, 'Model for predicting micrometeoroid/debris impacts and damage to composite materials', *1st Eur Conf Orbital Debris SD-01*, 1993.

9 Tennyson R C and Manuelpillai G, 'Prediction of space hypervelocity impact damage in composite materials', *8th CASI Conf Astronautics*, 1994.

10 Silvestrov V V, Plastinin A V and Gorshkov N N, 'Hypervelocity impact on laminate composite panels', *Int J Impact Eng*, 1995.

11 Tennyson R C and Shortliffe G, 'Hypervelocity impact damage to composite structures', *1st Int Conf Composite Science and Technology*, 1996.

12 Lamontagne C G, Manuelpillai G N, Taylor E A and Tennyson R C, 'Normal and oblique hypervelocity impacts on carbon fibre/PEEK composites', *Proc Hypervelocity Impact Symp*, 1998, *Int J Impact Eng*, 1999.

13 Christiansen E L, 'Investigation of hypervelocity impact damage to space station truss tubes', *Int J Impact Eng*, 1990.

14 Unda J, Weisz J, Uriarte A and Capitano R S, 'Residual strength of CFRP tubes subjected to hypervelocity debris impact', *45th Congr of the IAF*, 1994.

15 Yasaka T, Meguro A and Watanabe M, 'Debris impact damage and fragmentation of antenna structure in geostationary orbit', *45th Congr of the IAF*, 1994.

16 Shortliffe G D and Tennyson R C, 'Hypervelocity impact tests on composite boom structures for space robot applications', *J Can Aeronauti Space Inst*, 1997.

17 Taylor E A, Herbert M K, Gardner D J, Thomson R and Burchell M J, 'Hypervelocity impact on spacecraft carbon fibre-reinforced plastic/aluminum honeycomb', *Proc Inst Mech Eng*, 1997 **211**.

18 Taylor E A, Herbert M K and Kay L, 'Hypervelocity impact on carbon fibre-reinforced plastic/aluminum honeycomb at normal and oblique angles', *Proc 2nd Eur Space Debris Conf*, ESA SD-02, 1997.

19 Frost C L and Rodriguez P I, 'AXAF hypervelocity impact test results', *Proc 2nd Eur Space Debris Conf*, ESA SD-02, 1997.

20 Taylor E A, Herbert M K, Vaughan A M and Mcdonnell J A M, 'Hypervelocity Impact on carbon fibre-reinforced plastic/aluminum honeycomb: comparison with Whipple bumper shields', *Proc Hypervelocity Impact Symp*, 1998.

21 Robinson J H, 'Orbital debris impact damage to reusable launch vehicles', *Proc Hypervelocity Impact Symp*, 1998.

Index